uOttawa

L'Université canadienne
Canada's university

FACULTÉ DES ÉTUDES SUPÉRIEURES
ET POSTOCTORALES

uOttawa

L'Université canadienne
Canada's university

FACULTY OF GRADUATE AND
POSDOCTORAL STUDIES

Christopher Rowley
AUTEUR DE LA THÈSE / AUTHOR OF THESIS

Ph.D. (Chemistry)
GRADE / DEGREE

Department of Chemistry
FACULTÉ, ÉCOLE, DÉPARTEMENT / FACULTY, SCHOOL, DEPARTMENT

Transition Path Sampling in Organometallic Catalysis : Overcoming the Rare Event Problem *in Ab* initio Molecular Dynamics
TITRE DE LA THÈSE / TITLE OF THESIS

Tom Woo
DIRECTEUR (DIRECTRICE) DE LA THÈSE / THESIS SUPERVISOR

CO-DIRECTEUR (CO-DIRECTRICE) DE LA THÈSE / THESIS CO-SUPERVISOR

Maria De Rosa

Javier Giorgi

Michael Klein (Temple University)

Alain St-Amant

Gary W. Slater
Le Doyen de la Faculté des études supérieures et postdoctorales / Dean of the Faculty of Graduate and Postdoctoral Studies

Transition Path Sampling in Organometallic Catalysis: Overcoming the Rare Event Problem in *Ab Initio* Molecular Dynamics

Christopher N. Rowley

Thesis submitted to the
Faculty of Graduate & Postdoctoral Studies
University of Ottawa
in partial fulfillment of the requirements for the
Ph.D. degree in the

Ottawa-Carleton Chemistry Institute

Library and Archives Canada

Published Heritage Branch

395 Wellington Street
Ottawa ON K1A 0N4
Canada

Bibliothèque et Archives Canada

Direction du Patrimoine de l'édition

395, rue Wellington
Ottawa ON K1A 0N4
Canada

Your file Votre référence
ISBN: 978-0-494-61380-1
Our file Notre référence
ISBN: 978-0-494-61380-1

NOTICE:

The author has granted a non-exclusive license allowing Library and Archives Canada to reproduce, publish, archive, preserve, conserve, communicate to the public by telecommunication or on the Internet, loan, distribute and sell theses worldwide, for commercial or non-commercial purposes, in microform, paper, electronic and/or any other formats.

The author retains copyright ownership and moral rights in this thesis. Neither the thesis nor substantial extracts from it may be printed or otherwise reproduced without the author's permission.

AVIS:

L'auteur a accordé une licence non exclusive permettant à la Bibliothèque et Archives Canada de reproduire, publier, archiver, sauvegarder, conserver, transmettre au public par télécommunication ou par l'Internet, prêter, distribuer et vendre des thèses partout dans le monde, à des fins commerciales ou autres, sur support microforme, papier, électronique et/ou autres formats.

L'auteur conserve la propriété du droit d'auteur et des droits moraux qui protège cette thèse. Ni la thèse ni des extraits substantiels de celle-ci ne doivent être imprimés ou autrement reproduits sans son autorisation.

In compliance with the Canadian Privacy Act some supporting forms may have been removed from this thesis.

While these forms may be included in the document page count, their removal does not represent any loss of content from the thesis.

Conformément à la loi canadienne sur la protection de la vie privée, quelques formulaires secondaires ont été enlevés de cette thèse.

Bien que ces formulaires aient inclus dans la pagination, il n'y aura aucun contenu manquant.

Canada

ABSTRACT

Since the advent of density functional theory (DFT), computational modelling has become a widely-used tool in organometallic chemistry. This modelling is typically limited to identifying the minima and transition states on the potential energy surface (PES) of a reaction and calculating free energies using the harmonic approximation. *Ab initio* molecular dynamics (AIMD) is an obvious strategy to address these issues. Within these simulations, the full range of thermally accessible structures is explored and anharmonicity is expressed intrinsically. As AIMD simulations are computationally demanding, the maximum length of a simulation is on the order of 100 ps. It is exceedingly rare for a chemical reaction to occur within this time scale, which precludes the use of straightforward AIMD simulations to study organometallic reaction dynamics or to calculate free energy barriers. We attempt to resolve this time scale limitation by adapting Transition Path Sampling (TPS) for use in organometallic chemistry. TPS is a novel Monte Carlo technique to focus an MD simulation on a reactive event. We present new algorithms to generate initial reactive trajectories for TPS and a novel trajectory generation algorithm which uses a variable perturbation size to improve the sampling efficiency. Our first path sampling study investigated the Ru–hydride catalyzed H_2-hydrogenation of olefins. We identified non-RRKM behaviour of the elimination step of a critical reaction intermediate of the hydrogenation catalytic cycle. Through a spectral decomposition of the vibrational energy, we determined the non-RRKM behaviour results from a localization of vibrational energy in the reactive modes of this intermediate following the rate-limiting insertion step. Our second TPS study modelled the *β*-hydrogen transfer chain termination reaction of a zirconocene polymerization catalyst.

The reaction dynamics showed that the barrier of the β-hydrogen transfer is atypically flat due to a Zr–H interaction in the transition state. We subsequently used AIMD to study the equilibrium structure and β-hydrogen transfer free energy profile of this system with and without a counteranion present. These simulations showed that the counteranion-dipole interactions have a significant impact on the preferred configuration of the catalyst and the free energy profile of the transfer.

ACKNOWLEDGMENTS

First and foremost, I would like to thank my thesis supervisor, Professor Tom Woo. Tom has been an inspiring supervisor who has given me enormous freedom to pursue my research in the directions I chose. He has allowed me to take on challenging and ambitious research projects on a great diversity of research subjects, which helped me to develop scientifically to a degree beyond my expectations. Tom has worked tirelessly to provide the group with resources that would be the envy of any graduate student and to afford me every opportunity to succeed. I have also been fortunate enough to get to know Tom personally over the years. Tom is a man of great humour and fairness, as well as devoted husband and father. He has an exceptionally steady temperament and a level of humility that is uncharacteristic of a scientist of his abilities.

I have a great debt of gratitude to my experimentalist collaborators: Professors Darrin Richeson, Deryn Fogg, Warren Piers, Rob Ben, and Keith Fagnou. I am equally grateful to the graduate students I worked with on these collaborations: Heather Foucault, Edwin van der Eide, and Roger Tam. Professor Darrin Richeson deserves special mention as he was willing to pursue one of my ideas in his lab, which was an incredible vote of confidence and resulted in a very productive collaboration. I am also particularly grateful to another collaborator, Professor Deryn Fogg, who was very generous with her time and working with her taught me a great deal about scientific writing. Although most of the research that resulted from these collaborations is not included in this thesis, I consider them some of my proudest accomplishments.

I also want to thank the members of my thesis committee, Professors Alain St-Amant, David Bryce, and Javier Giorgi. Professor St-Amant is an unparalleled advocate

for students and has consistently provided me with candid advice and support. Professor Bryce has also given me a lot of encouragement and working for him as a teaching assistant taught me a lot.

I am also grateful to the members of the Woo group, both past and present. In particular, Dr. Saman Alavi has been an extraordinary scientific resource and teacher. Dr. Serge Gorelsky's incomparable knowledge of transition metal electronic structure has been of great benefit to me. James Hooper and I have worked through our Ph.Ds side-by-side since the beginning and during that time he has been a constant friend and selfless colleague. Professor Nick Mosey was the first Ph.D. student to graduate from the Woo group and I have benefited greatly from his experience and advice, but also his stellar example of accomplishment. I have also had the opportunity to work with three exceptional undergraduates: Peter Dornan, Tianyi Zhang, and Antonia Pandelieva. I could not have hoped for more talented and enthusiastic students to work with.

I also want to thank my parents, Betty and Brian Rowley for their support, as well as my siblings, Janet and Michael. I am also thankful for my good friends Erin, Owen, Amanda, Ian, and Meredith. Finally, I want to thank my friend Sishi, who has been a constant companion throughout my Ph.D.

As an addendum, with great sadness I must also acknowledge two members of the chemistry faculty who have passed away recently. Professor David Bishop, a renowned theoretician, very generously relinquished his office to me not long before his death. Professor Keith Fagnou, who was an extraordinary collaborator, passed away suddenly during the closing months of my Ph.D. These colleagues set the highest standard of personal and professional accomplishment and will be deeply missed.

TABLE OF CONTENTS

Appendices:

LIST OF FIGURES

LIST OF SCHEMES

LIST OF TABLES

LIST OF ABBREVIATIONS

AIMD	*Ab initio* Molecular Dynamics
CDA	Charge Decomposition Analysis
CPMD	Car-Parrinello Molecular Dynamics
DFT	Density Functional Theory
EDA	Energy Decomposition Analysis
ELF	Electron Localization Function
HOMO	Highest Occupied Molecular Orbital
LUMO	Lowest Unoccupied Molecular Orbital
MD	Molecular Dynamics
MM	Molecular Mechanics
PES	Potential Energy Surface
PMF	Potential of Mean Force
QC	Quantum Chemical
QM	Quantum Mechanics
QM/MM	Quantum Mechanics/Molecular Mechanics
TPE	Transition Path Ensemble
RRKM	Rice, Ramsperger, Kassel, Marcus (theory)
TPS	Transition Path Sampling
TS	Transition State
WCA	Weeks–Chandler–Andersen
WHAM	Weighted Histogram Analysis Method

CHAPTER 1

Introduction

1.1. Homogeneous Catalysis

Catalysis plays a fundamental role in modern chemistry.[1] Historically, heterogeneous catalysts, such as metal surfaces and microporous solids, have played the greatest role in chemical industry.[2] More recently, homogeneous catalysts[3] have experienced rapid development and are now used in a wide range of important chemical transformations, such as the hydrogenation of unsaturated bonds,[4,5] olefin metathesis,[6-10] and olefin polymerization.[11,12] In most instances, homogeneous catalysts are transition metal containing compounds, which can effect complex transformations of organic substrates under mild conditions and with high efficiency. These catalysts are now an integral part of the production of polymers,[13] fine chemicals,[14,15] and pharmaceuticals.[16] Synthetic inorganic chemists have been able to achieve exceptional control over the selectivity and activity of these catalysts by variation of the ligands and metal centers of these complexes, which has led to the establishment of organometallic chemistry as a vital branch of inorganic chemistry.

Typically, these organometallic catalysts operate through a series of reaction steps, known as the catalytic cycle. This cycle includes the initiation of the catalyst to its active form, the transformation of the substrate, and the regeneration of the active catalyst. Understanding the catalytic cycle assists researchers in the rational design of improved catalysts and the application of existing catalysts to new reactions. As many of the putative intermediates within a catalytic cycle are short-lived, the individual steps of a catalytic cycle can be difficult to study experimentally. For this reason, there has been intense interest in using computer modelling to provide insight into the inner workings of organometallic catalytic cycles. In the next section, we describe how quantum chemical (QC) calculations are used to model chemical reaction mechanisms, particularly those involving an organometallic reaction.

1.2. Quantum Chemical Studies of Reaction Mechanisms

Since the advent of quantum chemistry in the 1930s, theoretical chemists have played a significant role in the development of chemical theories on structure, bonding, and reactivity. One of the most powerful tools that emerged from this research are the *ab initio* QC methods, which calculate the electronic structures of chemical species from first principles.[17] These methods made it possible to use computational chemistry as a tool to explore unknown chemical structures systematically. With the proliferation of more powerful computers during the 1980s, QC calculations gained wide usage as a tool to model all the species in a reaction mechanism.[18-22]

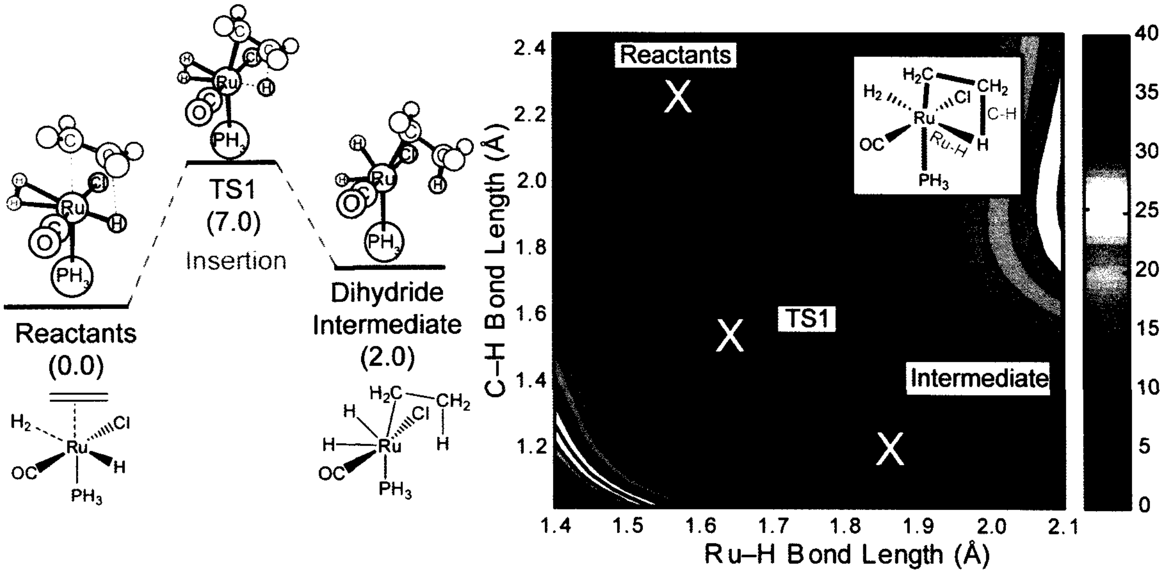

Figure 1.1. Example 2D PES of the insertion of ethylene into a Ru–H bond. The optimized structures of the reactant, intermediate, and transition state are indicated by white X's. Energies are reported in kcal mol^{-1}.

Fundamentally, reaction mechanisms are modeled using QC methods by calculating the potential energy of a chemical complex at a given set of nuclear coordinates. This allows researchers to model the potential energy surface (PES) of a reaction. Using numerical optimization algorithms, the minimum-energy structures on the PES of a reaction mechanism can be located. These minima correspond to stable or metastable species, such as reactants, products, and intermediates. The second stage of a QC mechanistic study is to identify the transition states connecting these minima. The transition state (TS) of a reaction corresponds to a saddle point on the PES, which is the highest point on the minimum energy path between the two minima. This process is illustrated in Figure 1.1, where C–H and Ru–H coordinates of the PES of a ruthenium-hydride ethylene complex studied in Chapter 3 is plotted. The reaction corresponding to ethylene insertion into the Ru–H bond (Figure 1.1, TS1) is apparent in this 2D PES and the reactant, intermediate, and TS are indicated.

The final component of this method is the calculation of free energies. Conventional statistical mechanics can be used calculate the free energies of the optimized structures by assuming each molecule is independent and that the energy within the molecule can be divided into transitional, rotational, and vibrational energy components. The vibrational component of the free energy is the most difficult to calculate, so it is generally approximated by performing normal-mode analysis at the minimum-energy structures and treating the vibrational modes of the complex as quantum harmonic oscillators.[23]

In this branch of modelling, which we refer to as static QC modelling, a reaction mechanism is described by the set of potential energy minima and transition states of the PES. This procedure has obvious value in homogeneous catalysis, as it can be used to model a complete catalytic cycle, including the transition states and short-lived intermediates which are difficult to study experimentally.

Early modelling of organometallic reactions using *ab initio* calculations had only moderate success. Calculations using the relatively inexpensive Hartree-Fock method tended to be unreliable for organometallic structures and reaction energetics.[24] More sophisticated post-Hartree-Fock methods were too computationally demanding for use with most organometallic complexes, so progress in this field was impeded by the lack of an efficient computational method with sufficient accuracy.

1.3. The Rise of Density Functional Theory

The emergence of density functional theory (DFT), an alternative branch of QC, was pivotal in organometallic modelling. Although DFT had been under development through the 1970s, these early DFT methods did not have sufficient accuracy in chemical applications to merit use in the place of established QC methods.[25] Beginning in the late 1980s and early 1990s, new gradient-corrected exchange-correlation functionals were developed,[26,27] which marked the beginning of the widespread adoption of DFT. These methods were demonstrated to have a reasonable computational cost and were sufficiently accurate to give quantitative agreement with experimental structures and activation parameters for many organometallic reactions. This represented a major advance in the modelling of organometallic reactions, as it became possible to perform QC calculations on complex organometallic compounds with sufficient accuracy to explain subtle differences in reactivity and even predict potential catalytic activity.

Since its first applications by Ziegler and coworkers in the late 1980s and early 1990s,[28-38] DFT has been used to a progressively greater extent for modelling organometallic chemistry. A search for articles with the keywords "density functional theory" and "organometallic" shows the extraordinary growth in the application of DFT in the field of organometallic chemistry (Figure 1.2). DFT modelling is now a routine part of this discipline and is frequently used by experimentalists to support and interpret experimental results. In some recent instances, DFT modelling has even been used to evaluate a potential catalyst prior to its synthesis.[39-41]

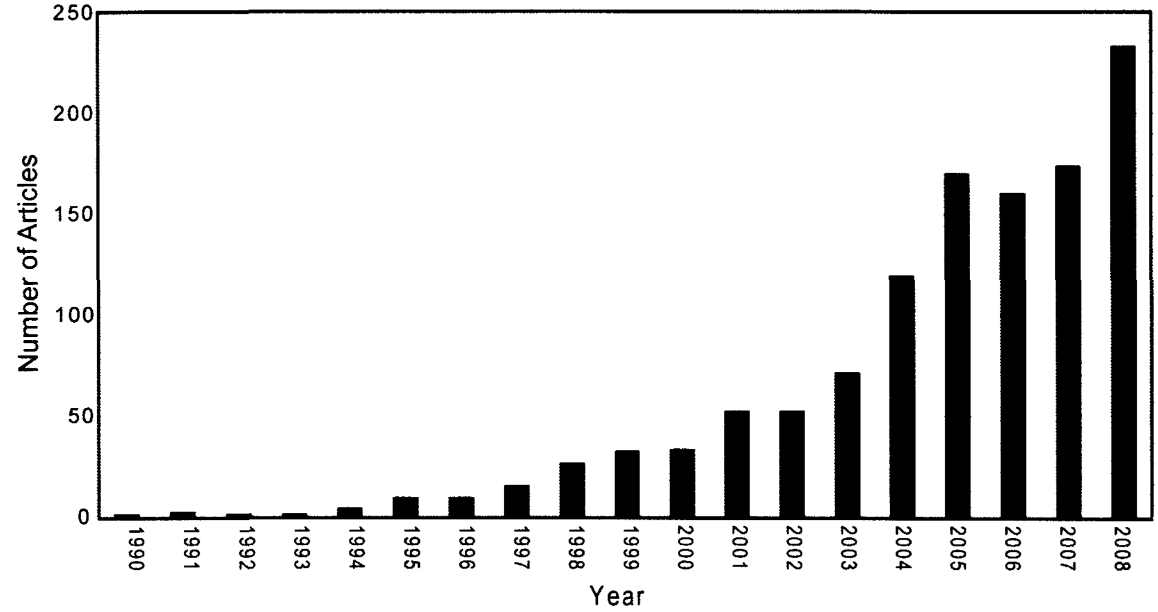

Figure 1.2. Articles published containing the keywords "organometallic" and "density functional theory" by year (SciFinder Scholar 2009, accessed October 9, 2009).

Modern DFT calculations have been found to match experimental reaction energies within 3–7 kcal mol^{-1} and match experimental barrier heights within 5–10 kcal mol^{-1}.[42,43] This accuracy is sufficient to provide an excellent qualitative or even quantitative model of many reactions. In recent years, improvements in DFT methodology have been mostly incremental, such as the introduction of meta-functionals[44] and dispersion corrections.[45,46] More dramatic advances have been made in the speed and scale of DFT calculations due to improvements in computer hardware and the development of more efficient algorithms, such as QM/MM methods.[47]

1.4. Beyond Static Calculations

Although DFT made it possible to calculate realistic PESs of organometallic reactions, the basic procedure of QC modelling has remained the same for the last 30 years; a reaction mechanism is characterized by identifying the minima and transition states on the PES. As some organometallic complexes are highly fluxional,[48] the minimum-energy geometry does necessarily provide a complete description of these structures. Furthermore, in static modelling, vibrational effects on the free energies and reaction rates are calculated using the harmonic oscillator appoximation.[49] The weak metal-ligand interactions in some inorganic complexes can lead to a large degree of anharmonicity, making the harmonic approximation inappropriate. Lastly, static modelling does not provide any direct information about the dynamics of a reaction, a fundamental aspect of chemical reactivity.

Generally, the problems associated with static modelling result from only considering the minimum-energy structures on of the PES rather than the complete range of structures available to the complex at the temperatures at which these catalysts are employed. These problems can be resolved by using molecular dynamics (MD) to simulate the catalytic system. In an MD simulation, the constituent atoms of the system are treated as classical particles and their positions are propagated through time using Newton's equations of motion. This generates a trajectory of the movement of the particles which samples an ensemble of thermally accessible structures. From these ensembles, free energies can be calculated without invoking the harmonic approximation.[50]

MD simulations have been used for decades to model complex systems, such as materials, liquids, and biomolecules.[51] These simulations typically use a computationally inexpensive molecular mechanical (MM) model where the interactions between the atoms are approximated by simple, empirical potentials. Generally, chemical reactions cannot be modeled using MM, as these simple potentials cannot describe the process of chemical bond breaking/making. The natural solution to this problem is to use MD in conjunction with an *ab initio* QC method, such as DFT, which are inherently capable of representing these features. These *ab initio* molecular dynamics (AIMD) simulations have made significant contributions to our understanding of both fundamental[52-54] and complex chemical systems,[55-58] including many notable examples in organometallic chemistry.[59-66] Nevertheless, there are significant challenges in the application of AIMD for modelling organometallic reactions, which has precluded its more extensive use.

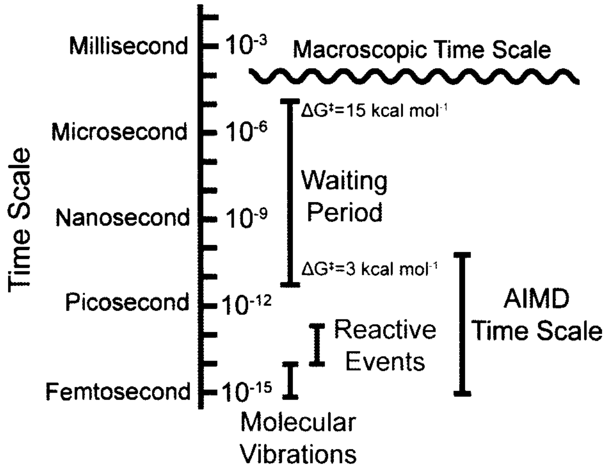

Figure 1.3. Time scales associated with steps of a chemical reaction at 300 K.

The largest challenge to more extensive applications of AIMD in organometallic chemistry is the limits on the time scales of the simulation, which is illustrated in Figure 1.3. Molecular vibrations and fluctuations within the minima are typically of the order of 10–100 fs, so these motions can be sampled within relatively short simulations (~10 ps); however, this also necessitates a time step of approximately 1 fs in order to capture the highest frequency vibrations. The actual reactive event where the barrier is crossed occurs rapidly, on the 20–200 fs time scale,[67] but the waiting period spent in the reactant minimum prior to the reactive event is much longer. This waiting period can be on the order of 20 ps for reactions with small barriers ($\Delta G^{\ddagger} \approx 3$ kcal mol^{-1}), but can be higher than a microsecond for reactive events with larger barriers ($\Delta G^{\ddagger} \approx 10$ kcal mol^{-1}). For example, even the most efficient olefin polymerization catalysts have turnover frequencies of roughly 65000 s^{-1} atm^{-1},[68] which corresponds to a waiting period of 1.5 μs for the olefin-insertion step at atmospheric pressure. As the time steps in these simulations are short and the computational expense of evaluating the DFT potential and gradients at each time step is substantial, 200 ps is currently a rough upper limit on the time scales that can be feasibly simulated using AIMD.

As the waiting period of an activated processes can be orders of magnitude longer than the longest possible MD simulations, these events cannot be studied using a straightforward MD simulation. This is a fundamental challenge in molecular simulation, known as the rare event problem.[69] Even a lengthy 100 ps AIMD simulation is unlikely to observe a single chemical reaction with an activation energy above 4 kcal mol^{-1} (assuming a simulation temperature of 300 K) and this simulation would only sample the minimum the simulation was initiated in. Overcoming this rare event problem is the primary challenge faced by researchers attempting to use AIMD to model the dynamics of organometallic reactions.

1.5. Simulation of Rare Events

A wide variety of techniques have been developed to overcome the rare event problem in MD simulations. One common approach is to impose artificial forces on the simulation to induce the MD simulation to sample the barrier and product state. This encompasses well-established techniques such as umbrella sampling,[70] but also more recent refinements, such as metadynamics,[71,72] adaptively biased molecular dynamics,[73] and the finite-temperature string method.[74] Recently, a second class of rare event simulation methods has emerged that do not require these artificial forces. Instead, transition path sampling,[75] transition interface sampling,[76] and milestoning[77] sample unbiased trajectories which cross the reaction barrier. In the following subsections, we present a brief overview of the two rare event simulation methods used in this thesis: biased sampling and transition path sampling (TPS).

1.5.1. Biasing Sampling

Reaction free energy profiles can be calculated by using an MD simulation to sample the accessible configurations along a reaction coordinate. This sampling allows the probability distribution of this coordinate to be determined, which can be directly related to the relative free energies along this coordinate. This direct strategy for calculating free energy profiles is only effective for reactions where the barrier is thermally accessible and the full profile of interest is sampled sufficiently during the MD simulation. In most chemical reactions of practical interest, the reaction barrier and higher-energy intermediates and products will not be sampled sufficiently in a straightforward MD simulation for the full free energy profile to be calculated

A simple solution to this problem is to use a series of simulations with constraints or restraints imposed to ensure every point along the coordinate is sampled sufficiently. The effect of these forces can then be analytically removed, enabling the calculation of the unbiased free energy profile.[78] Constraint-biased simulations have been used in conjunction with AIMD to model organometallic reactions in a series of papers by Ziegler and coworkers.[60,79-83] This procedure has not been widely adopted by other computational organometallic chemists due to the high computational cost and the technical complexity of these simulations. Biased AIMD simulations have been more extensively used to calculate the free energy profile of organic reactions in solution[84-87] and enzyme-catalyzed reactions.[88-94]

There are several drawbacks to using biases to overcome the rare event problem. The bias is typically defined by the user and selecting an appropriate coordinate to represent the transition is not always intuitive. An inappropriate bias can result in poor sampling, yielding inaccurate results. Although unbiased free energy profiles can be calculated from the biased simulations, the artificial forces imposed on the simulation mask the true dynamics of the system. Dynamic, time-resolved quantities, such as the half-life of a reaction intermediate, the reaction transmission coefficient, and the vibrations involved in the reaction, cannot be examined with a biased MD simulation, as the bias irrevocably changes these properties. In this respect, biased MD simulations only provide a means to sample a reaction coordinate for the calculation of a free energy profile and do not provide true dynamics.

1.5.2. Transition Path Sampling

Transition path sampling (TPS) is a novel Monte Carlo technique that avoids some of the drawbacks associated with biased MD. Rather than introducing a bias or constraint to induce sampling of the reaction barrier, a Monte Carlo procedure is used to focus an MD simulation on the rare event. The result of a TPS simulation is an unbiased ensemble of short, reactive trajectories.[75,95] In recent years, path sampling has been used in several landmark studies of chemical reaction dynamics[96-98] and is emerging as a promising tool to study organometallic reaction mechanisms.[99,100]

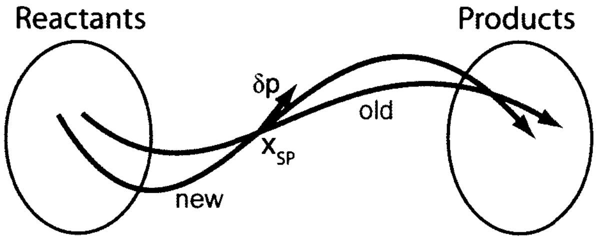

Figure 1.4. Schematic of a shooting move of a TPS simulation. A new trajectory (red) is generated from old trajectory (blue) by a perturbation to the atomic momenta (δp) at the shooting point (x_{SP}).

The fundamental algorithm used in TPS to generate new trajectories is the shooting algorithm (Figure 1.4). This algorithm generates a new reactive trajectory by selecting a random time step from an existing trajectory, perturbing the momenta of the atoms at this step (δp), then integrating forward and backwards in time from this point to generate a distinct trajectory. If this newly generated trajectory is reactive, it is added to the transition path ensemble (TPE). This process can be repeated as many times as is necessary to generate a complete description of the reaction mechanism. The TPE generated from a TPS simulation of the conformational isomerization of the alanine dipeptide is illustrated in Figure 1.5.

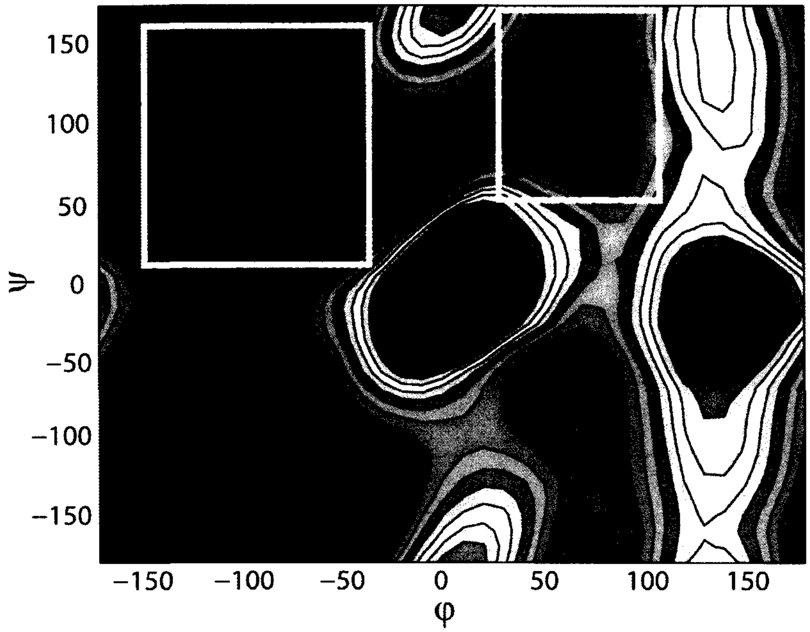

Figure 1.5. Illustration of the path sampling process on the isomerization between two conformations of the alanine dipeptide (indicated by the white boxes) on the φ/ψ torsional free energy surface. The ensemble of reactive trajectories is plotted in black, with one trajectory highlighted in red.

Although it is possible to determine the rate constant of a rare event using TPS, this process is extremely computationally demanding[101] and TPS has only been used for this purpose in a handful of instances.[102-105] TPS has been more frequently used to study the dynamics of important rare events, such as protein conformational changes,[106-110] DNA base-pair binding,[111] lipid bilayer flip-flop transitions,[112] and phase changes.[113-122]

Of particular relevance to this thesis are the instances where TPS has been used to study the dynamics of chemical reactions, including the autoionization in water,[96,123] the pressure induced incorporation of helium into C60, ion dissociation in aqueous acetic acid solutions,[124] and hydride transfer in the enzyme lactate dehydrogenase.[98,125] The ability of TPS to circumvent the rare event problem is of particular value in these studies, as it is necessary to use computationally demanding AIMD to model these bond breaking/making processes.

Perhaps the greatest advantage of using TPS simulations to model chemical reactions is its unique ability to simulate unbiased reaction dynamics, which is the fundamental process underlying a chemical reaction. In contrast to biased MD simulations, TPS trajectories show the true dynamics of the reactive event, so properties such as intermediate lifetimes, recrossing, and the intense vibrations associated with bond-breaking chemical reactions can be examined directly.

1.6. Goals and Overview

In this thesis, we present our research towards extending computational modelling of organometallic reactions beyond the standard static procedures. Specifically, we aim to use MD to explore the full range of possible structures present in a reaction mechanism rather than describing reaction mechanisms exclusively in terms of optimized structures on the PES. The primary obstacle to the use of MD to study organometallic reactions is the rare event problem, which is particularly serious when computationally expensive AIMD simulations are used. To overcome this problem it will be necessary to use established simulation techniques such as biased MD, but also the newly-developed TPS algorithms. As TPS has not been applied to organometallic reactions in the past, new methods will need to be developed to make these studies practical and efficient.

The balance of this thesis is comprised of seven chapters, organized in the chronological order that the research was performed. The following is a brief summary of each chapter.

Chapter 2 describes our attempt to solve the "initial path problem" in TPS. When we began researching TPS, it became apparent that an inherent limitation of TPS is that the researcher must provide an initial reactive simulation of the process under investigation. This is particularly problematic for chemical reactions, where there is generally no obvious means to generate this initial path. Previous TPS studies addressed this issue on an *ad hoc* basis and no general technique had been developed. We devised, implemented, and tested three novel techniques to generate these initial paths for a range of chemical reactions. These methods served as the groundwork for our subsequent applied studies using TPS.

Chapter 3 stems from an exciting collaboration with Professor Deryn Fogg, a synthetic inorganic chemist in our department. In this study, we modeled the catalytic cycle of a mainstay ruthenium-hydride catalyst for the H_2-hydrogenation of olefins using static DFT calculations. Significantly, the catalytic cycle derived from our calculations was distinct from the "textbook" pathway, as an unusual Ru(IV) dihydride intermediate is present in the catalytic cycle. This initial study motivated us to study other aspects of this catalyst in the next two chapters.

In Chapter 4, we present the results of our first application of TPS to an organometallic reaction. TPS was used to examine the reaction dynamics of the ethylene insertion into a Ru–H bond and the subsequent reductive elimination of ethane, which are the critical reactive steps of the catalytic cycle elucidated in Chapter 3. Although our traditional static QC study in Chapter 3 identified a metastable dihydride intermediate in the catalytic cycle, the TPS simulation showed that the lifetime of this intermediate is reduced by non-RRKM effects.

In Chapter 5, we use the results of Chapters 3 and 4 to rationally design a new hydrogenation catalyst. As we had concluded in Chapter 3 that olefin insertion will not occur without the presence of H_2 as a stabilizing 2-electron donor, we evaluated several hemilabile ligands that could stabilize the metal during the insertion. This work was published in the Canadian Journal of Chemistry in a special issue dedicated to Professor Tom Ziegler. As permitted by our faculty, we have included this article in its published form.

In Chapter 6, we present an equilibrium AIMD and TPS study of $Cp_2Zr(CH_2CH_2)(CH_2CH_3)^+$, a model for the olefin-complex of a metallocene polymerization catalyst. These MD simulations show a large degree of fluxional character in metal-ligand interactions, which would not have been apparent using static calculations alone. These studies also illustrate the different time scales of organometallic processes, ranging from facile in-place methyl rotation to the relatively rare β-hydrogen transfer reaction.

In Chapter 7, we expand on our study of $Cp_2Zr(CH_2CH_2)(CH_2CH_3)^+$ to examine the effect of a counteranion ($[CH_3B(C_6F_5)_3]^-$) on the solution configuration and reactivity of this complex. We used equilibrium MD to examine the preferred ion pair orientations and isomerization dynamics. Subsequently, restraint-biased MD was used to calculate the free energy barrier of the β-hydrogen transfer from a series of restrained MD simulations, with and without the counteranion present. To the best of our knowledge, this is the first instance where restraint-biased AIMD has been used to determine the free energy profile of an organometallic reaction.

In Chapter 8, we return to TPS method development. In conventional TPS shooting moves, shooting points near the transition event have a much higher probability of being accepted than shooting points further away. This introduces a degree of inefficiency to these calculations, as some shooting moves that are attempted have effectively no probability of being accepted. In this chapter, we attempt to modify the shooting algorithm reduce this inefficiency.

Chapter 9 is a general discussion of our research results and possibilities for future research in this field.

We have also included four appendices (A–D) to provide more extensive discussion and derivations of some of the theories and methods used in the main text of this thesis. Appendix A describes MD, periodic boundary conditions, and thermostats. Appendix B describes the calculation of free energy profiles using biased MD. Appendix C relates to the RRKM unimolecular reaction rate theory. Appendix D relates to the calculation of free energies using static calculations.

References

1. van Leeuwen, P. W. N. *Homogeneous Catalysis: Understanding the Art*; Kluwer Academic Publishers: Dordrecht, 2004.

2. *Handbook of Heterogeneous Catalysis* Ertl, G.; Knozinger, H.; Weitkamp, J., Eds., 1997.

3. Crabtree, R. H. *The Organometallic Chemistry of the Transition Metals*; 4th ed.; John Wiley and Sons, Inc.: Hoboken, NJ, 2005.

4. Machado, R. M.; Heier, K. R.; Broekhuis, R. R. *Curr. Opin. Drug Discovery Dev.* **2001**, *4*, 745.

5. Clapham, S. E.; Hadzovic, A.; Morris, R. H. *Coord. Chem. Rev.* **2004**, *248*, 2201.

6. Schuster, M.; Blechert, S. *Angew. Chem. Int. Ed.* **1997**, *36*, 2037.

7. Pederson, R. L.; Fellows, I. M.; Ung, T. A.; Ishihara, H.; Hajela, S. P. *Adv. Synth. Catal.* **2002**, *344*, 728.

8. Trnka, T. M.; Grubbs, R. H. *Acc. Chem. Res.* **2001**, *34*, 18.

9. Furstner, A. *Angew. Chem. Int. Ed.* **2000**, *39*, 3012.

10. Grubbs, R. H. *Handbook of Metathesis*; Wiley-VCH: Weinheim, 2003.

11. Ittel, S. D.; Johnson, L. K.; Brookhart, M. *Chem. Rev.* **2000**, *100*, 1169.

12. Gibson, V. C.; Spitzmesser, S. K. *Chem. Rev.* **2003**, *103*, 283.

13. Kaminsky, W. *Macromol. Chem. Phys.* **1996**, *197*, 3907.

14. Parshall, G. W. *Organometallics* **1987**, *6*, 687.

15. Hans-Ulrich, B.; Christophe, M.; Benoît, P.; Felix, S.; Heinz, S.; Martin, S. *Adv. Synth. Catal.* **2003**, *345*, 103.

16. Farina, V.; Reeves, J. T.; Senanayake, C. H.; Song, J. J. *Chem. Rev.* **2006**, *106*, 2734.

17. Szabo, A.; Ostlund, N. S. *Modern Quantum Chemistry: Introduction to Advanced Electronic Structure Theory*; McGraw-Hill Publishing Company: New York, 1989.

18. Bellville, D. J.; Bauld, N. L. *J. Am. Chem. Soc.* **1982**, *104*, 5700.

19. Renugopalakrishnan, V.; Walter, R. *J. Am. Chem. Soc.* **1984**, *106*, 3413.

20. Goddard, W. A., III *Science* **1985**, *227*, 917.

21. Hess, B. A.; Schaad, L. J.; Carsky, P.; Zahradnik, R. *Chem. Rev.* **1986**, *86*, 709.

22. Houk, K. N.; Paddon-Row, M. N.; Rondan, N. G.; Wu, Y. D.; Brown, F. K.; Spellmeyer, D. C.; Metz, J. T.; Li, Y.; Loncharich, R. J. *Science* **1986**, *231*, 1108.

23. See Appendix D for a description of the equations used to calculate free energies using static calculations

24. Ziegler, T. *Can. J. Chem.* **1995**, *73*, 743.

25. Parr, R. G.; Yang, W. *Density-Functional Theory of Atoms and Molecules*; Oxford University Press: Oxford, 1994.

26. Becke, A. D. *Phys. Rev. A: At. Mol. Opt. Phys.* **1988**, *38*, 3098.

27. Becke, A. D. *J. Chem. Phys.* **1993**, *98*, 5648.

28. Ziegler, T.; Tschinke, V.; Becke, A. *Polyhedron* **1987**, *6*, 685.

29. Ziegler, T.; Tschinke, V.; Becke, A. *J. Am. Chem. Soc.* **1987**, *109*, 1351.

30. Ziegler, T.; Tschinke, V.; Ursenbach, C. *J. Am. Chem. Soc.* **1987**, *109*, 4825.

31. Versluis, L.; Ziegler, T. *J. Chem. Phys.* **1988**, *88*, 322.

32. Ziegler, T.; Cheng, W.; Baerends, E. J.; Ravenek, W. *Inorg. Chem.* **1988**, *27*, 3458.

33. Versluis, L.; Ziegler, T.; Baerends, E. J.; Ravenek, W. *J. Am. Chem. Soc.* **1989**, *111*, 2018.

34. Harrod, J. F.; Ziegler, T.; Tschinke, V. *Organometallics* **1990**, *9*, 897.

35. Versluis, L.; Ziegler, T. *Organometallics* **1990**, *9*, 2985.

36. Versluis, L.; Ziegler, T. *J. Am. Chem. Soc.* **1990**, *112*, 6763.

37. Jacobsen, H.; Kraatz, H. B.; Ziegler, T.; Boorman, P. M. *J. Am. Chem. Soc.* **1992**, *114*, 7851.

38. Ziegler, T.; Versluis, L. *Adv. Chem. Ser.* **1992**, *230*, 75.

39. Wang, Y.; Wang, J.; Su, J.; Huang, F.; Jiao, L.; Liang, Y.; Yang, D.; Zhang, S.; Wender, P. A.; Yu, Z.-X. *J. Am. Chem. Soc.* **2007**, *129*, 10060.

40. Houk, K. N.; Cheong, P. H.-Y. *Nature* **2008**, *455*, 309.

41. Wondimagegn, T.; Wang, D.; Razavi, A.; Ziegler, T. *Organometallics* **2008**, *27*, 6434.

42. Friesner, R. A. *Proc. Natl. Acad. Sci. U. S. A.* **2005**, *102*, 6648.

43. Zhao, Y.; Gonzalez-Garcia, N.; Truhlar, D. G. *J. Phys. Chem. A.* **2005**, *109*, 2012.

44. Tao, J.; Perdew John, P.; Staroverov Viktor, N.; Scuseria Gustavo, E. *Phys. Rev. Lett.* **2003**, *91*, 146401.

45. Antony, J.; Grimme, S. *PCCP* **2006**, *8*, 5287.

46. Becke, A. D.; Johnson, E. R. *J. Chem. Phys.* **2005**, *123*, 154101.

47. Bo, C.; Maseras, F. *Dalton Trans.* **2008**, 2911.

48. Gielen, M.; Willem, R.; Wrackmeyer, B. *Fluxional Organometallic and Coordination Compounds*; John Wiley & Sons: Hoboken, NJ, 2004.

49. See Appendix D for a description of the equations used to calculate free energies using static calculations

50. Frenkel, D.; Smit, B. *Understanding Molecular Simulation*; 2nd ed.; Academic Press: San Diego, 2002.

51. Leach, A. R. *Molecular Modelling: Principles and Applications*; 2nd ed.; Pearson Education Limited: Essex, 2001.

52. Marx, D.; Tuckerman, M. E.; Hutter, J.; Parrinello, M. *Nature* **1999**, *397*, 601.

53. Raugei, S.; Klein, M. L. *J. Am. Chem. Soc.* **2001**, *123*, 9484.

54. Kuo, I. F. W.; Mundy, C. J. *Science* **2004**, *303*, 658.

55. Reinhardt, S.; Marian, C. M.; Frank, I. *Angew. Chem. Int. Ed. Engl.* **2001**, *40*, 3683.

56. Tse, J. S. *Annu. Rev. Phys. Chem.* **2002**, *53*, 249.

57. Minary, P.; Tuckerman, M. E. *J. Am. Chem. Soc.* **2005**, *127*, 1110.

58. Mosey, N. J.; Mueser, M. H.; Woo, T. K. *Science* **2005**, *307*, 1612.

59. Margl, P.; Lohrenz, J. C. W.; Ziegler, T.; Bloechl, P. E. *J. Am. Chem. Soc.* **1996**, *118*, 4434.

60. Woo, T. K.; Margl, P. M.; Bloechl, P. E.; Ziegler, T. *J. Phys. Chem. B* **1997**, *101*, 7877.

61. Margl, P. M.; Woo, T. K.; Bloechl, P. E.; Ziegler, T. *J. Am. Chem. Soc.* **1998**, *120*, 2174.

62. Woo, T. K.; Margl, P. M.; Deng, L.; Cavallo, L.; Ziegler, T. *Catal. Today* **1999**, *50*, 479.

63. De Angelis, F.; Fantacci, S.; Sgamellotti, A. *Coord. Chem. Rev.* **2006**, *250*, 1497.

64. Magistrato, A.; Togni, A.; Rothlisberger, U. *Organometallics* **2006**, *25*, 1151.

65. Buhl, M.; Golubnychiy, V. *Organometallics* **2007**, *26*, 6213.

66. Gossens, C.; Tavernelli, I.; Rothlisberger, U. *J. Am. Chem. Soc.* **2008**, *130*, 10921.

67. Zewail, A. H. *J. Phys. Chem. A.* **2000**, *104*, 5660.

68. Haruyuki, M.; Norio, K.; Terunori, F. *Adv. Synth. Catal.* **2002**, *344*, 477.

69. Chandler, D. In *Computer Simulation of Rare Events and Dynamics of Classical and Quantum Condensed-Phase Systems – Classical and Quantum Dynamics in Condensed Phase Simulations*; Berne, B. J., Ciccotti, G., Coker, D. F., Eds.; World Scientific: Singapore, 1998, p 51.

70. Torrie, G. M.; Valleau, J. P. *Chem. Phys. Lett.* **1974**, *28*, 578.

71. Ensing, B.; De Vivo, M.; Liu, Z.; Moore, P.; Klein, M. L. *Acc. Chem. Res.* **2006**, *39*, 73.

72. Alessandro, L.; Francesco, L. G. *Rep. Prog. Phys.* **2008**, 126601.

73. Volodymyr, B.; Christopher, R.; Celeste, S. *J. Chem. Phys.* **2008**, *128*, 134101.

74. E, W.; Ren, W.; Vanden-Eijnden, E. *J. Phys. Chem. B* **2005**, *109*, 6688.

75. Bolhuis, P. G.; Chandler, D.; Dellago, C.; Geissler, P. L. *Annu. Rev. Phys. Chem.* **2002**, *53*, 291.

76. Moroni, D.; van Erp, T. S.; Bolhuis, P. G. *Physica A* **2003**, *340*, 395.

77. West, A. M. A.; Elber, R.; Shalloway, D. *J. Chem. Phys.* **2007**, *126*, 145104/1.

78. Trzesniak, D.; Kunz, A.-P. E.; van Gunsteren, W. F. *ChemPhysChem* **2007**, *8*, 162.

79. Woo, T. K.; Margl, P. M.; Ziegler, T.; Bloechl, P. E. *Organometallics* **1997**, *16*, 3454.

80. Chan, M. S. W.; Ziegler, T. *Organometallics* **2000**, *19*, 5182.

81. Cooper, J.; Ziegler, T. *Inorg. Chem.* **2002**, *41*, 6614.

82. Yang, S.-Y.; Ziegler, T. *Organometallics* **2006**, *25*, 887.

83. Yang, S.-Y.; Xiang, M.-L.; Chen, L.-J.; Xie, G.-B.; Shi, B.; Wei, Y.-Q.; Ziegler, T. *J. Comput. Chem.* **2007**, *28*, 513.

84. Hartsough, D. S.; Merz, K. M., Jr. *J. Phys. Chem.* **1995**, *99*, 384.

85. Blumberger, J.; Klein, M. L. *Chem. Phys. Lett.* **2006**, *422*, 210.

86. Zheng, H.; Zhang, Y. *J. Chem. Phys.* **2008**, *128*, 204106/1.

87. Acevedo, O.; Jorgensen, W. L. *Acc. Chem. Res.*, ACS ASAP.

88. De Vivo, M.; Ensing, B.; Klein, M. L. *J. Am. Chem. Soc.* **2005**, *127*, 11226.

89. Dal Peraro, M.; Vila, A. J.; Carloni, P.; Klein, M. L. *J. Am. Chem. Soc.* **2007**, *129*, 2808.

90. Li, G.; Cui, Q. *J. Am. Chem. Soc.* **2003**, *125*, 15028.

91. Riccardi, D.; Koenig, P.; Guo, H.; Cui, Q. *Biochemistry* **2008**, *47*, 2369.

92. Xu, D.; Guo, H. *J. Am. Chem. Soc.* **2009**, *131*, 9780.

93. Hu, P.; Wang, S.; Zhang, Y. *J. Am. Chem. Soc.* **2008**, *130*, 3806.

94. Wang, L.; Broyde, S.; Zhang, Y. *J. Mol. Biol.* **2009**, *389*, 787.

95. Rowley, C. N.; Woo, T. K. *J. Chem. Phys.* **2007**, *126*, 024110/1.

96. Geissler, P. L.; Dellago, C.; Chandler, D.; Hutter, J.; Parrinello, M. *Science* **2001**, *291*, 2121.

97. van Erp, T. S.; Meijer, E. J. *Angew. Chem. Int. Ed.* **2004**, *43*, 1660.

98. Basner, J. E.; Schwartz, S. D. *J. Am. Chem. Soc.* **2005**, *127*, 13822.

99. Snee, P. T.; Shanoski, J.; Harris, C. B. *J. Am. Chem. Soc.* **2005**, *127*, 1286.

100. Bergeron, D. E.; Coskuner, O.; Hudgens, J. W.; Gonzalez, C. A. *J. Phys. Chem. C* **2008**, *112*, 12808.

101. Dellago, C.; Bolhuis, P. G.; Chandler, D. *J. Chem. Phys.* **1999**, *110*, 6617.

102. Bolhuis, P. G.; Dellago, C.; Chandler, D. *Proc. Natl. Acad. Sci. U. S. A.* **2000**, *97*, 5877.

103. Geissler, P. L.; Dellago, C.; Chandler, D. *J. Phys. Chem. B* **1999**, *103*, 3706.

104. Jorge, R.; Manuel, L. *J. Chem. Phys.* **2001**, *115*, 7285.

105. Vlugt, T. J. H.; Dellago, C.; Smit, B. *J. Chem. Phys.* **2000**, *113*, 8791.

106. Bolhuis, P. G. *Proc. Natl. Acad. Sci. U. S. A.* **2003**, *100*, 12129.

107. Bolhuis, P. G. *Biophys. J.* **2005**, *88*, 50.

108. Chopra, M.; Reddy, A. S.; Abbott, N. L.; de Pablo, J. J. *J. Chem. Phys.* **2008**, *129*, 135102/1.

109. Juraszek, J.; Bolhuis, P. G. *Biophys. J.* **2008**, *95*, 4246.

110. Saen-oon, S.; Schramm, V. L.; Schwartz, S. D. *Z. Phys. Chem. (Muenchen, Ger.)* **2008**, *222*, 1359.

111. Hagan, M. F.; Dinner, A. R.; Chandler, D.; Chakraborty, A. K. *Proc. Natl. Acad. Sci. U. S. A.* **2003**, *100*, 13922.

112. Marti, J.; Csajka, F. S. *Phys. Rev. E* **2004**, *69*, 061918/1.

113. Laria, D.; Rodriguez, J.; Dellago, C.; Chandler, D. *J. Phys. Chem. A* **2001**, *105*, 2646.

114. Leoni, S.; Zahn, D. *Z. Krist.* **2004**, *219*, 339.

115. Zahn, D. *J. Solid State Chem.* **2004**, *177*, 3590.

116. Zahn, D.; Leoni, S. *Z. Kristallogr.* **2004**, *219*, 345.

117. Zahn, D.; Grin, Y.; Leoni, S. *Phys. Rev. B: Condens. Matter Mater. Phys.* **2005**, *72*, 064110/1.

118. Zahn, D.; Hochrein, O.; Leoni, S. *Phys. Rev. B: Condens. Matter Mater. Phys.* **2005**, *72*, 094106/1.

119. Grunwald, M.; Rabani, E.; Dellago, C. *Phys. Rev. Lett.* **2006**, *96*, 255701.

120. Zahn, D. *J. Chem. Theory Comput.* **2006**, *2*, 107.

121. Boulfelfel, S. E.; Zahn, D.; Hochrein, O.; Grin, Y.; Leoni, S. *Phys. Rev. B: Condens. Matter Mater. Phys.* **2006**, *74*, 094106/1.

122. Zahn, D. *Chem. Phys. Lett.* **2008**, *467*, 80.

123. Geissler, P. L.; Dellago, C.; Chandler, D.; Hutter, J.; Parrinello, M. *Chem. Phys. Lett.* **2000**, *321*, 225.

124. Park, J. M.; Laio, A.; Iannuzzi, M.; Parrinello, M. *J. Am. Chem. Soc.* **2006**, *128*, 11318.

125. Quaytman, S. L.; Schwartz, S. D. *J. Phys. Chem. A* **2009**, *113*, 1892.

CHAPTER 2

Generation of Initial Trajectories for Transition Path Sampling of Chemical Reactions with *Ab Initio* Molecular Dynamics

Reproduced in part from: Rowley, C. N.; Woo, T. K. *J. Chem. Phys.* **2007**, *126*, 024110/1.

Abstract

Transition path sampling is an innovative method for focusing a molecular dynamics (MD) simulation on a reactive event. Although transition path sampling methods can generate an ensemble of reactive trajectories, an initial reactive trajectory must be generated by some other means. In this chapter, we have evaluated three methods for generating initial reactive trajectories for transition path sampling with *ab initio* molecular dynamics (AIMD). We have tested each of these methods on a set of chemical reactions involving the breaking and making of covalent bonds: the 1,2-hydrogen elimination in the borane-ammonia adduct, a tautomerization, and the Claisen rearrangement. The first method is to initiate trajectories from the potential energy transition state, which was effective for all reactions in the test set. Assigning atomic velocities found using normal-mode analysis greatly improved the success of this method. The second method uses a high temperature MD simulation and then iteratively reduces the total energy of the simulation until a low temperature reactive trajectory is found. This was effective in generating a low temperature trajectory from an initial trajectory run at 3000 K of the tautomerization reaction, although it failed for the other

two. The third uses an orbital based bias potential to find a reactive trajectory and uses this trajectory to initiate an unbiased trajectory. We found that a HOMO-LUMO bias could be used to find a reactive trajectory for the Claisen rearrangement, although it failed for the other two reactions. These techniques will help make it practical to use transition path sampling to study chemical reaction mechanisms that involve bond breaking and forming.

2.1. Introduction

Ab initio molecular dynamics (AIMD) simulation has emerged as a powerful technique for the study of chemical reactions.[1,2] In an AIMD simulation, the forces acting on the nuclei are determined by a computationally expensive quantum chemical calculation. As a result, AIMD simulation times are limited to the sub-nanosecond regime, even with modern computers. Unfortunately, reactions with modest barriers of 10 kcal mol^{-1} are typically not observed because they require simulation times on the order of microseconds or longer to occur. Furthermore, even when a reaction does occur, most of the simulation time will be spent in the potential energy minima, providing only limited information about the reactive event. Many more reactive trajectories are needed to get a complete description of the reaction mechanism. Addressing these problems will make it possible to apply AIMD to a wider range of chemical systems.

One technique that has the potential to resolve these problems is transition path sampling (TPS), developed by Chandler and coworkers to focus MD simulations on a reactive event.[3,4] This process generates an ensemble of reactive trajectories that can be analyzed to determine reaction mechanisms,[5] activation energies,[6] and rate constants.[7] In conjunction with AIMD, this technique promises to make it possible to study the dynamics of an enormous range of chemical reactions in a way that was previous impractical. To date, TPS using AIMD has been used to study a variety of chemical reactions,[8-12] notably a landmark investigation of the autoionization of water.[13]

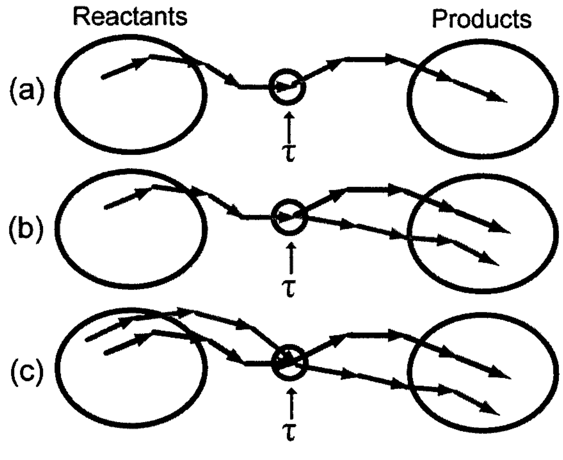

Figure 2.1. An illustration of the shooting algorithm. (a) A point τ is selected from a reactive trajectory and the momenta at that point are perturbed, (b) the trajectory is integrated forward with the new momenta to time T, (c) the trajectory is integrated backwards to time 0. Grey lines represent the old trajectory.

The fundamental algorithm used in TPS to generate reactive trajectories is the shooting algorithm (Figure 2.1). This algorithm generates an ensemble of reactive trajectories by selecting a random time step from a reactive trajectory. The momenta of the atoms at this step are perturbed and the simulation is run forward and backward in time from this point. For deterministic simulations in the microcanonical ensemble, the newly generated trajectory is accepted and added to the transition path ensemble if it connects the products and reactants.[14] This process can be repeated an arbitrary number of times until a sufficient number of reactive trajectories have been found.

Although the shooting algorithm can generate new trajectories given an initial reactive trajectory, transition path sampling does not provide any means for generating this initial trajectory. For some simulations, an initial trajectory can be found by running an MD simulation until the reactive event occurs. As transition path sampling is primarily used for rare events, the length of this simulation would be prohibitively long in many cases. This is especially relevant for AIMD simulations, where the length of the simulations is severely limited by computer resources. For most practical cases, the researcher must generate this initial trajectory using another technique.

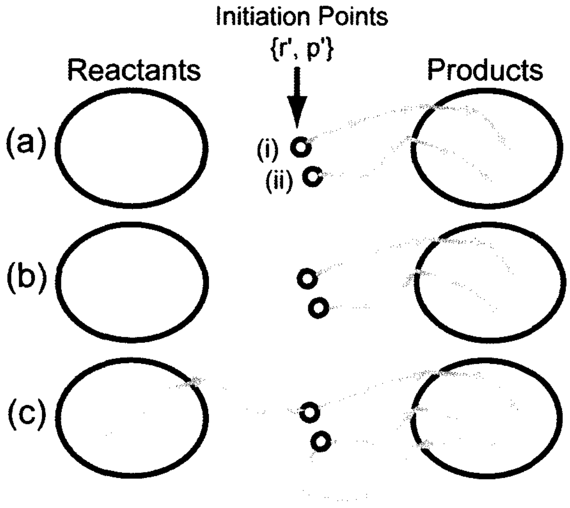

Figure 2.2. An initial trajectory is generated by (a) generating an initiation point with atomic coordinates r′ and atomic momenta p′ (b) integrating forward in time (c) integrating backward in time. Initiation point (i) leads to a reactive trajectory, while initiation point (ii) does not reach the reactants and is therefore unreactive.

In principle, a method such as Action-Derived Molecular Dynamics[15] could be used to find a true dynamical trajectory given product and reactant structures. These methods tend to be computationally demanding, so most transition path studies to date have used simpler methods. The commonly used approaches for finding an initial reactive trajectory generate an initiation point in phase space that is likely to lead to a reactive trajectory when integrated forward and backward in time (Figure 2.2). If the trajectory produced is reactive, it can serve as the initial path for a transition path sampling study. Otherwise, this process can be repeated for a series of initiation points until a reactive trajectory is found. An effective algorithm of this kind generates initiation points with a high probability of leading to a reactive trajectory, thereby reducing the number of attempts needed.

A common technique that has been used in previous transition path sampling studies is to generate an initiation point by estimating reasonable atomic coordinates for a time step of a reactive trajectory in the transition region. The transition region is the section of a trajectory that has left the reactants but has not yet reached the products. In some cases, this is the potential energy or free energy transition state, but it can also be a simple estimate of an intermediary geometry. The atoms are then assigned random velocities that are rescaled to the selected kinetic energy and a trajectory is initiated from this point. Zahn and coworkers have developed and applied a geometric model for generating intermediate structures in solid-to-solid phase transitions[16] as well as a more general method of geometric interpolation.[5] Although initiating from an intermediate geometry has been effective in a variety of studies,[17-19] the researcher must generate the intermediate structure themselves or assume that the mechanism found by interpolation is correct.

Many reactive events that are rare at low temperatures occur readily at elevated temperatures. This has been utilized in other methods for studying complex potential energy surfaces, such as parallel tempering[20] and hyperdynamics.[21] Similarly, an intuitive technique for finding a reactive trajectory is to run a simulation at a higher temperature or pressure, where a reaction is more likely to occur. This technique has been used to generate initial trajectories for a variety of simulations.[22-24] A notable example of this is Zahn's path sampling study of water boiling.[25] The initial trajectory was found by running a simulation of liquid water at 300°C. At this temperature, the transition to water vapour occurred in a rapid, explosive boiling. A new trajectory was initiated by selecting a step from the high temperature trajectory as an initiation point. The atomic velocities of the initiation point were rescaled to the appropriate kinetic energy and a new trajectory at 100°C was initiated. By the same principle, Zahn used a high pressure simulation to generate an initial trajectory for the B1 to B2 phase transition of RbBr.[26]

A third method that has been reported in the literature is to apply external forces to an MD simulation that cause the transition to occur within a short simulation. One such method is to apply geometric constraints to the simulation that make the transition more likely.[8-10] A notable example of this method was the transition path sampling study of the C–C bond forming step of the methanol coupling reaction in the zeolite chabazite by Trout *et al.*[10] The key C–C bond length was constrained at varying distances until a reaction occurred. This trajectory was then used to initiate a new, unconstrained trajectory.

Another method of this type is to modify the Hamiltonian of the simulation to increase the probability of the reaction. An elegant example of this was the transition path sampling study of the association of NaCl in an aqueous solution.[27] The van der Waals radii of the ion-water atom interactions were increased to make the association occur readily. The reactive trajectory found with the modified parameters was used to initiate a trajectory using the correct parameters. Similarly, artificial forces were used to generate an initial path in a study of ligand exchange between $Cr(CO)_5$ and a methanol solvent.[28] Very recently, Hu *et al.* have presented a method where a bias potential is used to generate an initial trajectory, then the bias is iteratively eliminated in a series of shooting moves.[29] The metadynamics method has also been used to generate an initial path for the dissociation of acetic acid in water.[30]

The shooting moves of transition path sampling are analogous to the sampling iterations of a Monte Carlo simulation. As such, an initial path that is not representative of a typical transition trajectory is sufficient, provided that the shooting moves will move the sampling to more representative trajectories in a reasonable number of iterations.[31] This may not be possible if the initial path follows a substantially different mechanism than the more probable transitions. Preferably, the initial path used in a transition path sampling simulation will be at least qualitatively similar to the more representative trajectories.

In this chapter, we evaluate three techniques to generate initial reactive trajectories expressly for simulating covalent bond breaking and forming reactions (Scheme 2.1) with AIMD. We focus on methods that are based on techniques that are already established in the chemical simulation literature and are therefore practical to implement and apply. These methods will make it more practical to apply transition path sampling in the study of chemical reaction mechanisms, which is where our interest lies. The appropriate algorithm for generating an initial reactive trajectory depends on both the type of reaction being studied and the conditions under which the reaction occurs. As such, there is no method that would be suitable in every case. We aim to formalize and test the more intuitive techniques that could be used to find initial reactive trajectories and discuss where they can be applied and what their potential pitfalls are.

Each of the methods we present here finds initial trajectories by generating initiation points, although two different approaches are used for this purpose. The first is to use static calculations to generate initiation points. The second is to find a reactive trajectory under different conditions (i.e. temperature) or with a different Hamiltonian (i.e. a bias potential) and then initiate a new trajectory from a time step selected from the transition regions of these trajectories.

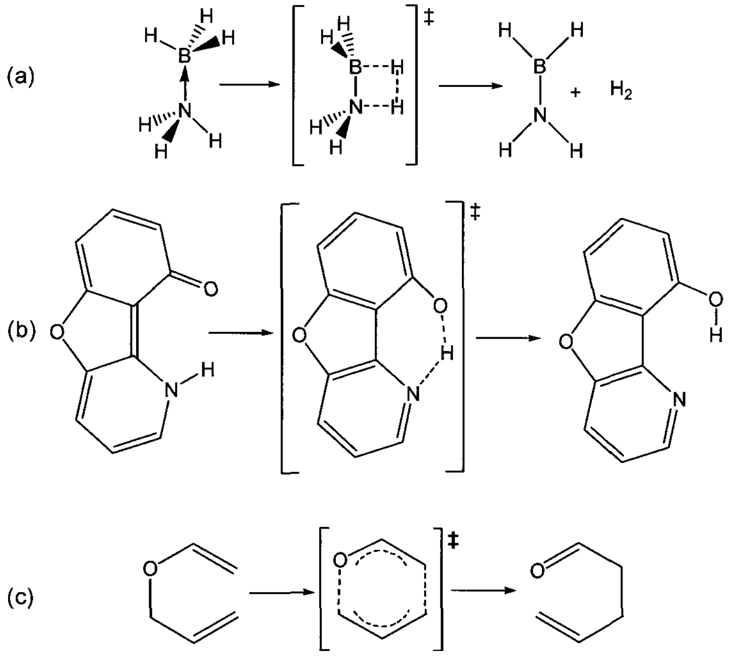

Scheme 2.1. Chemical reactions used to evaluate the proposed algorithms.

We have chosen three simple reactions to test these methods on. The first is the unimolecular 1,2-hydrogen elimination from the ammonia-borane adduct (Scheme 2.1a). Several previous theoretical studies using static *ab initio* calculations have found the barrier to be roughly 34 kcal mol^{-1},[32-34] which provides a difficult test for an initial path method as the barrier is high and the potential energy surface is complex. The second reaction is an aromatic tautomerization, representing a simpler, lower barrier transition. The last reaction we have studied is the Claisen rearrangement, a reaction commonly used in organic synthesis. Previous theoretical studies found that this reaction follows a concerted mechanism that is driven by the rearrangement of the π system, with a barrier of roughly 28 kcal mol^{-1}.[35,36]

In brief, the remainder of this chapter is as follows: the computational details are given in Section 2.2, a presentation and discussion of the results is given in Section 2.3, where each of the three methods is evaluated in separate subsections. Finally, the conclusions are presented in Section 2.4.

2.2. Computational Methods

All AIMD simulations were performed with the CPMD package version 3.9.2.[32] The PBE functional[33] with Goedecker pseudopotentials and a kinetic energy cutoff of 70 Ry were used for all MD simulations. The transition path sampling simulations were performed with our own code interfaced with CPMD. Trajectories were initiated, in both the forward and backward direction, by quenching the wave function to the Born-Oppenheimer surface and assigning initial orbital velocities of zero.

Three trajectory initiation algorithms were evaluated (*vide infra*) - the first involving initiation from a transition state optimized structure, the second starting from a high temperature MD trajectory, and the third using a electronic structure based biasing potential. Static DFT calculations for transition state optimizations and normal analysis were performed using the PBE functional with a 6-31G(d) basis set in Jaguar 5.5. HOMO-LUMO biasing code used a modified version of MNDO97 interfaced with CPMD. The bias and bias correction to the gradients were calculated using MNDO. The HOMO-LUMO biased potential energy surface presented in Figure 2.5 was calculated with NWChem 4.7 [34] interfaced with MNDO97.

Simulations of the borane-ammonia complex were done in a simple cubic cell with a length of 12 Bohr. The reactants were defined as the N–H bond length being between 1.6 Å and 1.7 Å and the B–H bond length being between 1.1 Å and 1.3 Å. The products were defined as structures where the H–H bond length was between 0.74 and 0.78 Å and the B–N bond length was between 1.36 Å and 1.41 Å.

The tautomerization reaction was simulated in an orthorhombic cell with lattice parameters a = 17.0 Bohr b = 22.0 Bohr and c = 10.0 Bohr. The reactants were defined as structures the N–H bond length being between 0.95 Å and 1.1 Å and the O–H bond length being between 1.9 Å and 2.1 Å. The products were defined as structures where the O–H bond length was between 0.9 Å and 1.0 Å.

The Claisen rearrangement was simulated in a face centered cubic cell with a lattice parameter of 15 Bohr. The reactants were defined as structures where the C–O bond length was between 1.4 Å and 1.6 Å. The products were defined as structures where the C–C bond length was between 1.45 Å and 1.55 Å and the C–O bond length was between 1.1 Å and 1.3 Å.

2.3. Results and Discussion

2.3.1. Transition State Structure Initiation

Transition state optimizations are routine practice for studying molecular reactions in the gas phase. As a result, methods to optimize potential energy transition state structures are available in most electronic structure programs. The transition state geometry is an obvious initiation point for generating a trajectory, as it lies between the two potential energy minima. To initiate a trajectory from a transition state, the potential energy transition state is found using conventional static quantum chemical calculations. This geometry can be used as the initial atomic coordinates, where the atomic velocities can be assigned at random or by a more sophisticated means.

We have applied this method to generate initial trajectories for the three reactions in our test set. We initiated 50 trajectories for each reaction from the transition state structure using random velocities from a Boltzmann distribution at 200 K. The trajectories were run forward and backward in time by 2000 time steps (6 a.u. per time step). This method was highly effective for the tautomerization reaction and the Claisen rearrangement, where 94% and 96% of the trajectories initiated were reactive, respectively. The 1,2-hydrogen elimination reaction had a lower acceptance rate, as only 74% of trajectories were reactive. We attribute this to the more complex potential energy surface of this reaction.

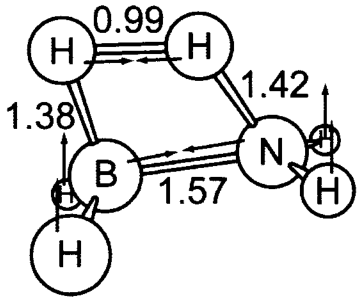

Figure 2.3. Cartesian displacements of the imaginary mode for the transition state of the 1,2-elimination of H_2 from the borane-ammonia adduct. These atomic coordinates and Cartesian displacements serve as initial atomic positions and velocities, respectively. Key bond lengths (Å) are adjacent to the bonds.

Although there was a reasonable acceptance rate for trajectories initiated with purely random velocities for all the reactions investigated, the acceptance rate clearly depends on the type of reaction being studied. More complex reactions may have acceptance rates that would be unacceptably low. This led us to consider methods that would generate initial velocities that would be more likely to result in a reactive trajectory than random velocities. The most obvious is to use a portion of the imaginary transition mode of the transition state structure (Figure 2.3). We have used the Cartesian displacements for this mode to generate initial velocities likely to produce a reactive trajectory on the 1,2-hydrogen elimination reaction with the hope of improving the acceptance rate. When the velocities were assigned exclusively from the imaginary mode of the transition state, the resulting trajectory was reactive.

Table 2.1. The percentage of trajectories initiated from the potential energy transition state structure of reaction (a) that are reactive. Atomic velocities at the initiation point are a combination of the Cartesian displacements of the transition mode and a Boltzmann distribution of random velocities.

Scale Factor	Acceptance Probability (%)
100	74
90	80
80	82
70	86
60	100
40	100
20	100

To investigate how important the atomic velocities are to the probability that the trajectory is reactive, we have attempted to initiate trajectories with velocities generated by mixing a random Boltzmann distribution of the velocities with the velocities generated from the transition mode for this reaction. The initial velocities were generated by adding the velocities generated from the imaginary mode and the velocities from a Boltzmann distribution with the appropriate weights. This new distribution was then rescaled to a temperature of 200 K. We have found that we can incorporate a large component from a Boltzmann distribution and still have a high acceptance rate for generating reactive trajectories, as shown in Table 2.1. The acceptance rate was 100% even when there was a 60% Boltzmann distribution velocity component, although the acceptance rate dropped to 80% when a 90% Boltzmann distribution component was used.

These results suggest that the initial atomic velocities can have a large effect on the probability that a trajectory will be reactive. The probability of generating a reactive trajectory may be dramatically improved by using normal-mode analysis or other methods to provide better initial velocities in cases where the acceptance rate is low. The high acceptance rates observed here suggest that this approach may work effectively with approximate transition states, such as those obtained from a transition state optimization that has not fully converged or from a simple linear scan of the reaction coordinate.

2.3.2. High Temperature Initiation

Increasing the temperature of an MD simulation is a simple technique used to observe more reactive events in a short simulation. One of the most obvious schemes to generate an initial path utilizes this by running a simulation at a high temperature until the reactive event occurs. Time steps from this high temperature trajectory can be used as initiation points for a lower temperature trajectory by rescaling the atomic velocities to a lower kinetic energy.

Previous studies initiated the lower temperature trajectory from the high temperature trajectory directly; however, we have implemented an iterative algorithm instead, where the change from the high temperature trajectory to the low temperature trajectory takes place through a series of intermediate steps, which was first used by Hagen *et al.*[23] In this algorithm, a time step is selected at random from the higher temperature trajectory and the atomic positions and velocities from this step are used to initiate a lower temperature trajectory. The velocities are rescaled by a constant coefficient ($0<\alpha<1$) to decrease the kinetic energy (Eq. (2.1)) and a new trajectory is generated by integrating forward and backward in time. If a reactive trajectory is generated, it is used as the starting point for the next iteration. Otherwise, another attempt is made using a different time step of the trajectory. This process is repeated until a reactive trajectory at the targeted total energy is found.

$$v_i^{k+1} \rightarrow \alpha v_i^k \tag{2.1}$$

Within the microcanonical ensemble, this process corresponds to running a trajectory at a high total energy, causing the system to undergo large fluctuations that drive the system across a barrier to another stable state. Rescaling the velocities lowers the kinetic energy component of the total energy such that the total energy of the new trajectory is lower than the previous iteration by a fraction of the kinetic energy of the time step it was initiated from (Eq. (2.2)). The total energy of the simulation is gradually lowered over a series of iterations, as fluctuations unrelated to the transition are quenched. This process can be stopped when the total energy is lowered to the energy the transition path sampling process is intended to operate at.

$$E_{tot}^{k+1} = E_{tot}^{k} - \left(1 - \alpha^2\right) E_{kin,i}^{k} \tag{2.2}$$

The scaling factor (α) is chosen to give a high acceptance rate while still making significant progress at reducing the total energy of the trajectory. Cooling the trajectory iteratively rather than in one step may make it possible to reach a lower total energy than could be done in one step and can help to eliminate prejudices introduced by the high temperature trajectory. This process is similar to the algorithm used by Zahn to find minimum energy trajectories within transition path sampling.[5]

To test this technique on practical molecular chemical reactions, we ran high temperature MD simulations on all three of our test reactions. No reactions were seen in the simulations of the BH_3NH_3 adduct or the Claisen rearrangement (Scheme 2.1a and 2.1c, respectively) in 7 ps simulations initialized with random velocities from a Boltzmann distribution scaled to 3000 K. This is likely due to the relatively high barrier heights of these reactions. Conversely, the simple tautomerization reaction (Scheme 2.1b) occurred within a simulation time of 1.8 ps. Using the high temperature initiation algorithm, we were able to make 10 iterations with a scaling coefficient of 0.95 (Figure 2.4), considerably lowering the total energy of the simulation.

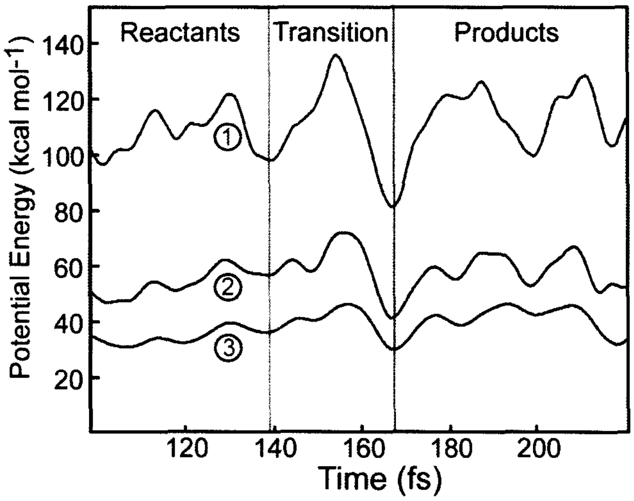

Figure 2.4. Potential energy profiles for trajectories produced by the iterations of the high temperature initiation algorithm (α=0.95) for reaction (b). The initial trajectory (1), the 5th iteration (2), and the 10th iteration (3) are shown here. The potential energy is calculated relative to the optimized reactants. Time is roughly partitioned into reactant, transition, and product regions.

To determine the effect of the scaling factor on the acceptance probability, we selected random initiation points from the transition region of the initial high temperature trajectory for a range of scaling factors. 50 trajectories were initiated for each scaling factor, which ranged from 0.2 to 0.8, as given in Table 2.2. All 50 trajectories were reactive when a scaling factor of 0.8 was used. Only 24 were accepted when a scaling factor of 0.6 was used, suggesting that the acceptance rate can be very sensitive to the scaling factor used. Scaling factors of 0.2 and 0.4 each had low acceptance rates. Selecting an appropriate scaling factor depends on the initial and final total energies needed by the simulation, as well as the properties of the system being studied, such as the barrier height and transition lengths. For molecular reactions like this, it would generally be most efficient to use scaling factors near 0.8, as the lower acceptance probability seen when a smaller scaling factor is used outweigh the gains made by reducing the total energy by a larger amount in each iteration.

Table 2.2. The percentage of trajectories initiated from the initial high temperature trajectory that were reactive, using various scaling factors used to rescale the atomic velocities.

Scale Factor	Acceptance Probability (%)
0.80	100
0.60	48
0.40	30
0.20	22

Although this method was effective for this reaction, there are many reactions where we would not expect this method to be effective for generating an initial reactive trajectory. Static calculations using PBE/6-31G(d) determined that this tautomerization has a barrier height of only 5.7 kcal mol^{-1}, while the calculated barrier heights for the 1,2-hydrogen elimination and the Claisen rearrangement are much higher (34.1 and 22.7 kcal mol^{-1}, respectively). Many chemical reactions of interest have much higher barrier heights, where the simulation temperature would have to be extremely high to generate a reactive trajectory in a short simulation time. Furthermore, the reaction mechanism of this tautomerization is simple; other reactions may have different mechanisms at high and low temperatures, making this method inappropriate.

2.3.3. Orbital Biased Trajectory Switching

A common technique to promote a rare event in an MD simulation is to introduce an arbitrary potential energy term into the Hamiltonian, known as a bias potential. A bias potential can be used to selectively lower the barrier for a particular reaction. With the barrier lowered, the system can undergo the reaction during a much shorter simulation. For instance, Rothlisberger used a classical molecular mechanical bias potential on an AIMD simulation to accelerate the methyl group rotation of ethane and the isomerization of peroxnynitrous acid.[35] These bias potentials are based on geometrical parameters, such as bond lengths, bond angles, and dihedrals. The drawback of methods like these is that the bias potential is chosen *a priori*. The mechanism must be known in advance, as selecting a bias that favours a less probable mechanism would prejudice the sampling. Ideally, the bias will not require any *a priori* information about the reaction mechanism, but the simulation will nonetheless quickly undergo a reaction of chemical interest when the bias is applied.

An attractive alternative to geometry based bias potentials is available in AIMD. As the electronic structure is determined at each time step, a bias can be calculated from electronic properties instead. The trajectory can be biased to undergo a type of electronic rearrangement that is reflected in geometrical changes rather than defining geometrical changes directly.

In many chemical reactions, the HOMO-LUMO gap is larger at the minima and smaller at the transition state.[36] A HOMO-LUMO bias stabilizes the transition states with respect to the minima, effectively lowering the reaction barrier. This technique has been successfully applied to accelerate a variety of chemical reactions.[37] Similarly, Rothlisberger has used single-electron orbital energies as biases in the isomerization of 1,3-butadiene.[38]

Although the potential energy correction in the biased simulation can be calculated trivially based on the electronic structure, as this term is simply the difference between the orbital energies of the LUMO and the HOMO (Eq. (2.3)), corrections to the atomic gradients are also needed for orbital biased MD simulations. The correction to the gradient requires an additional calculation that can be very expensive. We resolve this problem by calculating the unbiased potential energy and gradients using the same DFT method used elsewhere in this chapter and calculating the bias and correction to the gradients using an inexpensive semi-empirical method.[37]

$$E_{biased} = E_{DFT} + \beta\left(\varepsilon_{LUMO} - \varepsilon_{HOMO}\right) \tag{2.3}$$

The reactive trajectory generated by these biased dynamics can potentially follow a very similar mechanism to what an unbiased simulation would produce. An excellent initiation point can be generated by selecting a time step from the transition region of a reactive biased trajectory. We call this technique biased trajectory switching as we are switching between Hamiltonians.

We ran 4 ps simulations with a variety of HOMO-LUMO biases on all three reactions in the test set. Trajectories produced from small biases (β<0.4) run on the

BH_3NH_3 adduct and the tautomerization system were not reactive. When an MD simulation with a bias of β=0.5 was run on the BH_3NH_3 adduct, the molecule decomposed through the loss of a proton from the borane. Similarly, the trajectory with β=0.5 on the tautomerization reaction led to the fragmentation of the ketone containing ring, rather than the tautomerization. We conclude that a HOMO-LUMO bias is not suitable for finding initial trajectories of these reactions.

This method had more success on the Claisen rearrangement (Scheme 2.1c). The potential energy surface (PES) of the transition state region of the rearrangement shows that the barrier height is lowered from 22.7 kcal mol^{-1} to 12.4 kcal mol^{-1} when a HOMO-LUMO bias is applied (β=0.2) (Figure 2.5). Reactive biased trajectories were found by running MD simulations from reactant structures using a HOMO-LUMO bias with a coefficient of β=0.2. We have made 50 switching attempts from random time steps from the biased trajectory to test how effective a biased trajectory is as a means to generate initial trajectories. There was a reasonable acceptance rate for switching to unbiased dynamics, as 52% of the trajectories initiated from the biased trajectory were reactive.

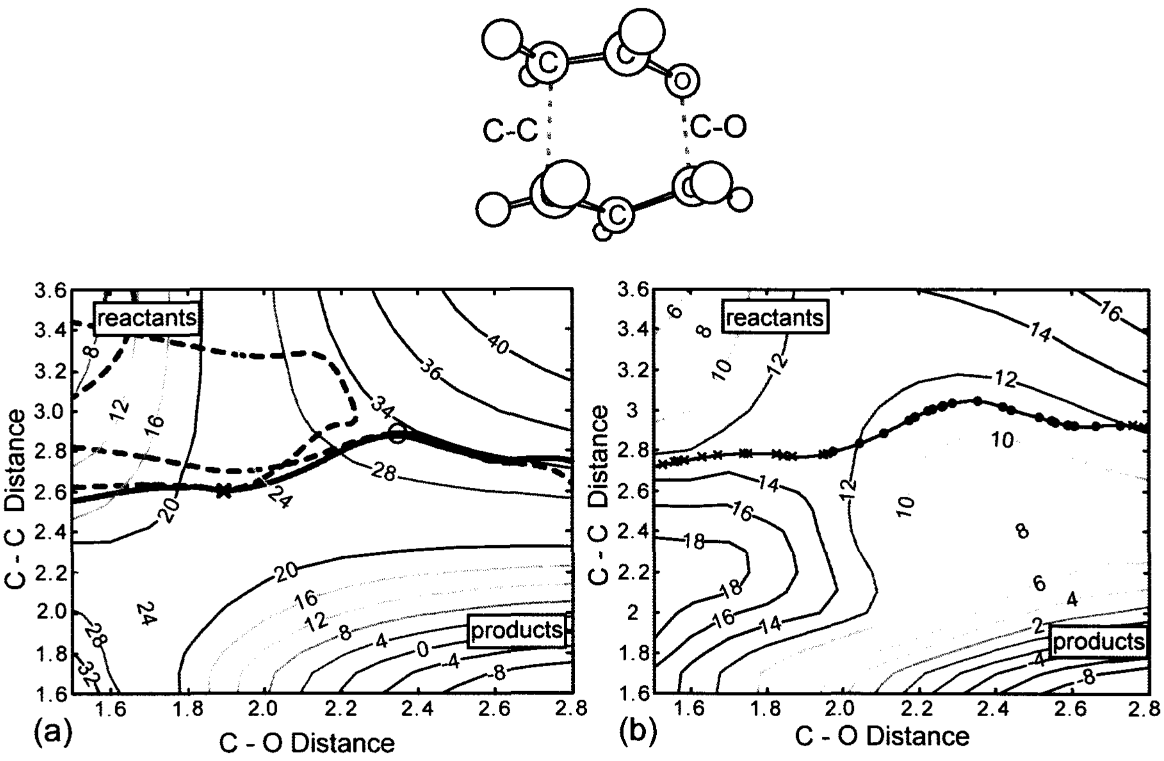

Figure 2.5. PES of the Claisen rearrangement. (a) PBE/6-31G(d) surface without a bias (b) PBE/6-31G(d) surface with a HOMO-LUMO bias (β=0.2). Distances are in Å. Energies are in kcal mol^{-1} and are calculated relative to the optimized reactant structure. The biased trajectory is shown in black on (a), while the dashed red line shows an unsuccessful switching attempt and the dashed green line shows a successful switching attempt. The biased trajectory is also shown in black on (b), as well as accepted (green circles) and rejected (red X's) initiation points. The C–C and C–O bond length parameters used in the potential energy surface scan are indicated on the schematic diagram of the transition state structure (top).

A comparison of the biased and unbiased PES surfaces of the Claisen rearrangement shows a significant change in the position of the transition state when the bias is applied. Large differences in the PES could lead to a low acceptance rate for generating an initial path, as the biased trajectory will provide poor initiation points for switching to the unbiased trajectory. Nonetheless, unbiased reactive trajectories were found with a reasonable acceptance rate, even with a significant change in the position of the transition state. To illustrate this, we have plotted one reactive and one non-reactive trajectory on the unbiased PES (Figure 2.5a) as well as the reactive and non-reactive initiation points from the biased trajectory on the biased PES (Figure 2.5b). Initiation points from time steps that had not crossed the transition state on the unbiased PES were mostly rejected, as they returned to the reactant basin when integrated forward in time. Trajectories initiated from time steps later in the biased trajectory were more likely to be accepted. As the barrier for this reaction remains significant, even with the bias potential applied, the successful generation of a reactive trajectory was likely due a fortuitous starting geometry.

2.4. Conclusions

We have developed and evaluated three methods for generating initial reactive trajectories for bond breaking – forming reactions for transition path sampling with AIMD. Initiating a trajectory from a transition state is an efficient technique when it is possible to find the transition state geometry using static calculations. This method successfully generated initial trajectories for all three reactions. Generating atomic velocities based on normal-mode analysis has been found to greatly increase the probability of generating a reactive trajectory. This method can be used for systems with arbitrarily high barriers; however, the location of the transition state on the potential energy surface must be identified first.

The high temperature initiation algorithm can generally be applied to systems where a reaction will occur in during a short MD simulation at a high temperature. We successfully used this method to find a reactive trajectory for a tautomerization reaction, reaction (b). No *a priori* information about the reaction mechanism is needed, but this technique assumes that the reaction mechanism at a high temperature is essentially the same as it is at a low temperature. Only reactions with low barriers can be studied, as prohibitively high temperatures may be needed for reactions with high barriers. Case in point, high temperature simulations did not lead to reactive trajectories for the 1,2-hydrogen elimination reaction or the Claisen rearrangement.

Initiating from an orbital-biased trajectory is a very promising method for orbital-driven reactions. Trajectories for reactions with sizeable barriers can be efficiently found and "un-biased" by the biased switching algorithm. We have found that the biased switching algorithm has a high acceptance rate for trajectories initiated from a HOMO-LUMO gap biased trajectory when we applied it to the Claisen rearrangement, reaction (c). No *a priori* information about the reaction mechanism is needed. This method was not successful for the 1,2-hydrogen elimination reaction or the tautomerization reaction, as the HOMO-LUMO biased trajectory led to fragmentation reactions instead. Finding electronic biases appropriate for a wider range of chemical reactions will extend the range of chemical reactions that can be studied using transition path sampling, but this is beyond the scope of this work. Nonetheless, the results suggest that generating initial trajectories from simulations where the Hamiltonian has been modified or biased is viable.

Each of these methods can generate an initial path with a reasonable computational cost. Each attempt to find an initial trajectory from an initiation point requires an MD simulation that is of the length that the transition path ensemble is harvested from, which are generally short. An efficient algorithm must be able to generate initiation points with modest expense and a high acceptance rate. The high temperature initiation algorithm is likely the most expensive of the methods that we present here, as a relatively long initial high temperature MD is needed, plus a large number shorter simulations for the iterations to reduce the total energy of the trajectory.

Biased MD is a relatively inexpensive method, as only a short initial trajectory is needed, along with a few short simulations to switch to the unbiased Hamiltonian; however, calculating the bias correction for the biased initial trajectory can be very expensive. The transition state structure initiation method is arguably the most efficient, as we observed high acceptance rates for the reactions tested here, although the transition state must be optimized using static calculations, which can be computationally demanding, especially if normal-mode analysis is needed to generate initial velocities.

The high temperature initiation algorithm and biased trajectory switching are a particularly interesting as they are open-ended. Only the reactant structures are provided by the user. The reaction mechanism and even the products are determined by the simulation. In many catalytic processes, the reaction mechanism is not known, and therefore open-ended methods can "scout out" potential reactions to be used to initiate a transition path sampling to examine the process in more detail.

References

1. Parrinello, M. *Comput. Sci. Eng.* **2000,** *2,* 22.

2. Tse, J. S. *Annu. Rev. Phys. Chem.* **2002,** *53,* 249.

3. Dellago, C.; Bolhuis, P. G.; Geissler, P. L. *Adv. Chem. Phys.* **2002,** *123,* 1.

4. Bolhuis, P. G.; Chandler, D.; Dellago, C.; Geissler, P. L. *Annu. Rev. Phys. Chem.* **2002,** *53,* 291.

5. Zahn, D. *J. Chem. Theory Comput.* **2006,** *2,* 107.

6. Dellago, C.; Bolhuis, P. G. *Mol. Simulat.* **2004,** *30,* 795.

7. Dellago, C.; Bolhuis, P. G.; Chandler, D. *J. Chem. Phys.* **1999,** *110,* 6617.

8. Ensing, B.; Baerends, E. J. *J. Phys. Chem. A* **2002,** *106,* 7902.

9. Zahn, D. *Chem. Phys.* **2004,** *300,* 79.

10. Lo, C. S.; Radhakrishnan, R.; Trout, B. L. *Catal. Today* **2005,** *105,* 93.

11. Basner, J. E.; Schwartz, S. D. *J. Am. Chem. Soc.* **2005,** *127,* 13822.

12. Geissler, P. L.; Dellago, C.; Chandler, D.; Hutter, J.; Parrinello, M. *Chem. Phys. Lett.* **2000,** *321,* 225.

13. Geissler, P. L.; Dellago, C.; Chandler, D.; Hutter, J.; Parrinello, M. *Science* **2001,** *291,* 2121.

14. Bolhuis, P. G.; Dellago, C.; Chandler, D. *Faraday Discuss.* **1998,** *110,* 421.

15. Passerone, D.; Ceccarelli, M.; Parrinello, M. *J. Chem. Phys.* **2003,** *118,* 2025.

16. Leoni, S.; Zahn, D. *Z. Krist.* **2004,** *219,* 339.

17. Bolhuis, P. G.; Dellago, C.; Chandler, D. *Proc. Natl. Acad. Sci. U. S. A.* **2000,** *97,* 5877.

18. Ma, A.; Dinner, A. R. *J. Phys. Chem. B* **2005,** *109,* 6769.

19. Pan, A. C.; Chandler, D. *J. Phys. Chem. B* **2004,** *108,* 19681.

20. Hansmann, U. H. E. *Chem. Phys. Lett.* **1997,** *281,* 140.

21. Voter, A. F. *J. Chem. Phys.* **1997**, *106*, 4665.

22. Bolhuis, P. G.; Chandler, D. *J. Chem. Phys.* **2000**, *113*, 8154.

23. Hagan, M. F.; Dinner, A. R.; Chandler, D.; Chakraborty, A. K. *Proc. Natl. Acad. Sci. U. S. A.* **2003**, *100*, 13922.

24. Bolhuis, P. G. *Biophys. J.* **2005**, *88*, 50.

25. Zahn, D. *Phys. Rev. Lett.* **2004**, *93*, 227801/1.

26. Zahn, D. *J. Solid State Chem.* **2004**, *177*, 3590.

27. Zahn, D. *Phys. Rev. Lett.* **2004**, *92*, 040801.

28. Snee, P. T.; Shanoski, J.; Harris, C. B. *J. Am. Chem. Soc.* **2005**, *127*, 1286.

29. Hu, J.; Ma, A.; Dinner, A. R. *J. Chem. Phys.* **2006**, *125*, 114101.

30. Park, J. M.; Laio, A.; Iannuzzi, M.; Parrinello, M. *J. Am. Chem. Soc.* **2006**, *128*, 11318.

31. Zahn, D. *J. Chem. Phys.* **2005**, *123*, 044104/1.

32. CPMD, http://www.cpmd.org/, Copyright IBM Corp 1990-2008, Copyright MPI für Festkörperforschung Stuttgart 1997-2001.

33. Perdew, J. P.; Burke, K.; Ernzerhof, M. *Phys. Rev. Lett.* **1996**, *77*, 3865.

34. E. J. Bylaska, W. A. de Jong, N. Govind, K. Kowalski, T. P. Straatsma, M. Valiev, D. Wang, E. Apra, T. L. Windus, J. Hammond, P. Nichols, S. Hirata, M. T. Hackler, Y. Zhao, P.-D. Fan, R. J. Harrison, M. Dupuis, D. M. A. Smith, J. Nieplocha, V. Tipparaju, M. Krishnan, Q. Wu, T. Van Voorhis, A. A. Auer, M. Nooijen, E. Brown, G. Cisneros, G. I. Fann, H. Fruchtl, J. Garza, K. Hirao, R. Kendall, J. A. Nichols, K. Tsemekhman, K. Wolinski, J. Anchell, D. Bernholdt, P. Borowski, T. Clark, D. Clerc, H. Dachsel, M. Deegan, K. Dyall, D. Elwood, E. Glendening, M. Gutowski, A. Hess, J. Jaffe, B. Johnson, J. Ju, R. Kobayashi, R. Kutteh, Z. Lin, R. Littlefield, X. Long, B. Meng, T. Nakajima, S. Niu, L. Pollack, M. Rosing, G. Sandrone, M. Stave, H. Taylor, G. Thomas, J. van Lenthe, A. Wong, and Z. Zhang, "NWChem, A Computational Chemistry Package for Parallel Computers, Version 5.1" (2007), Pacific Northwest National Laboratory, Richland, Washington 99352-0999, USA.

35. VandeVondele, J.; Rothlisberger, U. *J. Chem. Phys.* **2000**, *113*, 4863.

36. Pearson, R. G. *Acc. Chem. Res.* **1993**, *26*, 250.

37. Mosey, N. J.; Hu, A.; Woo, T. K. *Chem. Phys. Lett.* **2003**, *373*, 498.

38. Guidoni, L.; Rothlisberger, U. *J. Chem. Theory Comput.* **2005**, *1*, 554.

CHAPTER 3

The Mechanism of Olefin Hydrogenation Catalyzed by $RuHCl(CO)(PR_3)_2$ Complexes: A DFT Study

This work has been published in part in Rowley, C. N.; Foucault, H. M.; Woo, T. K.; Fogg, D. E. *Organometallics* **2008**, *27*, 1661.

Abstract

Static DFT calculations were used to study the full catalytic cycle for H_2-hydrogenation of olefins by the catalyst $RuHCl(CO)(PR_3)_2$ (**2a**) using the model substrate ethylene. The mechanism we elucidated follows the sequence: dissociation of a coordinated phosphine, coordination of ethylene, coordination of H_2, simultaneous ethylene insertion into the Ru–H bond and oxidative addition of H_2 to form a Ru(IV) dihydride intermediate, and reductive elimination of this intermediate to form ethane product and regenerate the active catalyst. This mechanism differs from those proposed in the literature in two significant respects. Firstly, it had generally been thought that olefin insertion occurs prior to the coordination of the H_2, however it was found that the presence of H_2 was essential to stabilize the alkyl intermediate. Secondly, ethane loss proceeds through a readily accessible Ru(IV) dihydride intermediate, an intermediate that had been thought to be too unstable to be present in a catalytic reaction. These static QC calculations are the basis for our subsequent TPS simulation of this reaction in Chapter 4.

3.1. Introduction

Hydrogenation of unsaturated bonds by homogenous transition-metal complexes offers tremendous potential to specify regio-, chemo-, and stereo-selectivity, as well as overall system productivity.[1-5] While many metal complexes catalyze hydrogenation reactions, the late metals of groups 8-10 are most active.[6,7] Ruthenium catalysts of the general class $RuHCl(PR_3)_2(L)$ (e.g. **1-2**) are of particular interest for their relatively low cost, their versatility, and their efficiency in reduction of challenging substrates, including unsaturated polymers.[8-10] This capacity has been recently exploited in tandem metathesis-hydrogenation catalysis.[11-16]

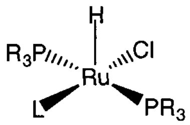

1: L=PR_3, R=Ph
2: L=CO, R=$^{i}Pr_3$
3: L=CO, R=H

Hydridoruthenium catalysts have been the subject of extensive development and study since Wilkinson's original report[17] of H_2-hydrogenation of terminal alkenes by **1**. Early kinetic experiments on **1** established that the reaction is zero to first order in [olefin], first order in [H_2], first order in [Ru], and inversely dependent on [PR_3].[7] Related Ru-monohydride catalysts, including **2a**, obey the same rate law.[18,19] Based on these data, a five step catalytic cycle (Figure 3.1) has been widely accepted as the mechanism of hydrogenation for this catalyst.[20] In the first step, a phosphine ligand dissociates from the precatalyst (**1a/2a**) to form the active catalyst (**1b/2b**). Olefin coordination to the active catalyst at the site vacated by the phosphine forms an ethylene adduct, (**1c/2c**). The critical reactive step follows, where the olefin will insert into the Ru–H bond to form a putative Ru(II) square planar intermediate (**1d/2d**). The earliest reports assumed that coordination of H_2 to this intermediate would immediately yield a Ru(IV) dihydride intermediate.[7] Subsequent reports of nonclassical ruthenium dihydrogen complexes led to a revised catalytic cycle where the complexation of H_2 to the metal forms a nonclassical Ru(II) dihydrogen complex (**1e**/**2e**) instead. Heterolytic cleavage of H_2 in conjunction with elimination of the hydrogenated alkane regenerates the active catalyst (**1b**/**2b**), completing the catalytic cycle.

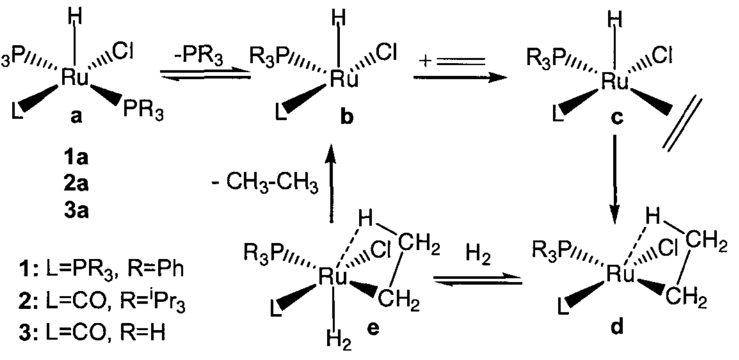

Figure 3.1. Literature catalytic cycle for the Ru-hydride H_2-hydrogenation of olefins with ethylene as the example substrate.

Although computer modelling could facilitate the design of improved catalysts, no computational study of the full catalytic cycle of catalysts of the class **1a** and **2a** had been reported. Previous quantum chemical investigations on ruthenium hydride complexes have studied the effect of hydride orientation,[21] olefin insertion into Ru–H bonds,[22] and Ru–H and Ru–H_2 interactions,[23] but never reported a model of the complete reaction mechanism. Our aim in this project was to generate a comprehensive model of the catalytic cycle using static DFT calculations. See Section 3.3 for the full computational details.

As a model catalyst, we have chosen the carbonyl complex **2a**. Although a wide variety of catalysts have been developed within this framework, contemporary variants typically feature a CO auxiliary ligand and an alkyl phosphine. Trisisopropyl phosphine ligands have a moderate computational cost compared to larger cyclohexyl phosphines, although the steric and electronic properties of this ligand are similar. This compound is itself a potent hydrogenation catalyst[24-26] and serves as an analogue of other benchmark alkylphosphine systems.[6]

3.2. Results and Discussion

3.2.1. Reaction Mechanism

We began our study by examining the structures present in the catalytic cycle proposed in the literature (Figure 3.1). The diphosphine precatalyst **2a** is square pyramidal, with the hydride ligand occupying the apical site. Our proposed mechanism begins with loss of one phosphine ligand, in keeping with the accepted scheme. η^2-Coordination of ethylene takes up the vacant site trans to phosphine (**2c**), the high trans influence of hydride disfavouring the site trans to the hydride. While insertion of the alkene into the Ru–H bond (**2c-2d**), followed by coordination of H_2, are generally depicted as the next steps, attempts to optimize the Ru–ethyl intermediate regenerate the ethylene adduct **2c**. As this complex is a key step in the proposed catalytic cycle, it was necessary to explore alternative reaction mechanisms. A full account of the mechanisms we considered is presented in the Supplementary Section 3.6 of this chapter. Upon exhausting these other possibilities, we found that when H_2 is coordinated in vacant axial site, an ethyl-containing dihydride intermediate (*vide infra*) could be identified (Figure

3.2, **2g**). This led us to investigate an alternative reaction mechanism wherein coordination of H_2 precedes olefin insertion, which we present in detail in the following subsections.

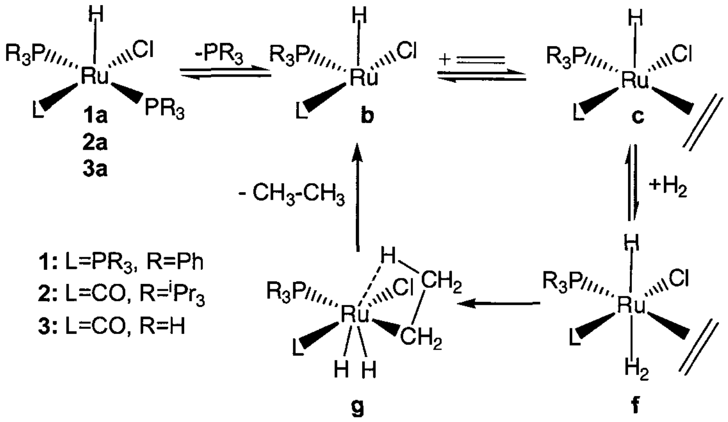

Figure 3.2. Revised catalytic cycle for the Ru–hydride H_2-hydrogenation of olefins with ethylene as the example substrate.

3.2.2. Reaction Potential Energy Surfaces

To better understand why the putative ethyl intermediate **d** is not a potential energy minimum, while the analogous complex with the vacant coordination site occupied by H_2 (**g**) is, the potential energy surfaces (PES) of the ethylene insertion step were calculated for complexes with and without H_2 coordinated trans to the hydride ligand. The potential-energy minimum structure was optimized for a grid of distances ranging from Ru–H = 1.4 Å to 2.1 Å and C–H = 1.1 Å to 2.4 Å in 0.025 Å increments. We used the truncated phosphine (PH_3) model (**3**) in these calculations to lower the computational cost.

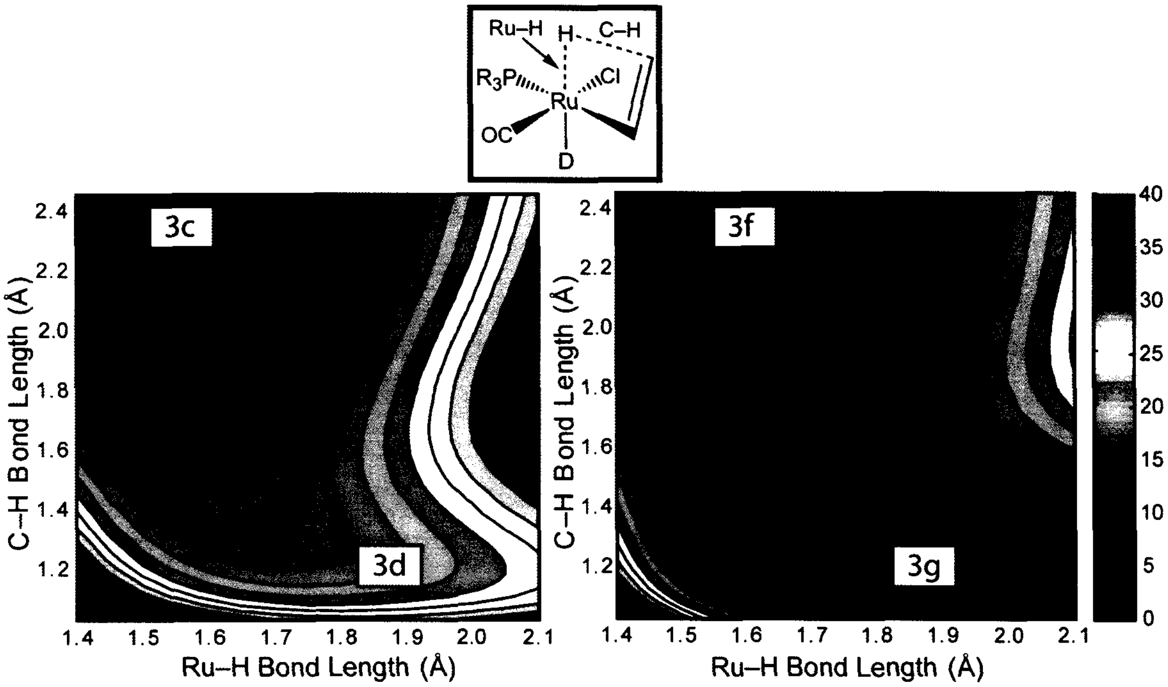

Figure 3.3. PES of ethylene insertion into the Ru–H bond step without (left, D=vacant) and with (right, D=H_2) dihydrogen coordinated. Energies are reported in kcal mol^{-1}.

The leftmost PES in Figure 3.3 corresponds to the insertion when the coordination site trans to the hydride is vacant. The top left corner is the section of the PES where the Ru–H bond is still present and the C–H bond has not yet formed (Ru–H < 1.7 Å and C–H distances > 2.0 Å), corresponding to the ethylene adduct (**3c**). There is no potential energy minimum on this surface that corresponds to the ethyl intermediate (**3d**). Furthermore, structures corresponding to the insertion product (Ru–H distance > 1.6 Å and C–H distances < 1.3 Å) are highly unstable (~20 kcal mol^{-1}) with respect to the reactant complex.

The rightmost PES corresponds to the insertion when the coordination site trans to the hydride is occupied by a dihydrogen ligand. The minimum in the top left corresponding to **3f** is somewhat broader to that of **3c**, as the H_2 ligand stabilizes structures with elongated Ru–H bonds. Most significantly, when the coordination site trans to the hydride is occupied by an η^2-coordinated dihydrogen, there is a low-energy minimum corresponding to the ethyl-containing intermediate (**2g**) where the newly-formed ethyl group interacts with the metal through a *β*-agostic interaction. This minimum is connected to the ethylene adduct (**3c**) structure through a modest energetic barrier (5.3 kcal mol^{-1}). Based on these PESs and our exhaustive search of other mechanisms, we propose that olefin insertion occurs only after coordination of H_2.

3.2.3. Insertion Step

Having established that the coordination of H_2 precedes the olefin insertion step, we will now consider the insertion step itself. The coordination of H_2 prior to the insertion is weak due to the strong trans influence of the hydride ($Ru–\eta^2(H_2)$ = 1.81 Å). The transition state structure (TS1, Figure 3.4) is similar to that found for other such insertion reactions,[22] with a coplanar Ru–C–C–H segment. The intrinsic reaction coordinate (IRC) of this insertion (Figure 3.4) shows a significant potential energy barrier (5.4 kcal mol^{-1} with respect to **2e**) that is strongly dependent on the length of the C–H bond formed in this insertion, with the transition state occurring when C–H = 1.54 Å. A strong *β*-agostic interaction between Ru and newly-formed C–H bond is found in **2g** (Ru–H = 1.89 Å; C–H = 1.19 Å).

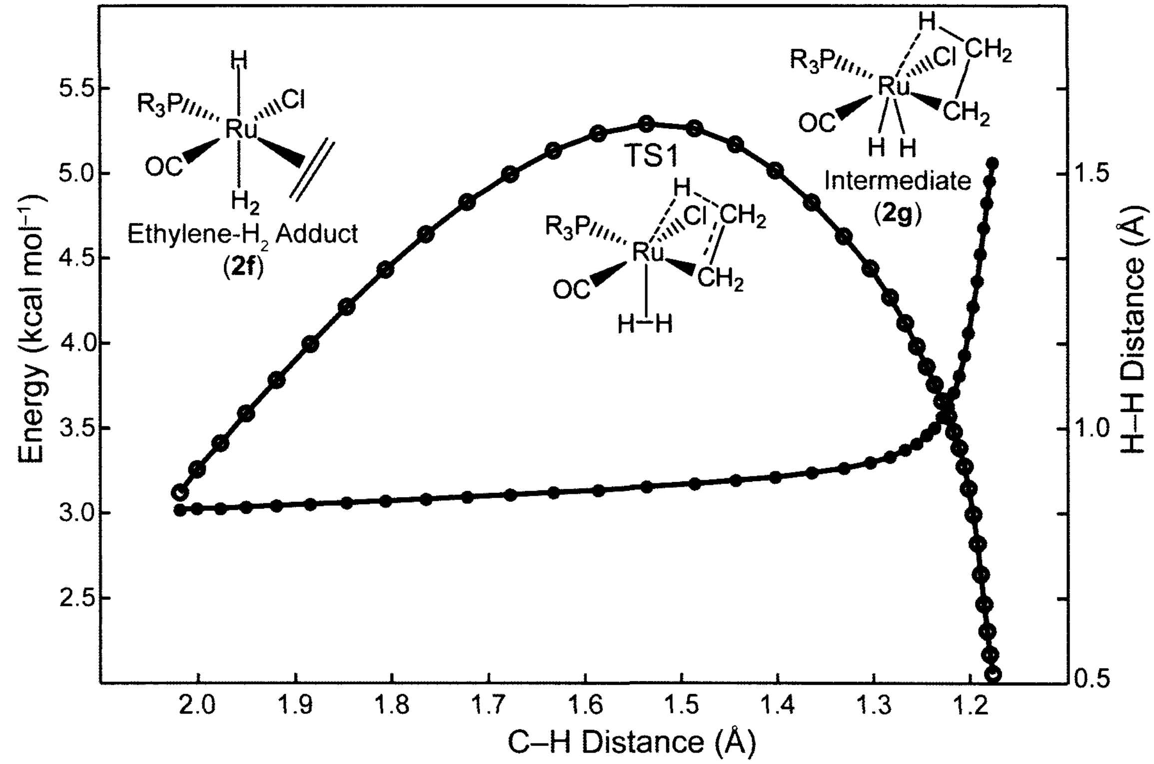

Figure 3.4. Energies of the Intrinsic Reaction Coordinate (IRC) for the oxidative addition of the ethylene H_2 adduct (**2f**) to the Ru(IV) dihydride intermediate (**2g**) through **2-TS1**, plotted along the C–H axis (blue). The internuclear distance of the coordinated dihydrogen (red) is plotted on the secondary axis.

The H–H distance of the coordinated dihydrogen changes dramatically over the course of the insertion. The coordination is weakest in the **2f** (H–H = 0.84 Å) due to the strong trans influence of the hydride ligand. The H–H distance increases linearly along the IRC such that H–H = 0.88 Å at the transition state. Charge Decomposition Analysis (CDA)[27] of the reactant and transition state structures indicates that the relative weight of back-donation from the metal from the σ*-antibonding HOMO of the H_2 increases along the reaction coordinate, consistent with the elongation of the H–H bond (Table 3.1). This stronger back-donation results from the loss of the trans influence of the hydride, as the Ru–H(hydride) bond is broken during the insertion. Further, the metal becomes more electron deficient during the insertion, as the ethylene ligand no longer serves as a two-electron donor to the metal.

Table 3.1. CDA of the metal-H_2 interaction of **2c** and **2-TS1**.

Species	Donation	Back-donation	Repulsion
2c	0.35	0.16	-0.14
2-TS1	0.41	0.25	-0.13

Late in the reaction coordinate (C–H < 1.3 Å), the H–H distance increases sharply, consistent with cleavage of the H–H bond. This cleavage occurs only after the Ru–H bond is effectively broken and its trans influence is therefore eliminated. While these calculations indicate insertion and cleavage occur in a concerted process without any intervening intermediates, the Ru–H bond breaking and C–H bond formation occurs earlier on the reaction coordinate than the cleavage of H_2.

3.2.4. Ethyl Dihydride Intermediate

The intermediate formed by the insertion, **2g**, is a 7-coordinate distorted capped trigonal prismatic structure. Although we immediately classified this structure as a Ru(IV) dihydride, the presence of a dihydride intermediate in this catalytic cycle is a matter of some controversy. A Ru(IV) dihydride intermediate, formed *via* oxidative addition of H_2 to a Ru(II) precursor, was originally proposed to be active in this catalytic cycle by analogy to the Rh(I)/Rh(III) couple;[17,28] however, oxidative addition of H_2 to form a dihydride is strongly endergonic in some transition metal-H_2 complexes,[29] suggesting that this reaction would have to proceed through a heterolytic cleavage of H_2 in order to avoid the ethyl-dihydride intermediate (**2f**).

The two possible mechanisms for the cleavage of H_2 arise because transition metal complexes with H_2 are capable of forming two distinctly different bonding arrangements: classical and nonclassical complexes. Classical complexes are dihydrides wherein each hydrogen is a distinct ligand with a formal oxidation state of −1. Nonclassical dihydrogen complexes were discovered more recently and reflect a significantly different bonding arrangement. In these complexes, the hydrogen atoms comprising the H_2 ligand remain bound to each other. The H_2 ligand serves as a two-electron donor to the metal, interacting primarily through donation from the H_2 HOMO to the metal, but also through donation from the metal to the H_2 LUMO. Crabtree et al. determined that a complex $RuH_4(PPh_3)_3$, which had previously been assigned as a Ru(IV) tetrahydride,[30] was in fact a nonclassical complex of the form $RuH_2(H_2)(PPh_3)_3$.[31] This was used as evidence that Ru(IV) dihydrides are, as a rule, less stable than their nonclassical Ru(II)-dihydrogen analogues and that cleavage of H_2 within this catalytic cycle would occur heterolytically from an nonclassical dihydrogen complex.[20]

Rather than finding that the dihydride intermediate **2g** was highly unstable, we found that this intermediate is only 1.1 kcal mol^{-1} less stable than the preceding complex, **2f**. While this is contrary to the reported trend of Ru(IV) dihydrides being less stable than their Ru(II)-dihydrogen analogous, this is consistent with the observation by Morris and coworkers that small, electron-donating ligands can stabilize dihydride structures,[3] as well as numerous experimental reports of stable Ru(IV) dihydrides.[32-36]

To unambiguously characterize the bonding within **2g** as a Ru(IV) dihydride or a nonclassical Ru(II)-dihydrogen complex, we calculated the electron localization function (ELF)[37] of the putative $Ru(IV)(H)_2$ intermediate. Areas of high electron localization, such as core orbitals and chemical bonds have high ELF values, which makes the method appropriate for determining the nature of the bonding interaction between the dihydrogen and the metal. Colourmaps of the ELFs are plotted in the Ru–H–H plane of **2f** (Figure 3.5, left), **2-TS1** (Figure 3.5, center), and **2g** (Figure 3.5, right) to show the change in bonding over the course of the insertion. Plots for **2f** and **2-TS1** show high localization along the H–H internuclear axis, consistent with the H_2 serving as a two-electron donor. The analogous plot of **2g** shows two distinct basins for each Ru–H bond, consistent with H_2 being cleaved and the two hydrogen atoms serving as separate ligands. Furthermore, the H–H distance in **2g** is 1.62 Å, which is in the range ($d_{HH} > 1.6$ Å) that can be unequivocally designated as a dihydride.[29]

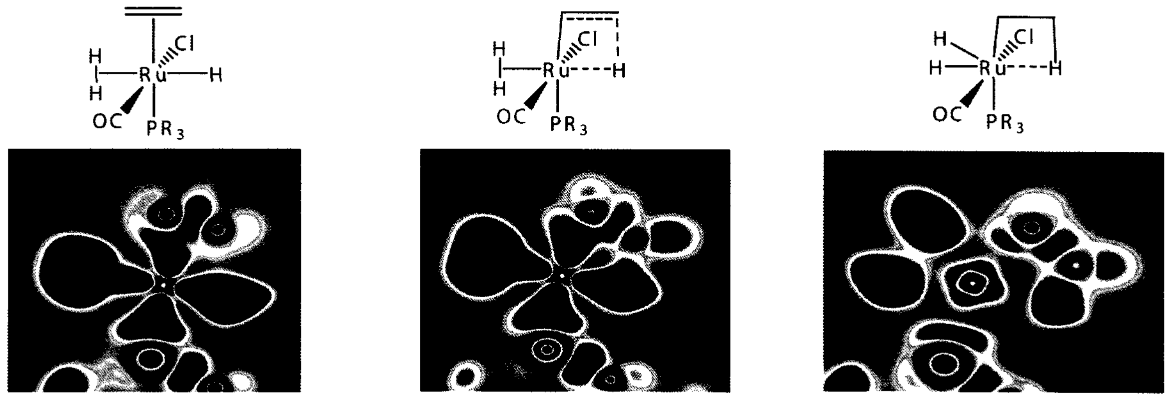

2f **2-TS1** **2g**

Figure 3.5. ELF plot of the Ru–H–H plane complexes **2f**, **2-TS1**, and **2g**. Locations of key hydrogens are indicated with a black dot while the location of the ruthenium is indicated with a white dot. Note that the core structure of the ruthenium atom is not present due to the use of an effective core potential.

The relative stabilities of the nonclassical and classical H_2 bonding arrangements can be interpreted from the PES of the H–H coordinate in complexes **2f** and **2g**, which we have designated as nonclassical and classical dihydrides, respectively (Figure 3.6). In **2f**, the global minimum on the H–H coordinate occurs near 0.82 Å and increases sharply outside of this range. Classical dihydride structures are considerably less stable for this complex and structures where H–H > 1.6 Å corresponds to a structure where one of the hydrogens has transferred to ethylene ligand to form an ethyl-containing trans-dihydride. In contrast, the minimum on the PES of **2g** is located at 1.6 Å but is very broad, similar to the profile of the oxidative addition of H_2 to IrCl(CO)(dppe).[38] Regions of short H–H distances (< 1.0 Å) that correspond to a nonclassical bonding mode are only 4 kcal mol^{-1} higher in energy than the minimum-energy dihydride structure, indicating that this structure experiences a significant, but lesser degree of stabilization in the nonclassical bonding mode compared to the classical dihydride bonding mode. The nonclassical bonding mode is not a minimum in **2g**, consistent with the cleavage of H_2 occurring concomitantly to the insertion. This preference for the classical dihydride bonding mode has been reported in a number of other transition metal complexes.[29]

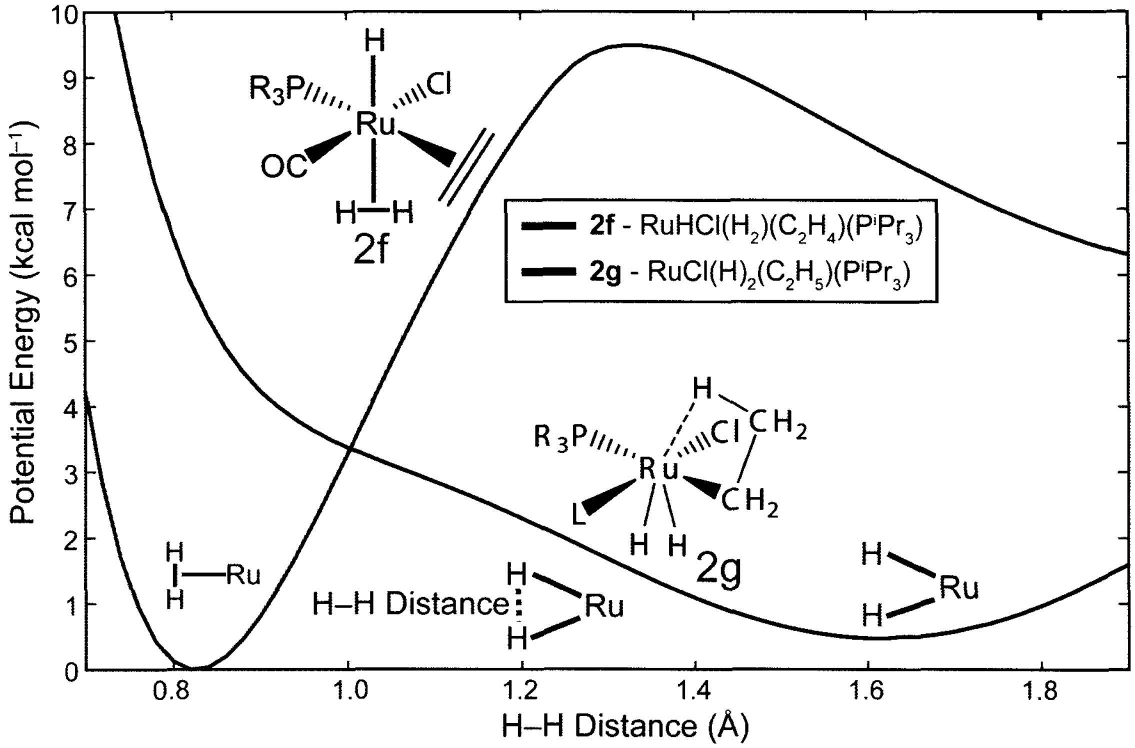

Figure 3.6. PES of the H–H coordinate in complexes **2f** and **2g**. A relaxed scan was performed on the H–H distance in 0.02 Å increments.

3.2.5. Elimination Step

Having formed the dihydride intermediate **2g**, the only remaining step in the catalytic cycle is the elimination of the hydrogenated product. There is an obvious route for this elimination in **2g**, as the two newly-formed hydride ligands are in the basal plane of the intermediate, cis to the ethyl ligand. Transfer of the nearest hydride to the methylene carbon of the ethyl ligand (**2-TS2**) is a facile process, with an energy barrier of 1.1 kcal mol^{-1} with respect to intermediate **2g**. This transition state releases the hydrogenated product (ethane) and regenerates the active catalyst. This step is strongly exergonic due to the formation of the C–H bond. We note that the stereochemistry of the active catalyst is opposite to that of the active catalyst at the start of the catalytic cycle, which precludes asymmetric hydrogenation activity for a catalyst operating through this catalytic cycle.

3.2.6. Reaction Profile

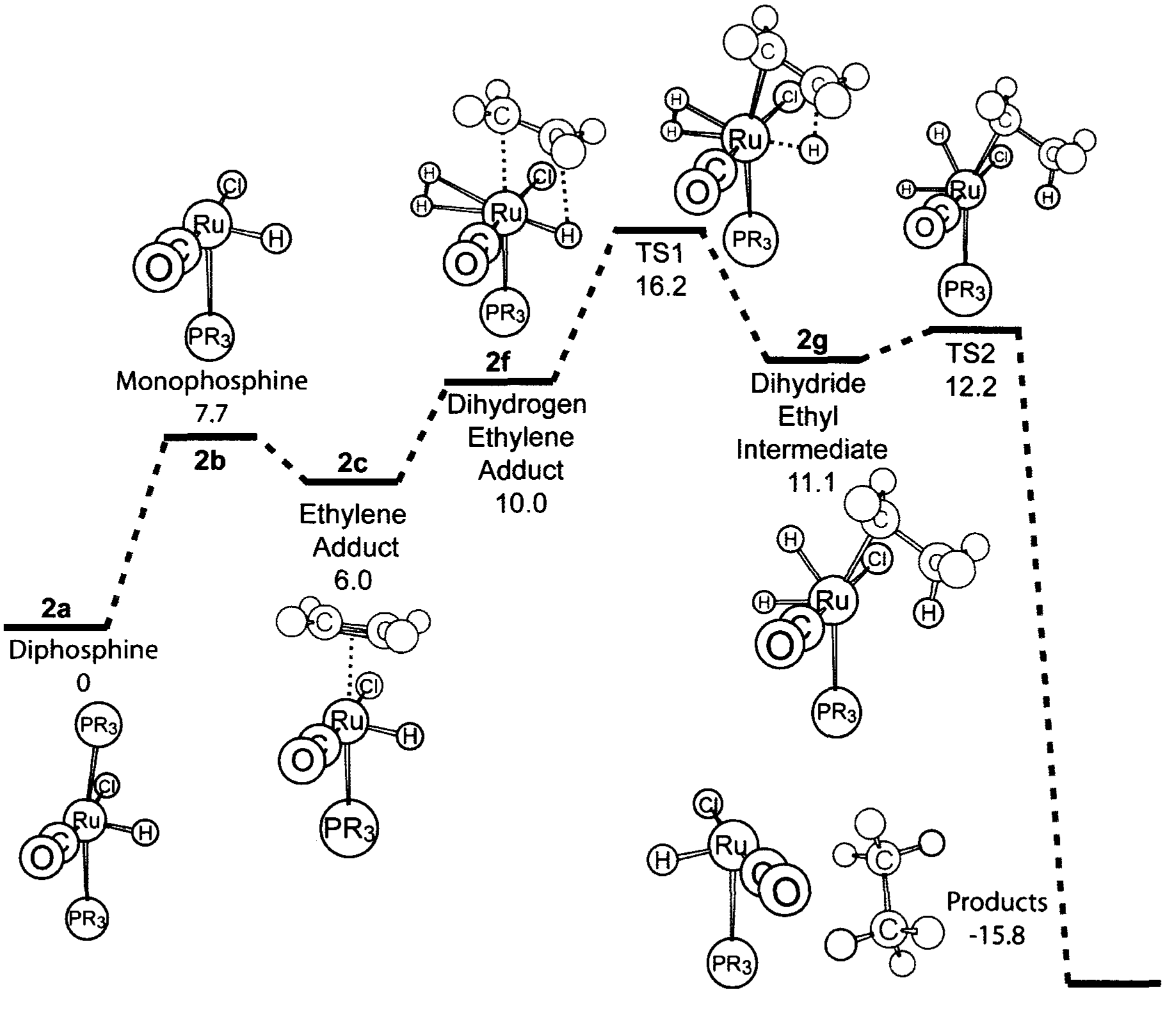

Figure 3.7. Gibbs free energy reaction profile of the full H_2-hydrogenation catalytic cycle (R = ^{i}Pr) . Energies are given beneath the title of the species in kcal mol^{-1}.

Our calculated free energy profile of the catalytic cycle summarized in Figure 3.2 is presented in Figure 3.7. Dissociation of one coordinating phosphine to form **2b** is endergonic (7.7 kcal mol^{-1}) due to the strong coordination energy of the phosphine. This is partially compensated for by the coordination of ethylene, although the coordination energy of ethylene to the metal is not as strong as that of the phosphine, so this complex is less stable (6.0 kcal mol^{-1}) than the diphosphine precatalysts (**2a**). As the coordination of dihydrogen to this complex is relatively weak at this stage, the formation of the dihydrogen ethylene adduct is endergonic (10 kcal mol^{-1}). The barrier corresponding to TS1 is the highest point on the reaction coordinate (16.2 kcal mol^{-1}), due in large part to the instability of the preceding dihydrogen ethylene adduct (**2c**). The insertion step is rate-limiting, which is consistent with the reports of Yi et al.[18,39] The dihydride intermediate is slightly less stable than the ethylene adduct (11.1 kcal mol^{-1}), although the barrier for the elimination transition state (TS2) is facile with respect to this intermediate (12.2 kcal mol^{-1}). The elimination of ethane is strongly exergonic due to the formation of the second C–H bond and the increase in entropy upon dissociation.

3.3. Computational Methods

All calculations we report here used DFT with the BP86 functional[40,41] and the def2-TZVP basis set and core potential combination.[42] Benchmarking calculations against the B3LYP and TPSS functionals were found to give similar results (see Section 3.5). Optimized structures were confirmed as stationary points using frequency analysis. Zero-point energy and Gibbs free energy corrections were determined using the calculated vibrational frequencies within the harmonic approximation. See Appendix D for the equations used to calculate the free energy corrections.

3.4. Conclusions

These findings update the long-standing mechanism for olefin hydrogenation *via* ruthenium hydride catalysts of the class **2a** in two significant aspects. First, the ethyl intermediate formed by olefin insertion utilizes an "ancillary" H_2 ligand to stabilize the electron-deficient ruthenium centre through σ-bond donation, where the classic model invoked ethylene insertion prior to H_2 binding. Secondly, activation of H_2 and elimination of alkane involve an oxidative addition-reductive elimination sequence (i.e. a Ru(IV) dihydride intermediate), rather than heterolytic cleavage of H_2 within Ru(II) species. This unusual metastable Ru(IV)–dihydride intermediate will be investigated further using MD in Chapter 4. We note that these revisions remain consistent with the experimentally determined rate law, as the rate-limiting step is **TS1**, which yields a rate law first order in [olefin] and first order in [H_2].

3.5. Supplementary Section: Computational Benchmarks

To validate of our computational methodology, we compared the relative energies for the reaction mechanism presented in Figure 3.7 calculated using BP86 to those calculated with two alternative DFT functionals: B3LYP and TPSS. These data are presented in Table 3.2. For both methods, the general structure and geometry of each species was similar to those we found using BP86. The largest differences occurred in the phosphine dissociation step, where the relative energy of complex **2b** ranges from 20.5 kcal mol^{-1} for B3LYP to 26.0 kcal mol^{-1} for TPSS. The reactive steps of species **2c-2g** and transition states **2-TS1** and **2-TS2** were generally more consistent, predicting a rate-limiting olefin insertion step and a facile reductive elimination step. Based on these data, we are confident that the general reaction mechanism we presented in this chapter is not an artifact of our use of the BP86 functional.

Table 3.2. Relative energies of species in reaction profile using the BP86, B3LYP, and TPSS functionals and the def2-TZVP basis set.

Species	**Relative Electronic Energy (kcal mol^{-1})**		
	BP86	**B3LYP**	**TPSS**
2a	0.0	0.0	0.0
2b	23.3	20.5	26.0
2c	7.0	8.7	7.2
2d	−0.9	3.2	−1.7
2-TS1	5.5	10.8	5.9
2g	−0.4	5.7	1.5
2-TS2	0.7	6.6	2.6
Products	−15.3	−17.3	−11.5

3.6. Supplementary Section: Alternative Mechanisms

Before concluding that the mechanism we have presented in the main section of this chapter was operative, we considered a range of other possible mechanisms. We considered four general variants of this mechanism: a unsaturated insertion (Section 3.6.1) where the complex isomerizes to a form where direct insertion is possible, a mechanism wherein the metal is in a triplet spin state (Section 3.6.2), a mechanism where the metal is stabilized by an agostic interaction with an aliphatic group on the phosphine (Section 3.6.3), and a mechanism where both phosphines remain coordinated to the metal during the insertion (Section 3.6.4). We ultimately rejected these mechanisms in favour of the mechanism presented in the main text

3.6.1. Unsaturated Insertion

To find possible unsaturated insertion mechanisms, we identified the minimum-energy isomer of the ruthenium hydride complex where ethylene has coordinated to the metal. In the minimum energy configuration, the hydride occupies the apical site and the coordinated ethylene is coordinated trans to the phosphine (**2c**). The energies of all the species reported in this section are reported relative to this complex.

Possible structures for the putative Ru(II)–ethyl intermediate were found using a systematic search of all possible configurational isomers. The 12 possible isomers were built in a square pyramidal geometry, where the ethyl ligand has a β-agostic interaction with the metal, then optimized. The calculated energies of these structures are reported in Table 3.3. We number these complexes **S2**-**S13** to differentiate them from the species we ultimately present as the presumptive reaction mechanism.

Table 3.3. Possible isomers corresponding to a 16-electron reaction intermediate containing an ethyl ligand. Energies are reported relative to the minimum energy isomer of the ethylene adduct **2c**.

Isomer	Structure	ΔE (kcal mol^{-1})
S2	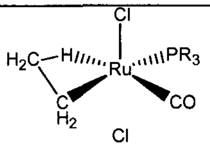	18.6
S3	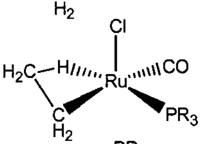	21.5
S4	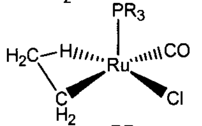	Optimizes to **S10**
S5	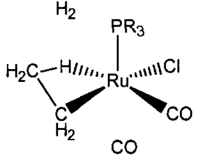	Optimizes to **S10**
S6	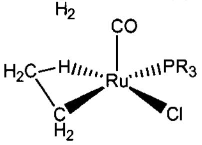	15.0
S7	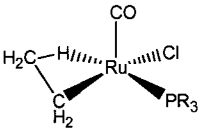	11.9
S8	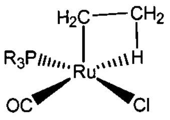	13.9
S9	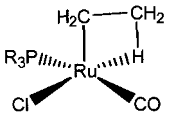	14.9
S10	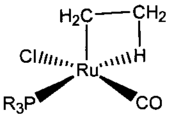	-1.6
S11	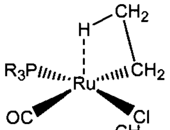	Optimizes to **S8**
S12	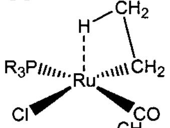	Optimizes to **S9**
S13	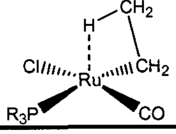	Optimizes to **2c**

Isomers **S2**, **S3**, **S6**, **S7**, **S8**, and **S9** were too high in energy to be considered viable intermediates. Isomers **S4**, **S5**, **S11**, **S12**, and **S13** were not potential energy minima and optimized to other isomers. Structure **S13**, corresponding to the commonly suggested form putative intermediate **2d**, reverted to the ethylene adduct (**2c**) structure when optimized. The lowest energy isomer found through this process was **S10**, which was 1.6 kcal mol^{-1} more stable than the ethylene adduct.

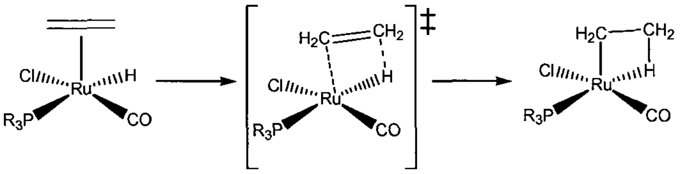

Scheme 3.1. Ethylene adduct and insertion transition state leading to **S10**.

Taking **S10** to be the only catalytically significant ethyl intermediate for this complex, we found its corresponding ethylene adduct and transition state (Scheme 3.1). The ethylene adduct leading to this intermediate is 14.0 kcal mol^{-1} less stable than the most stable ethylene adduct due to the unfavourable trans interaction between the hydride and the phosphine. As a result, the barrier to insertion is high (14.4 kcal mol^{-1}), despite the relative stability of the resulting intermediate. This leads to a rate-limiting barrier that is considerably higher than what we concluded was the minimum-energy mechanism.

3.6.2. Triplet Mechanism

As **S13** is not a stable intermediate in the singlet spin state, we attempted to optimize this structure in a triplet spin state. In a triplet spin state, isomer **S13** optimizes to a distorted square planar structure with no *β*-agostic interaction through the ethyl ligand (Scheme 3.2). Although this structure is a potential energy minimum, it is 19.4 kcal mol^{-1} less stable than the reference adduct. Based on its relative instability, we have also rejected this species as a possible intermediate.

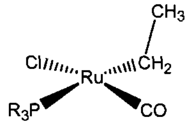

Scheme 3.2. Structure of triplet configuration of **S13**.

3.6.3. Agostic Phosphine Interactions

A ruthenium triscyclohexylphosphine complex stabilized by an agostic interaction with a cyclohexyl C–H bond has been reported by Arliguie *et al.*[43] In principle, such an interaction could stabilize the ethyl intermediate when the phosphine has flexible alkyl substituents, such as a cyclohexyl (Scheme 3.3). We attempted to optimize ethyl intermediate structures featuring this interaction using triscyclohexylphosphine. In all cases, the intermediate optimized to a structure where ethylene deinserted to revert to the ethylene adduct. This indicates that the agostic interaction through the cyclohexyl group is not strong enough to stabilize this intermediate.

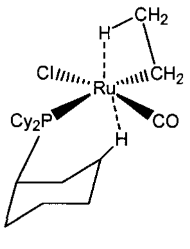

Scheme 3.3. Proposed ethyl intermediate stabilized through an agostic interaction with a cyclohexyl C–H bond.

3.6.4. Associative Insertion Mechanism

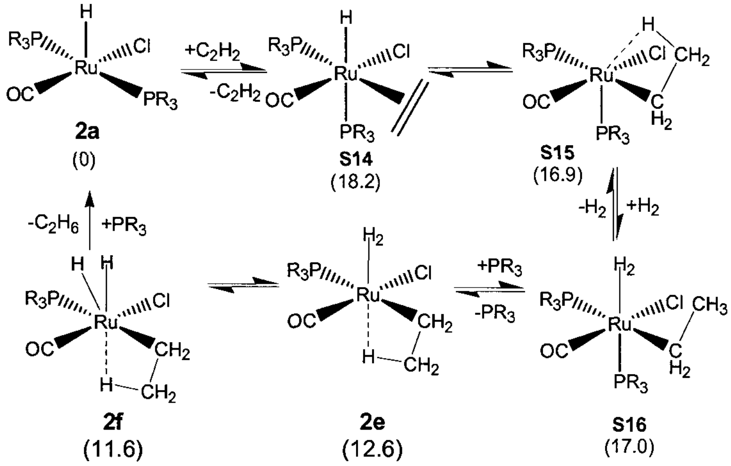

Scheme 3.4. Associative insertion mechanism. Free energies in kcal mol^{-1} are in parenthesis.

A remaining alternative is for both phosphines to remain coordinated to the metal during insertion (Scheme 3.4). Upon the coordination of ethylene, the complex isomerizes such that a phosphine is trans to the hydride (**S14**). This would allow the phosphine to serve as the two-electron donor that must be present for the insertion to occur. This insertion generates **S15**, where the phosphine is trans to the C–H agostic interaction. After the insertion, H_2 can coordinate to the metal by displacing the C–H agostic interaction between the ethyl group and the metal (**S16**). Subsequently, phosphine can dissociate from the metal to form **2e**. This mechanism coincides with the mechanism proposed in the main text of the manuscript from this point. This mechanism would be consistent with the inverse dependence on the concentration of phosphine in the experimental rate law, provided that the rate-limiting barrier occurs in the oxidative addition/reductive elimination steps after the dissociation of phosphine.

Our calculations indicate that this mechanism is a higher energy pathway than the dissociative mechanism we propose in the main text. **S14** is an unstable species (18.2 kcal mol^{-1}), as there is an unfavourable trans interaction between the phosphine and the hydride and significant steric repulsion between the cis-disposed phosphines. The insertion is rate-limiting in this mechanism, with a barrier of 24.9 kcal mol^{-1}. This mechanism is unlikely to be operative as this barrier is 8.9 kcal mol^{-1} higher than the rate-limiting insertion in our proposed mechanism. The ethyl intermediate formed from the insertion (**S15**) are both moderately stable, at roughly 17 kcal mol^{-1} less stable than the reactants. The analogous mechanism with $RuHCl(CO)(PH_3)(P^iPr_3)$ has a barrier for insertion of only 10.1 kcal mol^{-1}. This suggests that a catalyst of this class with sterically small phosphines may have an active associative pathway where the insertion occurs with both phosphines coordinated to the metal.

References

1. Blaser, H.-U.; Malan, C.; Pugin, B.; Spindler, F.; Steiner, H.; Studer, M. *Adv. Synth. Catal.* **2003**, *345*, 103.

2. Noyori, R.; Okhuma, T. *Angew. Chem. Int. Ed.* **2001**, *40*, 40.

3. Clapham, S. E.; Hadzovic, A.; Morris, R. H. *Coord. Chem. Rev.* **2004**, *248*, 2201.

4. Cui, X.; Burgess, K. *Chem. Rev.* **2005**, *105*, 3272.

5. Genet, J.-P. *Acc. Chem. Res.* **2003**, *36*, 908.

6. *Homogeneous Hydrogenation*; Chaloner, P. A.; Esteruelas, M. A.; Joo, F.; Oro, L. A., Eds.; Kluwer: Boston, 1994; Vol. 15.

7. James, B. R. In *Homogeneous Hydrogenation*; John Wiley & Sons, Inc.: New York, NY, 1973, p 83.

8. McManus, N. T.; Rempel, G. L. *Journal of Macromolecular Science, Reviews in Macromolecular Chemistry and Physics* **1995**, *C35*, 239.

9. Tangthongkul, R.; Prasassarakich, P.; Rempel, G. L. *J. Appl. Polym. Sci.* **2005**, *97*, 2399.

10. Martin, P.; McManus, N. T.; Rempel, G. L. *J. Mol. Catal. A: Chem.* **1997**, *126*, 115.

11. Camm, K. D.; Castro, N. M.; Liu, Y.; Czechura, P.; Snelgrove, J. L.; Fogg, D. E. *J. Am. Chem. Soc.* **2007**, *129*, 4168.

12. Drouin, S. D.; Zamanian, F.; Fogg, D. E. *Organometallics* **2001**, *20*, 5495.

13. Bielawski, C. W.; Louie, J.; Grubbs, R. H. *J. Am. Chem. Soc.* **2000**, *122*, 12872.

14. Watson, M. D.; Wagener, K. B. *Macromolecules* **2000**, *33*, 3196.

15. Dias, E. L.; Nguyen, S. T.; Grubbs, R. H. *J. Am. Chem. Soc.* **1997**, *119*, 3887.

16. McLain, S. J.; McCord, E. F.; Arthur, S. D.; Hauptman, E.; Feldman, J.; Nugent, W. A.; Johnson, L. K.; Mecking, S.; Brookhart, M. *Polym. Mater. Sci. Eng.* **1997**, *76*, 246.

17. Hallman, P. S.; Evans, D.; Osborn, J. A.; Wilkinson, G. *Chem. Commun.* **1967**, 305.

18. Yi, C. S.; Lee, D. W. *Organometallics* **1999**, *18*, 5152.

19. Yi, C. S.; Lee, D. W.; He, Z.; Rheingold, A. L.; Lam, K.-C.; Concolino, T. E. *Organometallics* **2000**, *19*, 2909.

20. Crabtree, R. H. *The Organometallic Chemistry of the Transition Metals*; 4th ed.; John Wiley and Sons, Inc.: Hoboken, NJ, 2005.

21. Heyn, R. H.; Macgregor, S. A.; Nadasdi, T. T.; Ogasawara, M.; Eisenstein, O.; Caulton, K. G. *Inorg. Chim. Acta* **1997**, *259*, 5.

22. Gerard, H.; Eisenstein, O. *Dalton Trans.* **2003**, 839.

23. Gusev, D. G.; Kuhlman, R. L.; Renkema, K. B.; Eisenstein, O.; Caulton, K. G. *Inorg. Chem.* **1996**, *35*, 6775.

24. Esteruelas, M. A.; Oro, L. A. *Adv. Organomet. Chem.* **2001**, *47*, 1.

25. Esteruelas, M. A.; Sola, E.; Oro, L. A.; Werner, H.; Meyer, U. *J. Mol. Catal.* **1988**, *45*, 1.

26. Esteruelas, M. A.; Sola, E.; Oro, L. A.; Werner, H.; Meyer, U. *J. Mol. Catal.* **1989**, *53*, 43.

27. Dapprich, S.; Frenking, G. *J. Phys. Chem.* **1995**, *99*, 9352.

28. Hallman, P. S.; McGarvey, B. R.; Wilkinson, G. *J. Chem. Soc. A* **1968**, 3143.

29. *Metal Dihydrogen and σ-Bond Complexes*; Kubas, G. J., Ed.; Kluwer: New York, 2001.

30. Knoth, W. H. *J. Am. Chem. Soc.* **1972**, *94*, 104.

31. Crabtree, R. H.; Hamilton, D. G. *J. Am. Chem. Soc.* **1986**, *108*, 3124.

32. Gruenwald, C.; Gevert, O.; Wolf, J.; Gonzalez-Herrero, P.; Werner, H. *Organometallics* **1996**, *15*, 1960.

33. Rodriguez, V.; Sabo-Etienne, S.; Chaudret, B.; Thoburn, J.; Ulrich, S.; Limbach, H.-H.; Eckert, J.; Barthelat, J.-C.; Hussein, K.; Marsden, C. J. *Inorg. Chem.* **1998**, *37*, 3475.

34. Ferrando-Miguel, G.; Wu, P.; Huffman, J. C.; Caulton, K. G. *New J. Chem.* **2005**, *29*, 193.

35. Oliván, M.; Clot, E.; Eisenstein, O.; Caulton, K. G. *Organometallics* **1998**, *17*, 3091.

36. Drouin, S. D.; Yap, G. P. A.; Fogg, D. E. *Inorg. Chem.* **2000**, *39*, 5412.

37. Becke, A. D.; Edgecombe, K. E. *J. Chem. Phys.* **1990**, *92*, 5397.

38. Sargent, A. L.; Hall, M. B.; Guest, M. F. *J. Am. Chem. Soc.* **1992**, *114*, 517.

39. Yi, C. S.; Yun, S. Y.; Guzei, I. A. *Organometallics* **2004**, *23*, 5392.

40. Becke, A. D. *Phys. Rev. A: At. Mol. Opt. Phys.* **1988**, *38*, 3098.

41. Perdew, J. P. *Phys. Rev. B* **1986**, *33*, 8822.

42. Weigend, F.; Ahlrichs, R. *PCCP* **2005**, *7*, 3297.

43. Arliguie, T.; Chaudret, B.; Jalon, F.; Lahoz, F. *J. Chem. Soc., Chem. Commun.* **1988**, 998.

CHAPTER 4

A Path Sampling Study of Ru–Hydride Catalyzed H_2–Hydrogenation of Ethylene

This work has been published in part in Rowley, C. N.; Woo, T. K. *J. Am. Chem. Soc.* **2008**, *130*, 7218.

Abstract

Ab initio molecular dynamics and transition path sampling were used to examine the dynamics of the H_2-hydrogenation of ethylene with the catalyst $RuHCl(CO)(PR_3)_2$. The simulations showed H_2 is coordinated very weakly to the metal until ethylene insertion, where it is cleaved into a dihydride intermediate. Reductive elimination of ethane proceeds shortly after the insertion ethylene and oxidative addition of H_2. The dihydride has a shorter lifetime than RRKM theory predicts due to the localization of kinetic energy into Ru–H vibrational modes after the insertion step.

4.1. Introduction

Computational chemistry has made many important contributions to the study of reaction mechanisms in organometallic chemistry, allowing the short-lived intermediate and transition states structures of a reaction mechanism to be located and analyzed.[1-3] Although computational chemistry has successfully modeled aspects of chemical reactivity, most studies only identify potential energy minima (reactants, products, and intermediates) and saddle points (transition states). Even at moderate temperatures, vibrational effects can be essential to the full understanding of a reaction mechanism.[4-6]

The range of thermally accessible structures, the intense molecular vibrations involved in crossing transition states, and the redistribution of vibrational energy in reaction intermediates are important features of a mechanism, but are unobtainable from the potential energy reaction profile alone. Simulating the motion of the atoms through time with *ab initio* molecular dynamics (AIMD) simulations is a powerful means to examine these effects;[7,8] however, reactions with significant barriers, such as those present in many organometallic reactions, need impractically long simulations to be observed.

Commonly, this timescale problem is circumvented by imposing artificial forces to drive the system across the reaction coordinate in a short simulation. While this approach has yielded many significant insights in a range of catalytic systems,[9-11] the true dynamics of the reaction are masked by these artificial forces. One promising technique for addressing this problem is transition path sampling (TPS); an innovative Monte Carlo scheme that allows reactive events, such as chemical reactions, to be studied with MD.[12] Given an initial trajectory,[13] path sampling can generate an ensemble of reactive, dynamical trajectories. This ensemble can then be analyzed to describe the dynamics of the reaction. Although the MD simulations used in these studies neglect nuclear-quantum effects, such as vibrational energy quantization and tunneling,[7,8] these simulations still serve as an approximate means to examine the dynamical features of chemical reactions.

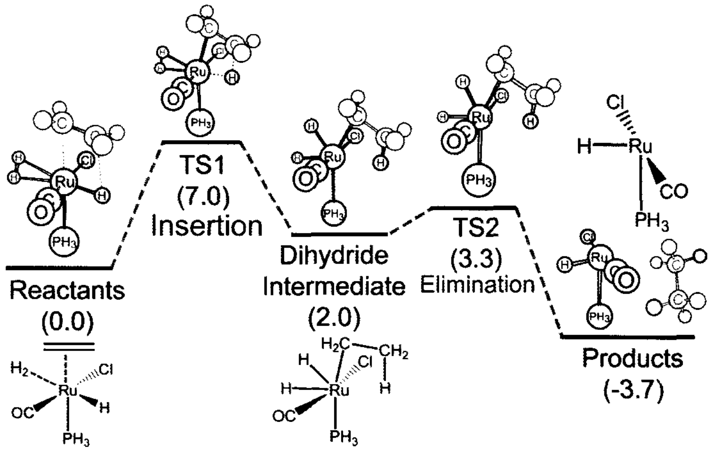

Figure 4.1. Potential energy reaction profile for the insertion (TS1) and elimination (TS2) steps of the H_2-hydrogenation of ethylene. Energies in parenthesis are in kcal mol^{-1}.

Combined with density functional theory (DFT), path sampling has great potential for investigating organometallic reactions. In this study, we have used AIMD in conjunction with path sampling to examine the dynamics of key steps in a notable catalytic reaction; the H_2-hydrogenation of ethylene with the catalyst $RuHCl(CO)(PR_3)_2$, a mainstay of homogenous catalysis which was modeled in Chapter 3.[14-17] The potential energy profile of the insertion and elimination steps is summarized in Figure 4.1 (not including zero-point corrections). The critical step of this mechanism is the insertion of ethylene into the Ru–H bond (TS1), which leads to a dihydride intermediate that undergoes reductive elimination of ethane through a 1.3 kcal mol^{-1} barrier (TS2). This is an exemplary subject for a path sampling study, as it involves three important organometallic reaction steps: olefin insertion into an M–H bond, oxidative addition of H_2 to a metal, and reductive elimination of an alkane. While our DFT calculations predicted that the intermediate was unambiguously an Ru(IV)–dihydride, previous reports had precluded this possibility, as nonclassical Ru(II)–H_2 complexes are more commonly observed experimentally.[18] Herein, we report an MD and path sampling study of the insertion and elimination steps of this catalytic cycle to analyze the dynamics of these reaction steps and resolve the nature of this surprising Ru(IV) dihydride intermediate.

4.2. Results and Discussion

4.2.1. Reactant Equilibrium Dynamics

Our reactant complex, $RuHCl(CO)(C_2H_4)(H_2)(PH_3)$, has not been reported experimentally due to the weak association of H_2 to the metal and the tendency of the precatalyst to form saturated, diphosphine ethyl complexes in solution with ethylene.[19] To establish a complete description of this reactant structure at room temperature, we ran a 20 ps molecular dynamics simulation initiated from the minimum-energy geometry, subject to a thermostat to maintain a constant temperature of 300 K. While nuclear-quantum effects will be significant for the dynamics of the coordinated H_2, we can infer from these simulations that the H_2 has a large degree of configurational freedom, with large fluctuations in the Ru–$\eta^2(H_2)$ distance (the RMSD of the Ru–$\eta^2(H_2)$ distance is 0.12 Å). Conversely, the Ru–$\eta^2(C_2H_4)$ distance fluctuates in a much smaller range, with an RMSD of 0.05 Å. The C=C axis of the ethylene remains close to its minimum energy orientation, eclipsing the Ru–H bond, with an RMSD of the Hydride–Ru-C=C dihedral angle of 11°. This is consistent with the stronger coordination of the ethylene to the metal (32.2 kcal mol^{-1}) compared to H_2 (7.2 kcal mol^{-1}) and literature reports that the Ru–η^2(olefin) rotation typically has a sizeable barrier.[20,21]

4.2.2. Insertion Reaction Dynamics

Having examined the equilibrium dynamics of this complex, we studied reaction dynamics of the ethylene insertion process using path sampling. 150 trajectories where ethylene insertion occurs were harvested. A typical trajectory shows localization of kinetic energy into the Ru–H stretching and bending modes prior to insertion, followed by alignment of the ethylene over the Ru–H bond. Simultaneously, the hydride is transferred to the ethylene and the coordinated dihydrogen cleaves, forming the intermediate. The C–H bond formed in this step immediately forms an agostic interaction with the metal. The TS1 barrier can be crossed (C–H = 1.58 Å in Figure 4.2) at a variety of Ru–H bond lengths; trajectories crossed the transition state with Ru–H distances that ranged between 1.65 Å and 1.75 Å. This reflects that the Ru–H bond is vibrationally excited during the insertion.

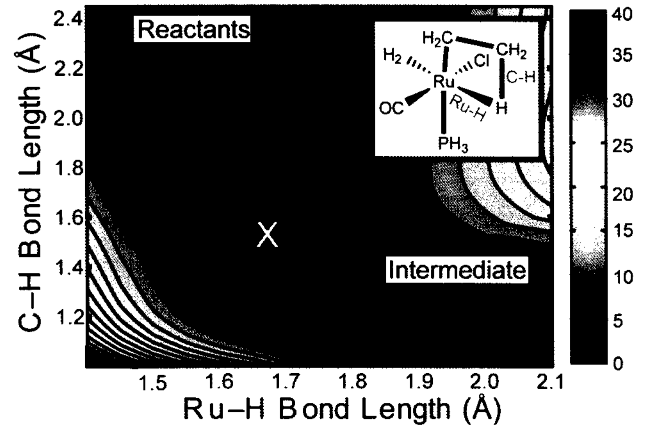

Figure 4.2. Reactive trajectories on the PES of the insertion (TS1). The indicated ruthenium–hydride bond and carbon–hydrogen bonds are used as the x and y axis, respectively. The white X indicates the location of the potential energy transition state. The trajectory analyzed in Figure 4.3 is shown in red. Energies are in kcal mol^{-1}, relative to the optimized reactants.

4.2.3. Intermediate Lifetime

After crossing TS1, only the 1.3 kcal mol^{-1} TS2 must be crossed to eliminate ethane, a common motif in reaction mechanisms, where a large, rate-limiting barrier precedes a small barrier. The lifetimes of these intermediates can be calculated from analysis of the PES using a unimolecular rate theory, of which RRKM is most common. The microcanonical RRKM model expresses the average lifetime (<τ>) of a reaction intermediate as the reciprocal of the microcanonical RRKM rate constant (k(E)) for a total energy, E,

$$\langle \tau \rangle = \frac{1}{k(E)} = \frac{h\rho(E)}{N\left(E - E^{\ddagger}\right)} \tag{4.1}$$

where ρ(E) is the density of vibrational states of the intermediate and $N\left(E - E^{\ddagger}\right)$ is the number of vibrational states in the energy range between the total energy of the complex and the reaction barrier (E‡). The vibrational energy levels can be calculated using normal-mode analysis at the intermediate minimum-energy geometry and the transition state, allowing the number and density of states to be calculated using Beyer and Swinehart's algorithm within the quantum harmonic oscillator model.[22] The dihydride intermediate is predicted to exist for a short but significant period, with an average lifetime of the 7.3 ps. See Appendix C for the full derivation and discussion of RRKM theory.

The classical microcanonical variant of RRKM theory, derived from a classical harmonic oscillator model, correlates most directly to our path sampling simulations, which uses Newtonian mechanics for the movement of the nuclei. In the equation for the average intermediate lifetime within this classical model (Eq. (4.2)), the average intermediate lifetime can be computed trivially from the total energy, the barrier height, and the normal-mode vibrational frequencies of the intermediate and transition state structures (ν_i and $\nu_i^{\ddagger}$, respectively). This model predicts a dihydride intermediate lifetime of 3.6 ps; somewhat shorter than the quantum RRKM model, but still significant. This difference between the quantum and classical RRKM lifetimes suggests that our classical simulations will underestimate the lifetime this intermediate; however, both models predict a lifetime of the order of ps.

$$\langle \tau \rangle = \left(\frac{E}{E - E^{\ddagger}} \right)^{m-1} \frac{\prod_{i=1}^{m-1} \nu_i^{\ddagger}}{\prod_{i=1}^{m} \nu_i} \tag{4.2}$$

RRKM models which use the harmonic approximation to represent vibrational modes can be significantly in error for predicting intermediate lifetimes if there is significant anharmonicity in key reactive modes. Furthermore, RRKM theory assumes equilibrium distribution of kinetic energy in the reaction intermediate, which may not be realistic following a reaction step where kinetic energy has been localized in specific vibrational modes.[23]

Path sampling is a promising means to examine intrinsic non-RRKM effects in chemical reactions. The trajectories harvested provide a range of vibrational energy distributions that reflect the localization of kinetic energy in the newly-formed intermediate. Additionally, the MD simulations underlying TPS intrinsically account for the anharmonicity of vibrational modes, which is an advantage over RRKM models that employ the harmonic oscillator approximation. An early path sampling simulation by Bolhuis et al.[24] found good agreement between rate constants calculated using path sampling and rate constants calculated using classical RRKM theory, although this real-world catalytic system has greater complexity than the 2D Lennard-Jones cluster used in that study. To determine the lifetime of the intermediate resulting from a trajectory were the insertion occurs, we extended the trajectories crossing TS1 forward in time until the simulation crossed TS2. Of the 150 trajectories sampled, 21 recrossed TS1 to revert to the reactants rather than undergoing elimination. Almost 70% of the remaining trajectories crossed TS2 within 1 ps of the formation of the intermediate and all trajectories underwent elimination within 3 ps.

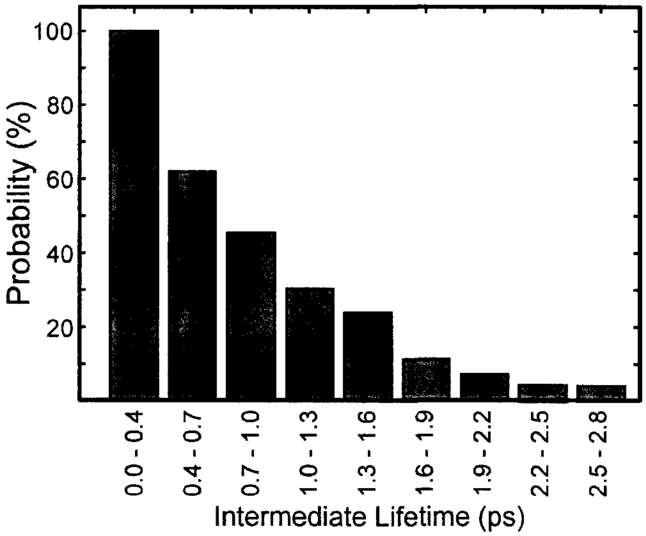

Figure 4.3. Lifetime distribution of dihydride intermediates.

The lifetime of the reaction intermediate was defined as the length of time between the first time step where the intermediate structure formed and the first time step where the ethane was formed (defined as all structures where the C(ethane)–H(hydride) bond length was less than 1.1 Å). A histogram of the distribution of these lifetimes for the trajectories in the ensemble is depicted in Figure 4.3. The y-axis represents the probability that an intermediate will still exist during a lifetime window given on the x-axis. This rapid decay is consistent with "apparent" non-RRKM behaviour,[25] where the non-random initial distribution of vibrational energy in the intermediate results in a faster decay of a reaction intermediate than RRKM theory predicts.

Apparent non-RRKM behaviour is difficult to characterize, as it results from a complex process of kinetic-energy transfer between the atoms of the reactive intermediate, a process is referred to as intramolecular vibrational redistribution (IVR). One way to describe this process is in terms of the intensity of the molecular vibrations, as the vibrational mode corresponding to the unimolecular decomposition must become vibrationally excited for the elimination to occur.

Yamauchi et al. have developed a technique to visualize IVR by performing a windowed Fourier transform on the velocity autocorrelation function of a trajectory.[26] This technique provides a time-resolved spectrogram of the relative intensities of vibrational modes, which has been applied to collision induced reactions[27] and proton transfer.[28] This method could also be an effective method for studying apparent non-RRKM behaviour in chemical reactions by visualizing IVR within a reaction intermediate through its vibrational spectrogram.

To quantify the apparent non-RRKM behaviour leading to the exceptionally short half-life of the Ru(IV)-dihydride intermediate, we have calculated the vibrational spectrogram of a representative trajectory with a short intermediate lifetime (Figure 4.4). The details of the generation of this spectrogram are provided in Section 4.4.3. The redistribution of vibrational energy over the course of the reaction is apparent in the intensities of the key reactive modes. Ru–H stretching and bending vibrations are notably excited prior to the insertion, as the Ru–H bond is stretched from its equilibrium length and bent towards the ethylene ligand in TS1. After the insertion, the hydrides formed by cleavage of the coordinated H_2 gain vibrational energy. Starting near 700 fs, the intermediate undergoes a fluctuation where the dihydride H–H distance contracts to 0.94 Å, transiently forming a nonclassical dihydride structure. This is consistent with the disappearance of the H–Ru–H bending modes starting at 700 fs in Figure 4.4. An H–H stretch causes this structure to revert to a dihydride. In this process, sufficient energy is localized in the H–Ru–H bending mode to cross TS2, causing elimination at 800 fs. We have examined the spectrograms of several other trajectories which have a short intermediate lifetime and they all showed the same qualitative behaviour.

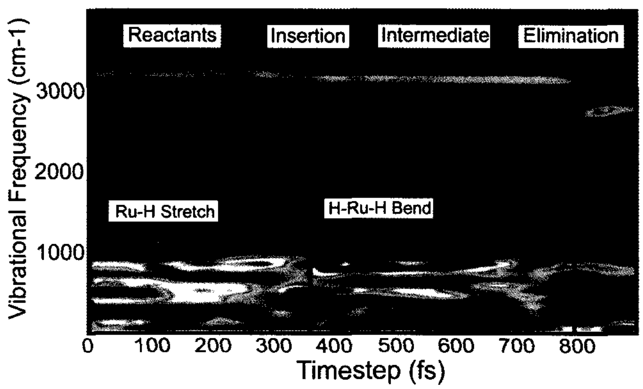

Figure 4.4. Vibrational spectrogram of a trajectory with a dihydride lifetime of 400 fs. Red and blue areas indicate high and low intensity, respectively.

4.3. Conclusions

In this study, we used AIMD in conjunction with transition path sampling to examine the reaction dynamics of the H_2-hydrogenation of ethylene using a mainstay ruthenium-hydride homogeneous hydrogenation catalyst. These simulations provided several insights that are not attainable using conventional QC calculations. Even at 300 K, the vibrational dynamics of this reaction have a significant effect on the molecular structure, how the rate-limiting barrier is crossed, and the elimination of the product. The localization of vibrational energy into H–Ru–H bending modes after the insertion step leads to rapid elimination of the ethane. As such, this mechanism is better understood as a concerted insertion-elimination mechanism with a transient Ru(IV) stage rather than a true stepwise mechanism, so observation of this Ru(IV) intermediate would require a spectroscopic technique operating on the sub-picosecond timescale. This facile and direct cleavage of H_2 through a transient Ru(IV) dihydride intermediate may be of great value to the development of novel hydrogenation catalysts.

4.4. Computational Details

4.4.1. Electronic Structure Methodology

Turbomole 5.8 with the TPSS[29] meta-functional and the def-SV(P) core potential and basis set[30] was used for all the QC calculations we report here. Energies in the reaction profile depicted in Figure 4.1 are calculated with respect to the minimum-energy structure of the reactants. The relative energies and structures of the species on this profile are in generally good agreement with those reported in Chapter 3. No zero-point energy corrections are included in order to be consistent with the classical Born-Oppenheimer molecular dynamics used in the path sampling simulation. A PH_3 group was used to represent the alkyl phosphine ligand to reduce the computational cost. Using static calculations, we found this truncation to be a good approximation for these steps of the reaction profile.

4.4.2. Simulation Methodology

The TPS and MD simulations reported here were performed using our own code interfaced with Turbomole. The reactant complex was equilibrated with a Lowe-Andersen thermostat[31] at 300 K for 10 ps. The average total energy (19.5 kcal mol^{-1} with respect to the optimized reactants) for the last 4 ps was used as the total energy for the 20 ps microcanonical simulation of the reactant complex and the path sampling simulation.

The initial trajectory was generated by assigning Boltzmann distribution velocities to the potential-energy transition state geometry at the total energy determined above, following the procedure described in Chapter 2. 500 fs trajectories were run forward and backward in time from this point, generating a reactive trajectory. 20 shooting moves were run from this initial trajectory to equilibrate the trajectory. These 20 trajectories were not included in the 150 trajectories analyzed in this chapter.

Within the path sampling simulation, the reactants were defined as all structures where the Ru–Hydride bond length was between 1.6 Å and 1.7 Å, the Ru–$\eta^2(H_2)$ distance was between 2.0 Å and 4.0 Å, the H_2 interatomic distance was between 0.6 Å and 1.0 Å and the distance between the hydride and the ethylene carbon it is transferred to is between 2.0 Å and 5.0 Å. The products were defined as all structures where the distance between the hydride and the ethylene carbon it is transferred to is between 0.9 Å and 1.15 Å. All trajectories that crossed between the reactants and products were considered reactive and were added to the transition path ensemble.

4.4.3. Vibrational Spectrogram

The trajectory presented in Figure 4.4 was generated though a Fourier transformation the velocity auto-correlation function, time-resolved using a Hanning window function with a window length of 100 fs. The trajectory was selected from the set of trajectories showing significant non-RRKM behaviour (a lifetime shorter than 600 fs). The vibrational spectrograms of several trajectories of this set were calculated, with each showing the same fundamental behaviour where there is a large vibrational energy redistribution into the H–Ru–H bending mode after the insertion. The spectrogram depicts the absolute value of the power spectrum, normalized by the maximum intensity. Assignment of some frequencies from the spectrogram to specific vibrational modes was not possible, as some frequencies are convoluted with each other and the resolution of the windowed Fourier transform is limited.

References

1. Niu, S.; Hall, M. B. *Chem. Rev.* **2000**, *100*, 353.

2. Ziegler, T.; Autschbach, J. *Chem. Rev.* **2005**, *105*, 2695.

3. Schlegel, H. B. *J. Comput. Chem.* **2003**, *24*, 1514.

4. Ammal, S. C.; Yamataka, H.; Aida, M.; Dupuis, M. *Science* **2003**, *299*, 1555.

5. Michalak, A.; Ziegler, T. *J. Phys. Chem. A* **2001**, *105*, 4333.

6. Seth, M.; Senn, H. M.; Ziegler, T. *J. Phys. Chem. A* **2005**, *109*, 5136.

7. Carloni, P.; Rothlisberger, U.; Parrinello, M. *Acc. Chem. Res.* **2002**, *35*, 455.

8. Tuckerman, M. E. *J. Phys.: Condens. Matter* **2002**, *14*, R1297.

9. Woo, T. K.; Margl, P. M.; Lohrenz, J. C. W.; Bloechl, P. E.; Ziegler, T. *J. Am. Chem. Soc.* **1996**, *118*, 13021.

10. Woo, T. K.; Margl, P. M.; Bloechl, P. E.; Ziegler, T. *J. Phys. Chem. B* **1997**, *101*, 7877.

11. Handgraaf, J.-W.; Meijer, E. J. *J. Am. Chem. Soc.* **2007**, *129*, 3099.

12. Bolhuis, P. G.; Chandler, D.; Dellago, C.; Geissler, P. L. *Annu. Rev. Phys. Chem.* **2002**, *53*, 291.

13. Rowley, C. N.; Woo, T. K. *J. Chem. Phys.* **2007**, *126*, 024110/1.

14. Beach, N. J.; Dharmasena, U. L.; Drouin, S. D.; Fogg, D. E. *Adv. Synth. Catal.* **2008**, *350*, 773.

15. Yi, C. S.; Lee, D. W. *Organometallics* **1999**, *18*, 5152.

16. Clapham, S. E.; Hadzovic, A.; Morris, R. H. *Coord. Chem. Rev.* **2004**, *248*, 2201.

17. Camm, K. D.; Castro, N. M.; Liu, Y.; Czechura, P.; Snelgrove, J. L.; Fogg, D. E. *J. Am. Chem. Soc.* **2007**, *129*, 4168.

18. Crabtree, R. H. *The Organometallic Chemistry of the Transition Metals*; 4th ed.; John Wiley and Sons, Inc.: Hoboken, NJ, 2005.

19. Yi, C. S.; Lee, D. W.; He, Z.; Rheingold, A. L.; Lam, K.-C.; Concolino, T. E. *Organometallics* **2000**, *19*, 2909.

20. Faller, J. W.; Johnson, B. V. *J. Organomet. Chem.* **1975**, *88*, 101.

21. del Klerk-Engels, B.; Delis, J. G. P.; Ernsting, J.-M.; Elsevier, C. J.; Frühauf, H.-W.; Stufkens, D. J.; Vrieze, K.; Goubitz, K.; Fraanje, J. *Inorg. Chim. Acta* **1995**, *240*, 273.

22. Beyer, T.; Swinehart, D. R. *ACM Commun.* **1972**, *16*, 379.

23. Carpenter, B. K. *Annu. Rev. Phys. Chem.* **2005**, *56*, 57.

24. Bolhuis, P. G.; Dellago, C.; Chandler, D. *Faraday Discuss.* **1998**, *110*, 421.

25. Baer, T.; Hase, W. L. *Unimolecular Reaction Dynamics*; Oxford University Press: New York, 1996.

26. Yamauchi, Y.; Nakai, H.; Okada, Y. *J. Chem. Phys.* **2004**, *121*, 11098.

27. Tamaoki, M.; Yamauchi, Y.; Nakai, H. *J. Comput. Chem.* **2005**, *26*, 436.

28. Yamauchi, Y.; Ozawa, S.; Nakai, H. *J. Phys. Chem. A* **2007**, *111*, 2062.

29. Staroverov, V. N.; Scuseria, G. E.; Tao, J.; Perdew, J. P. *J. Chem. Phys.* **2003**, *119*, 12129.

30. Schaefer, A.; Horn, H.; Ahlrichs, R. *J. Chem. Phys.* **1992**, *97*, 2571.

31. Koopman, E. A.; Lowe, C. P. *J. Chem. Phys.* **2006**, *124*, 204103/1.

CHAPTER 5

Computational Design of Ruthenium Hydride Olefin-Hydrogenation Catalysts Containing Hemilabile Ligands

This chapter is comprised of a paper published in the Canadian Journal of Chemistry in a special issue dedicated to Professor Tom Ziegler. As permitted by our faculty, we have included this article in its published form.

Computational design of ruthenium hydride olefin-hydrogenation catalysts containing hemilabile ligands[1,2]

Christopher N. Rowley and Tom K. Woo

Abstract: Three ruthenium hydridocarbonyl complexes containing bidentate hemilabile ligands have been evaluated as possible catalysts for the H_2 hydrogenation of olefins. Our previous investigations of the mainstay hydridoruthenium catalyst, $RuHCl(CO)(PR_3)_2$ (**1**), indicated that the rate-limiting olefin-insertion barrier was increased by the need for an H_2 molecule to act as a stabilizing two-electron donor. Using density functional theory (DFT) calculations, we have determined that a P,N phosphane-oxazoline would be suitable for stabilizing the metal center of the complex $RuHCl(CO)(P^iPr_3)(DZ)$, where DZ is a neutral bidentate hemilable ligand. In the reaction catalyzed by this complex, the olefin insertion occurs before the coordination of H_2, avoiding the entropic penalty of coordinating H_2. We predict that the phosphane-oxazoline containing catalyst will have higher activity than **1** and a different rate-law, zero-order in $[H_2]$. The oxazoline increases the strength of coordination of the ethylene due to stronger back-donation from destabilized Ru d-orbitals to the ethylene π^* molecular orbital.

Key words: catalyst design, catalysis, olefin, hydrogenation, DFT, hemilabile, phosphine, oxazoline.

Résumé : On a évalué la possibilité d'utiliser trois complexes hydridocarbonyle du ruthénium contenant des ligands bidentates hémilabiles comme catalyseurs pour l'hydrogénation d'oléfines. Les études antérieures effectuées avec le catalyseur traditionnel de l'hydridoruthénium, $RuHCl(CO)(PR_3)_2$, **1**, ont permis de déterminer que l'étape cinétiquement limitante à l'insertion de l'oléfine est rehaussée par la nécessité qu'une molécule d'hydrogène agisse comme donneur stabilisant de deux électrons. Se basant sur des calculs de la théorie de la fonctionnelle de la densité, on a pu déterminer qu'un ligand phosphane-oxazoline contenant un atome d'azote et un atome de phosphore devrait être approprié pour stabiliser le centre métallique du complexe RuHCl(CO)(*iso*Pr$_3$)(DZ) dans lequel le groupe DZ est un ligand bidentate hémilabile neutre. Dans la réaction catalysée par ce complexe, l'insertion de l'oléfine se produit avant la coordination du H_2 ce qui a pour effet d'éviter la pénalité entropique de la coordination du H_2. Sur la base des calculs, il est prédit que l'activité d'un catalyseur contenant un ligand phosphane-oxazoline sera plus élevée que celle du composé **1** et sera régit par une loi de vitesse différente, d'ordre zéro en $[H_2]$. L'oxazoline augmente la force de la coordination de l'éthylène en raison d'un pouvoir de rétrocession plus important à partir des orbitales d déstabilisée du ruthénium vers l'orbitale moléculaire π^* de l'éthylène.

Mots-clés : développement d'un catalyseur, catalyse, oléfine, hydrogénation, théorie de la fonctionnelle de la densité, hémilabile, phosphine, oxazoline.

[Traduit par la Rédaction]

Introduction

The homogeneous H_2 hydrogenation of olefins is of considerable importance in organic synthesis, fine chemical production, and polymer chemistry.[3–5] Among homogeneous catalysts, hydridoruthenium complexes of the class $RuHCl(L)(PR_3)$ are of notable use in the reduction of challenging substrates[6–12] or within a tandem ROMP-hydrogenation (ring-opening metathesis polymerization) process.[13–19]

The first example of this type of catalyst was the arylphosphine complex $RuHCl(PPh_3)_3$, reported 40 years ago by Wilkinson and co-workers.[20,21] Since then, this framework of a neutral Ru(II)–hydride with three two-electron donors has served as the basis for vast amounts of research in homogeneous hydrogenation. Variation of the two-electron donor trans to the chloride found that a strongly bonding but compact CO ligand yields exceptionally good catalytic activity.[11,12] Another branch of optimization led to the substitution of the aryl phosphines for alkyl phosphines.[22–24]

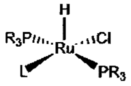

1: L = CO, R = ^{i}Pr

Computational modeling has made increasingly significant contributions in organometallic chemistry.[25,26] In particular, density functional theory (DFT) modeling of catalytic cycles has contributed greatly to catalyst design, and in some recent examples, novel catalysts have been designed computationally in advance of their synthesis.[27–30] In our own research, we have attempted to move beyond the traditional procedures for modeling organometallic reactions, which has led us to study the dynamic features of catalytic

Received 28 January 2009. Accepted 29 April 2009. Published on the NRC Research Press Web site at canjchem.nrc.ca on 25 June 2009.

C.N. Rowley and T.K. Woo.[1] Centre for Catalysis Research and Innovation, Department of Chemistry, University of Ottawa, Ottawa, ON K1N 6N5, Canada.

[1]Corresponding author (e-mail: twoo@uottawa.ca).

doi:10.1139/V09-077

reaction mechanisms,[31,32] to evaluate novel catalysts prior to experiment,[33,34] and to pursue in-depth collaborations with experimentalists.[35]

One exceptionally productive collaboration sparked our interest in this class of olefin-hydrogenation catalysts. In that study, we modeled the catalytic cycle of hydridoruthenium complex **1** using DFT calculations. Kinetic studies had established that the catalytic cycle begins with the dissociation of a phosphine from the metal, although the subsequent steps were more opaque. Some published catalytic cycles proposed that the olefin undergoes insertion into the Ru–H bond to form a four-coordinate alkyl-containing intermediate.[36] Instead, we found that the putative four-coordinate ethyl intermediate formed by this insertion is not a potential-energy minimum and H_2 must be coordinated trans to the hydride prior to the insertion to stabilize this intermediate. As the coordination of H_2 is initially weak due to the trans influence of the hydride, this association is endergonic and increases the activation free energy of the rate-limiting insertion step.

This need for an external stabilizing donor led us to consider how the catalyst could be modified so that it would not be necessary for H_2 to coordinate before the insertion. In principle, another two-electron donor could be introduced to stabilize the metal in the insertion step, although a strong donor could inhibit the activity of the catalyst or induce the complex to isomerize to an inactive form. Conversely, a weak donor may not be able to coordinate trans to the hydride ligand, which has a strong trans influence.

Hemilabile ligands[37–40] could provide an elegant solution to this problem. Hemilabile ligands are polydentate ligands with at least two different coordinating groups. Notably, these coordinating groups can be chosen to have dramatically different interactions with the metal centre. Many highly active catalysts from groups 8–10 contain bidentate DZ-type hemilabile ligands with a strongly coordinating soft donor (D), such as a phosphine or carbene, and a weakly coordinating hard N or O donor (Z). The weakly coordinating donor can stabilize the metal in some steps of the catalytic cycle, but can adjust to interact weakly in other steps. A hemilabile P,N,P ligand was recently used in a related Ru(II) hydride catalyst for the dehydrogenation of alcohols[41] and the hydrogenation of esters,[42] providing precedence for this strategy. In this study, we have used DFT calculations to explore whether incorporating a DZ-type hemilabile ligand to ruthenium–hydrido catalysts similar to **1** could eliminate the need for H_2 to serve as the trans-hydride two-electron donor in the insertion step.

This paper is divided into three sections. In the first section, we present the calculated reaction profile of H_2 hydrogenation of ethylene catalyzed by the benchmark monodentate phosphine complex **1**. In the second section, we screen three potential catalysts containing DZ-type hemilabile ligands. In the last section, we model the catalytic cycle of a novel complex featuring one of these ligands.

Results and discussion

Monodentate phosphine catalyst

To provide a consistent point of comparison, we have included the reaction profile for the catalytic cycle of **1**, based on the mechanism we previously reported. The specific numerical values differ from our earlier report as we have used a different computational procedure in this report; BP86/def2-TZVP is used throughout this paper (see Computational methods for full details), while B3LYP/LACV3P+** was used in our first report. The relative energies and structures are generally consistent for both methods, although in our first report we found that a metastable nonclassical ethyl-dihydrogen intermediate formed after the insertion step. This structure is not a potential-energy minimum with the methodology used in this paper and only the $Ru(H)_2$ intermediate is present in this revised reaction profile.

Fig. 1. Catalytic cycle of ethylene hydrogenation by **1**.

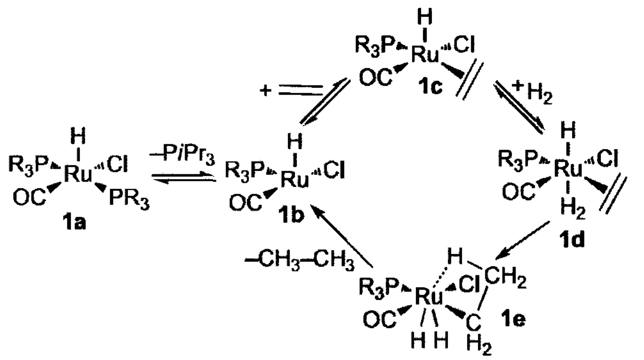

The catalytic cycle of **1** (Fig. 1) begins with the dissociation of P^iPr_3 to form a four-coordinate monophosphine complex **1b**. The olefin can then coordinate to the site vacated by the phosphine to form an η^2 metal-olefin complex (**1c**). Coordination of H_2 trans to the hydride forms **1d**, the immediate precursor to the olefin insertion. This insertion forms a metastable Ru(IV) dihydride intermediate (**1e**), which can facilely undergo reductive elimination to release the product alkane and regenerate **1b**. A path sampling study of this step demonstrated that this elimination generally occurs within 1 ps of the insertion due to localization of vibrational energy into the H–Ru–H bending mode.[33]

We have included the reaction profile of this catalytic cycle in Fig. 2. The dissociation of P^iPr_3 to form **1b** is significantly endergonic (11.8 kcal mol^{-1}). The coordination of ethylene is considerably weaker than that of the phosphine, so **1c** is only marginally more stable (10.1 kcal mol^{-1}). The reaction profile shows that **1d** is an unstable complex, at 14.6 kcal mol^{-1} with respect to the reactants. This is due to the strong trans influence of the hydride ligand and the entropic cost the complexation. As a result, subsequent olefin insertion into the ruthenium–hydride bond is the rate-limiting step on the reaction profile. Although the coordination of H_2 is weak in **1d**, our previous study[35] showed that the H_2 must be present to stabilize the metal during the insertion. The transition state of the insertion step (TS1) has a relative energy of 20.1 kcal mol^{-1}, the rate-limiting step of this profile.

The coordinated H_2 cleaves concurrently to the insertion, resulting in a Ru(IV) dihydride intermediate (**1e**), which is 1.4 kcal mol^{-1} less stable than **1d**. While Ru(IV) dihydrides had been thought to be generally less stable than the alternative non-classical $Ru(H_2)$ form,[43] a growing number of Ru(IV) dihydrides have been identified.[44–49] Given appropriate electron-donating auxiliary ligands and favourable trans

Fig. 2. Gibbs free-energy reaction profile of **1**. Free energies are given below the labels in kcal mol^{-1}.

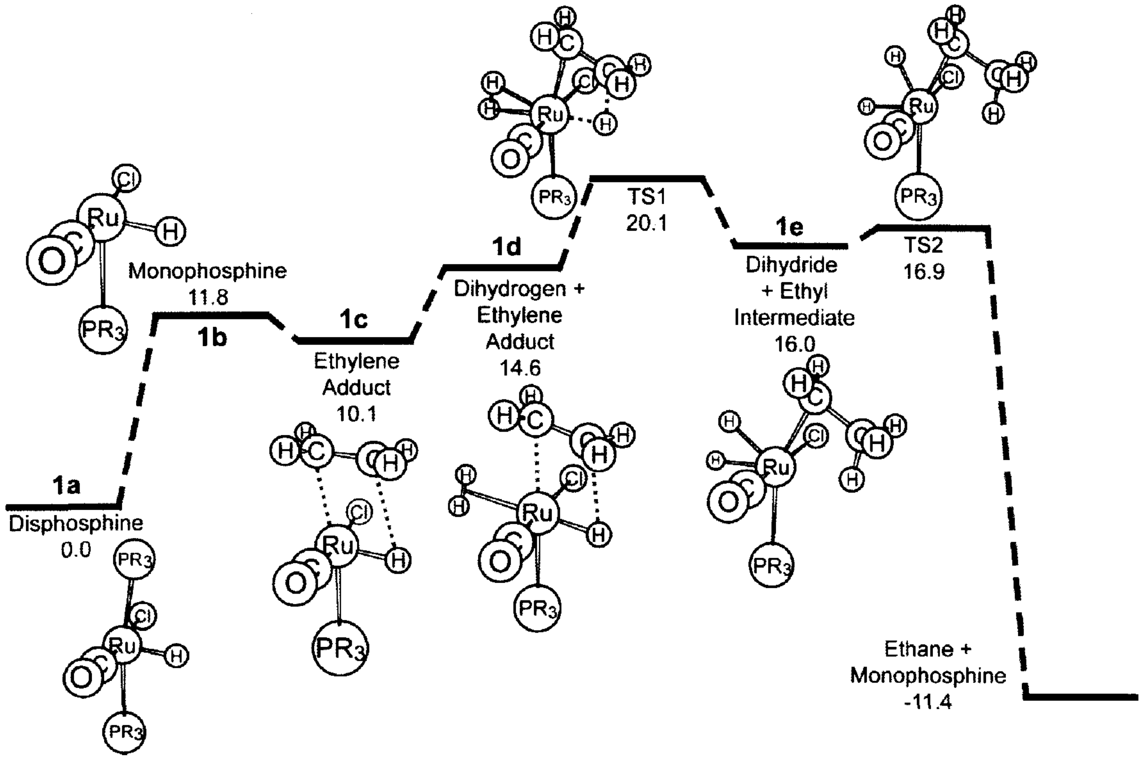

interactions, these dihydrides are viable reaction intermediates in some cases.

Potential hemilabile ligands

With the aim of identifying a ligand system that would allow the insertion to occur before the coordination of H_2, we have considered a series of complexes containing D–Z hemilabile ligands, where D is a strong donor and Z is a weak donor. In these complexes, the D donor occupies the coordinate site trans to the phosphine, while the Z donor occupies the site trans to the hydride (Fig. 3, **DZ-a**).

With the hemilabile ligand present, the catalytic cycle will be somewhat different than for **1** (Fig. 3). While the catalytic cycle still begins with the dissociation of phosphine (**DZ-b**) and the coordination of ethylene to form an olefin adduct (**DZ-c**), the donation from Z should allow the olefin insertion to occur directly from **DZ-c**. The insertion generates an alkyl-containing intermediate (**DZ-d**), which is stabilized by Z. As **DZ-d** is coordinately saturated, a ligand must dissociate to allow the coordination of H_2. Dissociation of Z would cause the complex to immediately revert to **DZ-c**, so the β-agostic interaction in **DZ-d** must be broken instead. This forms a square-pyramidal intermediate, **DZ-e**. Coordination of H_2 to this empty coordination site affords **DZ-f**, which can undergo reductive elimination to release the product and regenerate **DZ-b**.

We initially screened three catalysts containing established hemilabile ligands, **2**, **3**, and **4** with P–N, P–O, and C–N atoms acting as the DZ donors, respectively. The hemilabile ligand in **2** is diphenylphosphanodihydrooxazole, which coordinates to the metal through both the phosphine and the sp^2-hybridized N moiety. This type of ligand has been used extensively by Braunstein and co-workers in Pd-,[50] Ru-,[51,52] Cu-,[53] and Co-based[54] catalysts. **3** contains a benzamide-derived aryl phosphine, which was developed by Kwong et al. for Suzuki–Miyaura cross-coupling reactions.[55] We also evaluated **4**, where the hemilabile ligand is an N-heterocyclic carbene with a pendant pyridine group. This carbene was considered because Dharmasena et al. demonstrated that adding an N-heterocyclic carbene in the place of the alkyl phosphine in **1**, in conjunction with a more labile trans-phosphine, significantly improves hydrogenation activity.[56]

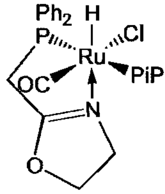

2

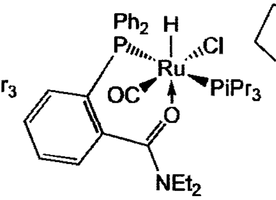

3

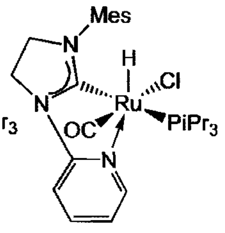

4

For these ligands to function effectively, they must stabilize **DZ-d** in the absence of H_2 coordinating trans to the hydride. To test this, we constructed **2d**, **3d**, and **4d**, then constrained the C–H(ag) distance to 1.1 Å to generate optimized structures corresponding to these intermediates. We then reoptimized these structures without the C–H(ag) constraint to test whether these complexes are stable. **3d** and **4d** are not potential-energy minima, as they reverted to their

Fig. 3. Catalytic cycle for H_2 hydrogenation of ethylene catalyzed by a hydridoruthenium complex with a hemilabile ligand (DZ).

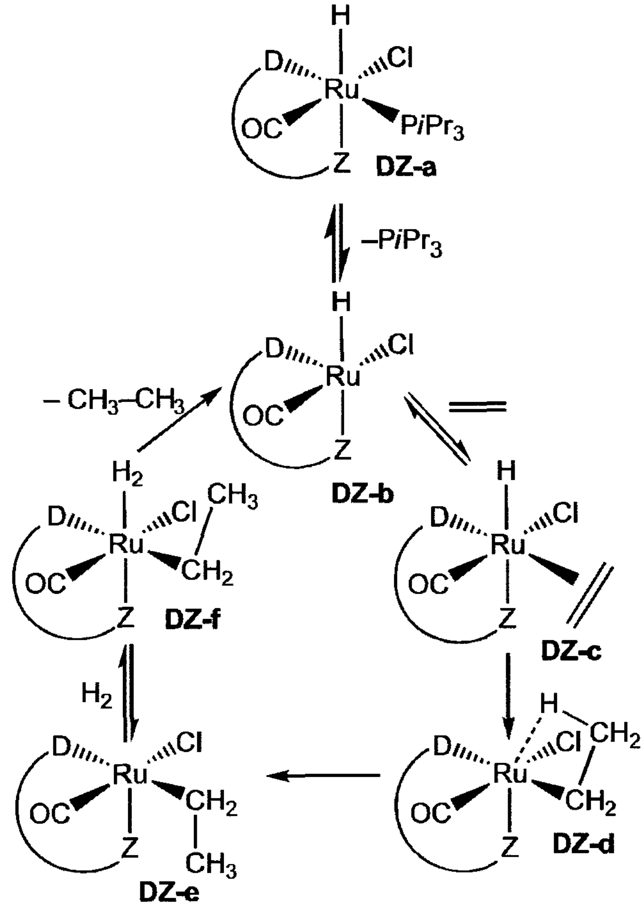

ethylene adduct structures (**3c** and **4c**, respectively), indicating that these hemilabile ligands are not sufficiently strong donors to stabilize this intermediate. The ethyl intermediate of **2** is a potential-energy minimum, indicating that the oxazoline is a strong enough donor to stabilize this intermediate. The relatively high basicity of the oxazoline, as well as the comparatively large bite angle of this ligand, appears to be critical for stabilizing the ethyl intermediate. We have focused our efforts on catalyst **2** as a result.

Evaluating the phosphaoxazoline-containing catalyst

We have calculated the full catalytic cycle for **2**, following the mechanism in Fig. 3. The reaction profile is presented in Fig. 4. The hydride is trans to the oxazoline donor in the minimum-energy isomer of the precatalyst (**2a**), although the alternative isomer where the hydride is trans to the chloride is close in energy. As in the catalytic cycle of **1**, the first step is the dissociation P^{i}Pr$_3$ ligand. This forms a square-pyramidal monophosphine complex (**2b**) with a vacant coordination site trans to the remaining phosphine. This occurs more readily for this catalyst, as this step is endergonic by 6.6 kcal mol^{-1} vs. 11.8 kcal mol^{-1} for **1**. We attribute this to steric repulsion between P^{i}Pr$_3$ and the oxazoline and more limited donation of the phosphine to the more electron-rich metal centre in **2**. The oxazoline–metal interaction is relatively weak in this step (the Ru–N bond order is 0.40), as the hydride has a strong trans influence (Table 1).

This step is followed by the η^2 coordination of ethylene to the vacant coordination site to form **2c**. This coordination is relatively strong, and the calculations predict a small preference to the coordination of ethylene (–0.9 kcal mol^{-1}) over the phosphine. This coordination is considerably stronger than in **1c** due to stronger back-donation interactions (vide infra).

As the oxazoline is able to stabilize the metal in this step, the insertion can proceed immediately after the coordination of ethylene (TS1). The catalytic cycle of **2** differs from **1** beginning at this step, as this insertion occurs prior to the coordination of H_2. The barrier to insertion is modest, at 6.2 kcal mol^{-1} with respect to the initial reactants, as opposed to 20.1 kcal mol^{-1} in the reaction profile of **1**. This indicates that this hemilabile ligand successfully lowers the activation free energy of the insertion step. The oxazoline begins to stabilize the metal significantly in this transition state, as the Ru–N distance decreases to 2.14 Å, and the bond order increases to 0.5.

This transition state leads to **2d**, an intermediate containing the newly formed ethyl ligand. The ethyl group interacts with the metal through an extremely strong β-agostic interaction (Ru–H(ag) = 1.75 Å; C–H(ag) = 1.27 Å). Further, this intermediate is very shallow, with a barrier of only 0.3 kcal mol^{-1} for the β-hydride elimination of the ethyl ligand. The Ru–N bond order increases even further in this step, to 0.54, indicating that the oxazoline is donating to the metal to a greater degree to stabilize this intermediate.

To coordinate H_2 to the metal, the β-agostic interaction in **2d** must be broken. As this agostic interaction is exceptionally strong and the metal is electron poor, the square-pyramidal intermediate formed in this process is 18.1 kcal mol^{-1} on the reaction profile, making this step the rate-limiting process in the catalytic cycle. With the agostic interaction broken, the oxazoline must donate strongly to the metal to stabilize this complex (**2e**); the Ru–N bond length is the shortest of any of the steps of the catalytic cycle (2.00 Å), and the Ru–N bond order is 0.73, considerably larger than in any other step. As this is the rate-limiting step, we would expect that this reaction would be zero order in [H_2], unlike related Ru–monohydride catalysts, which are first order in [H_2].[6,8,10,57]

This intermediate is the highest point on the reaction coordinate. The transition state preceding it would correspond to rotation of the Ru–ethyl segment to break the agostic interaction. This transition state could not be located on the potential-energy surface as this barrier is extremely flat, so we have assumed that the height of this barrier can be approximated by the energy of this intermediate.

With the β-agostic interaction broken, H_2 can coordinate to metal trans to the oxazoline, forming **2f**. This coordination is very strong, resulting in an elongation of the H–H bond to 0.92 Å. This coordination significantly stabilizes the metal and is considerably lower on the reaction profile than **2e** (7.0 kcal mol^{-1} vs. 18.1 kcal mol^{-1}).

The cleavage of dihydrogen and the elimination of the alkane occurs in a concerted fashion (TS2). This step is facile, with an energy barrier of only 11.2 kcal mol^{-1}. The metal

Fig. 4. Gibbs free-energy reaction profile of the catalytic cycle of **2**. Free energies are given below the labels in kcal mol^{-1}.

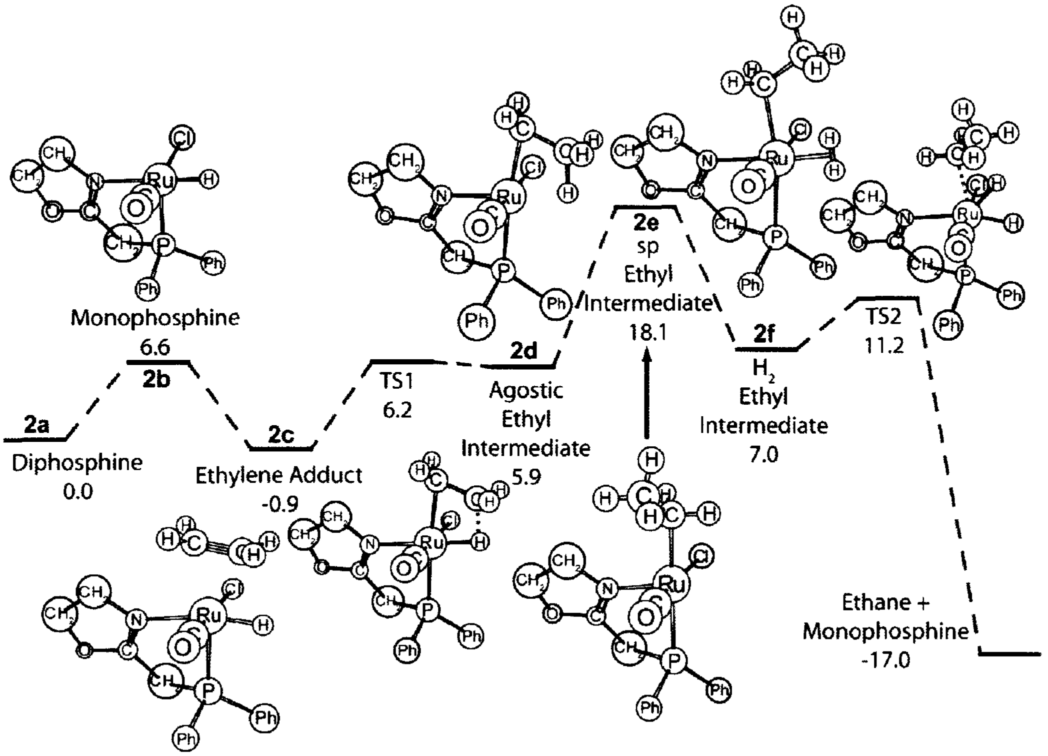

Table 1. Ru–N(oxazoline) bond lengths and Mayer bond orders for the reaction profile of **2**.

Reaction step	Ru–N bond length (Å)	Ru–N bond order
(**2a**) Diphosphine	2.35	0.37
(**2b**) Monophosphine	2.24	0.40
(**2c**) Ethylene adduct	2.24	0.41
TS1	2.14	0.50
(**2d**) β-Agostic ethyl intermediate	2.10	0.54
(**2e**) SP ethyl intermediate	2.00	0.73
(**2f**) H_2 + ethyl intermediate	2.12	0.53
TS2	2.24	0.40

Table 2. EDA of the coordination of ethylene to Ru(L) metal fragment in **1c** and **2c**.

		Energy (kcal mol^{-1})	
Component		**1**	**2**
Pauli repulsion		129.8	138.9
Electrostatic interaction		–92.1	–99.3
Orbital interactions		–66.5	–74.4
Preparation energy	Ru(L)	6.7	6.2
	Ethylene	4.4	6.1
Total		17.7	22.5

stabilizes the transition state via a partial hydridic bond with the transferred hydrogen. In contrast to **1**, no transient dihydride intermediate is formed in this elimination. Avoiding this unstable Ru(IV) dihydride intermediate is another advantage of the use of this hemilabile ligand.

Ethylene coordination

The free energy of coordination of ethylene to **1b** is exergonic by 1.7 kcal mol^{-1}, but the coordination to **2b** is exergonic by 7.7 kcal mol^{-1}. This difference is predominately due to the bond energy of the Ru–ethylene bond, which is

Table 3. Donation, back-donation, and repulsion components of CDA for Ru(L)↔ethylene interactions for the ethylene adducts of **1** and **2**.

Complex	Donation	Back-donation	Repulsion
1c	0.74	0.25	–0.41
2c	0.75	0.33	–0.45

Fig. 5. MO scheme of back-donation interaction in the complex between the monophosphine complex and ethylene for **1c** and **2c**.

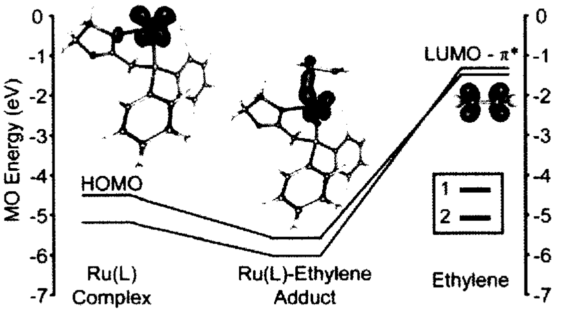

approximately 5 kcal mol^{-1} higher in **2c** than **1c** (Table 2).[58] The alternative conformation of **2c** where the oxazoline is not coordinated to the metal is 6.7 kcal mol^{-1} less stable with respect to the analogous reactants than structures where the oxazoline is coordinated, indicating that the coordination of the oxazoline causes this difference. This is surprising given that the oxazoline donor should make the metal centre more electron-rich and therefore have a lower Lewis acidity. Intrigued by this effect, we used fragment bonding analysis to investigate this further.

In the first stage of our analysis, we applied Ziegler–Morokuma energy decomposition analysis (EDA)[59–61] to complexes **1c** and **2c** (Table 2). EDA divides the bonding energy of two molecular fragments (in these cases, the ethylene ligand is one fragment, and the metal plus all the other ligands is the second fragment) into four components: the Pauli energy, the electrostatic interaction, the orbital interactions, and the preparation energies. The Pauli energy originates from the repulsion of the electron density of the two fragments, the electrostatic term includes the Coulomb interactions between the two fragments, and the orbital interactions term originates from covalent overlap between the fragment orbitals. The preparation energy results from the distortion of each fragment from their minimum-energy geometry to the geometry they adopt in the complex.

2c has a 4.8 kcal mol^{-1} stronger total bond energy than **1c** (Table 2). The Pauli repulsion term is larger for **2c**, although this repulsion is approximately cancelled by greater electrostatic interactions. Metal-fragment preparation energies are roughly equivalent, although the ethylene in **2c** has a higher preparation energy due to greater C=C bond elongation, typical of more strongly coordinated olefins. The crucial difference is that **2c** experiences 7.9 kcal mol^{-1} stronger orbital interactions. As this difference in coordination energies stems from the orbital interaction component, we next investigated the donation and back-donation interactions in complexes **1c** and **2c**.

Charge decomposition analysis (CDA) is a fragment analysis technique for investigating metal–ligand interactions[62] that is complimentary to EDA. This method calculates the relative weights of ligand-to-metal donation, metal-to-ligand back-donation, and an electron repulsion term resulting from the change in interelectron repulsion when the complex is formed. Within Dewar–Chatt–Duncanson theory,[63,64] bonding between transition-metal complexes and olefins results from two types of MO interactions: donation from the π bonding orbital of the olefin to the metal and back-donation from the metal to the π* antibonding orbital of the olefin. CDA data for the interaction between the coordinated ethylene and the metal fragment are presented in Table 3. **2c** has a distinctly higher proportion of back-donation than **1c** relative to the donation and repulsion terms. This indicates that the coordination of the oxazoline increases the interaction between the metal and the π* orbital of the ethylene.

We have identified the origin of this greater orbital interaction by examining the molecular orbitals corresponding to the metal–ethylene bonding. In each complex, the MO corresponding to back-donation is a predominantly combination of the d-character HOMO of the monophospine complex and the unoccupied ethylene π* orbital. Fragment orbital analysis shows that the Ru d-orbitals involved in this back-donation are destabilized by a repulsive interaction with the lone pair of the oxazoline (Fig. 5). This raises the energy of the back-donating Ru d-orbital, thereby reducing the energy difference between the interacting orbitals and making the interaction stronger.

As strong coordination of the olefin substrate is essential in this catalytic cycle, the increase in olefin coordination energy when the oxazoline is coordinated provides an additional benefit for the hemilabile ligand catalyst. Generally, it may be possible to increase the partitioning between ethylene and alkyl phosphines in Ru(II) complexes by introducing a hard, electron-donating ligand to destabilize filled d-orbitals. This favours bonding to olefins, which have higher back-bonding abilities than phosphines.

Conclusions

We have designed and computationally tested RuHCl(CO)(PR$_3$)(DZ) hydrogenation catalysts with hemilabile DZ-type ligands and compared them with an established catalyst RuHCl(CO)(P^{i}Pr$_3$)$_2$ (**1**). In a previous mechanistic study of **1**, it was determined that H$_2$ must coordinate to the catalyst before ethylene can insert into the Ru–H bond of the catalyst. In this work, we have proposed that a hemilabile ligand could act as a two-electron donor to stabilize the metal during the insertion step such that it would not be necessary for H$_2$ to coordinate before ethylene coordination.

Three catalysts, **2**, **3**, and **4**, with P,N, P,O, and C,N hemilabile ligands, respectively, were computationally screened. Of the three hemilabile ligands that we considered, we determined that only a P,N coordinating phospha-oxazoline (**2**) could stabilize the metal sufficiently for the olefin insertion to occur prior to coordinating H_2 to the metal. In principle, such a catalyst would be more active, as the entropic cost of weakly coordinating H_2 to the metal during the rate-limiting process is avoided.

Somewhat surprisingly, the introduction of the hemilabile ligand was found to significantly increase the olefin complexation energy relative to **1**. The reason for this was found to be a stronger Ru–ethylene back-donating interaction that was enhanced by a destabilization of the d-orbitals on the metal by the lone pair on the oxazoline ligand. This was found to lower the energy barriers associated with the ethylene coordination steps of the catalytic cycle.

On the other hand, the introduction of the hemilabile ligand has the detrimental consequence of producing a metal center that is coordinatively saturated after the insertion step. This results in an additional step where the β-agostic interaction between the newly formed alkyl ligand and the metal must be broken in to coordinate H_2. This process is rate-limiting, and we predict that the reaction should be zero-order in $[H_2]$, whereas this reaction with the traditional catalysts is known to be first-order in $[H_2]$. The formation of the intermediate with the strong β-agostic interaction therefore mitigates the rate enhancement induced by the hemilabile ligand.

The calculations presented here suggest that the overall ethylene hydrogenation barrier for the proposed hemilabile phospha-oxazoline containing catalyst, **2**, should be comparable to the more established $RuHCl(CO)PR_3)_2$, **1**, catalyst. Although simulating the reaction on the computer can never replace actually testing the catalyst in the lab, we have rationally designed a new catalyst motif based on our theoretical analysis of the parent catalyst system (**1**). This proposed catalyst motif may provide experimentalists with additional avenues to tune and optimize an important class of catalysts. For example, we believe there are opportunities to further optimize the donor properties of the hemilabile ligands as to stabilize the formation of the rate-determining ethyl intermediate (**2e**).

In addition to any rate enhancement resulting from the hemilabile ligand, the presence of the N donor may improve the catalyst lifetime. Fogg and co-workers have recently concluded that catalyst stability is critical for high activity in these systems,[11] which suggests that blocking decomposition pathways could be a fruitful approach to developing a more robust catalyst. Coordinately saturating the metal and inhibiting the dissociation of the hemilabile phosphine through the chelate effect could deter the degradation of the catalyst.

Computational methods

The calculations presented here were made with DFT,[26] as implemented in Turbomole 5.9[65] using the BP86[66,67] functional and the def2-TZVP basis set.[68] Thermal corrections were determined by reoptimizing these structures with the def2-SV(P) basis set, then running frequency analysis. We confirmed that the imaginary mode of the reported transition-state structures connects the adjacent steps in the reaction profile. Our first report used the B3LYP functional; however, the larger systems we have studied here required that we adopt a "pure" DFT functional so that the resolution-of-identity (RI)[69] approximation could be used. The BP86 calculations were benchmarked against the alternative PBE functional[70] and found to be consistent. Ziegler–Morokuma EDA analysis was performed by reoptimizing the complexes in ADF 2007.1 with the BP86 functional and the TZP basis set. Fragment orbital analysis was performed using the AOmix package.[71,72]

Acknowledgement

We thank Professor D. Fogg and Heather M. Foucault for useful discussions and getting us interested in this catalytic system. We thank the Natural Sciences and Engineering Research Council of Canada (NSERC) and the Canada Research Chairs program for funding. C.N.R. thanks NSERC for a PGS scholarship and HPCVL for research scholarships. We are also grateful to the Canadian Foundation for Innovation (CFI), the Ontario Research Fund, IBM Canada, HPCVL, and SharcNet for providing computing resources.

References

(1) This article is part of a Special Issue dedicated to Professor T. Ziegler.

(2) This paper is dedicated to Tom Ziegler to celebrate his numerous contributions to the fields of organometallic chemistry and catalysis.

(3) Blaser, H.-U.; Malan, C.; Pugin, B.; Spindler, F.; Steiner, H.; Studer, M. *Adv. Synth. Catal.* **2003**, *345* (12), 103–151. doi:10.1002/adsc.200390000.

(4) Genet, J.-P. *Acc. Chem. Res.* **2003**, *36* (12), 908–918. doi:10.1021/ar020152u. PMID:14674782.

(5) Clapham, S. E.; Hadzovic, A.; Morris, R. H. *Coord. Chem. Rev.* **2004**, *248* (21-24), 2201–2237. doi:10.1016/j.ccr.2004.04.007.

(6) McManus, N. T.; Rempel, G. L. *Rev. Macromol. Chem. Phys.* **1995**, *C35*, 239.

(7) Guo, X.-Y.; Rempel, G. L. *J. Appl. Polym. Sci.* **1997**, *65* (4), 667–675. doi:10.1002/(SICI)1097-4628(19970725)65:4<667::AID-APP5>3.0.CO;2-I.

(8) Martin, P.; McManus, N. T.; Rempel, G. L. *J. Mol. Catal. A* **1997**, *126* (2-3), 115–131. doi:10.1016/S1381-1169(97)00102-7.

(9) Pan, Q.; Rempel, G. L. *Macromol. Rapid Commun.* **2004**, *25* (8), 843–847. doi:10.1002/marc.200300275.

(10) Tangthongkul, R.; Prasassarakich, P.; Rempel, G. L. *J. Appl. Polym. Sci.* **2005**, *97* (6), 2399–2406. doi:10.1002/app.21922.

(11) Beach, N. J.; Dharmasena, U. L.; Drouin, S. D.; Fogg, D. E. *Adv. Synth. Catal.* **2008**, *350* (5), 773–777. doi:10.1002/adsc.200800056.

(12) Beach, N. J.; Blacquiere, J. M.; Drouin, S. D.; Fogg, D. E. *Organometallics* **2009**, *28* (2), 441–447. doi:10.1021/om800778h.

(13) Drouin, S. D.; Zamanian, F.; Fogg, D. E. *Organometallics* **2001**, *20* (26), 5495–5497. doi:10.1021/om010747d.

(14) Fogg, D. E. *Can. J. Chem.* **2008**, *86*, 931.

(15) Fogg, D. E.; dos Santos, E. N. *Coord. Chem. Rev.* **2004**, *248* (21-24), 2365–2379. doi:10.1016/j.ccr.2004.05.012.

(16) Louie, J.; Bielawski, C. W.; Grubbs, R. H. *J. Am. Chem. Soc.* **2001**, *123* (45), 11312–11313. doi:10.1021/ja016431e. PMID:11697983.

(17) Schmidt, B. *Pure Appl. Chem.* **2006**, *78* (2), 469–476. doi:10.1351/pac200678020469.

(18) Wasilke, J.-C.; Obrey, S. J.; Baker, R. T.; Bazan, G. C. *Chem. Rev.* **2005**, *105* (3), 1001–1020. doi:10.1021/cr020018n. PMID:15755083.

(19) Watson, M. D.; Wagener, K. B. *Macromolecules* **2000**, *33* (9), 3196–3201. doi:10.1021/ma991595p.

(20) Hallman, P. S.; Evans, D.; Osborn, J. A.; Wilkinson, G. *Chem. Commun.* **1967**, *305*, 229.

(21) Hallman, P. S.; McGarvey, B. R.; Wilkinson, G. *J. Chem. Soc. A* **1968**, *3143*.

(22) Yi, C. S.; Lee, D. W. *Organometallics* **1999**, *18* (24), 5152–5156. doi:10.1021/om990493k.

(23) Esteruelas, M. A.; Sola, E.; Oro, L. A.; Werner, H.; Meyer, U. *J. Mol. Catal.* **1988**, *45* (1), 1–5. doi:10.1016/0304-5102(88)85024-7.

(24) Esteruelas, M. A.; Sola, E.; Oro, L. A.; Werner, H.; Meyer, U. *J. Mol. Catal.* **1989**, *53* (1), 43–52. doi:10.1016/0304-5102(89)85028-X.

(25) Niu, S.; Hall, M. B. *Chem. Rev.* **2000**, *100* (2), 353–406. doi:10.1021/cr980404y. PMID:11749240.

(26) Ziegler, T.; Autschbach, J. *Chem. Rev.* **2005**, *105* (6), 2695–2722. doi:10.1021/cr0307188. PMID:15941226.

(27) Busico, V.; Cipullo, R.; Pellecchia, R.; Ronca, S.; Roviello, G.; Talarico, G. *Proc. Natl. Acad. Sci. U.S.A.* **2006**, *103* (42), 15321–15326. doi:10.1073/pnas.0602856103. PMID:17032770.

(28) Wang, Y.; Wang, J.; Su, J.; Huang, F.; Jiao, L.; Liang, Y.; Yang, D.; Zhang, S.; Wender, P. A.; Yu, Z.-X. *J. Am. Chem. Soc.* **2007**, *129* (33), 10060–10061. doi:10.1021/ja072505w. PMID:17655302.

(29) Houk, K. N.; Cheong, P. H.-Y. *Nature* **2008**, *455* (7211), 309–313. doi:10.1038/nature07368. PMID:18800129.

(30) Wondimagegn, T.; Wang, D.; Razavi, A.; Ziegler, T. *Organometallics* **2008**, *27* (24), 6434–6439. doi:10.1021/om800731y.

(31) Rowley, C. N.; Woo, T. K. *Organometallics* **2008**, *27* (24), 6405–6407. doi:10.1021/om800891w.

(32) Rowley, C. N.; Woo, T. K. *J. Am. Chem. Soc.* **2008**, *130* (23), 7218–7219. doi:10.1021/ja802219a. PMID:18481857.

(33) Rowley, C. N.; Ong, T.-G.; Priem, J.; Richeson, D. S.; Woo, T. K. *Inorg. Chem.* **2008**, *47* (24), 12024–12031. doi:10.1021/ic801739a.

(34) Rowley, C. N.; Ong, T.-G.; Priem, J.; Woo, T. K.; Richeson, D. S. *Inorg. Chem.* **2008**, *47* (20), 9660–9668. doi:10.1021/ic801028m. PMID:18811151.

(35) Rowley, C. N.; Foucault, H. M.; Woo, T. K.; Fogg, D. E. *Organometallics* **2008**, *27* (8), 1661–1663. doi:10.1021/om7012698.

(36) Crabtree, R. H. *The organometallic chemistry of the transition metals*; 4th ed; John Wiley and Sons, Inc.: Hoboken, NJ,2005.

(37) Bader, A.; Lindner, E. *Coord. Chem. Rev.* **1991**, *108* (1), 27–110. doi:10.1016/0010-8545(91)80013-4.

(38) Slone, C. S.; Weinberger, D. A.; Mirkin, C. A. *Prog. Inorg. Chem.* **1999**, *48*, 233–350. doi:10.1002/9780470166499.ch3.

(39) Weng, Z.; Teo, S.; Hor, T. S. A. *Acc. Chem. Res.* **2007**, *40* (8), 676–684. doi:10.1021/ar600003h. PMID:17461542.

(40) Kwong, F.; Chan, A. *Synlett* **2008**, 1440–1448. doi:10.1055/s-2008-1078425.

(41) Zhang, J.; Leitus, G.; Ben-David, Y.; Milstein, D. *J. Am. Chem. Soc.* **2005**, *127* (31), 10840–10841. doi:10.1021/ja052862b. PMID:16076184.

(42) Zhang, J.; Leitus, G.; Ben-David, Y.; Milstein, D. *Angew. Chem., Int. Ed.* **2006**, *45* (7), 1113–1115. doi:10.1002/anie.200503771.

(43) Morris, R. H. *Coord. Chem. Rev.* **2008**, *252* (21-22), 2381–2394. doi:10.1016/j.ccr.2008.01.010.

(44) Grünwald, C.; Gevert, O.; Wolf, J.; González-Herrero, P.; Werner, H. *Organometallics* **1996**, *15* (8), 1960–1962. doi:10.1021/om9509554.

(45) Rodriguez, V.; Donnadieu, B.; Sabo-Etienne, S.; Chaudret, B. *Organometallics* **1998**, *17* (17), 3809–3814. doi:10.1021/om980141y.

(46) Rodriguez, V.; Sabo-Etienne, S.; Chaudret, B.; Thoburn, J.; Ulrich, S.; Limbach, H.-H.; Eckert, J.; Barthelat, J.-C.; Hussein, K.; Marsden, C. J. *Inorg. Chem.* **1998**, *37* (14), 3475–3485. doi:10.1021/ic970697y. PMID:11670430.

(47) Ferrando-Miguel, G.; Wu, P.; Huffman, J. C.; Caulton, K. G. *N. J. Chem.* **2005**, *29* (1), 193. doi:10.1039/b411487f.

(48) Oliván, M.; Clot, E.; Eisenstein, O.; Caulton, K. G. *Organometallics* **1998**, *17* (14), 3091–3100. doi:10.1021/om971109r.

(49) Drouin, S. D.; Yap, G. P. A.; Fogg, D. E. *Inorg. Chem.* **2000**, *39* (23), 5412–5414. doi:10.1021/ic000102q. PMID:11154602.

(50) Braunstein, P.; Fryzuk, M. D.; Le Dall, M.; Naud, F.; Rettig, S. J.; Speiser, F. *Dalton Trans.* **2000**, 1067.

(51) Braunstein, P.; Graiff, C.; Naud, F.; Pfaltz, A.; Tiripicchio, A. *Inorg. Chem.* **2000**, *39* (20), 4468–4475. doi:10.1021/ic0000754.

(52) Braunstein, P.; Naud, F.; Rettig, S. J. *N. J. Chem.* **2001**, *25* (1), 32–39. doi:10.1039/b0047860.

(53) Braunstein, P.; Clerc, G.; Morise, X. *N. J. Chem.* **2003**, *27* (1), 68–72. doi:10.1039/b206410n.

(54) Jie, S.; Agostinho, M.; Kermagoret, A.; Cazin, C. S. J.; Braunstein, P. *Dalton Trans.* **2007**, (39): 4472–4482. doi:10.1039/b706818b. PMID:17909659.

(55) Yee Kwong, F.; Har Lam, W.; Hung Yeung, C.; Shing Chan, K.; Chan, A. S. C. *Chem. Commun. (Camb.)* **2004**, (17): 1922–1923. doi:10.1039/b407243j. PMID:15340602.

(56) Dharmasena, U. L.; Foucault, H. M.; dos Santos, E. N.; Fogg, D. E.; Nolan, S. P. *Organometallics* **2005**, *24* (6), 1056–1058. doi:10.1021/om049041k.

(57) James, B. R. In *Homogeneous hydrogenation*; John Wiley & Sons, Inc.: New York, NY, 1973; pp. 83–88.

(58) [The bond energies we report here differ slightly from those reported in Figs. 1 and 2, as we have performed this analysis in ADF using a different basis set. See Computational methods for full details.

(59) Kitaura, K.; Morokuma, K. *Int. J. Quantum Chem.* **1976**, *10* (2), 325–340. doi:10.1002/qua.560100211.

(60) Ziegler, T.; Rauk, A. *Theor. Chim. Acta* **1977**, *46*, 1.

(61) Bickelhaupt, F. M.; Baerends, E. J. Kohn–Sham density functional theory: predicting and understanding chemistry; In *Rev. Comput. Chem.* Wiley-VCH: New York, 2000; pp. 1–86.

(62) Dapprich, S.; Frenking, G. *J. Phys. Chem.* **1995**, *99* (23), 9352–9362. doi:10.1021/j100023a009.

(63) Winterton, N. Some notes on the early development of models of bonding in olefin-metal complexes; In *Modern coordination chemistry: the legacy of Joseph Chatt*; Leigh, G. J. and Winterton, N., Eds.; Royal Society of Chemistry: Cambridge, UK, 2002.

(64) Frenking, G. The Dewar–Chatt–Duncanson bonding model of transition metal-olefin complexes examined by modern quantum chemical methods;In *Modern coordination chemistry: the legacy of Joseph Chatt*; Leigh, G. J. and Winterton, N., Eds.; Royal Society of Chemistry: Cambridge, UK, 2002.

(65) Ahlrichs, R.; Bar, M.; Haser, M.; Horn, H.; Kolmel, C.

Chem. Phys. Lett. **1989**, *162* (3), 165–169. doi:10.1016/0009-2614(89)85118-8.

(66) Becke, A. D. Phys. Rev. A: At. Mol. Opt. Phys. 1988, 38.

(67) Perdew, J. P.; Yue, W. *Phys. Rev. B* **1986**, *33* (12), 8800–8802. doi:10.1103/PhysRevB.33.8800.

(68) Weigend, F.; Ahlrichs, R. *Phys. Chem. Chem. Phys.* **2005**, *7* (18), 3297–3305. doi:10.1039/b508541a. PMID:16240044.

(69) Eichkorn, K.; Treutler, O.; Ohm, H.; Haser, M.; Ahlrichs, R. *Chem. Phys. Lett.* **1995**, *240* (4), 283–289. doi:10.1016/0009-2614(95)00621-A.

(70) Perdew, J. P.; Burke, K.; Ernzerhof, M. *Phys. Rev. Lett.* **1996**, *77* (18), 3865–3868. doi:10.1103/PhysRevLett.77.3865. PMID:10062328.

(71) Gorelsky, S. I.; Lever, A. B. P. *J. Organomet. Chem.* **2001**, *635* (1-2), 187–196. doi:10.1016/S0022-328X(01)01079-8.

(72) Gorelsky, S. I. *AOMix: Program for molecular orbital analysis*; University of Ottawa, Ontario. Available from http://www.sg-chem.net. 2009.

CHAPTER 6

Reaction Dynamics of *β*-Hydrogen Transfer in the Zirconocene Olefin Polymerization Catalyst: A DFT Path Sampling Study

This work has been published in part in Rowley, C. N.; Woo, T. K. *Organometallics* **2008**, *27*, 6405.

Abstract

We have used *ab initio* molecular dynamics (AIMD) in conjugation with transition path sampling (TPS) to model the *β*-hydrogen transfer reaction in $Cp_2Zr(C_2H_5)(C_2H_4)^+$, a model for the zirconocene olefin polymerization catalyst. An equilibrium MD simulation of the reactant complex showed that there is a broad range of movement along the Zr–H(agostic) coordinate and that the Zr–$\eta^2(C_2H_4)$ coordination was unusually fluxional due to the relatively weak metal-olefin orbital interactions. In-place methyl group rotation was observed in the MD simulation and found to be a simple thermally-accessible fluctuation rather than an activated process. The reaction dynamics of *β*-hydrogen transfer were modeled using transition path sampling (TPS). Trajectories were found to cross the reaction barrier at a broad range due to a flat barrier along the Zr–H axis. We found that Zr–H bonding increases during the reaction due to dynamic effects. A Zr–$\eta^2(C_2H_4)$ fluctuation is critical to inducing the transfer.

6.1. Introduction

Group IV metallocene olefin polymerization catalysts have been the subject of intensive research in recent decades, serving as framework for the development of alternatives to heterogeneous Ziegler-Natta catalysts.[1-3] While a great variety of catalysts within this motif have been proposed, with different metals and auxiliary ligands, the mechanism of polymerization is straightforward: repeated insertion of the substrate olefins into the M(IV)–alkyl bond generates a long polymer chain.

The average chain length of a polymer has a major influence on its physical properties, with high molecular weight polymers being of particular interest.[4] The length of the polymer chain produced by a catalyst is largely determined by the relative rates of chain propagation and chain termination processes.[5] As a result, there is significant interest in better understanding the chain termination mechanisms so that new catalysts can be developed that minimize this activity.

By analogy to other organometallic catalysts, it had been presumed that the chain termination mechanism for these catalysts was β-hydride elimination, where a β-hydrogen of the growing alkyl chain is transferred to the metal to form a metal hydride, with the alkyl chain converted to a terminal olefin.[6] β-Hydrogen transfer is an chain termination mechanism that has been identified as an alternative to β-hydride elimination in these catalysts, elucidated in large part through a series of computational studies by Ziegler and coworkers.[8-10] In this mechanism, a hydrogen (denoted here as H_T) is transferred from the C_β of the growing chain to a coordinated olefin monomer, terminating the growing chain as an olefin. As in β-hydride elimination, the incoming monomer becomes the growing alkyl chain, restarting the chain propagation process. It was predicted in these studies that the activation energy for *β*-hydrogen transfer is lower than that of *β*-hydride elimination for a broad range of metals and auxiliary ligands, often by a wide margin.[7] A recent pair of computational studies by Talarico and Buzelaar identified unusual features on the *β*-hydrogen transfer potential energy surface (PES),[8,9] implying that the dynamics of this reaction could have interesting characteristics (*vide infra*). This led us to study this reaction using AIMD. Based on our success in using TPS to model the Ru–H ethylene insertion in Chapter 4, we used TPS in this chapter to examine the reaction dynamics of *β*-hydrogen transfer.

6.2. Results and Discussion

We have investigated the reaction dynamics of the *β*-hydrogen transfer using three complimentary approaches: an examination of the PES of the *β*-hydrogen transfer reaction, an equilibrium MD simulation of the reactant complex, and a TPS simulation of the *β*-hydrogen transfer reaction. We have used the cationic complex $Cp_2Zr(C_2H_5)(C_2H_4)^+$ as our model for the degenerate transfer a *β*-hydrogen from the ethyl ligand to the η^2-coordinated ethylene ligand. This complex has been used in many instances to model chain transfer in the mainstay zirconocene olefin polymerization catalyst.[8-14]

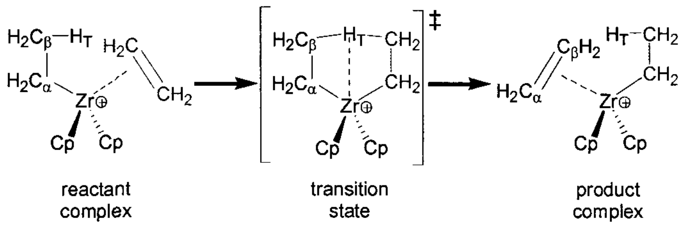

6.2.1. *Potential Energy Surface of the β-Hydrogen Transfer*

Before beginning our MD simulations of the *β*-hydrogen transfer reaction, we examined the PES of this reaction using static DFT calculations. The full details of our calculations are available in the Computational Details section (Section 6.4).

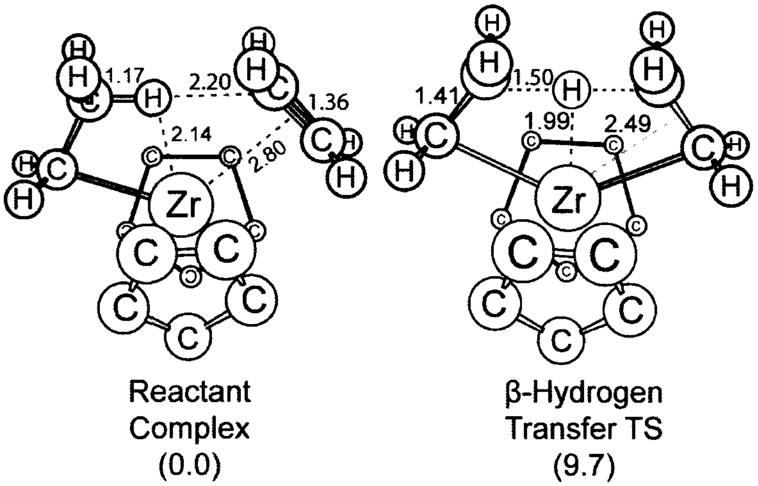

Figure 6.1. Schematic structures of reactant complexes and the *β*-hydrogen transfer transition state. Key distances are shown adjacent to their coordinate. Relative energies in kcal mol^{-1} are given in parenthesis. Cp hydrogens are excluded for clarity.

The reactant complex is a distorted tetrahedral structure with two η^5-coordinating Cp ligands, an η^2-coordinating ethylene ligand, and an ethyl ligand which has a *β*-agostic interaction with the metal (Figure 6.1, left). The ethylene coordination is relatively weak, with a considerable Zr– $\eta^2(C_2H_4)$ distance of 2.80 Å and only a small elongation of the ethylene C=C bond upon coordination to the metal (1.36 Å in the complex compared to 1.34 Å in the minimum-energy structure of free ethylene). This is consistent with the long

Zr–olefin distances observed in the XRD structure of the analogous Zr(IV)–olefin complex $Cp_2Zr(OCMe_2CH_2CH_2CH=CH_2)^+$, reported by Wu et al. (Zr–C(terminal) = 2.68 Å and Zr–C(internal) = 2.89 Å).[15]

The agostic interaction formed between the ethyl C_β–H_T bond and the metal is substantial, as the C_β–H_T bond is elongated to 1.17 Å and the Zr–H distance is relatively short (Zr–H = 2.15 Å). Wiberg bond order analysis[16] also indicates that there is a significant β-agostic interactions as the Zr–H_T bond order and Zr–C_β–H_T 3-center bond order are 0.15 and 0.09, respectively. This interaction places the β-hydrogen of the ethyl ligand and the ethylene in suitable geometry for β-hydrogen transfer, as distance between the β-hydrogen and the nearest carbon of the ethylene ligand is only 2.20 Å.

The β-hydrogen transfer transition state is a symmetric structure where the β-hydrogen is equidistant ($C_{\beta 1}$–H_T = $C_{\beta 2}$–H_T = 1.50 Å) from the β-carbons (Figure 6.1, right). The C_α–C_β unit of the ethylene moves closer to the metal, with a distance between the metal and the C_α–C_β centroid of 2.49 Å, compared to the Zr–$\eta^2(C_2H_4)$ distance of 2.80 Å in the reactant complex. This transition state is stabilized by a significant Zr–H_T bonding interaction, evidenced by the shorter Zr–H_T distance of 1.99 Å and an increased Zr–H_T bond order of 0.22. As the geometry of the reactants is conducive for transfer and the transition state is stabilized by the Zr–H_T interaction, the barrier height for this reaction is only 9.7 kcal mol^{-1}. These structures and barriers heights are generally consistent with those reported in other DFT studies of this catalyst and those similar to it.[7-9,12,17]

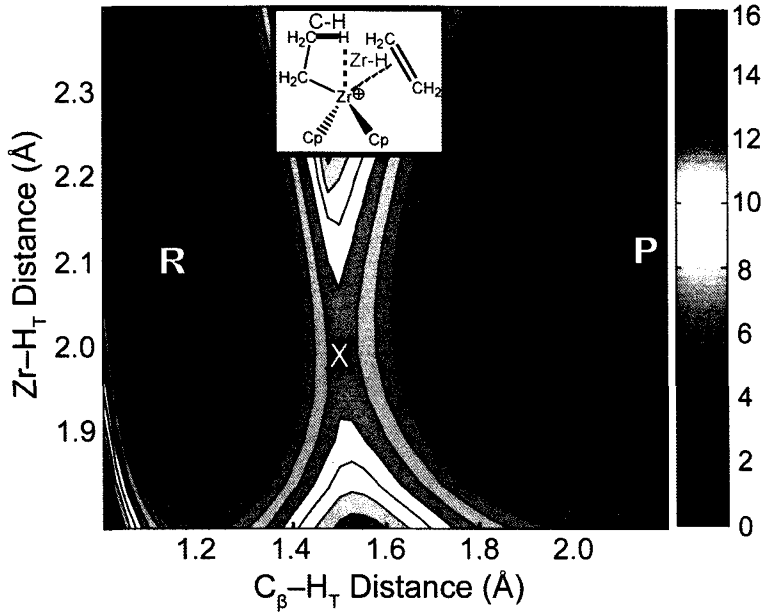

Figure 6.2. The PES of the β-hydrogen transfer with respect to the Zr–H_T and C_β–H_T coordinates. R and P indicate the reactant and product potential energy minima, respectively, and X indicates the TS. Energies are in kcal mol^{-1}.

To further characterize the β-hydrogen transfer reaction, we calculated the 2D PES of this reaction with respect to two critical coordinates: the C_β–H_T bond length and the Zr–H_T distance. The reactant minimum is extremely flat along the Zr–H_T coordinate due to a competition between two effects: the C_β–H_T agostic interaction and C_α–Zr–C_α angle strain. The complex can adopt stable configurations with short Zr–H_T distances (Zr–H_T < 2.1 Å) due to an increase in the C_β–$H_T \rightarrow$Zr agostic interaction, although the C_α–Zr–C_α angle strain becomes dominant at Zr–H_T distances shorter than 1.9 Å. Conversely, when the Zr–H_T distance is large (Zr–H_T > 2.2 Å), the C_β–$H_T \rightarrow$Zr agostic interaction is weakened, but the angle strain is eliminated. The resulting minimum is nearly flat in the range of Zr–H_T = 1.9–2.4 Å. The reactant minimum is also broadened along the C_β–H_T coordinate due to the C_β–$H_T \rightarrow$Zr interaction, which extends the range of low-energy C_β–H_T bond lengths. At Zr–H_T distances where the agostic interaction is largest (Zr–H_T between 1.95 Å to 2.1 Å), the minimum is particularly broad along the x-axis.

The product minimum (indicated with a P on Figure 6.2) is similar to the reactant minimum, although the C_β–H_T bond that is used as the C_β–H_T coordinate is broken in this minimum and movement along the x-axis corresponds only to the facile movement of ethylene ligand with respect to the H_T atom that was transferred to the of the incoming ethylene ligand. As a result, this minimum is extremely flat along the x-axis, but otherwise shows similar features to the reactant minimum.

The reactant and product minima are connected through the β-hydrogen transfer transition state (indicated by an X on Figure 6.2). This transition state occurs at 1.5 Å on the C_β–H_T coordinate, consistent with the optimized transition state structure. The transition state is located at 2.0 Å on the Zr–H_T coordinate, where a strong Zr–H_T interaction stabilizes the TS. The PES is very broad along Zr–H_T coordinate near the TS, with energies within 1 kcal mol^{-1} of the 9.7 kcal mol^{-1} barrier height in the range of Zr–H_T = 1.9–2.1 Å. As in the broad reactant and product minima, this flat TS surface results from the competition of the Zr–H_T bonding, which favours short Zr–H_T distances, and C_α–Zr–C_α angle strain, which favours large Zr–H_T distances. This feature was first noted by Talarico and Budzelaar, who identified this broad transition state in a range of d^0 olefin polymerization catalysts.[12,13]

6.2.2. Reactant Equilibrium Geometry

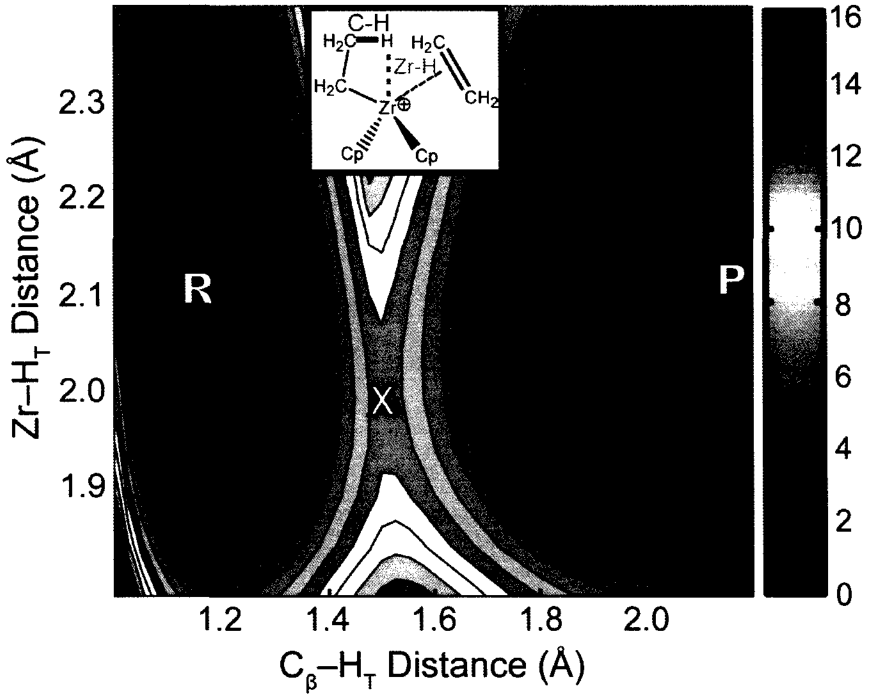

Figure 6.3. Course of equilibrium MD simulation of the reactant complex at 300 K plotted on the PES of the Zr–H_T and C_β–H_T coordinates. Energies are in kcal mol^{-1}.

Having examined the PES of the reaction, we used MD to study the equilibrium structure of the reactant complex. A 40 ps simulation was run with a thermostat to maintain the temperature of the complex at 300 K. The course of this simulation is plotted in Figure 6.3. The MD simulation passed through the full range of low-energy structures of the reactant minimum, confirming that a wide range of structures are thermally accessible.

The average C_β–H_T bond length from the ensemble of structures sampled using MD is 1.16 Å, approximately equal to its equilibrium distance. The average Zr–H_T distance is 2.28 Å, which is substantially longer than the 2.14 Å distance observed in the minimum-energy structure. This increase in the Zr–H_T distance results from the anharmonicity of the elliptical reactant minimum, which increases in energy more rapidly when the Zr–H_T distance is shortened than it does when it is lengthened. As the PES is very flat along this coordinate, the distribution is broad (σ = 0.22 Å) and the full range of Zr–H_T distances within the reactant minimum were sampled in this MD simulation, including the highly anharmonic regions. This anharmonicity of the thermally accessible region of the Zr–H_T coordinate results in an average Zr–H_T distance that is larger than the minimum-energy distance.

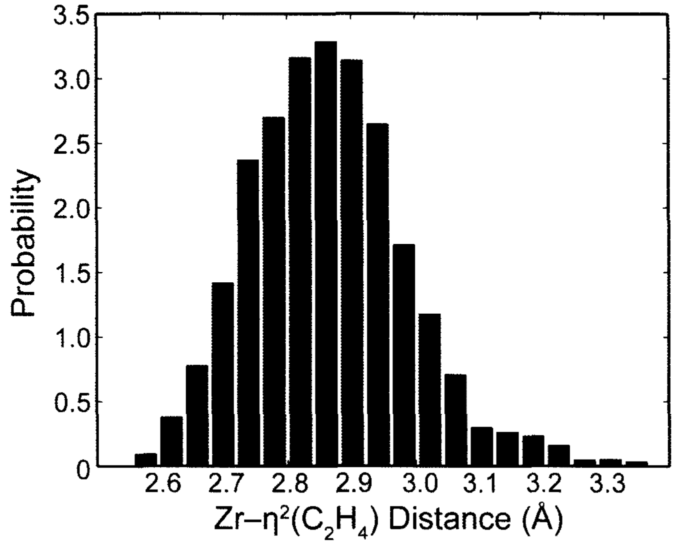

Figure 6.4. Probability distribution of the Zr–$\eta^2(C_2H_4)$ distance from the equilibrium MD simulation.

The final structural property of the MD simulation that we have considered is the coordination of the ethylene ligand. The Zr–$\eta^2(C_2H_4)$ distance is relatively long compared to other metal-olefin complexes, with an minimum-energy distance of 2.80 Å. This distance is slightly longer in the MD simulation, with an average distance of 2.85 Å. This is consistent with the probability distribution of this distance (Figure 6.4), which shows a maximum at 2.85 Å, with a broad distribution (σ = 0.12 Å) and a small skew towards larger distances. As for the Zr–H_T distance, we attribute this difference between the finite-temperature and minimum-energy structures to the anharmonicity of the Zr–$\eta^2(C_2H_4)$ bonding. The largest values of the distribution are in the range near Zr–$\eta^2(C_2H_4)$ = 3.2 Å, representing a large deviation from the minimum-energy structure but still well short of ethylene dissociation. Conversely, the shortest distances present in the distribution occur near Zr–$\eta^2(C_2H_4)$ = 2.6 Å. Integration of this region of the probability distribution indicates that these configurations occur with the small but significant probability of 2%.

The second critical structural property of the coordination of the ethylene ligand is the rotation of this ligand around the Zr–$\eta^2(C_2H_4)$ axis. An experimental study by Stoebenau and Jordan, who found that olefin rotation in a related zirconocene complex was rapid on the NMR timescale.[18] We have defined this angle as the dihedral angle between the Zr–C_α axis and the C=C axis of the ethylene ligand. We have plotted the probability distribution of this angle in Figure 6.5. This distribution is centered at 0°, consistent with the minimum-energy structure where the ethylene ligand eclipses the ethyl C_α–C_β bond. The distribution shows a significant degree of rotational freedom, as angles between –20° and 20° have significant occupation probabilities. Despite this significant degree of rotational freedom, no full rotations of this ligand were observed in the simulation, as the maximum rotational angle that occurs is only 60°, while the potential-energy TS occurs at 90°. The potential energy barrier to this rotation is 3.2 kcal mol^{-1}, which equates to average waiting period of 34 ps between rotations. As our MD simulation was only 40 ps in length, our simulation simply was not long enough to ensure an observation of this event.

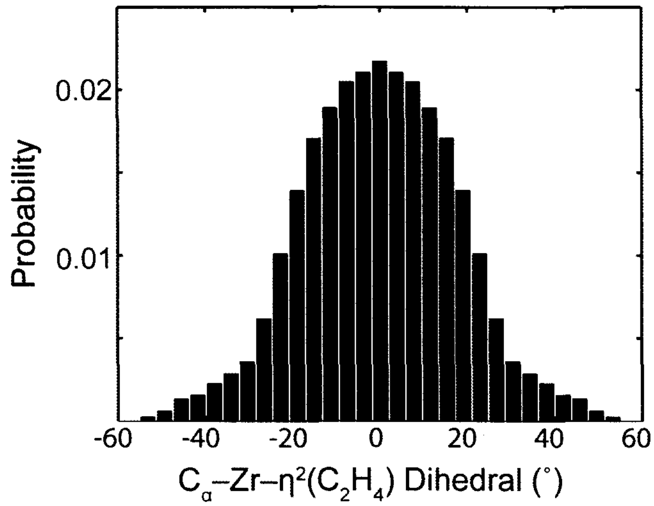

Figure 6.5. Probability distribution of the Zr–$\eta^2(C_2H_4)$ rotational angle from the equilibrium MD simulation.

The relatively free movement of the coordinated ethylene is in strong contrast with other metal-olefin complexes, where the degree of configurational freedom is strongly restricted due to olefin rotation barriers that are typically above 6 kcal mol^{-1}.[21-25] We have investigated this difference by applying Energy Decomposition Analysis (EDA) to the Zr–$\eta^2(C_2H_4)$ interaction. This method can divide the interaction energy of two fragments into Pauli repulsion, electrostatic interactions, and orbital interactions.[19] These data are collected in Table 6.1.

Table 6.1. Energy Decomposition analysis of the Zr–$\eta^2(C_2H_4)$ interaction.

Bond Energy Component	**Energy (kcal mol^{-1})**
Pauli repulsion	34.7
electrostatic interactions	–26.1
orbital interactions	–26.4
total bonding energy	–17.7

The lack of back-bonding interactions between the d^0 metal and the π* orbital of ethylene causes the orbital interactions term to be relatively small and approximately equal in magnitude to the metal-olefin electrostatic interactions, with bond energy components of –26.4 and –26.1 kcal mol^{-1} respectively. In comparison, EDA of the metal-ethylene bonding in late transition metal complexes $Pt(PH_3)_2(C_2H_4)$ and $Os(PH_3)_2(C_2H_4)$ by Li et al. found that orbital interactions components were –76 and –104 kcal mol^{-1} respectively, by far the dominant contribution to the metal-olefin bonding.[20] This weak, largely electrostatic coordination allows the coordinated olefin in this zirconocene complex to have a greater degree of configurational freedom than is seen in other metal-olefin complexes.

6.2.3. β-Methyl Rotation

The methyl group of the ethyl ligand undergoes an in-place rotation 24.8 ps into the MD simulation, such that the initial C_{β}–H_{T1}→Zr agostic interaction is broken and an C_{β}–H_{T2}→Zr interaction replaces it. The key property of an in-place rotation is that the rotation occurs without isomerising to an η^1-alkyl intermediate. This type of rotation has frequently been invoked to explain relative hydrogen exchange rates in metal-alkyl complexes featuring *β*-agostic interactions.[21-27] The activation energies for these process have most commonly been found in a range near 7–9 kcal mol^{-1}. DFT calculations reported by Kogut et al. are consistent with this, with the calculated barrier of 7.5 kcal mol^{-1} for the in-place rotation of a *β*-CH_3 group in a Ni(II) *β*-diketiminate alkyl complex.

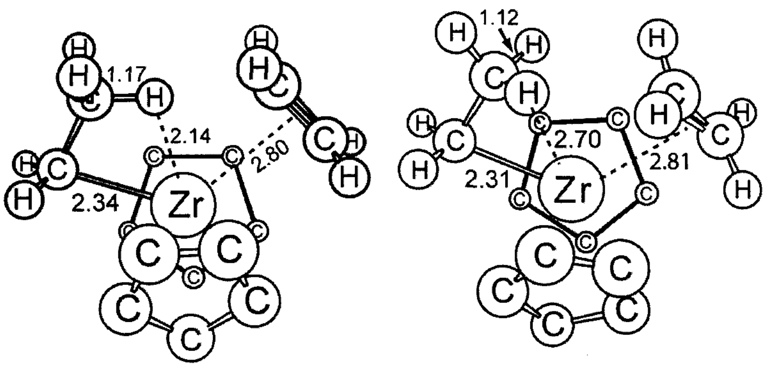

Reactant
Complex
(0.0)

In-Place –CH_3
Rotation TS
(2.7)

Figure 6.6. Schematic structures of reactant complexes and the in-place methyl rotation transition state. Key distances are shown adjacent to their coordinate. Relative energies are given in parenthesis. Cp hydrogens are excluded for clarity.

To allow us to compare the rotation observed in our MD simulation and predictions from static calculations, we located the potential energy TS of this rotation, which is presented in Figure 6.6. In this structure, the $Zr–C_{\alpha}–C_{\beta}–H_{T1}$ dihedral angle, which is 0° in the reactant complex, rotates to an eclipsed geometry of 62°. The most significant structural change is the decrease in the $C_{\beta}–H_{T1}$ from 1.17 Å in the reactant complex to 1.12 Å at the transition state, due to the weakening of the β-agostic interaction. At the transition state, both the $C_{\beta}–H_{T1}$ bond, which is rotating away from interaction with the metal, and the $C_{\beta}–H_{T2}$ bond, which is replacing it, form weak agostic interactions with the metal, with 3-center bond orders 0.075 and direct $Zr–H_{T1,2}$ bond orders of 0.076. These interactions partially compensate for the loss of the β-agostic interaction present in the reactant complex. There is a small decrease in the $Zr–C_{\alpha}$ bond length, from 2.34 Å in the reactant complex to 2.31 Å at the transition state. The barrier to this rotation is 2.7 kcal mol^{-1}, which is considerably smaller than those reported for late transition metal complexes, most likely due to the comparatively weak agostic interaction in this complex.

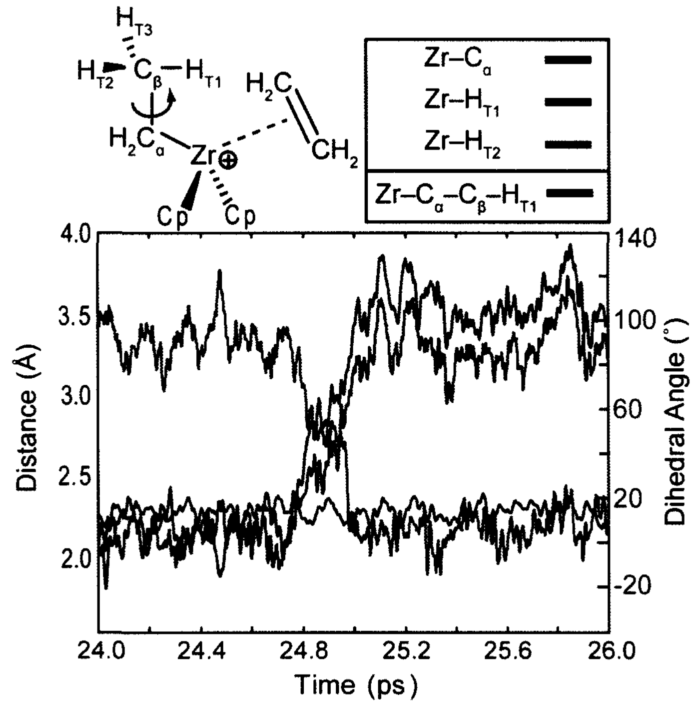

Figure 6.7. Key coordinates involved in the methyl group rotation during the methyl rotation event of the MD simulation. The Zr–C_α bond length (red), Zr–H_{T1} distance (green), and Zr–H_{T2} distance (blue) are plotted on the primary axis. The Zr–C_α–C_β–H_{T1} dihedral angle is plotted on the secondary axis (purple).

We have examined the rotation that occurs in our MD simulation by plotting several structural coordinates related to the rotation in the period where the event occurs (Figure 6.7). The Zr–C_α–C_β–H_{T1} dihedral, which is the obvious coordinate for this rotation, undergoes fluctuations within a range of ±20° around its 0° minimum prior to the point in the simulation where the rotation begins. Beginning at 24.8 ps in the simulation, this dihedral angle increases sharply to a range near 100°, corresponding to its non-agostic geometry. The rotation ends at the 25.0 ps point in the trajectory, giving the process a sizable transition time of approximately 200 fs.

A second significant coordinate in this rotation is the distance between the metal and the hydrogen initially in interaction with it, designated Zr–H_{T1}. This distance undergoes fluctuations in the range of 2.0–2.3 Å leading up to the rotation. This is consistent with the broad range of motion available along the Zr–H_{T1} coordinate in the reactant complex (see Section 6.2.1). This distance increases sharply into the 3.5 Å range concomitantly with the methyl rotation, reflecting the new structure where H_{T1} does not have a direct interaction with the metal. The Zr–H_{T2} coordinate follows the opposite course, as the C_β–H_{T2}→Zr agostic interaction is formed through the rotation. Although there is a small change in the Zr–C_α bond length in the static transition state, this coordinate undergoes regular fluctuations leading up to and during the rotation, suggesting that it is not strongly coupled to the methyl rotation, despite the change in the Zr–C_α observed in the static calculations.

As the potential energy barrier to this rotation is only is 2.7 kcal mol^{-1}, is it thermally accessible at 300 K. Neither the Zr–C_α–C_β–H_{T1} coordinate nor the other coordinates show exceptionally large fluctuations leading up to the transition, indicating that this event does not require a localization of vibrational energy prior to crossing the barrier. This rotation appears to be best described as a thermal fluctuation rather than an activated process where vibrational energy must be localized in a reactive mode or several modes must work in concert to cross the barrier.

Although the barrier to β-methyl rotation is only 0.5 kcal mol^{-1} smaller than the barrier to ethylene rotation, this decreases the expected waiting period from 34 ps to 14 ps, dramatically increasing the likelihood that the transition would be observed in our 40 ps simulation. This illustrates the sensitivity of MD simulations to the size of the barriers of rare events, as even a slightly higher barrier can increase the waiting period of an event outside the range where it is likely to be observed in a picosecond-scale MD simulation.

6.2.4. β-Hydrogen Transfer Reaction Dynamics

The 40 ps trajectory generated by our MD simulation remains in the reactant complex where the trajectory began throughout the simulation (the course of this trajectory is plotted in Figure 6.3). The MD simulation predominantly remains near the low-energy structures of the reactant minimum (dark blue areas on the PES), with rare fluctuations to higher energy configurations (light blue areas on the PES). The C_β–H_T distance never exceeds 1.34 Å, well short of the C_β–H_T distance of 1.50 Å for the TS of the β-hydrogen transfer. Further, the Zr–H_T distance is near 2.1 Å during this fluctuation, outside the range where facile transfer can occur. A reactive event would require a much larger C_β–H_T fluctuation to occur when the Zr–H_T distance is in the appropriate range for transfer to occur. This is consistent with the waiting period predicted using classical transition state theory; at 300 K the lifetime of the reactant complex between β-hydrogen transfer events is approximately 4 μs, making it extremely unlikely that this event would be observed in a 40 ps MD simulation.

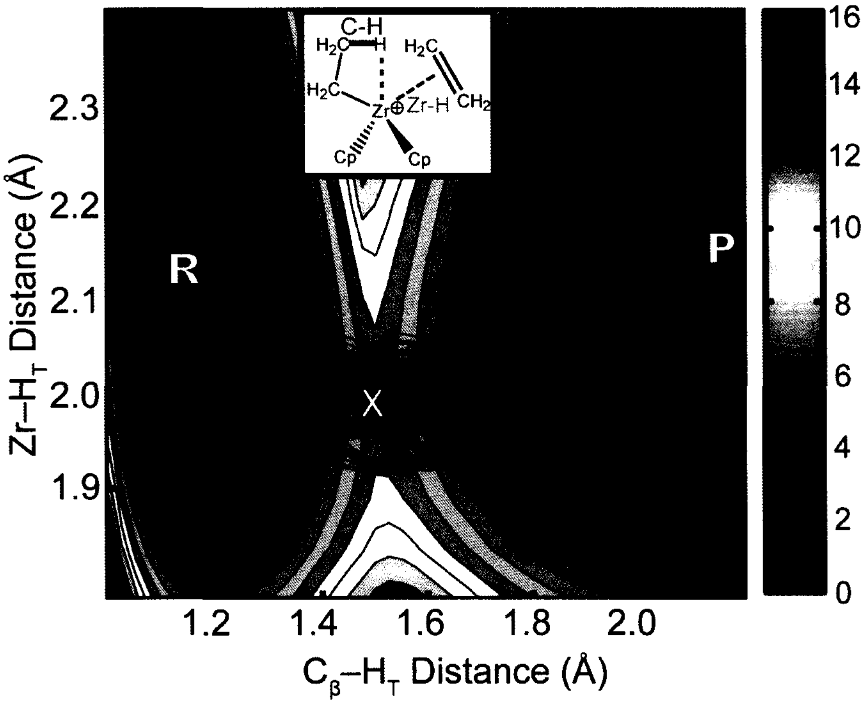

Figure 6.8. All 350 reactive trajectories sampled using path sampling plotted on the β-hydrogen transfer PES.

As the estimated waiting period of the β-hydrogen transfer reaction is far too long for the reaction dynamics to be studied using a straightforward MD simulation, we used transition path sampling to harvest 350 trajectories where this reaction occurs. The full transition path ensemble is plotted on the PES in Figure 6.8. None of the trajectories recrossed the barrier to revert to the reactant state during the length of the trajectories, consistent with low recrossing probabilities in reactions with stable products and high barriers. Due to the broad TS, trajectories in the path ensemble are able to cross the barrier throughout the range of Zr–H$_T$ = 1.95–2.05 Å. Although analysis of the path ensemble shows that the barrier crossing occurs quickly, with an average transition time of 38 ± 9 fs, the range is broad (20–63 fs) and the trajectories exhibit complicated reaction dynamics.

6.2.5. Reaction Dynamics of the Electronic Structure

We have selected four trajectories to illustrate the variety of transitions in the path ensemble: (**A**) crosses the barrier near the potential energy TS, (**B**) crosses the barrier low on the Zr–H_T coordinate, (**C**) crosses the barrier high on the Zr–H_T coordinate and (**D**) shows an interesting partial recrossing where the trajectory temporarily reverses course, performing a "figure-8" on the PES before relaxing to the product minimum. The course of these trajectories is plotted on the PES in Figure 6.9.

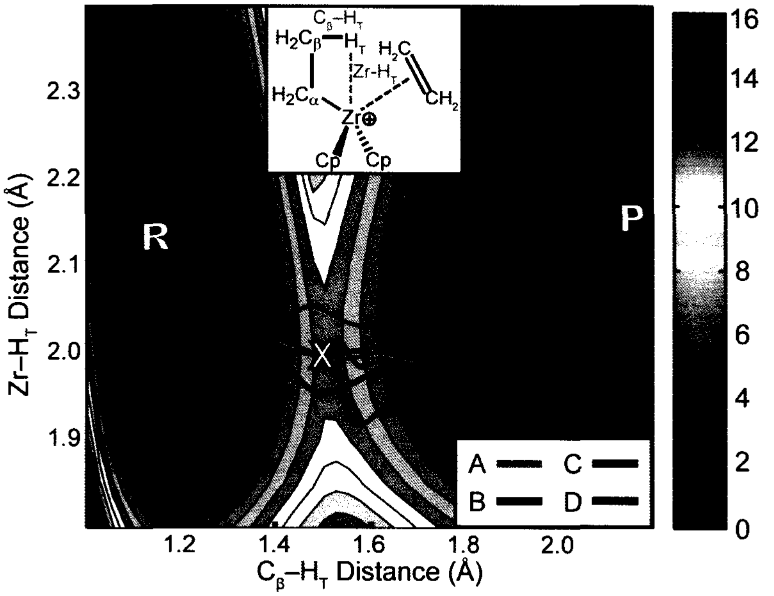

Figure 6.9. PES of the β-hydrogen transfer reaction with the course of selected trajectories plotted.

To examine dynamic effects on the electronic structure of the β-hydrogen transfer reaction, we have calculated the C_β–H_T and Zr–H_T Wiberg bond orders in the four selected trajectories, as shown in Figure 6.10. **B** crosses the barrier closest to the metal and consequently experiences strong Zr–H_T bonding, although **D** experiences even stronger bonding during its descent to the product minimum. Despite crossing considerably further from the metal, **C** experiences Zr–H_T bonding comparable to **A**, which crosses near the TS. Interestingly, all four trajectories show Zr–H_T bond orders that are notably greater than the bond order value from the transition state, beyond the regular fluctuations seen in the Zr–H_T bond orders in the reactant and product minima. It should also be noted that the Zr–H_T bond order has a maximum value at the potential energy transition state along the intrinsic reaction coordinate. This indicates that the dynamic effects increase the role of Zr–H_T bonding during the transfer. Another notable dynamic effect is observed with the sum of the two C_β–H_T bond orders ($C_{\beta1}$–H_T + $C_{\beta2}$–H_T). As shown in the lower part of Figure 6.10, this sum of bond orders for the dynamic trajectories is consistently below the value experienced at the potential energy TS.

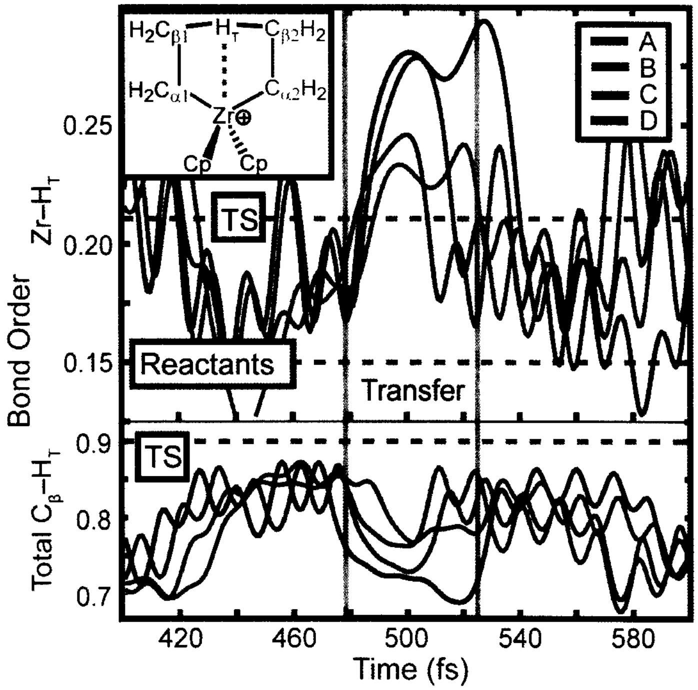

Figure 6.10. The Zr–H_T bond order and sum of C_β–H_T bond orders during the transition event of trajectories **A–D**. Bond orders of potential energy TS and minimum are in grey.

These two effects can be quantified by comparing the bond orders of the static transition state to the bond orders of the step in the dynamic trajectories where H_T is equidistant from $C_{\beta 1}$ and $C_{\beta 2}$. The average Zr–H_T bond order at these "dynamic transition states" is 0.24 ± 0.01, indicating a systematically larger bond order than the static value of 0.21, with a significant range. Similarly, the average sum of C_β–H_T bond orders is 0.76 ± 0.02, a fairly broad range that is significantly lower than the static transition state value of 0.90. One possible explanation of this phenomenon is that the localization of vibrational energy in the reactive C_β–H_T bond results in a distortion away from the optimal TS geometry, where C_β–H_T bonding is maximized. The Zr bonding adjusts to compensate for this *via* the Zr–H_T interaction, originating from persistent Zr(dz^2)–H_T(1s) overlap. The tools available to study the bonding in this system are somewhat restricted, as the relevant components of the transition state cannot be decomposed into chemically meaningful fragments. Bonding analysis of reactive trajectories in other organometallic reactions could allow this phenomenon to be better described.

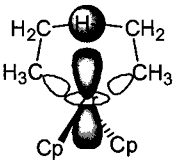

6.2.6. *Structural Fluctuations Associated with β-Hydrogen Transfer*

The large fluctuations in Zr–H_T bond orders prior to the transfer led us to analyze the geometric parameters of the reactive trajectories in order to identify the important molecular fluctuations involved in this reaction. The Zr–H_T, C_β–H_T, and Zr–$\eta^2(C_2H_4)$ distances of **A** are plotted for the period in the trajectory immediately around the *β*-hydrogen transfer in Figure 6.11. The C_β–H_T bond broken in the reaction undergoes only modest oscillations in the range between 1.05 Å and 1.2 Å prior to the reactive event. Similarly, although the Zr–H_T distance undergoes a fluctuation into the 2.0 Å range during the transfer, this fluctuation occurs a number of times in the simulation without inducing a reaction.

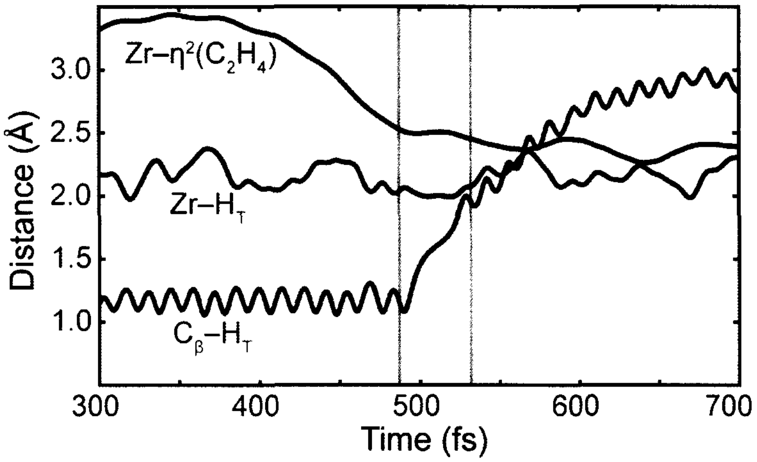

Figure 6.11. Structural fluctuations in **A** during the *β*-hydrogen transfer. The red line represents the distance between the Zr and the centroid of the species which is originally the ethylene ligand, the green line represents the distance between the Zr and the hydrogen undergoing transfer, and the blue line represents the distance between H_T and the *β*-carbon it is originally bonded to.

The distance between the incoming ethylene and the metal is more determinative; in each trajectory sampled, there is a sharp decrease in the Zr–$\eta^2(C_2H_4)$ distance prior to the insertion. This fluctuation, beginning 120 ± 27 fs prior to the reactive event, corresponds to the orientation of the incoming ethylene close to the metal, where it can accept the *β*-hydrogen from the ethyl ligand. During this fluctuation, the Zr–$\eta^2(C_2H_4)$ distance occupies the shortest range in the equilibrium distance probability distribution (Figure 6.4), which is occupied 2% of the time in the reactant complex. We can interpret from this that the *β*-hydrogen transfer reaction is an activated process at 300 K, where fluctuations in the C_β–H_T and Zr–H_T coordinates must coincide with a longer timescale fluctuation in the Zr–$\eta^2(C_2H_4)$ distance for the reaction to occur.

6.3. Conclusions

We have used a combination of static calculations, equilibrium MD simulations, and TPS to examine the reaction dynamics of the *β*-hydrogen transfer reaction in $Cp_2Zr(C_2H_5)(C_2H_4)^+$. The reactant minimum was found to be very broad along the Zr–H_T coordinate due to close competition between Zr–H_T bonding and Zr–C_α–C_β angle strain. The full reactant minimum was thermally accessible in a 40 ps equilibrium MD simulation of this complex at 300 K. An in-place methyl rotation in the ethyl ligand occurred at one point in the MD simulation. As the barrier height of this rotation is low, this rotation could occur thermally, within a picosecond-scale MD simulation. The coordination of the ethylene ligand was shown to have significant configurational freedom due to the lack of metal–ethylene back-bonding. The Zr–$\eta^2(C_2H_4)$ distance fluctuated in a range of 2.6–3.0 Å and a 20° range of rotational movement, although neither complete dissociation nor rotation was observed.

TPS was used to harvest an ensemble of 350 trajectories where the *β*-hydrogen transfer occurs. The path ensemble shows that this reaction exhibits diverse and complex reaction dynamics due to the broad reaction barrier. In this instance, the potential energy minima and transition states do not give a complete description of the reaction mechanism, as a broad range of reactant and transition state structures were observed in the path sampling simulation.

Remarkably, in the dynamic trajectories, Zr–H_T bonding became stronger and C_β–H_T bonding became weaker during the transfer, suggesting that finite-temperature effects in organometallic reactions can significantly affect metal bonding interactions. While C_β–H_T and Zr–H_T fluctuations are essential to the transfer, a decrease in the Zr–$\eta^2(C_2H_4)$ distance beginning on average 120 fs prior to the transfer appears to be the critical event to induce the reaction.

These simulations provide an elegant illustration of the rare event problem. The entire range of low-energy structures in the potential energy minimum of the reactant complex were effectively sampled in the equilibrium MD simulation. In-place methyl rotation, which requires the system to cross a modest 2.7 kcal mol^{-1} barrier, was observed only once in the 40 ps equilibrium simulation. Ethylene rotation, which has a slightly higher barrier of 3.2 kcal mol^{-1}, was not observed at any point in the equilibrium MD simulation, nor was the β-hydrogen transfer reaction, which has a sizable 9.7 kcal mol^{-1} barrier. The transition path sampling simulation of the β-hydrogen transfer reaction illustrated that crossing a barrier of this magnitude at 300 K requires that concerted motion occurs along several independent coordinates.

6.4. Computational Methods

Turbomole 5.9 with the TPSS[28] meta-functional and the def2-SV(P) core potential and basis set[29] was used for all the calculations we report here, except for the hydrogen undergoing transfer, where the larger def2-TZVPP basis set was used. All energies are calculated with respect to the minimum-energy structure of the reactants. No zero-point energy corrections are included in order to be consistent with the classical Born-

Oppenheimer molecular dynamics used in the path sampling simulation. The reactant complex was equilibrated with a Lowe-Andersen thermostat[30] at 300 K for 20 ps. The average total energy (34 kcal mol^{-1} with respect to the optimized reactants) for the last 5 ps was used as the total energy of the path sampling simulation. The simulation of the reactant complex was generated by extending this equilibrated MD simulation by an additional 40 ps.

The initial trajectory was generated from the static TS using the procedure described in Chapter 2. 500 fs trajectories were run forward and backward in time from this point, generating a reactive trajectory. The MD and TPS simulations were performed using our own code, interfaced with Turbomole.

Within the path sampling simulation, the reactants were defined as all structures where the $C_{\beta 1}$–H_T distance was between 1.0 Å and 1.2 Å and the Zr-H_T distance is between 1.9 Å and 2.4 Å. The product complex was defined symmetrically to the reactant complex, with the $C_{\beta 2}$–H_T distance used as the order parameter instead of the $C_{\beta 1}$–H_T distance. All trajectories that crossed between the reactants and products were considered reactive and were added to the transition path ensemble. The path length of the trajectories was 1 ps, using 1 fs time steps. Shooting points were selected in a range 100 fs before and after the transition event.

References

1. Mohring, P. C.; Coville, N. J. *J. Organomet. Chem.* **1994**, *479*, 1.
2. Brintzinger, H. H.; Fischer, D.; Muelhaupt, R.; Rieger, B.; Waymouth, R. M. *Angew. Chem. Int. Ed.* **1995**, *34*, 1143.
3. Resconi, L.; Cavallo, L.; Fait, A.; Piemontesi, F. *Chem. Rev.* **2000**, *100*, 1253.
4. Kaminsky, W. *Macromol. Chem. Phys.* **1996**, *197*, 3907.
5. Alt, H. G.; Koppl, A. *Chem. Rev.* **2000**, *100*, 1205.
6. Crabtree, R. H. *The Organometallic Chemistry of the Transition Metals*; 4th ed.; John Wiley and Sons, Inc.: Hoboken, NJ, 2005.
7. Margl, P.; Deng, L.; Ziegler, T. *J. Am. Chem. Soc.* **1999**, *121*, 154.
8. Talarico, G.; Budzelaar, P. H. M. *J. Am. Chem. Soc.* **2006**, *128*, 4524.
9. Talarico, G.; Budzelaar, P. H. M. *Organometallics* **2008**, *27*, 4098.
10. Janiak, C. *J. Organomet. Chem.* **1993**, *452*, 63.
11. Woo, T. K.; Fan, L.; Ziegler, T. *Organometallics* **1994**, *13*, 2252.
12. Lohrenz, J. C. W.; Woo, T. K.; Ziegler, T. *J. Am. Chem. Soc.* **1995**, *117*, 12793.
13. Borrelli, M.; Busico, V.; Cipullo, R.; Ronca, S.; Budzelaar, P. H. M. *Macromolecules* **2003**, *36*, 8171.
14. Coussens, B. B.; van Besien, E.; Budzelaar, P. H. M.; Friederichs, N. *Organometallics* **2008**, *27*, 1804.
15. Wu, Z.; Jordan, R. F.; Petersen, J. L. *J. Am. Chem. Soc.* **1995**, *117*, 5867.
16. Wiberg, K. B. *Tetrahedron* **1968**, *24*, 1083.
17. Talarico, G.; Blok, A. N. J.; Woo, T. K.; Cavallo, L. *Organometallics* **2002**, *21*, 4939.
18. Stoebenau, E. J., III; Jordan, R. F. *J. Am. Chem. Soc.* **2006**, *128*, 8162.
19. Bickelhaupt, F. M.; Baerends, E. J. In *Rev. Comput. Chem.*; Wiley-VCH: New York, 2000; Vol. 15, p 1.

20. Li, J.; Schreckenbach, G.; Ziegler, T. *Inorg. Chem.* **1995**, *34*, 3245.

21. Byrne, J. W.; Blaser, H. U.; Osborn, J. A. *J. Am. Chem. Soc.* **1975**, *97*, 3871.

22. Brookhart, M.; Green, M. L. H. *J. Organomet. Chem.* **1983**, *250*, 395.

23. Brookhart, M.; Green, M. L. H.; Wong, L. L. *Prog. Inorg. Chem.* **1988**, *36*, 1.

24. Green, M. L. H.; Wong, L. L. *J. Chem. Soc., Chem. Commun.* **1988**, 677.

25. Bercaw, J. E.; Burger, B. J.; Green, M. L. H.; Santarsiero, B. D.; Sella, A.; Trimmer, M. S.; Wong, L. L. *J. Chem. Soc., Chem. Commun.* **1989**, 734.

26. Brookhart, M.; Lincoln, D. M.; Volpe, A. F., Jr.; Schmidt, G. F. *Organometallics* **1989**, *8*, 1212.

27. Green, M. L. H.; Sella, A.; Wong, L. L. *Organometallics* **1992**, *11*, 2650.

28. Staroverov, V. N.; Scuseria, G. E.; Tao, J.; Perdew, J. P. *J. Chem. Phys.* **2003**, *119*, 12129.

29. Weigend, F.; Ahlrichs, R. *PCCP* **2005**, *7*, 3297.

30. Koopman, E. A.; Lowe, C. P. *J. Chem. Phys.* **2006**, *124*, 204103/1.

CHAPTER 7

A QM/MM *Ab Initio* Molecular Dynamics Study of Solution Dynamics and Counteranion Effects in $[Cp_2Zr(C_2H_5)(C_2H_4)][CH_3B(C_6F_5)_3]$

Abstract

QM/MM MD simulations were used to study the structure and dynamics of $Cp_2Zr(C_2H_5)(C_2H_4)^+$ (**1**), a model olefin complex of a mainstay polymerization catalyst, as well as the methyl tris(pentafluorophenyl) borate ion pair of this complex ($[Cp_2Zr(C_2H_5)(C_2H_4)][CH_3B(C_6F_5)_3]$) (**1-IP**) in an explicit pentane solvent. These calculations indicate that **1** preferentially exists in a β-agostic configuration, consistent with its minimum-energy structure. In contrast, **1-IP** isomerizes to an α-agostic configuration to maximize the dipole-counteranion interaction through a facile, three-stage mechanism. The free energy profile of β-hydrogen transfer was calculated for **1** and **1-IP** using the Weighted Histogram Analysis Method (WHAM). The presence of the counteranion destabilized the product state where the counteranion is oriented adjacent to the anionic ethyl ligand, resulting in an asymmetric reaction profile. Vibrational entropy was found to have a large contribution to the free energy of activation, amounting to approximately 20% of the total barrier, six times larger than was predicted using the harmonic oscillator approximation. Parameters for an MM force field of the $[CH_3B(C_6F_5)_3]^-$ counteranion were developed and are presented here.

7.1. Introduction

Single-site group IV metallocene catalysts are of major importance in olefin polymerization chemistry. These catalysts have demonstrated excellent catalytic activity[1-3] and have allowed exceptional control of polymer microstructure.[4] While the metallocene is the species directly involved in the polymerization process, a cocatalyst (Scheme 7.1, A) plays an essential role in the catalytic cycle. For the specific zirconocene catalyst modeled in this chapter, the active, cationic form of the metallocene is formed by a reaction with a cocatalyst, such as methylaluminoxane (MAO) or tris(pentafluorophenyl)borane ($B(C_6F_5)_3$), which abstracts a methyl ligand from the neutral precatalyst to activate the catalyst (Scheme 7.1a).

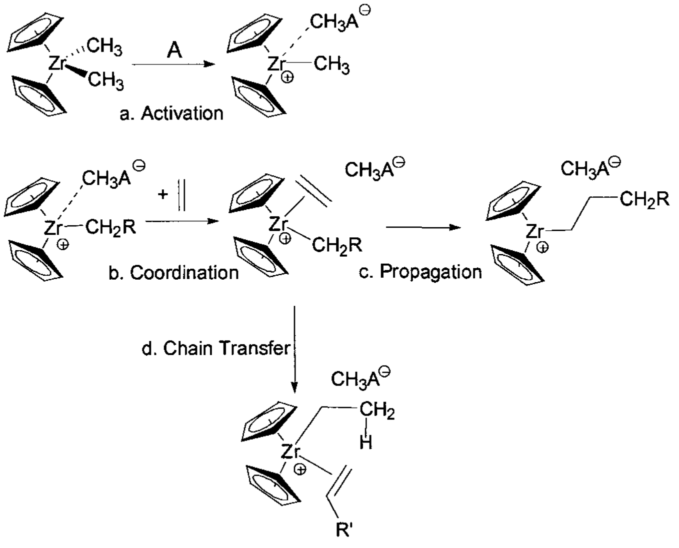

Scheme 7.1. Key reaction mechanisms of zirconocene-catalyzed ethylene polymerization.

After activation, the olefin substrate can coordinate to the metal to form a metal-olefin complex (Scheme 7.1b). From this complex, the olefin can undergo insertion into the $\sigma(Zr–C_\alpha)$ bond, extending the length of the polymer chain by one unit (Scheme 7.1c).

Alternatively, the growing alkyl chain can be terminated through β-hydrogen transfer to the coordinated olefin (Scheme 7.1d), which is discussed in detail in Chapter 6.

It had originally been assumed that the cationic active catalyst and the anionic cocatalyst dissociate after initiation; however, more recently it has been demonstrated that these species remain in close proximity in the non-polar solvents that these catalysts are most commonly used in.[5-7] This ion-pairing has been demonstrated to affect polymerization kinetics[8,9] and stereochemistry.[10-13] Understanding the structure and reactivity of these ion pairs has emerged as challenging objective for researchers attempting to develop new catalysts within this framework. Characterizing the olefin-coordinated ion pairs is of particular interest, as they are central to the polymerization activity of these catalysts, but have not been observed directly.

Single-crystal X-ray structures of metallocene-counteranion ion pairs provided the earliest data on the nature of the cation-anion orientation.[14-16,17] The X-ray structures of several ion pairs where the anion is methyl tris(pentafluorophenyl)borate have been collected. These are generally inner-sphere ion pairs, where the methyl ligand of the counteranion bridges with the cation *via* donation from the methyl C–H bonds to the metal (Scheme 7.2). While these structures provide important data on the ion-pairing of unsaturated metallocenes, the structures of the critical olefin-bound intermediates are unknown. Further, these crystallographic structures are not necessarily representative of the solution structures, where the ion pair has greater configurational freedom.

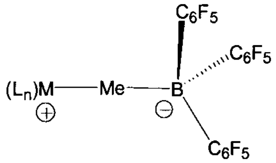

Scheme 7.2. Schematic methyl-bridged inner sphere ion pair orientation of $[ML_n][CH_3B(C_6F_5)_3]$.

Brintzinger and coworkers recently published an NMR study of alkyl zirconocene – borate ion pairs.[18] Although the unsaturated metallocene formed a methyl-bridged complex with the counteranion, Lewis bases, such as THF, displaced the counteranion from the metal so that the counteranion is in the outer coordination sphere. As the olefin substrates will also serve as coordinating Lewis bases, these experiments indicated that the metal-olefin complexes are likely outer-sphere ion pairs as well, where the counteranion has only non-covalent interactions with the cation when the olefin is coordinated.

Although the ions of an outer-sphere ion pair have a significant freedom of movement, Brintzinger and coworkers concluded that there are preferred orientations of the ions within the ion pair. Subsequent solution NMR studies by Marks el al. on the ion pair $[Me_2SiCp_2Zr(Me)THF][CH_3B(C_6F_5)_3]$ found that the interionic NOE between the B–CH_3 and THF protons were absent, suggesting an orientation where the B–CH_3 bond axis is oriented away from the counteranion (Scheme 7.3).[6,19] This arrangement allows closer interactions between the negatively charged fluorines on the counteranion pentafluorophenyl ligand and the cation, similar to the structures of ion pairs where $B(C_6F_5)_4^-$ is the counteranion.[20] This is in contrast to the orientation seen in inner-sphere ion pairs, where the methyl ligand of the counteranion bridges with the metal.

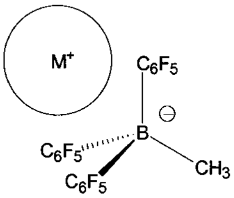

Scheme 7.3. Schematic outer-sphere ion pair orientation.

This class of catalysts has been studied intensively using quantum chemistry, although most computational studies have represented this catalyst as the bare cation, without its counteranion.[21-37] This includes our TPS study of the *β*-hydrogen transfer reaction presented in Chapter 6. More recently, there have been several computational studies that have included a counteranion in the model.[38-45,46] These studies utilize optimizations of estimated preferential ion pair geometries, typically based on the inner-sphere ion pair geometry observed in X-ray structures. This approach is well-suited for modelling catalyst initiation and inner-sphere ion pair bonding; however, some characteristics of ion pairs are not suitable for studying using optimizations on the potential energy surface (PES) alone. The NMR studies of ion pair structures in solution found that although there are preferred ion pair orientations, there is significant configurational freedom within these orientations and that the ion pair orientation can readily adjust to changes in the solvent or the coordination sphere of the metal.[6,18,19] Optimized structures of these ion pairs do not capture the configurational freedom of these complexes, which is exceptionally large in outer-sphere ion pairs as the pairing is due to relatively weak and largely isotropic cation-anion electrostatic interactions.

Molecular dynamics (MD) simulations provide an obvious strategy for modelling ion pairs. With these simulations, the accessible ion pair orientations can be sampled to generate a representative ensemble of structures. Cavallo and coworkers have performed nanosecond length MD simulations on metallocene ion pairs, although this necessitated the use of empirical force fields to represent the catalyst.[47,48] The intricate metal-ligand bonding in these complexes is challenging to represent using force fields and is highly sensitive to the quality of the parameterization. Further, these simulations represent electrostatic interactions using constant atomic charges, so the charge distribution and bonding of the metallocene cannot adjust within this model. Alternatively, a quantum chemical (QC) model can be used to represent the catalyst, although the computational cost of these calculations is much greater; the length of the AIMD simulation of a metallocene ion pair by Ziegler and coworkers was limited to 2.8 ps due to the high computational cost of *ab initio* calculations on systems of this size.[39]

Improvements in scientific computing hardware and more efficient QC methods have made it possible to run longer simulations of these systems using AIMD. In particular, QM/MM methods[49] can dramatically reduce the cost of simulations of these systems, as the entire counteranion of an outer-sphere ion pair can be accurately represented using an inexpensive molecular mechanical model, while only the cation is represented with a computationally demanding QC model.

In this chapter, we present the results of AIMD simulations of the model metallocene polymerization catalyst olefin complex $Cp_2Zr(C_2H_5)(C_2H_4)^+$ and its outer-sphere ion pair analogue ($[Cp_2Zr(C_2H_5)(C_2H_4)][CH_3B(C_6F_5)_3]$) in an explicit pentane solvent using QM/MM methods. To explore the effect of the counteranion on catalyst reactivity, we used MD simulations of these complexes in conjunction with the Weighted

Histogram Analysis Method (WHAM)[50] to determine the free energy profile of the β-hydrogen chain termination reaction, with and without the counteranion present.

7.2. Results and Discussion

7.2.1. Preferred Ion Pair Orientations via Static Calculations

We began our study by searching for the preferred configurations of $Cp_2Zr(CH_2CH_3)(C_2H_4)^+$ (**1**) and $([Cp_2Zr(C_2H_5)(C_2H_4)][CH_3B(C_6F_5)_3])$ (**1-IP**). The putative configurations we selected are based on the preferred outer-sphere zirconocene orientations proposed by Marks and coworkers[6] and the computational literature. We evaluated these structures using potential energy optimizations with static DFT calculations on **1** and our QM/MM model for **1-IP**. Within this QM/MM model, the entire zirconocene is calculated at the QM level, while the counteranion is represented with an MM force field. See the Computational Methods section (Section 7.4) for the full details of these calculations.

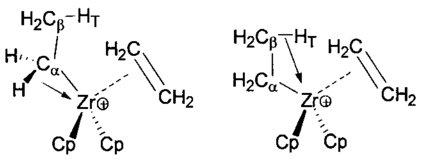

1A **1B**

Scheme 7.4. Reported low-energy configurations of **1**: an α-agostic configuration (left) and β-agostic configuration (right). C–H agostic interactions are indicated by the red arrow.

DFT calculations by Ziegler and coworkers on the cation-only complex, $Cp_2Zr(CH_2CH_3)(C_2H_4)^+$ (**1**), concluded that the most stable form of this complex is a distorted tetrahedral structure where a C–H bond of the methyl group in the ethyl ligand forms a β-agostic interaction with the metal (Scheme 7.4, **1B**). This C–H bond (designated C_β–H_T) coordinates to the face opposite to the Cp ligands. The ethylene ligand is coordinated to the metal in an approximately symmetric η^2-fashion, eclipsing the C_α–C_β internuclear axis of the ethyl ligand. An alternative configuration has been identified where the ethyl ligand has an α-agostic interaction with the Zr instead of the β-agostic interaction (Scheme 7.4, **1A**) and the Cp and ethylene ligands are distorted towards planarity. This α-agostic configuration has generally been found to be 2–3 kcal mol^{-1} higher in energy than **1B**.[22,23,51] Our own calculations are consistent with this, with the **1A** configuration determined to be 2.7 kcal mol^{-1} less stable than **1B**.

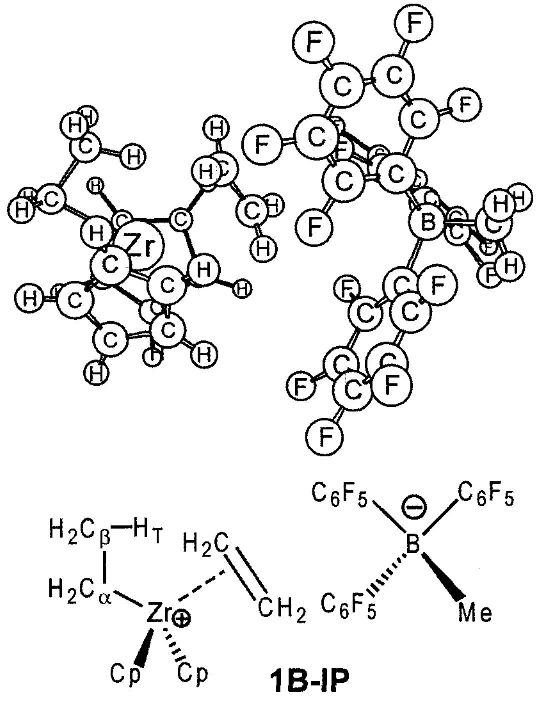

1B-IP

Figure 7.1. Orientation of the $[Cp_2Zr(C_2H_5)(C_2H_4)][CH_3B(C_6F_5)_3]$ ion pair (**1B-IP**).

To identify the preferred ion pair orientation, we made an exploratory search of ion pair orientations using our QM/MM model, assuming the cation remains in the **1B** orientation. Through a series of optimizations of prospective ion pair orientations, we found that the counteranion is preferentially located adjacent to the neutral ethylene ligand (Figure 7.1). Other low-energy geometries were less stable than this structure by several kcal mol^{-1}. This result is consistent with the NMR study by Marks and coworkers on the analogous [$Me_2SiCp_2Zr(CH_3)THF$][$CH_3B(C_6F_5)_3$] ion pair, where the counteranion was found to be preferentially located adjacent to the THF ligand, away from the methyl ligand of the cation.[6]

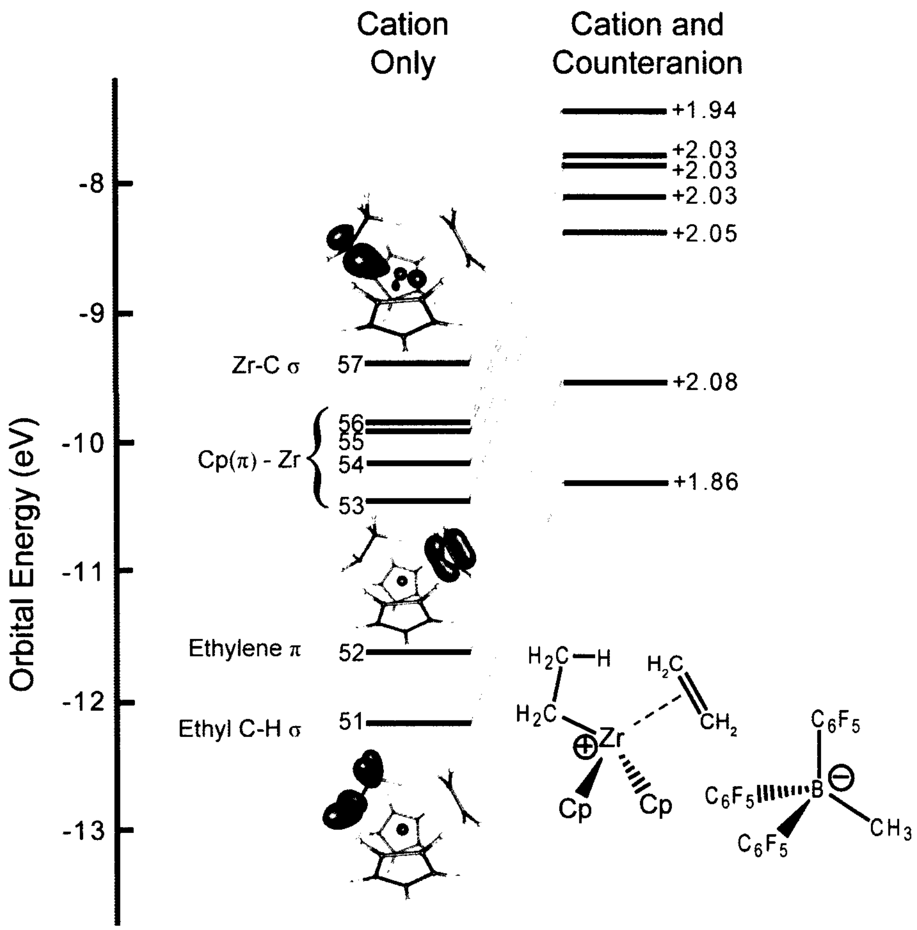

Figure 7.2. Orbital energy level diagram of key molecular orbitals for the optimized structure of **1B-IP**. Orbital energy levels are shown for the cation only (left) and with the counteranion present (right). The orbital energy difference between the cation and ion pair is given in red.

The origin of the preferential ion pair orientation can be interpreted from the orbital energy levels of **1B-IP**, determined with and without the effect of the counteranion charges (Figure 7.2). While the overall interaction between the cation and the anion is attractive, the electrons of the cation will experience a net electrostatic repulsion with the partial charges of the anion. This repulsion destabilizes the molecular orbitals of the metallocene in the ion pair relative to the orbitals of the unperturbed cation. As these orbitals correspond to specific bonding interactions, they are localized in different areas of the cation and will be destabilized differentially depending on the position of the counteranion.

In the preferential orientation of **1B-IP**, the counteranion is adjacent to the ethylene ligand and at maximal distance from the ethyl ligand. The molecular orbitals that are localized on the ethylene ligand experience destabilizations in the range of 2.0–2.1 eV, such the ethylene π MO, which is destabilized by 2.08 eV. The molecular orbitals that are localized on the ethyl ligand experience smaller destabilizations, in the range of 1.8–1.95 eV. For instance, the σ(C–H) and the σ(Zr–C$_\alpha$) orbitals localized on the ethyl ligand are destabilized by 1.86 eV and 1.94 eV, respectively. While the orbital energies do not fully describe the stability of the complex, they do indicate the sensitivity of the molecular orbitals to the position of the counteranion. As the ethyl ligand carries a formal charge of –1, the electronic structure of the cation experiences a greater degree of destabilization when the counteranion is adjacent to it, resulting in a preferred orientation where the counteranion is adjacent to the neutral ethylene ligand.

Despite these changes in orbital energies, the bonding and charge distribution in the cation of the optimized ion pair do not change significantly when the counteranion is present. The Mulliken charges of the cationic zirconocene complex changed by only hundredths of electrons when the calculation was repeated with the counteranion partial charges present (Figure 7.3). The atoms experiencing the largest change are those immediately adjacent to the counteranion, while those relating to the catalytic activity of the complex, such as Zr and C$_\alpha$, are only slightly changed by the presence of the counteranion. Similarly, the Wiberg bond orders within the zirconocene changed only slightly when the counteranion was introduced, with most bond orders changing by less than 0.5%.

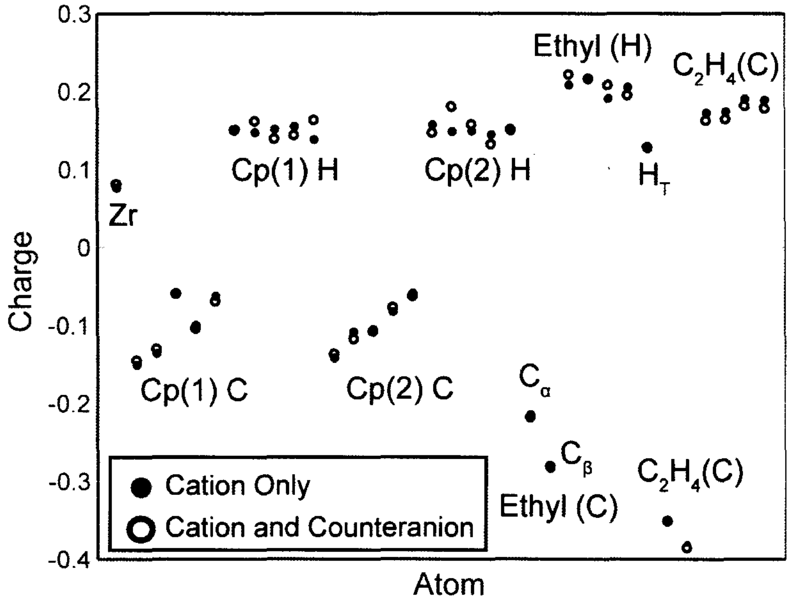

Figure 7.3. Mulliken charges of **1B-IP** with and without the counteranion present.

The lack of a strong effect of the counteranion on the bonding and charge distribution in the cation can be attributed to the relatively large cation-anion separation. Among counteranions, $[CH_3B(C_6F_5)_3]^{-1}$ is of moderate coordinating ability, as its bulky ligands prevent a close interaction with the cation. As the metal is formally d^0, there are no occupied d-orbitals that can be polarized. Likewise, the ligand set is resistant to induced polarization by the counteranion.

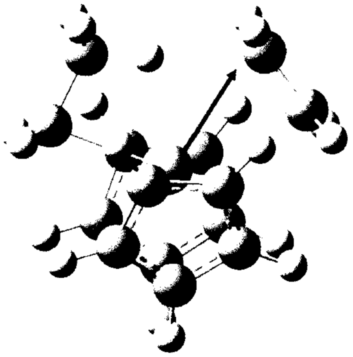

1B

μ = 2.30 D

Figure 7.4. Structure and dipole moment of **1B**. The dipole moment vector is indicated by the blue arrow.

Given that the electronic structure of the cation is essentially unaffected by the presence of the counteranion, a simple electrostatic explanation can be invoked to explain the preferred ion pair orientation without directly examining molecular orbitals. In addition to its cationic charge, **1B** has a significant dipole moment, with a magnitude of 2.30 D (Figure 7.4). This dipole moment is directed from the metal center towards the neutral ethylene ligand, as all other ligands are formally anionic. This leads to a minimum-energy orientation where the anion is adjacent to the ethylene ligand, as the dipole-anion interaction is stronger in this geometry. Like the orbital energy explanation presented earlier, this model reflects the greater electrostatic repulsion experienced between the counteranion and the anionic ligands *vs* the weaker repulsion experienced by the neutral ethylene ligand.

7.2.2. Equilibrium Molecular Dynamics

To compare the solution structures and dynamics of the cation-only (**1B**) and ion pair complexes (**1B-IP**), we have run 50 ps MD simulations of these complexes at 300 K in a periodic solvent box of pentane, starting from the preferred orientations identified in Section 7.2.1. The full details of our MD simulations are provided in Section 7.4.

The MD simulation of **1B** remains close to the minimum-energy structure throughout the simulation. Despite a significant degree of fluxional behaviour within the complex, the complex remains in a geometry consistent with an agostic interaction between the Zr and a C_β–H bond of the ethyl ligand. The equilibrium dynamics of **1B** are discussed in detail in Chapter 6.

In contrast to **1B**, **1B-IP** undergoes a significant rearrangement during the MD simulation. Within 1.4 ps of the beginning of the simulation, the complex undergoes an isomerization from the β-agostic configuration (**1B-IP**) to the α-agostic configuration (**1A-IP**). In this new geometry, the β-agostic interaction is absent, as the ethyl ligand is extended away from the metal (Figure 7.5). Instead, transient α-agostic interactions occur between the C_α–H bonds of the ethyl ligand and the metal, causing the average Zr–C_α–H angle to contract to 97°. Two other MD simulations initiated from other orientations of **1B-IP** also underwent the same isomerization, indicating that this rearrangement is a general phenomenon and not the result of a specific starting geometry.

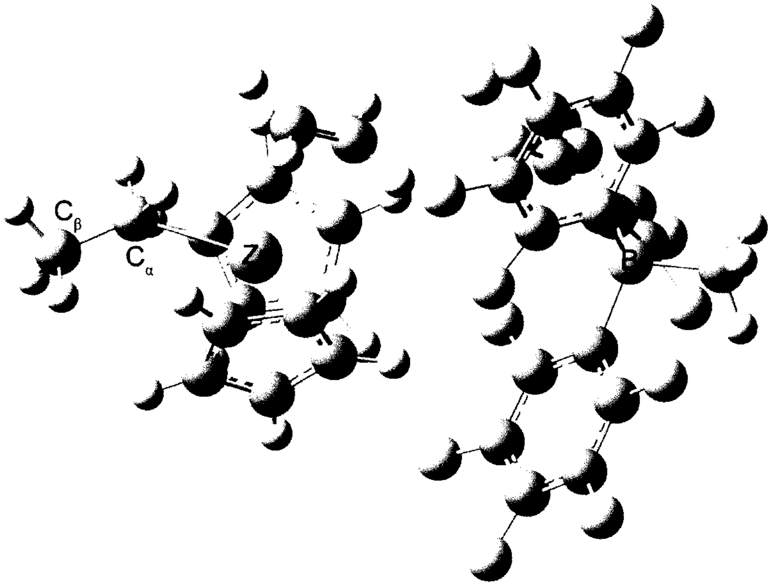

Figure 7.5. Representative configuration of **1A-IP** selected from the MD simulation.

This spontaneous isomerization is surprising given that static calculations on the cation-only system show that the *β*-agostic configuration (**1B**) is 2.7 kcal mol^{-1} more stable than the *α*-agostic configuration (Scheme 7.4, **1A**) on the PES. As this isomerization only occurs in the simulation of **1-IP** and not in **1**, we can surmise that the presence of the counteranion stabilizes the **1A-IP** configuration. As this isomerization occurs facilely and the complex remains in the **1A-IP** configuration during the rest of the simulation, we can infer that the free energy of **1A-IP** is lower than that of **1B-IP** by at least 1 kcal mol^{-1}. We can rationalize this difference in two ways: the greater entropy of the **1A** state and the electronic stabilization of the **1A** configuration by the counteranion.

While the 2.7 kcal mol^{-1} potential energy difference of **1A** and **1B** does not include the effects of the entropy difference of the two states, the MD simulations will inherently sample higher entropy states to a greater degree. We can approximate the effect of entropy on the relative free energies of the two states using static statistical mechanics calculations. When the free energies of these two configurations are calculated for the cation-only system using the classical harmonic oscillator approximation, **1A** is only 1.6 kcal mol^{-1} less stable than **1B** (1.8 kcal mol^{-1} using the quantum harmonic oscillator approximation, the calculations of free energies using static calculations is discussion in Appendix D). This 1.1 kcal mol^{-1} difference between the relative energies and the relative free energies reflects the higher vibrational entropy of **1A** compared to **1B**. The increase in vibrational entropy is due to the greater range of motion to the ethyl ligand in **1A** compared to **1B**, where the β-agostic interaction precludes free methyl group rotation within the ethyl ligand and rotation around the Zr–C(ethyl) axis. Nevertheless, the greater vibrational entropy in **1A** alone is insufficient to compensate for the enthalpic preference of **1B** in the cation-only system, as it remains in the **1B** configuration.

The second source of stabilization of **1A-IP** is due to the electronic effect of the counteranion. These effects can are apparent in the relative potential energies of the optimized structures of **1B-IP** and **1A-IP**. Within these calculations, **1A-IP** is 1.7 kcal mol^{-1} higher in potential energy than **1B-IP**. As **1A** is 2.7 kcal mol^{-1} less stable than **1B**, we can infer that the α-agostic configuration is stabilized by 1.0 kcal mol^{-1} relative to the β-agostic configuration when the counteranion is present.

To identify the origin of the electronic stabilization of **1A-IP** by the counteranion, we have examined the electronic structure of the optimized structures of **1A-IP** and **1B-IP** with and without the counteranion present. One possible explanation of this effect is that the counteranion is destabilizing **1B-IP** by weakening the β-agostic interaction; however, we found that the 3-center bond orders for this interaction were not affected by introduction of the counteranion and remained constant at 0.08. As we observed in the static structures of **1B-IP**, the Mulliken charges and Wiberg bond orders in the zirconocene catalyst were only slightly perturbed by the presence of the counteranion (~1% difference), suggesting that the rearrangement to the α-agostic configuration is not directly caused by a change in the zirconocene electronic structure.

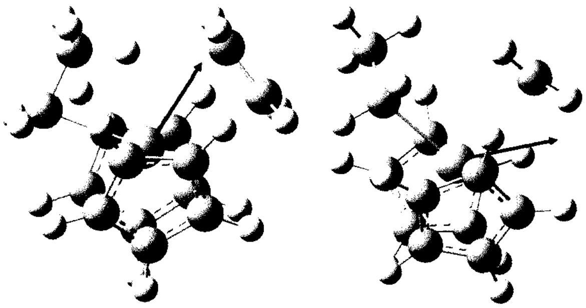

1B
$\mu = 2.30$ D

1A
$\mu = 2.54$ D

Figure 7.6. Structures and dipole moments of **1B** and **1A**. Dipole moment vectors are indicated by the blue arrows.

As we found for the preferred ion pair orientation of **1B-IP**, the dipole moments of **1A** and **1B** a simple explanation of their relative stabilities in the ion pairs (Figure 7.6). In both cases, there is a net attractive Columbic interaction between the cationic charge of the zirconocene and the counteranion, although their dipole moments result in differing stabilities. The dipole moment in **1B** is 2.30 D and the dipole moment vector extends from the Zr center towards the coordinated ethylene ligand. The dipole moment in **1A** is 2.54 D, a significant increase compared to **1B**. In this configuration, the dipole moment vector extends in the opposite direction from the extended anionic ethyl ligand. As the ion pair can have a stronger dipole-anion interaction in the **1A** configuration than in the less polar β-agostic form, the α-agostic configuration becomes the thermodynamically favoured configuration in the presence of the counteranion.

When the effect of the increased vibrational entropy of **1A** is combined with the electronic stabilization due to the counteranion, **1A-IP** becomes approximately equally stable to **1B-IP**. These two terms alone do not fully capture the increased stability of **1A-IP**, as the α-agostic configuration is distinctly more stable than **1B-IP** within the MD simulation. This reaffirms the value of MD simulations, as the stabilizing effect of the counteranion is not fully realized by the static calculations.

7.2.3. β-Agostic to α-Agostic Isomerization Dynamics

The transformation of the β-agostic to the α-agostic configuration is an intriguing example of a facile configurational isomerization of a coordination complex. Although these isomerizations are ubiquitous in organometallic chemistry, they are often difficult to model computationally, as they involve subtle, low-energy changes in many coordinates simultaneously. In this instance, we can gain insight into the β-agostic to α-agostic isomerization process by analysis of the critical coordinates in the MD simulation where the isomerization occurred spontaneously.

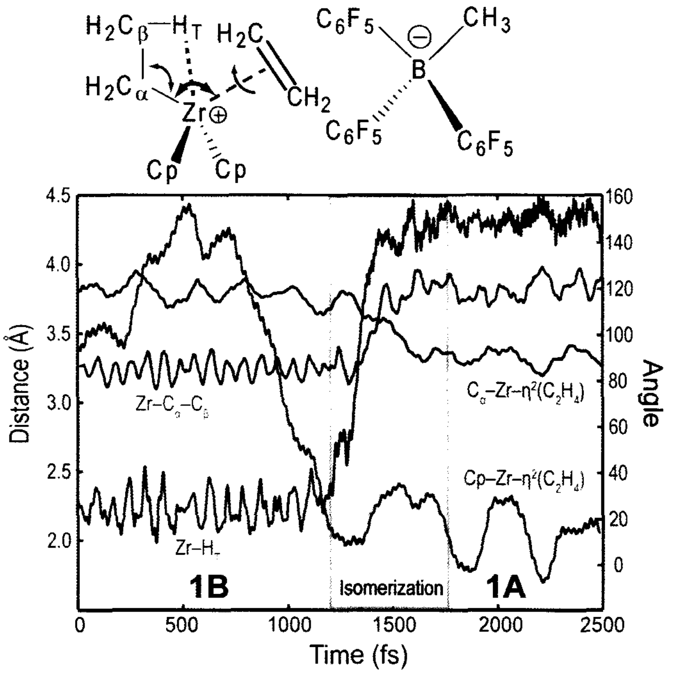

Figure 7.7. Structural parameters during the isomerization from **1B-IP** to **1A-IP**. The Zr–H_T distance is plotted on the primary axis, while all angles are plotted on the secondary axis.

The most obvious coordinate for this isomerization is the Zr–H_T distance, which undergoes normal oscillations for the first 1000 fs of the simulation (Figure 7.7). At the 1200 fs point in the trajectory the Zr–H_T distance increases to a range near 2.5 Å, corresponding a transient structure where the β-agostic interaction is broken but the ethyl ligand has not extended into the α-agostic structure. The complex remains in this geometry for approximately 100 fs before the Zr–H_T distance increases sharply into a range near 4.4 Å, completing the isomerization to the extended ethyl geometry at 1400 fs. A second structural metric of this interaction is the Zr–C_α–C_β angle. This angle undergoes minor fluctuations near its minimum-energy angle of 84° until the 1300 fs point in the simulation, at which point this angle increases to a range near 120° that it holds in the **1A-**

IP configuration. The angle between the C_α of the ethyl ligand and the centroid of the ethylene ligand (C_α–Zr–η^2(C_2H_4)) undergoes the opposite change, decreasing to 90° from 120°, consistent with a change in the coordination mode of the metal. This change also occurs late in the isomerization, beginning only after the β-agostic interaction is broken.

An unintuitive coordinate for the isomerization is the rotation of the η^2-coordinated ethylene ligand (defined by the dihedral angle between the centroid of the Cp ligand, the metal, and the C–C axis of the ethylene). This dihedral angle begins in the 90–100° range, corresponding to the minimum potential-energy structure of **1B** where the ethylene eclipses the ethyl C_α–C_β bond. Over the course of the first 1 ps of the simulation, this dihedral undergoes a large fluctuation, rotating into a range between −10 to 20°, an orientation normal to the ethyl C_α–C_β bond. The β-agostic interaction breaks at 1200 fs, which coincides with the ethylene ligand assuming this new orientation.

Based on the analysis of this trajectory, it appears that this isomerization occurs in three distinct stages rather than in a single concerted process. In the first stage, the ethylene ligand rotates to be perpendicular to the ethyl C_α–C_β axis. In the second stage, the β-agostic interaction breaks, but the complex briefly retains the coordination mode of **1B-IP**. In the last stage, the Zr–C_α–C_β and C_α–Zr–η^2(C_2H_4) angles change from the values they hold in the **1B-IP** coordination mode to their values in the coordination mode of **1A-IP**. The other trajectories where this isomerization occurs show the same qualitative mechanism.

7.2.4. Ion Pair Dynamics

To better understand the solution structure of **1A-IP**, we analyzed the ensemble of ion pair structures generated from a 50 ps MD simulation of **1A-IP**. Throughout the MD simulation, the complex maintained a general orientation where the ethyl group of the cation is positioned opposite to the counteranion. The cation remains located adjacent to the counteranion at the face opposite to the methyl ligand (Figure 7.5).

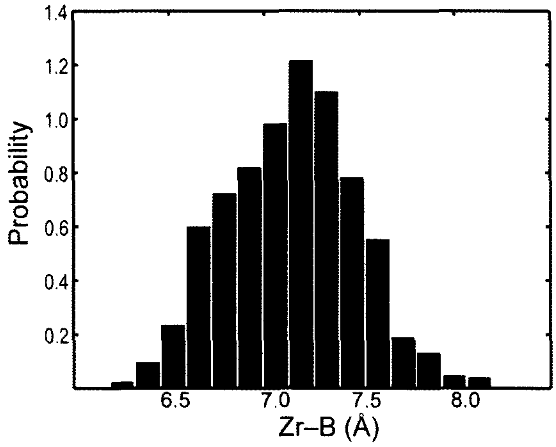

Figure 7.8. Probability distribution of the Zr–B distance in **1A-IP**.

The first structural parameter we examined is the Zr–B distance, which is a metric for the interionic distance. The Zr–B distance has a broad distribution, with distances through the range 6.5–7.5 Å all having significant probabilities (Figure 7.8). In comparison, the minimum-energy geometry of **1A-IP** is 6.6 Å, on the lower end of the distribution and significantly different than the most probable distance of 7.2 Å. The Zr–B distance remains below 8 Å throughout the bulk of the simulation as the electrostatic attraction between the cation and anion prohibits further dissociation in a non-polar solution. The lower end of this range is 6.4 Å, the point where steric repulsion between the pentafluorophenyl substituents of the counteranion and the auxiliary Cp ligands of the cation begins to dominate.

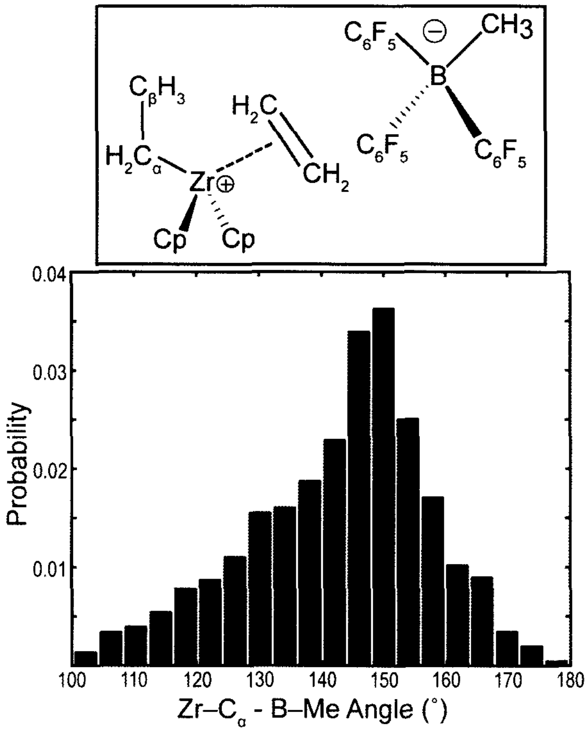

Figure 7.9. Probability distribution of the angle formed between the Zr–C_α and B–CH_3 bonds (red) in the MD simulation of **1A-IP**.

The second descriptor of the ion pair orientation we have considered is the angle formed between the Zr–C_α bond and the B–CH_3 bond. This indicates the variability of the angular orientation of the cation and anion. This angle also has a broad distribution, although it is restricted to the range of 90–180° (Figure 7.9). The most probable angle within the distribution is 150°, compared to a minimum-energy angle of 163°. The distribution has a strong bias for angles ±20° of the 150° maximum.

The breadth of these distributions and the large difference between the minimum-energy geometry and the most probable geometries illustrates the difficulty of modelling ion pairs using geometry optimizations alone. As these outer-sphere ion pairs interact predominantly through non-bonded electrostatic and van der Waals interactions, a broad range of orientations can be achieved at 300 K and individual minimum potential-energy orientations are not necessarily representative of this distribution.

7.2.5. β-Hydrogen Transfer

In addition to our study of the preferred ion pair structure and dynamics, we also used QM/MM calculations to study the effect of the counteranion on the β-hydrogen reaction. In the first stage of our study, we performed a static coordinate scan along the C_β–H_T coordinate of **1** and **1-IP**, beginning in **1B** and **1B-IP** geometries, respectively. The complex was optimized subject to a constraint of the C_β–H_T bond length at 0.025 Å increments in the range of 1.0–2.5 Å, corresponding to the β-hydrogen transfer of H_T. The potential energy profiles of these coordinate scans are plotted in Figure 7.10.

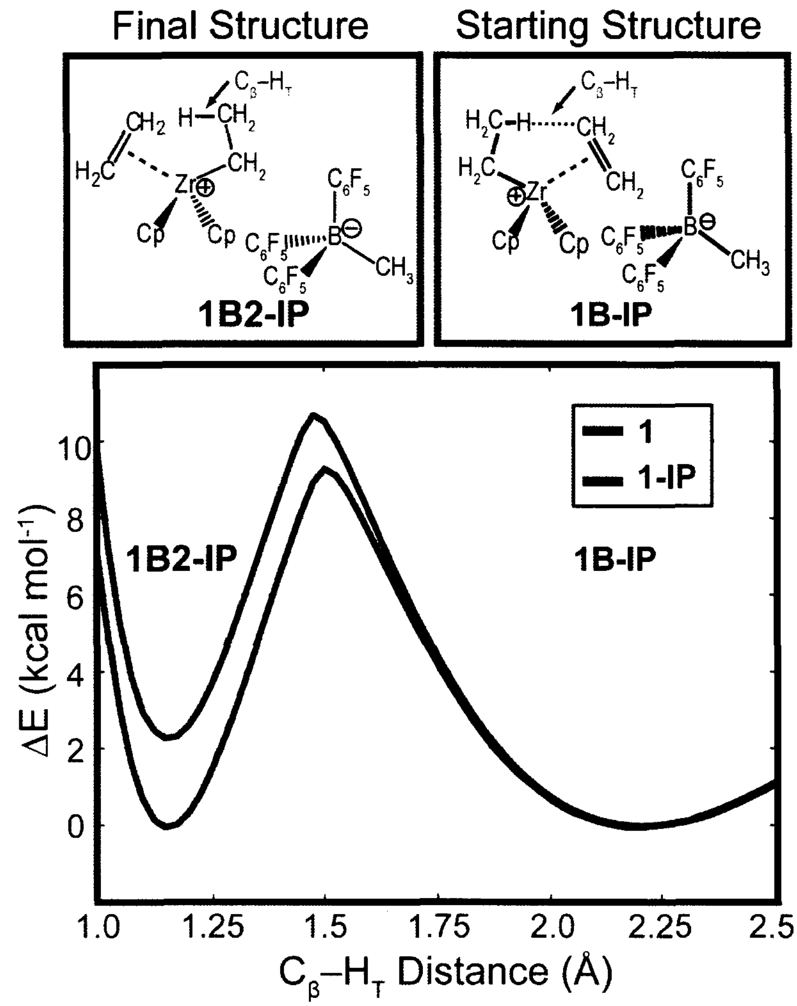

Figure 7.10. Potential-energy coordinate scan of the C_{β}–H_T bond for β-hydrogen transfer for **1B** and **1B-IP**.

In the profile of **1**, the reactant and product structures are equivalent. The transition state occurs at C_{β}–H_T = 1.5 Å for **1B**, with a barrier height of 9.5 kcal mol^{-1}. For the profile of **1-IP**, the minimum located at C_{β}–H_T = 2.2 Å is more stable than the minimum located at C_{β}–H_T = 1.15 Å by 2.2 kcal mol^{-1}. This difference in stability is due to the orientation of the counteranion, as the more stable minimum corresponds to **1B-IP**, while the second minimum corresponds to an orientation where the counteranion is adjacent to the anionic ethyl ligand (Figure 7.10, **1B2-IP**). This is in keeping with the results of Section 7.2.1, where we found that there is an energetic preference for ion pair orientations where the counteranion is adjacent to the formally neutral ligands. With the counteranion present, the transition state occurs slightly later (C_β–H_T = 1.475 Å) and the barrier height is marginally higher (10.7 kcal mol^{-1} with respect to **1B-IP**). Both these effects reflect that the product state is less stable than the reactant state due to the orientation of the counteranion. In keeping with Hammond's postulate,[51] the higher-energy product results in a destabilization of the late portion of the reaction coordinate and a higher barrier.

To determine the effect of the counteranion on the *β*-hydrogen transfer reaction more rigorously, we have calculated the potential of mean force (PMF) for this reaction using 15 40 ps MD simulations in an explicit pentane solvent, restrained at 0.1 Å increments between C_β–H_T = 1.0–2.5 Å. These simulations used harmonic restraints with force constants of 150 kcal mol^{-1} Å^{-2}. Each simulation was equilibrated for 10 ps before the production run. The PMF was determined from these simulations using the Weighted Histogram Analysis Method (WHAM), which is widely used to calculate free energy profiles in conjunction with MM force fields, but has only recently been applied using AIMD (see Appendix B for a full derivation and discussion of WHAM).[52-55] Error bars were determined based on an estimated correlation time of 50 fs. The PMF of the *β*-hydrogen transfer in **1** and **1-IP** are presented in Figure 7.11. Although in principle the counteranion could move to an entirely distinct orientation during these simulations, in practice this does not occur, as the length of the simulation is shorter than the time scale for a large-scale repositioning of the counteranion.

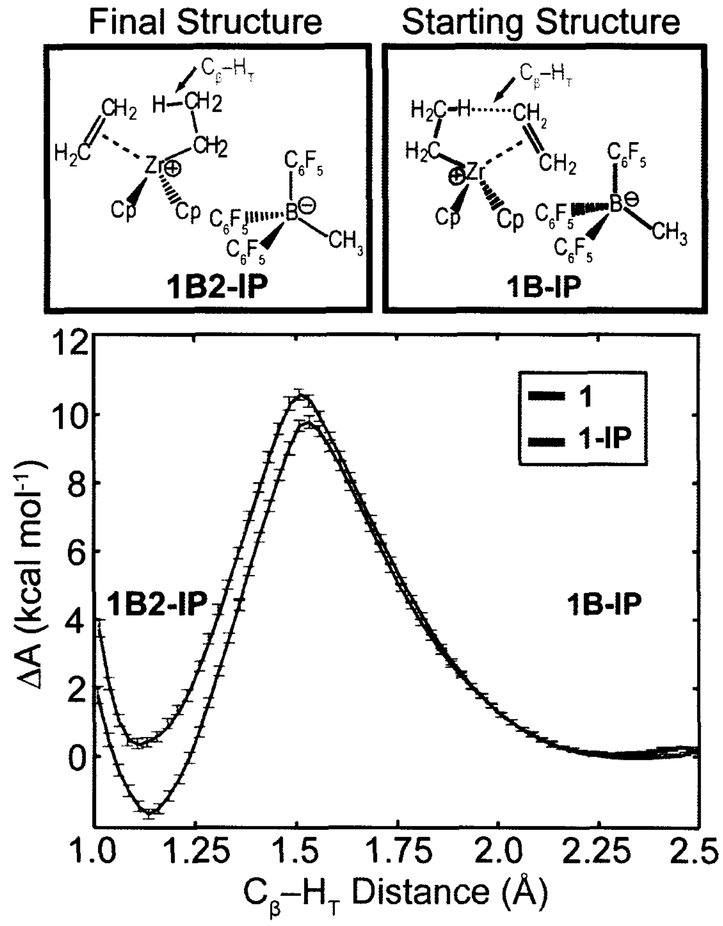

Figure 7.11. PMF of the C_β–H_T bond for β-hydrogen transfer for **1** and **1-IP**.

The computed PMF gives the relative Helmholtz free energies along the reaction coordinate. The effects of entropy, the solvent, and in the case of **1-IP**, the counteranion are inherently expressed in the free energy at that point of the coordinate, without relying on the harmonic approximation. Although the Helmholtz free energy strictly relates to the thermodynamic internal energy (ΔU) of the system (Eq. (7.1)), we can relate the PMF to our potential-energy coordinate scan by assuming that ΔU at a point on the coordinate can be approximated by the relative potential energy (ΔE) at that the same point in the potential-energy coordinate scan. Within this approximation, the difference between energies on the two profiles is due entirely to entropy term in Eq. (7.1) (–TΔS).

$$\Delta A = \Delta U - T\Delta S \tag{7.1}$$

One result of the inclusion of entropy in the reaction profile is that the minima on the energy profile of **1** are no longer symmetric. This is due to the presence of the C_β–H_T restraint, which prevents the Zr–η^2(C_2H_4) stretch and internal rotation in **1B**, as the C_β(ethylene)–H_T distance is restrained in the **1B** minimum but not in the **1B2** minimum. This causes to a free energy difference of 2.1 kcal mol^{-1} between the two minima, reflecting the large degree of configurational freedom associated with the ethylene ligand in **1**, which was discussed in detail in Chapter 6.

We can determine the relative free energies of **1B-IP** and **1B2-IP** despite the bias due to the restraint by noting the **1B2-IP** minimum is 2.0 kcal mol^{-1} higher in free energy than **1B2**. As the **1B** and **1B2** are equivalent structures, their unbiased free energies are necessarily equal. Therefore, if we assume that the counteranion does not have large impact of the relative entropies of the two states, **1B2-IP** must also be 2.0 kcal mol^{-1} higher in free energy than **1B-IP**. This is in good agreement with the 2.1 kcal mol^{-1} difference determined with the PES scan.

The free energy barriers of *β*-hydrogen transfer show a sizable influence of vibrational entropy. As the free energies of **1B** and **1B-IP** are affected by the restraint, these barriers are best discussed in terms of the barriers of the reverse reactions, from **1B2** and **1B2-IP** to **1B** and **1B-IP**, respectively. The activation energy for *β*-hydrogen transfer from **1B2** to **1B** is 11.8 kcal mol^{-1}, compared to the potential energy barrier height for this reaction of 9.5 kcal mol^{-1}. Similarly, the activation energy for *β*-hydrogen transfer from **1B2-IP** to **1B-IP** is 10.5 kcal mol^{-1}, compared to the potential energy barrier height for this reaction of 8.2 kcal mol^{-1}. The activation free energy of **1B2-IP** to **1B-IP** is 1.3 kcal mol^{-1} lower than the **1B2** to **1B** reaction, which is equal to the difference in potential energy barriers, indicating that the effect of the counteranion on this reaction can be successfully explained by potential energy effects alone and are effectively unchanged on the free energy surface.

The absolute differences between the free energy barriers and the potential energy barriers show a notable trend. Applying the assumption that the relative internal energy can be approximated at the relative potential energy again, we can approximate the difference between the free energy barriers and the potential energy barriers as the vibrational entropy component of free energy of activation ($-T\Delta S^{\ddagger}$), as translational and rotational entropy changes are negligible. This difference is 2.3 kcal mol^{-1} for both the **1B2** to **1B** and the **1B2-IP** to **1B-IP** β-hydrogen transfer, yielding an entropy of activation of –7.7 eu. The entropy of activation calculated using static QC calculations within the harmonic oscillator approximation is only –1.3 eu (both the classical and quantum harmonic oscillator approximations give the same result), a factor of 6 smaller than the activation entropy estimated from the PMF calculation.

The general guidelines for the entropy of activation of an intramolecular reaction is that it should be small and negative (–1 to –4 eu). This reflects that the transition state is more ordered and vibrationally stiffer than the reactants, although this change in entropy is characteristically an order of magnitude smaller than those seen for associative or dissociative reactions.[56] Several intramolecular organometallic reactions with larger entropies of activation have been recently been reported; such as $\Delta S^{\ddagger} = -5.2$ eu for a β-

hydride elimination of a Pd–ethyl ligand[57] and $\Delta S^{\ddagger} = -6.7$ eu for the insertion of styrene into a Pd–Me bond.[58] Large vibrational entropy changes in inorganic reactions have been investigated Marder et al., who ascribed the large vibrational entropy change of –30 eu in the oxidation of an iron tris(α-diimine) complex to the stiffening of metal-ligand vibrational modes when the metal is oxidized.[59-61] This large contribution of the vibrational entropy to the activation free energy could be a common feature in inorganic chemical reactions.

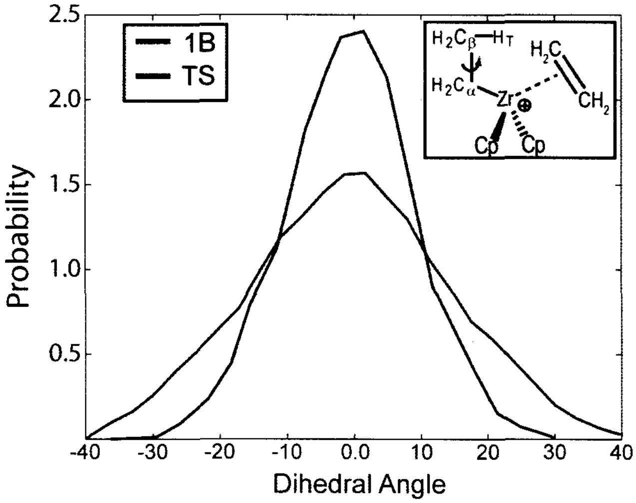

Figure 7.12. Probability distributions of Zr–C_α–C_β–H_T (inset, labelled red) dihedral angle for MD simulations of the free reactant complex and a restrained simulation at the transition state on the PMF.

The decrease in vibrational entropy in the transition state of the β-hydrogen transfer reaction can be attributed to several sources. The most obvious is the loss of Zr–$\eta^2(C_2H_4)$ stretching and hindered rotation at the TS. Less obvious is the loss of vibrational freedom of the ethyl ligand. The β-agostic interaction in **1B** is relatively weak, so there is significant torsional flexibility in the Zr–C_α and C_α–C_β bonds in **1B** (Figure 7.12, inset). For example, Figure 7.12 shows the distributions of the Zr–C_α–C_β–H_T

dihedral in the free MD simulation of **1B** and distribution sampled near the transition state (the restraint parameters were: $r_0 = 1.5$ Å, $k = 300$ kcal mol^{-1} Å^{-2}). This corresponds to a decrease in the configurational freedom of the ethyl ligand when it assumes an appropriate geometry for the *β*-hydrogen transfer, consistent with the large entropy of activation. In this case, the harmonic oscillator approximation underestimates the configurational freedom of the complex, which causes the entropy of activation calculated with this method to be much smaller.

Both the PES and PMF profiles indicate that the effective barrier for the reaction of **1B-IP** to **1B2-IP** is increased by approximately 1 kcal mol^{-1} due to the presence of the counteranion. This can be attributed to the formation of **1B2-IP** in the *β*-hydrogen transfer, which has a less favourable counteranion orientation. These calculations indicate that the presence of the counteranion lowers the absolute rate of the *β*-hydrogen transfer, as this reaction leads to a state where the ion pair is in a less stable orientation.

Quantitatively modelling the effect of the counteranion on the polymerization activity of this catalyst would require simulations of all the steps in the catalytic cycle, including the coordination of the olefin to the metal, the isomerization between the *α*-agostic to *β*-agostic configurations, and the olefin insertion step. Nevertheless, we can draw some inferences on the influence of counteranion on the catalytic activity from these simulations. The stabilization of the *α*-agostic configuration relative to the *β*-agostic configuration should favour propagation over chain termination as the olefin complex is in an appropriate geometry for insertion in the *α*-agostic configuration, but would have to go through an endergonic isomerization from the *α*-agostic configuration to undergo *β*-hydrogen transfer. Furthermore, the effective increase in the *β*-hydrogen transfer barrier due to the destabilization of the **1B2-IP** configuration lowers the rate of chain termination. This suggests that the presence of the counteranion should favour the production of high molecular weight polymers.

7.3. Conclusions

We have used AIMD simulations of the cation-only model zirconocene catalyst $Cp_2Zr(CH_2CH_3)(C_2H_4)^+$ **(1)** and its analogous ion pair $[Cp_2Zr(CH_2CH_3)(C_2H_4)][CH_3B(C_6F_5)_3]$ **(1-IP)** in an explicit MM pentane solvent to study the effect of a counteranion on the zirconocene-olefin complex. We found that the most stable configuration of **1** contains a β-agostic interaction between the ethyl ligand and the metal **(1B)** and this structure is preserved throughout our MD simulation of this complex. In contrast, although there is an analogous minimum-energy of **1-IP** with a β-agostic interaction **(1B-IP)**, this complex underwent a facile isomerization to an α-agostic configuration **(1A-IP)** during the MD simulation. This α-agostic configuration is stabilized by the presence of the counteranion, as the dipole moment of **1A** is larger than that of **1B**, giving **1A-IP** a more favourable electrostatic interaction with the counteranion. The bonding and charge distribution in the cation was not strongly affected by the presence of the counteranion and the preferred orientations of these outer-sphere ion pairs is predominantly due to electrostatic effects alone. Synthesis of ion pairs analogous to those studied by Brintzinger and Marks that contain alkyl ligands that can bond in α-agostic or β-agostic modes could provide an experimental test for the preference for the α-agostic configuration seen in these simulations.

In the second stage of this study, the effect of the counteranion of the β-hydrogen transfer chain termination reaction was determined using a coordinate scan on the PES and through calculating the PMF of the reaction using restrained MD simulations. The PMF determined using MD simulations was in good qualitative agreement with the PES scan of the C_β–H_T coordinate, consistent with the counteranion effects being primarily electrostatic in origin. The role of entropy was surprisingly large, with an estimated entropy of activation of –7.7 eu, much larger than that determined using the harmonic oscillator approximation. This large entropy of activation results from the torsional rotations in the ethyl ligand and Zr–η^2(C_2H_4) stretches and rotations, which have a high degree of configurational freedom in the reactants, but are diminished or lost at the transition state. In this reaction, the vibrational entropy of activation is fully 20% of the activation free energy. Although the vibrational entropy is typically thought to have a small contribution to activation and reaction energies, many reactions involving transition metal complexes could have large vibrational entropy effects due to their fluxional structures.

7.4. Computational Methods

The static DFT calculations we reported here were performed using Turbomole 5.9[62] with the TPSS functional and def2-SV(P) basis set,[63] with exception of H_T, where a def2-TZVPP basis set was used to correctly represent the polarization of this atom during the β-hydrogen transfer. Static QM/MM calculations were performed using our own QM/MM code interfaced with Turbomole 5.9.

This QM/MM code was also used to perform the MD simulations reported in this chapter. QM/MM MD simulations were performed by placing the **1** and **1-IP** in a cubic periodic box of length 44.16 Å. A non-bonded cut-off of 10 Å was used, with a switching function engaged at 8 Å. The pentane solvent was represented using the OPLS force field.[64] The solutes were embedded into a simulation box of neat pentane, equilibrated to the experimental density of 0.626 g cm^{-3}. All MD simulations reported here used the velocity-Verlet integration algorithm.[65] The simulations were maintained a constant temperature of 300 K using a Langevin thermostat[66,67] with a frictional coefficient of χ = 0.1 ps^{-1}. The technical details of this thermostat are included in Appendix A.

The QM region was coupled to the solvent through Lennard-Jones interactions only, as pentane has a very low dielectric constant (ϵ=1.83)[68] and the polarization of the solute by the solvent is likely to be very small. Electrostatic interactions between the cation and the anion partial charges were treated within the QM calculation. A 1 fs time step was used in all the simulations. A full description of our code is included in Section 7.4.1. The details of our parameterization of the MM force field for the counteranion are included in Section 7.4.2.

7.4.1. Description of the QM-MM/MD Code

To perform the QM/MM MD simulations in this study, we implemented our own MM code interfaced to Turbomole. The code is compatible with PDB coordinate files, CHARMM topology (PSF), and CHARMM parameter (PRM) files. The code implements the CHARMM force field for MM calculations. Orthorhombic periodic boundary conditions with constant dimensions are supported. Non-bonded (electrostatic and Lennard-Jones) interactions between MM atoms are calculated using a fixed distance cut-off, such that the non-bonded forces between two particles is zero outside the cut-off distance. The cut-off for the electrostatic interactions uses a polynomial scaling function,

$$U_{elect} = \begin{cases} \dfrac{Cq_1q_2}{r_{12}}\left(1-\dfrac{r_{12}^2}{R_{cutoff}^2}\right), & r \le R_{cutoff} \\ 0, \quad r > R_{cutoff} \end{cases} \tag{7.2}$$

The cut-off for the Lennard-Jones function uses a switching function,

$$U_{LJ} = \begin{cases} 4\in\left[\left(\dfrac{\sigma}{r}\right)^{12}-\left(\dfrac{\sigma}{r}\right)^{6}\right], & r \le R_{switch} \\ 4\in\left[\left(\dfrac{\sigma}{r}\right)^{12}-\left(\dfrac{\sigma}{r}\right)^{6}\right]SW(r), & R_{switch} \le r \le R_{cutoff} \\ 0, \quad r > R_{cutoff} \end{cases} \tag{7.3}$$

$$SW(r) = \frac{\left(r^2-R_{switch}^2\right)^2\left(r^2-R_{cutoff}^2-3\left(r^2-R_{switch}^2\right)\right)}{\left(R_{cutoff}^2-R_{switch}^2\right)} \tag{7.4}$$

where the switching function, SW (Eq. (7.4)), is activated between the distance R_{cutoff} and R_{switch}. The switching function is a polynomial function that ranges continuously from 1 to 0 between R_{switch} and R_{cutoff}.

The QM region was coupled with the MM region using the Hamiltonian,

$$H_{QM/MM} = \sum_{i}^{\substack{\text{QM}\\\text{electrons}}} \sum_{m}^{\substack{\text{MM}\\\text{anion}\\\text{atoms}}} \frac{q_m}{r_{i,m}} + \sum_{k}^{\substack{\text{QM}\\\text{nuclei}}} \sum_{m}^{\substack{\text{MM}\\\text{anion}\\\text{atoms}}} \frac{Z_k q_m}{r_{k,m}} + \sum_{k}^{\substack{\text{QM}\\\text{nuclei}}} \sum_{m}^{\substack{\text{MM}\\\text{atoms}}} E_{LJ;k,m} \tag{7.5}$$

The counteranion atoms were coupled to the QM region through the electrostatic terms (the first and second terms on the r.h.s.), where q_m is the charge of the MM atom m and Z_k is the nuclear charge of QM atom k. All the MM atoms (both counteranion and solvent) were coupled to the QM region through the Lennard-Jones term defined in Eq. (7.5) *via* the third term of the r.h.s.

7.4.2. Development of Counteranion Force Field Parameters

In order to represent the counteranion of this system using an MM force field a complete set of parameters was developed. We have used the CHARMM force field in this study to make use of existing parameters for organic solvents. CHARMM force field parameters have been developed for a range of solvents, amino acids, proteins, and lipids; however, few parameters have been developed for boron. In this section, we describe our process for assigning a complete set of parameters for the counteranion.

The CHARMM force field is comprised of bonded and non-bonded potentials. The bonded potential is comprised of a series of summations that model the potentials due to bonds, bond angles, dihedral angles, improper dihedral angles, and Urey-Bradley bond angle terms. The bond potential term is a sum over all covalent bonds in the system, where each bond is represented by a harmonic potential with a spring constant of k_b and an equilibrium bond length of r_0. The bond angle potentials are also harmonic functions, where k_θ is the spring constant and the equilibrium angle is θ_0. Dihedral potentials are represented by a series of cosine potentials dependent on the dihedral angle, ϕ. k_ϕ is the maximum potential energy of the dihedral term, n is the multiplicity, and δ is the phase of the dihedral term. Improper torsional terms are represented by harmonic potentials of the improper torsional angle ω, where k_ω is the spring constant and ω_0 is the equilibrium value of the angle. Harmonic 1,3 Urey-Bradley potentials are also included to improve the accuracy of bond angle deformations, where k_U is the spring constant and $r_{1,3;0}$ is the equilibrium distance between the two atoms,

$$\begin{aligned} U_{bonded} = \sum_{bonds} k_b (r - r_0)^2 + \sum_{angles} k_\theta (\theta - \theta_0)^2 + \sum_{dihedrals} k_\phi \left[1 + \cos(n\phi - \delta)\right] \\ + \sum_{impropers} k_\omega (\omega - \omega_0)^2 + \sum_{Urey-Bradley} k_U (r_{1,3} - r_{1,3;0})^2 \end{aligned} \tag{7.6}$$

The non-bonded potential is the sum of an electrostatic term and Lennard-Jones term. This summation runs over all relevant atoms-pairs, calculating the electrostatic energy using Coulomb's law and a 6-12 potential for the van der Waals interactions, which are pairwise, isotropic functions of the distance between the two atoms, denoted r_{ij}. q_i and q_j represent the partial charges of atoms i and j, ϵ_{ij} is the van der Waals well depth, and $R_{min,i,j}$ is the Lennard-Jones distance of the pair,

$$U_{nonbonded} = \sum_i \sum_j C \frac{q_i q_j}{r_{ij}} + 4\varepsilon_{ij} \left[\left(\frac{R_{\min,ij}}{r_{ij}} \right)^{12} - 2 \left(\frac{R_{\min,ij}}{r_{ij}} \right)^{6} \right] \tag{7.7}$$

For bond stretches and bond angles where no literature value was available, a potential energy scan of the bond of interest using an analogous complex was made using B3LYP/6-31G(d). The force constant of the B4–CA bond was fit to the B–C bond in the phenyl trihydroborate anion. This complex was also used to generate the force constant for the B4–CA–CA angle term. Similarly, the B4–CTL3 (tetravalent boron to tetravalent carbon) force constant and the B4–CTL3–HAL3 angle stretch force constants were fit using the B–C bond in the methyl trihydroborate anion. The CA–B4–CA bond angle parameters were fit to the corresponding angle in the diphenyl dihydroborate anion. Finally, the CTL3–B4–CA bond angle force constant was fit to the angle in the phenyl methyl dihydroborate anion.

Table 7.1. Bond stretch terms in counteranion force field.

Atom Types		**k_b (kcal mol^{-1})**	**r_0 (Å)**
B4	CA	198.5	1.60
B4	CTL3	189.7	1.60
CA	F	363.8	1.344

Table 7.2. Angle bending terms in counteranion force field.

Atom Types			**k_Θ (kcal mol^{-1} rad^{-2})**	**Θ_0 (°)**
B4	CA	CA	48.8	120.0
B4	CTL3	HAL3	33.43	109.1
HAL3	CTL3	B4	33.43	109.1
CTL3	B4	CA	58.47	109.1
CA	B4	CA	64.94	109.1

Parameters for CA–F bond, bond angles, and dihedrals terms are not part of the standard CHARMM force field, so parameters from the Generalized Amber Force Field (GAFF)[69] were used. Dihedral angles potentials were assigned by analogy to CHARMM potentials containing a tetravalent carbon in place of the tetravalent boron.

We have used the Lennard-Jones coefficients of $R_{min} = 1.98$ Å and $\epsilon = -0.0340$ kcal mol^{-1} for B4 proposed by Otkidach and Pletnev[70] based on a range of boranes, borates, and boric acids. Partial charges were calculated using the CHELPG method[71] using the structure and electrostatic potential of the counteranion calculated with B3LYP/6-31G(d). The charges on chemically equivalent atoms were averaged to ensure consistent values. These charges are presented in Table 7.3.

Table 7.3. $CH_3B(C_6F_5)_3$ counteranion partial charges.

Atom	**Charge**
B	+0.572
C(methyl)	+0.204
H(methyl)	–0.163
C(ipso)	–0.339
C(ortho)	+0.269
C(meta)	+0.167
C(para)	+0.236
F(ortho)	–0.268
F(meta)	–0.195
F(para)	–0.278

The charges generated using this procedure result in a slightly cationic boron center. The methyl-bound hydrogens are slightly anionic, although this is to some degree an artifact of the ESP-based CHELPG method, as Mulliken and NPA analysis do not predict anionic hydrogens in this case. The pentafluorophenyl ligands have a net charge of –0.238. The ipso carbon is the most significantly anionic, while all other carbons in the phenyl rings are significantly cationic, as they are bonded to highly electron-withdrawing fluorines. Each fluorine carries a significant charge, ranging from –0.195 for the meta position to –0.278 in the para position.

The energy-minimized structure of the counteranion using this force field was consistent with the B3LYP/6-31G(d) optimized structure, indicating that these parameters are sufficiently accurate to provide a good description of the counteranion geometry. An MD simulation of the counteranion in gas phase at 300 K using this force field revealed that the geometry of the counteranion is largely static in a tetrahedral geometry. Although the methyl group undergoes frequent rotations, the rotation of the pentafluorophenyl groups is hindered by the steric repulsion between the ortho fluorines of the pentafluorophenyls and the other substituents of the boron.

References

1. Mohring, P. C.; Coville, N. J. *J. Organomet. Chem.* **1994**, *479*, 1.

2. Brintzinger, H. H.; Fischer, D.; Muelhaupt, R.; Rieger, B.; Waymouth, R. M. *Angew. Chem. Int. Ed.* **1995**, *34*, 1143.

3. Resconi, L.; Cavallo, L.; Fait, A.; Piemontesi, F. *Chem. Rev.* **2000**, *100*, 1253.

4. Coates, G. W. *Chem. Rev.* **2000**, *100*, 1223.

5. Stahl, N. G.; Zuccaccia, C.; Jensen, T. R.; Marks, T. J. *J. Am. Chem. Soc.* **2003**, *125*, 5256.

6. Zuccaccia, C.; Stahl, N. G.; Macchioni, A.; Chen, M.-C.; Roberts, J. A.; Marks, T. J. *J. Am. Chem. Soc.* **2004**, *126*, 1448.

7. Rocchigiani, L.; Zuccaccia, C.; Zuccaccia, D.; Macchioni, A. *Chem. Eur. J.* **2008**, *14*, 6589.

8. Landis, C. R.; Rosaaen, K. A.; Sillars, D. R. *J. Am. Chem. Soc.* **2003**, *125*, 1710.

9. Landis, C. R.; Sillars, D. R.; Batterton, J. M. *J. Am. Chem. Soc.* **2004**, *126*, 8890.

10. Chen, M.-C.; Marks, T. J. *J. Am. Chem. Soc.* **2001**, *123*, 11803.

11. Busico, V.; Cipullo, R.; Kretschmer, W. P.; Talarico, G.; Vacatello, M.; Van Axel Castelli, V. *Angew. Chem. Int. Ed.* **2002**, *41*, 505.

12. Mohammed, M.; Nele, M.; Al-Humydi, A.; Xin, S.; Stapleton, R. A.; Collins, S. *J. Am. Chem. Soc.* **2003**, *125*, 7930.

13. Chen, M.-C.; Roberts, J. A. S.; Marks, T. J. *J. Am. Chem. Soc.* **2004**, *126*, 4605.

14. Yang, X.; Stern, C. L.; Marks, T. J. *J. Am. Chem. Soc.* **1994**, *116*, 10015.

15. Bochmann, M.; Lancaster, S. J.; Hursthouse, M. B.; Malik, K. M. A. *Organometallics* **1994**, *13*, 2235.

16. Liu, Z.; Somsook, E.; Landis, C. R. *J. Am. Chem. Soc.* **2001**, *123*, 2915.

17. Chen, E. Y. X.; Kruper, W. J.; Roof, G.; Wilson, D. R. *J. Am. Chem. Soc.* **2001**, *123*, 745.

18. Schaper, F.; Geyer, A.; Brintzinger, H. H. *Organometallics* **2002**, *21*, 473.

19. Macchioni, A. *Chem. Rev.* **2005**, *105*, 2039.

20. Yang, X.; Stern, C.; Marks, T. J. *Organometallics* **1991**, *10*, 840.

21. Kawamura-Kuribayashi, H.; Koga, N.; Morokuma, K. *J. Am. Chem. Soc.* **1992**, *114*, 8687.

22. Woo, T. K.; Fan, L.; Ziegler, T. *Organometallics* **1994**, *13*, 432.

23. Woo, T. K.; Fan, L.; Ziegler, T. *Organometallics* **1994**, *13*, 2252.

24. Bierwagen, E. P.; Bercaw, J. E.; Goddard, W. A. *J. Am. Chem. Soc.* **1994**, *116*, 1481.

25. Weiss, H.; Ehrig, M.; Ahlrichs, R. *J. Am. Chem. Soc.* **1994**, *116*, 4919.

26. Fan, L.; Harrison, D.; Woo, T. K.; Ziegler, T. *Organometallics* **1995**, *14*, 2018.

27. Fan, L.; Harrison, D.; Deng, L.; Woo, T. K.; Swerhone, D.; Ziegler, T. *Can. J. of Chem.* **1995**, *73*, 989.

28. Lohrenz, J. C. W.; Woo, T. K.; Ziegler, T. *J. Am. Chem. Soc.* **1995**, *117*, 12793.

29. Yoshida, T.; Koga, N.; Morokuma, K. *Organometallics* **1995**, *14*, 746.

30. Yoshida, T.; Koga, N.; Morokuma, K. *Organometallics* **1996**, *15*, 766.

31. Woo, T. K.; Margl, P. M.; Lohrenz, J. C. W.; Bloechl, P. E.; Ziegler, T. *J. Am. Chem. Soc.* **1996**, *118*, 13021.

32. Margl, P.; Lohrenz, J. C. W.; Ziegler, T.; Bloechl, P. E. *J. Am. Chem. Soc.* **1996**, *118*, 4434.

33. Margl, P.; Deng, L.; Ziegler, T. *Organometallics* **1998**, *17*, 933.

34. Margl, P.; Deng, L.; Ziegler, T. *Top. Catal.* **1999**, *7*, 187.

35. Borrelli, M.; Busico, V.; Cipullo, R.; Ronca, S.; Budzelaar, P. H. M. *Macromolecules* **2003**, *36*, 8171.

36. Talarico, G.; Budzelaar, P. H. M. *J. Am. Chem. Soc.* **2006**, *128*, 4524.

37. Talarico, G.; Budzelaar, P. H. M. *Organometallics* **2008**, *27*, 4098.

38. Vanka, K.; Chan, M. S. W.; Pye, C. C.; Ziegler, T. *Organometallics* **2000**, *19*, 1841.

39. Chan, M. S. W.; Ziegler, T. *Organometallics* **2000**, *19*, 5182.

40. Klesing, A.; Bettonville, S. *Phys. Chem. Chem. Phys.* **1999**, *1*, 2373.

41. Lanza, G.; Fragala, I. L.; Marks, T. J. *J. Am. Chem. Soc.* **2000**, *122*, 12764.

42. Nifant'ev, I. E.; Ustynyuk, L. Y.; Laikov, D. N. *Organometallics* **2001**, *20*, 5375.

43. Lanza, G.; Fragala, I. L.; Marks, T. J. *J. Am. Chem. Soc.* **1998**, *120*, 8257.

44. Xu, Z.; Vanka, K.; Firman, T.; Michalak, A.; Zurek, E.; Zhu, C.; Ziegler, T. *Organometallics* **2002**, *21*, 2444.

45. Vanka, K.; Xu, Z.; Ziegler, T. *Organometallics* **2004**, *23*, 2900.

46. Xu, Z.; Vanka, K.; Ziegler, T. *Organometallics* **2004**, *23*, 104.

47. Alonso-Moreno, C.; Lancaster, S. J.; Wright, J. A.; Hughes, D. L.; Zuccaccia, C.; Correa, A.; Macchioni, A.; Cavallo, L.; Bochmann, M. *Organometallics* **2008**, *27*, 5474.

48. Correa, A.; Cavallo, L. *J. Am. Chem. Soc.* **2006**, *128*, 10952.

49. Bo, C.; Maseras, F. *Dalton Trans.* **2008**, 2911.

50. Kumar, S.; Rosenberg, J. M.; Bouzida, D.; Swendsen, R. H.; Kollman, P. A. *J. Comput. Chem.* **1992**, *13*, 1011.

51. Hammond, G. S. *J. Am. Chem. Soc.* **1995**, *77*, 334.

52. Hu, P.; Wang, S.; Zhang, Y. *J. Am. Chem. Soc.* **2008**, *130*, 16721.

53. Hu, P.; Wang, S.; Zhang, Y. *J. Am. Chem. Soc.* **2008**, *130*, 3806.

54. Yang, Y.; Yu, H.; York, D.; Elstner, M.; Cui, Q. *J. Chem. Theory Comput.* **2008**, *4*, 2067.

55. Ke, Z.; Zhou, Y.; Hu, P.; Wang, S.; Xie, D.; Zhang, Y. *J. Phys. Chem. B* **2009**, *113*, 12750.

56. Kettle, S. F. A. *Physical Inorganic Chemistry : A Coordination Chemistry Approach*; Oxford University Press: Oxford, 1998.

57. Shultz, L. H.; Brookhart, M. *Organometallics* **2001**, *20*, 3975.

58. Rix, F. C.; Brookhart, M.; White, P. S. *J. Am. Chem. Soc.* **1996**, *118*, 2436.

59. Mader, E. A.; Larsen, A. S.; Mayer, J. M. *J. Am. Chem. Soc.* **2004**, *126*, 8066.

60. Mader, E. A.; Davidson, E. R.; Mayer, J. M. *J. Am. Chem. Soc.* **2007**, *129*, 5153.

61. Mader, E. A.; Manner, V. W.; Markle, T. F.; Wu, A.; Franz, J. A.; Mayer, J. M. *J. Am. Chem. Soc.* **2009**, *131*, 4335.

62. Ahlrichs, R.; Bar, M.; Haser, M.; Horn, H.; Kolmel, C. *Chem. Phys. Lett.* **1989**, *162*, 165.

63. Weigend, F.; Ahlrichs, R. *PCCP* **2005**, *7*, 3297.

64. Jorgensen, W. L.; Maxwell, D. S.; Tirado-Rives, J. *J. Am. Chem. Soc.* **1996**, *118*, 11225.

65. Swope, W. C.; Andersen, H. C.; Berens, P. H.; Wilson, K. R. *J. Chem. Phys.* **1981**, *76*, 637.

66. Grest, G. S.; Kremer, K. *Phys. Rev. A* **1986**, *33*, 3628.

67. Izaguirre, J. A. In *Multiscale Computational Methods in Chemistry and Physics* Brandt A., Binder K., B. J., Eds. 2001; Vol. 117, p 34.

68. *CRC Handbook of Chemistry and Physics*; CRC Press: Cleveland, 2009.

69. Junmei, W.; Romain, M. W.; James, W. C.; Peter, A. K.; David, A. C. *J. Comput. Chem.* **2004**, *25*, 1157.

70. Otkidach, D. S.; Pletnev, I. V. *J. Mol. Struc: THEOCHEM* **2001**, *536*, 65.

71. Curt, M. B.; Kenneth, B. W. *J. Comput. Chem.* **1990**, *11*, 361.

CHAPTER 8

New Shooting Algorithms for Transition Path Sampling: Centering Moves and Varied Perturbation Sizes for Improved Sampling

This work has been submitted for publication in The Journal of Chemical Physics (A09.09.0559).

Abstract

Transition path sampling has been established as a powerful tool for studying the dynamics of rare events. The trajectory generation moves of this Monte Carlo procedure, shooting moves and shifting modes, were developed primarily for rate constant calculations, although this method has been more extensively used to study the dynamics of reactive processes. We have devised and implemented three alternative trajectory generation moves for use with transition path sampling. The centering-shooting move incorporates a shifting move into a shooting move, which centers the transition period in the middle of the trajectory, eliminating the need for shifting moves and generating an ensemble where the transition event consistently occurs near the middle of the trajectory. We have also developed varied perturbation size shooting moves, wherein smaller perturbations are made if the shooting point is far from the transition event. The trajectories generated using these moves decorrelate significantly faster than with conventional, constant sized perturbations. This results in an increase in the statistical efficiency by a factor of 2.5–5 when compared to the conventional shooting algorithm. On the other hand, the new algorithm breaks detailed balance and

introduces a small bias in the transition time distribution. We have developed a modification of this varied perturbation size shooting algorithm that preserves detailed balance, albeit at the cost of decreased sampling efficiency. Both varied perturbation size shooting algorithms are found to have improved sampling efficiency when compared to the original constant perturbation size shooting algorithm.

8.1. Introduction

Many important phase transitions, protein conformational changes, and chemical reactions are rare events on the microscopic timescale.[1] Atomistic computer simulations can offer valuable insights into these events; however, it is generally not possible to simulate rare events directly using molecular dynamics (MD) because the event will typically occur only after a long waiting period. In this waiting period, the simulation remains in the stable state where the simulation began, providing little information about the critical reaction event. Depending on the computer resources available and the system being studied, the waiting period for the simulation of a single rare event can exceed the length of the longest practical MD simulation by orders of magnitude.

Transition path sampling (TPS) was developed by Chandler and coworkers[2-5] as an alternative approach for modelling the dynamics of rare events. The fundamental process of TPS is to sample the transition path ensemble, an ensemble of MD trajectories of length L time steps that begin in reactant state A and end in product state B, capturing the reactive event that connects the two states. Path sampling requires that the user define two characteristic functions to identify whether a time step of a trajectory is in state A or B, but unlike other rare event simulation methods, it is not necessary to define a reaction coordinate. These characteristic functions are generally a function of the positions of the constituent particles, x (Eq. (8.1)).

$$h_{A,B}(x)=\begin{cases}1, & \text{if}\, x\in A,B \\ 0, & \text{if}\, x\notin A,B\end{cases} \tag{8.1}$$

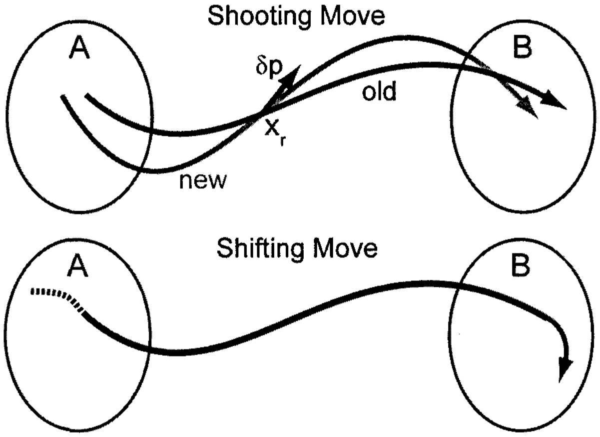

Figure 8.1. Schematics of a shooting move (top) and a shifting move (bottom). Deleted time steps of the shifted trajectory are dashed, while new steps are grey.

The transition path ensemble is generated through a Monte Carlo procedure, wherein a new trajectory is generated from an existing trajectory in the ensemble. Generation of the initial trajectory is discussed in detail in Chapter 2. All subsequent trajectories are generated by shooting moves and shifting moves, which we will briefly summarize here.

In a shooting move (Figure 8.1, top), a time step from a trajectory in the ensemble is selected at random to serve as the shooting point (x_r). The momenta of the particles at this time step are randomly perturbed and then MD simulations are run forward and backward in time from this new point in phase space. If the resultant trajectory is reactive ($h_A(x_0)=1$ and $h_B(x_L)=1$), it is added to the transition path ensemble. Otherwise, the trajectory is rejected and another shooting point is selected. The perturbation to the momenta causes the new trajectory to take a distinct course, so the trajectories sampled will be decorrelated from each other over a number of shooting moves. The size of the perturbation to the momenta can be adjusted so that the trajectories are accepted at an efficient rate. Based on efficiency analysis by Dellago et al.,[8] an acceptance probability of 40% has been widely adopted.

The second Monte Carlo move used in TPS simulations is the shifting move (Figure 8.1, bottom). In a shifting move, N time steps ($N \approx 0.01$ L) are deleted from one end of a trajectory in the path ensemble and the other end of this trajectory is extended by N time steps (thus, the trajectory "shifts" by length N). The new trajectory is accepted or rejected by the same criteria as for a shooting move. As only N time steps are calculated in a shifting move, they are far less expensive than a shooting move, so it is common for 100 shifting moves to be run for every shooting move. Typically, the majority of the time steps in the trajectories generated by shifting moves will be identical to the trajectory they were generated from. Most significantly, the time steps where the transition occurs will be identical and will not contribute new data about the transition itself. The critical property that is distinct in a trajectory generated by a shifting move is the time step in the trajectory where the trajectory enters the product region ($h_B(x_t)=1$), which is a critical property for calculating a rate constant using TPS (*vide infra*).

One challenge in the application of the TPS method is in sampling efficiency. As shifting moves only generate time-shifted trajectories, the sampling efficiency depends on how quickly shooting moves can generate independent trajectories. A trajectory generated by the shooting algorithm will intersect with the trajectory it was initiated from in the coordinate space of the shooting point. While the perturbation applied at the shooting point will cause the new trajectory to deviate from the old one, successive trajectories in the transition path ensemble tend to be significantly correlated. As in other Monte Carlo simulations, this correlation reduces the statistical efficiency of the sampling.[9]

Another limitation of shooting moves is that the acceptance probability can be extremely low for rare events where the free energy barrier is especially high or rough. Due to the high Lyapunov instability of these systems, even a shooting move made with the smallest possible perturbation size (of the order of machine precision) will overwhelmingly result in a trajectory that deviates from the reactive trajectory by a large enough degree that the generated trajectory will remain in the stable state where the shooting point lies, resulting in an unreactive trajectory. Several variations to original path sampling procedure have been proposed with the aim of resolving these issues.

One proposal to address these correlation and acceptance issues is the "one-way shooting" technique proposed by Bolhuis.[10] In this method, the equations of motion are weakly coupled to an Andersen thermostat,[11] introducing a stochastic component to course of the trajectory. In this way, a distinct trajectory will be generated upon integration in one direction from a shooting point, even if no perturbation is applied. The sampling using this method was 3 times more efficient than the original path sampling method for a model diffusive process, although it has the disadvantage of generating stochastic trajectories rather than deterministic trajectories.

Another method to address this problem was recently proposed by Grünwald et al.[12] The "precision shooting" method overcomes the low acceptance probabilities of shooting movies that occur in systems with long barriers or metastable intermediates. In this approach, it is possible to make a shooting move with an arbitrarily small perturbation through an iterative process. Initially, the system is propagated forward in time from the shooting point (x_r) to a later time step, x_{r+t}, with a normal-sized perturbation. Using a linear approximation to the equations of motion, a series of trial trajectories can be constructed such that the magnitude of the deviation from the original trajectory at x_t is within a fixed tolerance. In effect, this allows an arbitrarily small perturbation so that the trajectories will follow the same course to a sufficient degree to ensure a significant acceptance rate. In this way, trajectories can be generated with an acceptance probability that is sufficient for efficient sampling, even in difficult cases. This approach proved successful for the isomerization of a diatomic in a 389 particle purely repulsive fluid, where the diatomic interacts through a double-well potential with a long and rough barrier, although it was less successful for a system where a metastable intermediate exists between the two stable states of the diatomic potential.

Another path sampling technique employing a modified shooting algorithm is the aimless shooting method, developed for the purpose of identifying optimal reaction coordinates.[13,14] Here, a length, T, is defined with the criteria that is much shorter than the full length of the trajectory. One of three time steps is selected as the shooting point: L/2 – T, L/2, or L/2 + T. Rather than perturbing the momenta at this shooting point, entirely new momenta are generated from the Boltzmann distribution. Restricting the shooting points to this narrow range allows a significant acceptance rate without memory of the momenta of the previous trajectory. Trajectories initiated from shooting points with high probabilities of being in a transition path are more likely to join the reactant and product regions and thus be accepted. As a result, the simulation tends to remain in regions where the shooting points have high acceptance probabilities. In another approach, Zahn employed an adaptive modification of the shooting algorithm to optimize the magnitude of the perturbation in a path sampling simulation of the pressure induced B1 to B2 phase transitions of RbBr.[15]

These methods demonstrate that the efficiency of a TPS simulation can be significantly improved by modifying the shooting algorithm. Fundamentally, these methods adjust the way in which the perturbation of a trajectory is made. Shooting moves rely on a balance between two opposing features of the dynamics of the system; if the newly generated trajectory diverges too rapidly from the trajectory it was generated from, it will have a low probability undergoing the transition and being accepted, even for very small perturbations. Conversely, if a newly generated trajectory does not deviate from the old trajectory sufficiently, the two trajectories will be highly correlated and the sampling will be inefficient.

In order to improve the efficiency of TPS simulations, it is important to consider how TPS is used in practice. An important feature of TPS is that it can be used to calculate the rate constant of a rare event without defining a reaction coordinate. Dellago et al. defined a two step procedure to calculate a rate constant using TPS.[8] In the first stage, a large ensemble of transition paths are sampled so that the time derivative of $\langle h_B(x_t) \rangle$ can be calculated. In the second stage, a series of path sampling simulations are run with overlapping definitions of B to calculate the probability, $P(\lambda,t)$, of a trajectory of length L starting in state A and ending at a point along an order parameter λ at time t. Ref. 8 describes how these quantities can be used to calculate a rate constant. Shifting moves are important for these quantities, as they generate converged distributions of $<h_B(x_t)>$ and P(λ,t) far more efficiently than shooting moves alone.

Although TPS is an elegant and radically different approach for calculating rate constants, a large number of trajectories must be sampled for both the transition path ensemble and to calculate of P(λ,t). Calculating a rate constant using this two stage method was first demonstrated by Dellago et al.,[8] studying the isomerization of a diatomic in a 2D fluid. To sample the transition path ensemble in the first stage, 3.6×10^6 shooting moves were made. An additional 2.5×10^6 shooting moves were made in the second stage to calculate P(λ,t). Thus, excluding shifting moves, based on a path length of 2000 time steps, 5.1×10^9 MD time steps were needed to calculate the rate constant of this simple system using TPS. To date, only a handful of studies[16-19] have calculated a rate constant using TPS because the prohibitive computational cost.

Path sampling has been much more widely employed to study reaction mechanisms. Several important path sampling studies have been published on the reaction dynamics of conformational changes biological systems,[6,12,16,20-33] phase changes,[15,34-43] and chemical reactions.[44-53] If the purpose of a path sampling simulation is to examine reaction dynamics rather than to calculate a rate constant, such as in Chapters 4 and 6 of this thesis, it is generally sufficient to sample a far smaller number of trajectories and it is not necessary to calculate P(λ,t). Typically, this type of path sampling simulation has harvested hundreds or thousands of trajectories. Simulations involving a computationally expensive potential, such as an *ab initio* method, typically sample fewer trajectories, ranging from dozens to a few hundred. For instance, in Chapters 4 and 6 of this thesis, only 150 and 350 distinct trajectories were sampled, respectively. This led us to consider how the path sampling algorithms can be optimized if the only objective of the simulation is to study the dynamics of the reaction mechanism.

In this chapter, we introduce new methods to more efficiently sample the transition path ensemble within the framework of existing path sampling algorithms. This chapter is divided into three sections. In the first, we describe the model used to test our novel TPS algorithms. In the second, we discuss a modification to the path sampling procedure that avoids shifting moves. In the third section, we define a novel shooting algorithm where the size of the perturbation is varied as a function the position of the shooting point, as well as a variant of this method that preserves the detailed balance criterion. The sampling efficiency of these varied perturbation size shooting moves is compared to the traditional, constant perturbation shooting moves.

8.2. Model

A popular test system for path sampling is the isomerization of a diatomic in a 2D Weeks–Chandler–Andersen (WCA) fluid, based on a model developed by Straub et al.[54] Each particle interacts through a WCA potential, which is simply the repulsive component of the Lennard-Jones potential (Eq. (8.2), Figure 8.2, top).[55] A unique pair of these particles are defined as a diatomic that interacts through a radial potential with two minima: a compressed state and an extended state (Eq. (8.3), Figure 8.2, bottom). This potential is defined by two constants, w and h, which correspond to width and height of the barrier, respectively. Figure 8.3 shows the unit cell of the fluid with the diatomic in its compressed and extended states. The system is defined to be in state A (compressed) if $0.2\,\sigma \le r \le 1.3\,\sigma$ and to be in state B (extended) if $1.97\,\sigma \le r \le 2.3\,\sigma$.

$$U_{WCA}(r) = \begin{cases} 4\varepsilon\left[\left(\frac{\sigma}{r}\right)^{12} - \left(\frac{\sigma}{r}\right)^{6}\right] + \varepsilon & \text{if } \mathrm{r} \le \mathrm{r}_{\mathrm{WCA}} \equiv 2^{1/6}\sigma \\ 0 \quad \text{if } \mathrm{r} > \mathrm{r}_{\mathrm{WCA}} \end{cases} \tag{8.2}$$

$$U_{dw}(r) = h\left[1 - \frac{\left(r - r_{WCA} - w\right)^2}{w^2}\right]^2 \tag{8.3}$$

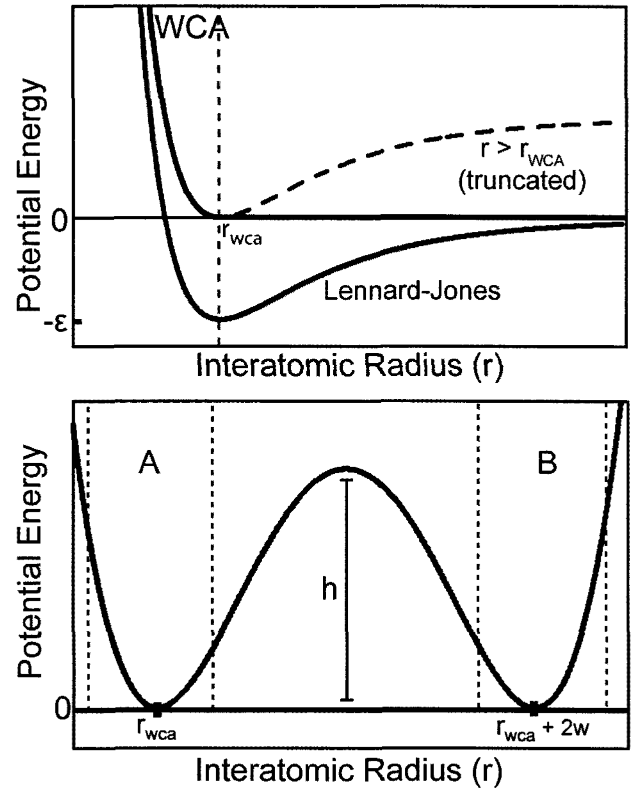

Figure 8.2. WCA (top) and double-well potentials (bottom). Compressed (A) and extended (B) diatomic states are indicated on the double-well potential.

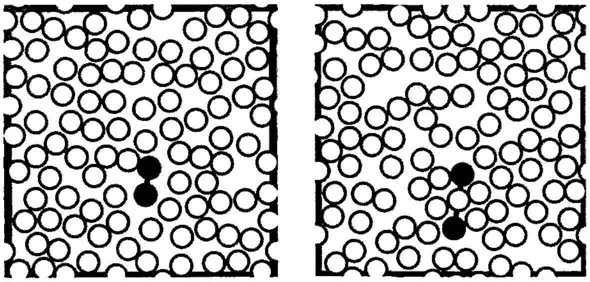

Figure 8.3. 2D WCA Fluid with double well diatomic in compressed (left) and extended (right) states.

The isomerization of the diatomic from the compressed state to the extended state is a rare event for low energy simulations, as sufficient energy must be localized into the vibrational mode of the diatomic in order to cross the barrier. This process occurs through collisions between the diatomic and the other particles of the fluid which transfers energy into the vibrational mode of the diatomic. Once in the extended state, this vibrational energy must be dissipated by the solvent to prevent the diatomic from recrossing to the compressed state. This model incorporates many of the important features of chemical reactions in solution, such as the localization of kinetic energy into a transitional mode and frictional effects of the solvent. The parameters we have chosen for this model tend to result in trajectories that cross the barrier ballistically, although other studies have adjusted of these parameters and the functional form of the diatomic to favour diffusive trajectories.[56]

We follow the system of reduced units used in Ref. 8, where masses are measured in units of single particles masses (m), lengths are measured in units of the Lennard-Jones radius (σ), and energies are measured in units of the Lennard-Jones well depth (ϵ). Units of time are defined as $T \equiv \sqrt{m\sigma / \varepsilon}$. The velocity-Verlet algorithm[57] was used for the MD simulations, with a time step of Δt=0.002 T. The system was composed of 100 particles in a box with a density of 0.7 m/σ^2. A barrier width parameter (w) of 0.5 σ and a barrier height (h) of 15 ϵ were used for the diatomic potential. The path sampling simulations were microcanonical, with a total energy of 100 ϵ.

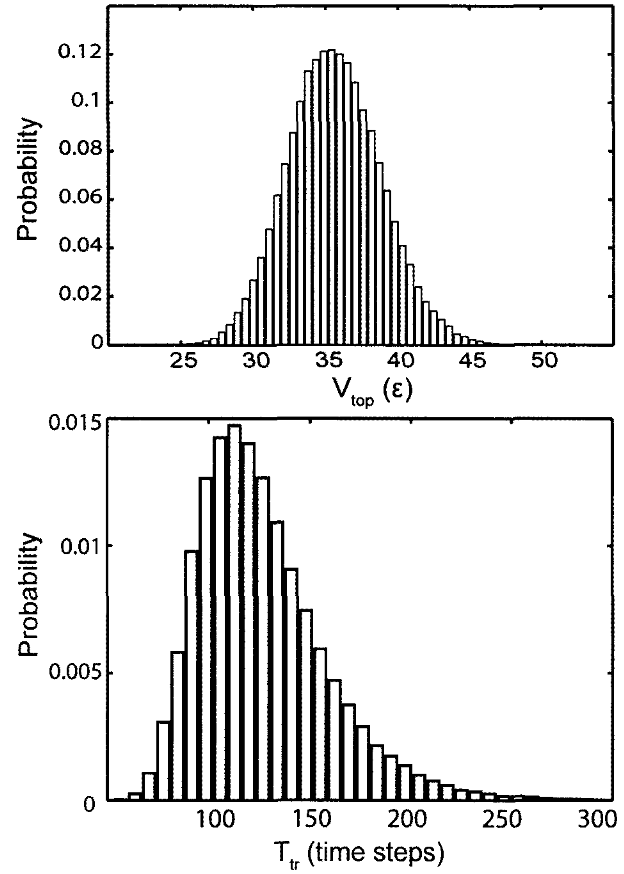

Figure 8.4. Histograms of V_{top} and T_{tr} distributions for a transition path ensemble of 10^5 trajectories.

Dellago et al.[8] defined two trajectory properties to monitor the sampling of the transition path ensemble of this system. The first, V_{top}, is the total potential energy of the system at the time step where the trajectory is at the top of the barrier ($r=r_{wca}+w$). The second, T_{tr}, is the transition time of the trajectory, which is the number of time steps between exiting the compressed state and entering the extended state. The distribution of V_{top} for a 10^5 trajectory transition path ensemble follows a Gaussian distribution with a mean of 35.7 ϵ and a standard deviation of 3.2 ϵ (Figure 8.4, top). The distribution shows a small positive skew. The distribution of T_{tr} (Figure 8.4, bottom) is broader and has a large positive skew. The mean is 126.5 time steps and the standard deviation is 32.1 time steps. As these are largely independent properties with vastly different distributions, they serve as distinct indicators of the sampling efficiency, correlation, and convergence of the transition path ensemble.

8.3. Centering-Shooting Moves

Our first modification to the original path sampling process relates to shifting moves. Although shifting moves are essential for calculating a rate constant, they are of limited benefit if the purpose of the path sampling simulation is only to study the dynamics of the reactive event. In this context, the primary benefit of shifting moves is to reposition the step in which the reaction event occurs; if the position of the reactive event has progressed to either the very start or the very end of the trajectory, the generation of new trajectories through shooting moves can be hindered. Additionally, many trajectories will spend a disproportionate period of time in either state A or B, which can complicate the analysis of these trajectories.

Shooting moves tend to generate trajectories where the reactive event occurs at roughly the same time step of the trajectory, so shooting moves alone cannot efficiently move the transition period away from the edge of the trajectory. It is possible to keep the reactive event in the middle of the trajectory and avoid shifting moves altogether with a minor variation on a shooting move, which we term a centering-shooting move. In these moves, the middle of the reaction event is estimated as middle time step of the transition period (Eq. (8.4)). t_{LA} is the last time step where the trajectory is in state A ($t_{LA} = \max(t) \in h_A(x_t) = 1$) and t_{FB} is the first time step where the trajectory is in state B ($t_{FB} = \min(t) \in h_B(x_t) = 1$). As in a conventional shooting move, a shooting point, x_r, is selected at random. A shifting move is then incorporated into the shooting move by shifting the shooting point, r, of the old trajectory by t_{mid} steps to generate a new position for the shooting point, s (Eq. (8.5)). The rest of this process is identical to a conventional shooting move, where the momenta at the shooting point are perturbed and a new trajectory is propagated forward and backward in time from this point, except that the shooting point now holds a different index within the new trajectory than it did in the old trajectory.

$$t_{mid} = t_{LA} + \left(\frac{t_{FB} - t_{LA}}{2} \right) \tag{8.4}$$

$$s = r + t_{mid} - \frac{L}{2} \tag{8.5}$$

This algorithm biases the path sampling to generate trajectories where the reactive event occurs at the middle of the trajectory. While this explicitly prevents correctly sampling the distribution of $\langle h_B(x_t) \rangle$, which is required for a rate constant calculation from the transition path ensemble, these centering-shooting moves are suitable for applications of TPS where it is more important to generate a consistent ensemble of trajectories for analysis. A similar tactic has been employed by Peters et al.,[13,14] where the trajectory is shifted such that the commitor probability is near ½ at t = L/2.

Centering-shooting moves break the detailed balance criterion because the generation probability of these moves is not symmetric. For example, the generation probability of a centering-shooting move that shifts the transition period from the edge of the trajectory to the center would not have an equal generation probability to the reverse move. Nonetheless, the distributions of V_{top} and T_{tr} calculated from centering-shooting moves are statistically equivalent to the distributions generated using a conventional shooting/shifting path sampling procedure ($\overline{V}_{top}$=35.7 ± 3.2 ϵ, $\overline{T}_{tr}$=126.5 ± 32.1 time steps), indicating that the dynamic properties of the trajectories sampled with this technique are not biased.

Centering-shooting moves are advantageous for TPS simulations which focus on mechanistic aspects, as a consistent ensemble of trajectories where the transition event occurs near the center of the trajectory are generated. The additional computational cost of shifting moves is avoided altogether. Further, the centering-shooting algorithm ensures that the randomly chosen shooting points will be no more than half the path length from the transition event, which leads to a slight improvement in the efficiency of shooting moves, as shooting points far from the transition event have a very low probability of being accepted (*vide infra*).

While our definition of t_{mid} given in Eq. (8.4) was found to be effective in this system, this definition is somewhat arbitrary and many other definitions could be used. An advantage of this definition is that it is not necessary to define a reaction coordinate or order parameter, as Eq. (8.4) determines t_{mid} based only on the characteristic functions. This definition is particularly appropriate for ballistic transitions, although a more sophisticated definition may be appropriate if frictional effects are dominant in the transition.

8.4. Varied Perturbation Size Shooting Algorithm

In the original definition of TPS, a shooting move is performed by selecting a random time step of a trajectory, referred to as the shooting point. The momenta of the particles at this point are then perturbed, typically by adding a component from a Boltzmann distribution to the momenta of each atom. In microcanonical TPS simulations, these momenta are then rescaled to conserve the total kinetic energy. A simulation is then run forward and backwards in time from the shooting point using the perturbed momenta. The magnitude of the perturbation is constant for all the shooting moves in a path sampling simulation. A calibration simulation is typically performed to determine the magnitude of the perturbation that results in an appropriate acceptance probability (P_{acc}). Correlation analysis by Dellago et al. found that an acceptance probability of 40% was most efficient,[8] which has been widely adopted in subsequent path sampling studies.

While Bolhuis[10] and Grünwald et al.[12] have proposed alternative methods of perturbing the trajectories, less attention has been devoted to the selection of the shooting point. Due to the Lyapunov instability, the new trajectory will deviate to an exponentially greater degree as the trajectories extend from the shooting point. As a result, shooting points that are close to the transition period are more likely to cross the reaction barrier as well and will therefore be accepted, whereas shooting points far from the transition period will result in trajectories that diverge to such a degree that they will not cross the reaction barrier.

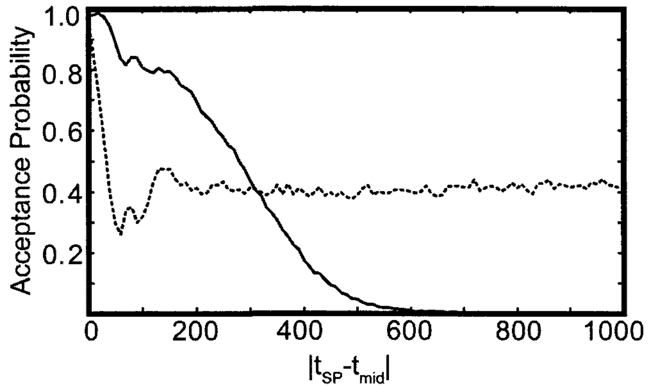

Figure 8.5. Acceptance probability of trajectories as a function of the number of time steps the shooting point (t_{SP}) is from the middle of the transition period (t_{mid}). The solid line depicts a routine 10^5 trajectory path sampling simulation with a constant perturbation size. The dotted line depicts a simulation where the varied perturbation size method is applied.

To quantify this trend, we have plotted in Figure 8.5 the acceptance probability from a simulation with 10^5 centering-shooting moves as a function of the number of time steps between the t_{mid} (Eq. (8.4)) and the shooting point. The probability that a trajectory will be accepted declines sharply as the distance between t_{mid} and the shooting point increases. For time steps close to the middle of the transition, the acceptance probability is nearly 100%, as the new trajectory is initiated from a point where the transition is occurring, with little opportunity to deviate from this path. Outside the region immediately adjacent to the transition period, the acceptance probability decays in a roughly exponential fashion, with extremely low acceptance probabilities for shooting points more than 600 time steps from the middle.

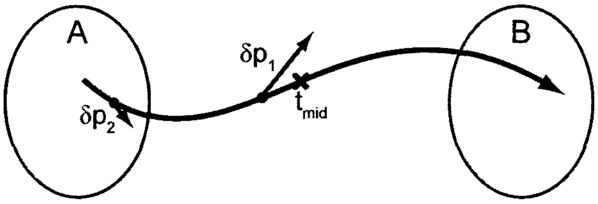

Figure 8.6. Schematic of varied perturbation size shooting move. The magnitude of the perturbation for the shooting point near the t_{mid} (δp_1) is large, while the shooting point further from t_{mid} experiences a smaller perturbation (δp_2).

This behaviour suggests a degree of inefficiency in the conventional TPS scheme due to the use of a constant-sized perturbation. To address this issue, larger perturbations could be applied to shooting points near the transition period, resulting in a greater degree of decorrelation, while smaller perturbations could be applied to shooting points far from the transition period so that they are accepted with an appropriate likelihood (Figure 8.6). A similar strategy has been proposed for use in transition interface sampling.[58]

From examination of Figure 8.5, we considered Eq. (8.6) as an appropriate form for the calculation of the size of perturbation. The appropriate magnitude of the perturbation is treated as an exponential decay function with its maximum at the middle step of the trajectory. In these moves, a perturbation is generated from a Boltzmann distribution then scaled such that its norm is equal to $|\delta p|_{opt}$, calculated using Eq. (8.6). This perturbation is added to the momenta at the shooting point, which is then rescaled to conserve the total energy, as in the normal path sampling procedure.

$$|\delta p|_{opt} = A \cdot \exp\left(-b \cdot |t_{SP} - t_{mid}|\right) \tag{8.6}$$

For our model system, constants A = 0.55 and b = 0.061 resulted in a nearly constant acceptance probability of 40% for shooting points up to 1000 time steps from the t_{mid} (Figure 8.5). In general, these parameters can be determined using two calibration path sampling simulations where the shooting points are selected from narrow ranges of time steps from the transition region and the appropriate perturbation size for an acceptance probability of 40% is determined for each window. Constants A and b can then be fit to match the appropriate perturbation size for both of these windows.

As in the centering-shooting algorithm, the shooting moves are now dependent on the identification of the 'middle' time step (t_{mid}). As such, this varied perturbation size shooting algorithm can be combined with the centering-shooting algorithm trivially. Nevertheless, the varied perturbation size shooting moves can also be applied in conjunction with the shifting moves of a traditional path sampling simulation without using centering-shooting moves.

To test this method, we sampled 10^5 trajectories using varied perturbation size shooting moves with the traditional shifting moves. The distribution of V_{top} is statistically equivalent the distribution sampled with the constant perturbation shooting moves, ($\overline{V}_{top}$=35.6 ± 3.2 ϵ); however, the distribution of T_{tr} was slightly biased towards shorter transition times and a more narrow distribution ($\overline{T}_{tr}$=125.9 ± 30.9 time steps for the varied perturbation size method *vs* $\overline{T}_{tr}$=126.5 ± 32.1 time steps for the constant perturbation method). This bias is apparent in the histogram of this distribution, presented in Figure 8.7.

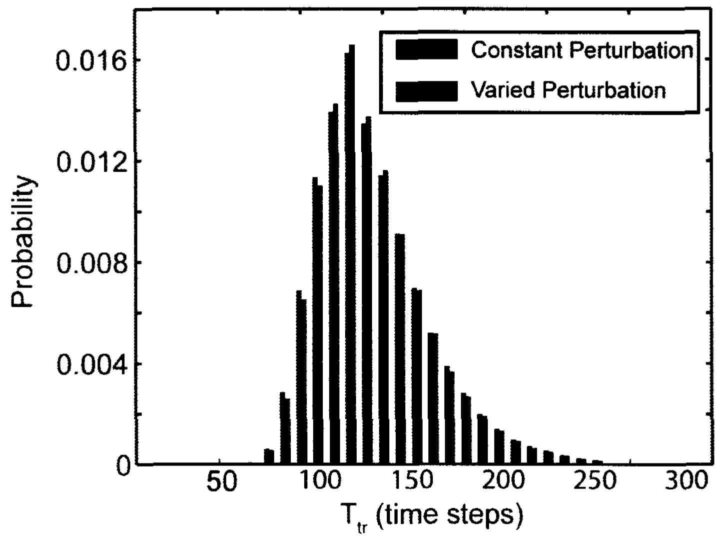

Figure 8.7. Histogram of the distribution of T_{tr} for a transition path ensemble of 10^5 trajectories sampled using shooting moves with a constant perturbation size (red) and varied perturbation sizes (blue).

We attribute the bias in the T_{tr} distribution to a small violation of detailed balance in the varied perturbation size shooting moves. In the original formulation, shooting moves were shown to satisfy microscopic reversibility because the generation probability of the forward and reverse generation of a trajectory was symmetric. Simply, the probability of generating a new trajectory by randomly selecting a time step and the perturbation to the momenta is equal to the probability of making a shooting move from the new trajectory that generates the old trajectory by selecting the same time step and opposite perturbation. The varied perturbation size shooting move we propose here violates this symmetry in generation probabilities because the t_{mid} varies between shooting moves; even if the same shooting point is selected, the magnitude of the perturbation will vary.

The correlation function $<h_B(x_t)>$ is essential for calculating rate constants using TPS and is closely related to the distribution of T_{tr}. To test whether the bias in T_{tr}

strongly affects this function, we have calculated <$h_B(x_t)$> *vs* t for this system with the traditional, constant sized perturbation shooting moves and the varied perturbation size shooting moves we present here. For this purpose, we used the acceptance criteria defined by Dellago et al.,[8] whereby a trajectory is accepted if $h_A(x_0)=1$ and if the trajectory crosses into B at any point between $0 \leq t \leq L$, defined as $H_B(x_0,L) = 1$ (Eq. (8.7)). To generate <$h_B(x_t)$>, 10^5 trajectories were sampled through shooting moves, where each shooting iteration was followed by 200 attempted shifting moves, following the procedure in Ref. 8. The agreement between the constant perturbation size method and the varied perturbation size method is good (Figure 8.8), with only a minor deviation between the two methods, indicating this method could be used in TPS rate constant calculations despite the bias.

$$H_B(x_0,L) \equiv \max_{0\leq t\leq L} h_B(x_t) \tag{8.7}$$

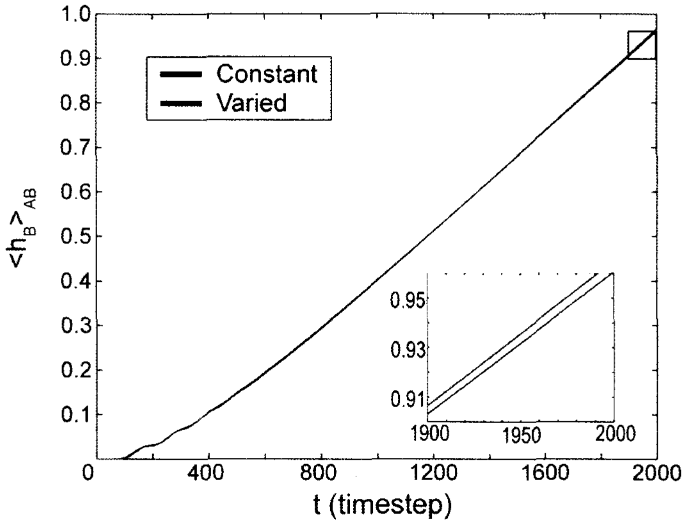

Figure 8.8. Comparison of a traditional, constant perturbation TPS simulation and a varied perturbation size simulation for the correlation function $<h_B(x_t)>_{AB}$.

8.5. Microscopically Reversible Varied Perturbation Size Shooting Algorithm

To correct the bias in the varied perturbation size shooting algorithm we proposed in Section 8.4, we have also developed an alternative varied perturbation size method which satisfies microscopic reversibility. Instead of using the optimal perturbation size calculated using Eq. (8.6), we draw the perturbation size, $|\delta p|$, from a normal distribution with a maximum at this optimal perturbation size, $|\delta p|_{opt}$, determined using Eq. (8.8).

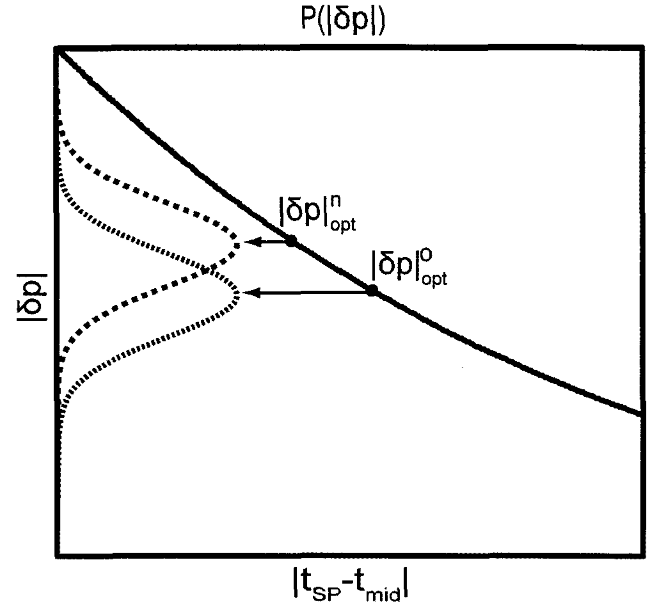

Figure 8.9. Schematic of the perturbation size calculation for the microscopically-reversible varied perturbation shooting move. The solid line shows the optimal perturbation size, $|\delta p|_{opt}$, as a function of the number of time steps between the shooting point and the middle step, $|t_{SP}-t_{mid}|$, (bottom axis) with optimal perturbations size calculated for a hypothetical old and new trajectory (superscripts o and n, respectively). The probability distributions (top axis) of the perturbation size for these optimal perturbations are plotted as dashed lines.

$$P_{pert}\left(|\delta p|\right)=\frac{1}{\sigma\sqrt{2\pi}}\exp\left(\frac{-\left(|\delta p|-|\delta p|_{opt}\right)^2}{2\sigma^2}\right) \tag{8.8}$$

A schematic of this method is presented in Figure 8.9. To maintain detailed balance with the varied perturbation shooting algorithm, the acceptance probability must be modified according to:

$$P_{acc}^{o\to n}=\min\left[1,h_A\left(x_0^n\right)H_B\left(x_0^n\right)\exp\left(\frac{2|\delta p|\left(|\delta p|^n_{opt}-|\delta p|^o_{opt}\right)+\left(|\delta p|^o_{opt}\right)^2-\left(|\delta p|^n_{opt}\right)^2}{2\sigma^2}\right)\right] \tag{8.9}$$

where $|\delta p|_{opt}^{o}$ and $|\delta p|_{opt}^{n}$ are the optimal perturbation sizes for the shooting point in the old and new trajectories, respectively. (Details of the derivation of the acceptance probability are given in Supplementary Section 8.8) We have run a 10^5 trajectory path sampling simulation using this method using a perturbation-size standard deviation of $\sigma = 0.005$. The method generates distributions of V_{top} and T_{tr} that are in close agreement with the standard path sampling method ($\overline{V}_{top}$ =35.6 ± 3.2 ϵ, $\overline{T}_{tr}$ = 126.3 ± 31.5 time steps). Significantly, the bias in the distribution of T_{tr} is eliminated and the distribution now matches that of a traditional, constant perturbation path sampling simulation within statistical error, as depicted in Figure 8.10.

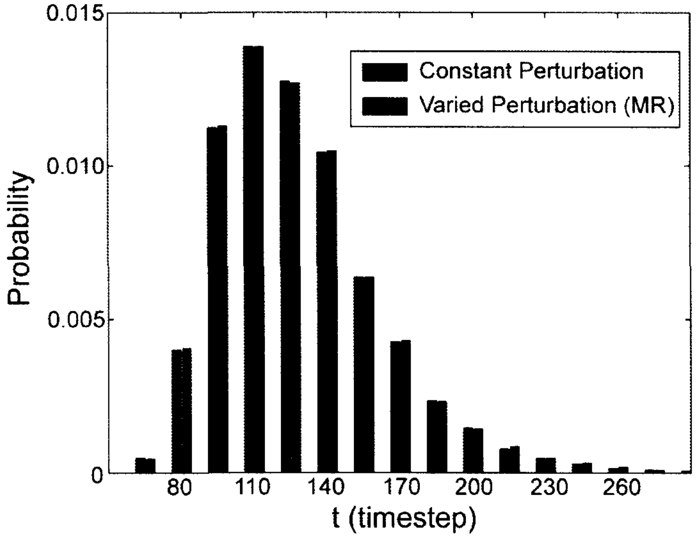

Figure 8.10. Histograms of transition time (T_{tr}) distribution for a transition path ensemble of 10^5 trajectories sampled using constant perturbation shooting moves and microscopically reversible varied perturbation size shooting moves.

8.6. Sampling Efficiency

To determine whether the varied perturbation size methods sample the transition path ensemble more efficiently than the traditional constant-perturbation shooting moves, we calculated the autocorrelation functions of V_{top} and T_{tr} as a function of the number of shooting iterations, including rejected attempts. The simulation perturbation sizes were adjusted so that the acceptance rate of the shooting moves was approximately 35% in each instance for an ensemble of 10^5 trajectories. For a quantity A, these autocorrelation functions are defined as,

$$c_A(n) \equiv \frac{\langle \delta A(0)\delta A(n)\rangle_{AB}}{\langle \delta A^2\rangle_{AB}} \tag{8.10}$$

where $\delta A(n) \equiv A(n) - \langle A(n)\rangle_{AB}$. The correlation functions we present are calculated form all possible starting points in the ensemble, such that the origin is shifted across the ensemble. The autocorrelation functions of both V_{top} and T_{tr} shows a significantly faster decay when varied perturbation size shooting moves are used in comparison to the traditional path sampling simulation (Figure 8.11). The autocorrelation function of V_{top} reaches a value of 10^{-1} after 200 iterations of the constant perturbation size shooting moves but drops to 10^{-2} after the same number of iterations when the varied perturbation size shooting moves are used. The autocorrelation function of T_{tr} shows a similar trend, with distinctively faster decorrelation when the varied perturbation size algorithm is used. This improved decorrelation can be attributed to the larger perturbations made at shooting points close to the transition period and a greater acceptance of trajectories generated from shooting points far from the transition period. As the additional computational cost of the calculation of the perturbation size is negligible, the computational cost of each varied perturbation size shooting move is essentially the same as a regular shooting move.

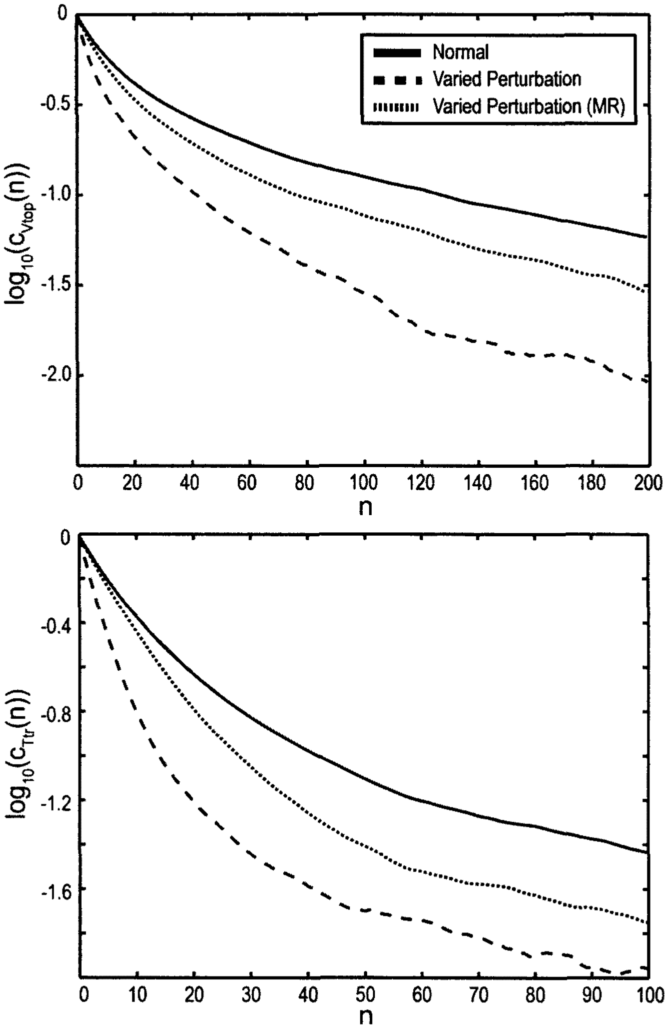

Figure 8.11. Logarithm of correlation functions as a function of the shooting move iteration, n, for properties V_{top} (top and T_{tr} (bottom) for 10^5 trajectory simulations with constant perturbation size shooting moves (solid), varied perturbation size shooting moves (dashed), and microscopically reversible varied perturbation size shooting moves (dotted).

The microscopically reversible variant of the varied perturbation size shooting move shows slower decorrelation that our original varied perturbation algorithm. We attribute this decrease in efficiency compared to the original varied perturbation size algorithm to several causes. Firstly, although we use a fairly narrow distribution, the perturbation size chosen from the distribution may be smaller or larger than the optimal perturbation size, eliminating some of the efficiency gained by the variable perturbation size. Secondly, not all reactive trajectories are now accepted due to the modified acceptance probability of Eq. (8.9) that is dependent on the difference in the optimal perturbation size, $|\delta p|_{opt}$, between the new and old trajectories. Due to the rejections resulting from this term, the optimal varied perturbation size parameter was adjusted to A = 0.25 from A = 0.55 to maintain an overall acceptance rate of 35%. With these parameters, approximately 29% of reactive trajectories are rejected by the perturbation size factor. This significant rejection rate due to the perturbation size is particularly problematic because the trajectories are more likely to be rejected if $|\delta p|_{opt}^{o}$ and $|\delta p|_{opt}^{n}$ are substantially different, indicative of highly decorrelated trajectories where the t_{mid} point has moved significantly between the old and new trajectories.

To further quantify the improvement in sampling that occurs when a varied perturbation size is used, we have calculated the statistical inefficiency of path sampling simulations with constant and varied perturbation sizes for the distributions of V_{top} and T_{tr}. The statistical inefficiency was calculated using block averaging,[59] where the ensemble is divided into blocks of n successive steps. As the block size becomes larger, their averages become statistically independent estimates of full ensemble average. Freudberg and Cameron define the statistical inefficiency (τ) as the limiting ratio of the variance of the block means calculated using a block of size n and the variance of the entire ensemble (Eq. (8.11)).[60] This inefficiency can be interpreted as the factor by which the sampling should be increased to compensate for the correlation between successive values in the ensemble.

$$\tau = \lim_{n\to\infty}\left[\frac{n\sigma_n^2}{\sigma_1^2}\right] \quad (8.11)$$

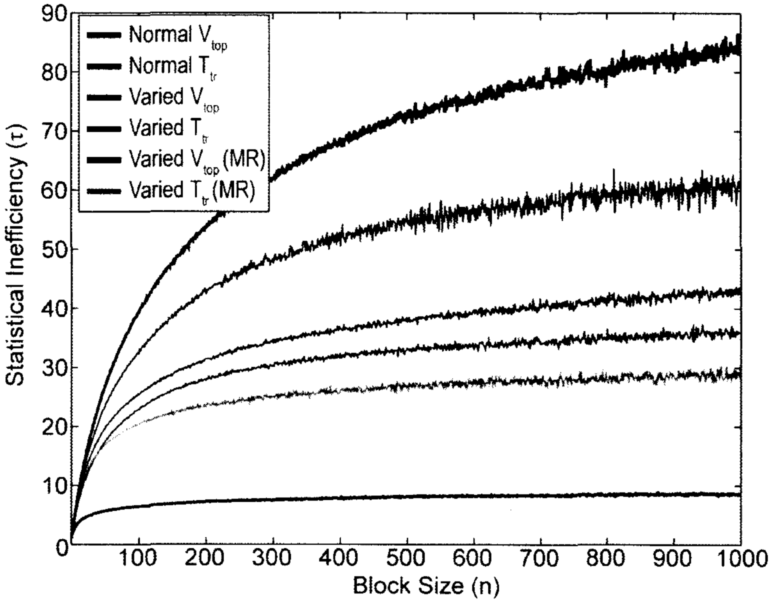

Figure 8.12. Statistical inefficiency of path sampling simulations for V_{top} and T_{tr} distributions using the constant perturbation size method, the varied perturbation size method, and the microscopically reversible varied perturbation size method.

For the path sampling simulation with a constant perturbation size, the statistical inefficiency of V_{top} converges to a value of approximately 90 (Figure 8.12). When a varied perturbation size is used, τ converges to 35, indicating that the varied perturbation size increases the efficiency by a factor of 2.5. Similarly, the statistical inefficiency of the sampling of T_{tr} converges to value of approximately 40 for constant perturbation size shooting moves, but drops to 8 when a varied perturbation size is used, indicating that the efficiency is improved by factor of 5. This is consistent with the results of the autocorrelation function, which showed significantly improved efficiency for the varied perturbation size shooting moves.

The microscopically reversible variant of the varied perturbation size shooting algorithm we describe in Section 8.5 has a significantly different statistical inefficiency than our original varied perturbation size shooting algorithm. The plot of the statistical inefficiency of both V_{top} and T_{tr} in Figure 8.12 shows that the microscopically reversible algorithm is significantly more statistically inefficient than the original varied perturbation size method, but is still less inefficient than the constant perturbation size algorithm. Specifically, the statistical inefficiency of the microscopically reversible method was found to be $\tau = 60$ and $\tau = 30$ for V_{top} and T_{tr}, respectively, which compares to $\tau = 35$ (V_{top}) and $\tau = 8$ (T_{tr}) for our original varied perturbation size method and $\tau = 90$ (V_{top}) and $\tau = 40$ (T_{tr}) for the constant perturbation size method.

This analysis demonstrates that the use of a varied perturbation size can significantly improve the efficiency of a transition path sampling simulation. As the varied perturbation size method we propose in Section 8.4 is significantly more efficient and generates only slightly biased distributions, we recommend the use of that method over the microscopically reversible method. It is possible that judicious variation of the simulation parameters or the type of distribution used to generate the perturbation sizes could improve the efficiency of the microscopically reversible method.

8.7. Conclusions

We have devised and evaluated three novel TPS trajectory generation moves. The centering-shooting move incorporates a shifting move into a shooting move such that the transition period occurs near the middle time step of the trajectory. While this biases the location of the transition period, the distributions of ensemble properties V_{top}

and T_{tr} match those generated with a conventional TPS simulation. This sampling procedure eliminates the need for shifting moves, which simplifies both the path sampling procedure and analysis of the trajectory ensemble if one is only interested in characterizing the transition paths. However, if one is interested in rate constant calculations, the centering-shooting moves cannot be used as the $<h_B(t)>$ correlation function will not be sampled properly.

The second move we have proposed is varied perturbation size shooting moves. In the original definition of shooting moves, the size of the perturbation made at a shooting point is constant, although shooting moves made further from the transition period have a much lower acceptance probability. We have found that it is possible to vary the perturbation size so that the acceptance probability is approximately constant for all shooting points by defining the perturbation size as an exponential decay with respect to the number of steps between the shooting point and the transition period. Correlation function and block average analysis of V_{top} and T_{tr} show that the sampling is 2.5–5 times more efficient when a varied perturbation size is used. This method can be easily implemented into existing path sampling codes and the additional computational cost is negligible.

A small bias was introduced into the distribution of the transition times sampled using the varied perturbation size shooting moves due to the violation of detailed balance in generating perturbations. We have developed an alternative varied perturbation size method where the perturbation is drawn from a Gaussian distribution centered at the optimal perturbation size for that shooting point. This introduces an additional acceptance criterion which restores detailed balance. Although this corrects the small bias in the transition times, the statistical efficiency is significantly poorer than for our original varied perturbation size method. Nevertheless, the microscopically reversible varied perturbation shooting algorithm remains more statistically efficient than the constant perturbation size method, suggesting that further development this method could be worthwhile.

8.8. Supplementary Section: Derivation of the Acceptance Probability of the Microscopically Reversible Varied Perturbation Size Shooting Algorithm

The derivation of the acceptance probability of the microscopically reversible varied perturbation size shooting algorithm (Eq. (8.9)) described in Section 8.5 follows the derivation of the acceptance probability of deterministic microcanonical TPS by Bolhuis et al.[61] The distribution function, $\rho_{MC}(x_0)$, for the microcanonical ensemble is a delta function of the Hamiltonian, H at the phase space coordinate, x, and the total energy, E, normalized by the partition function, Q_{MC}.

$$\rho_{MC}(x)=\frac{\delta\left[\mathrm{H}(x)-E\right]}{Q_{MC}} \tag{8.12}$$

The distribution function for the trajectories connecting states A and B with time T for this ensemble can be simplified to depend only on the phase space coordinates of the first step the trajectory, x_0.

$$f_{AB}(x_0)\equiv\frac{\rho_{MC}(x_0)h_A(x_0)H_B(x_0)}{\int\rho(x_0)h_A(x_0)H_B(x_0)dx_0} \tag{8.13}$$

As such, the detailed balance criterion for the generation of a new trajectory is,

$$f_{AB}\left(x_0^o\right)P_{gen}^{o\to n}P_{acc}^{o\to n} = f_{AB}\left(x_0^n\right)P_{gen}^{n\to o}P_{acc}^{n\to o} \tag{8.14}$$

where P_{gen} is the probability of generating a new trajectory and P_{acc} is the probability of accepting a trajectory. Acceptance of trajectories is now done according to the Metropolis criterion,

$$P_{acc}^{o\to n} = \min\left[1, \frac{f_{AB}\left(x_0^n\right)P_{gen}^{n\to o}}{f_{AB}\left(x_0^o\right)P_{gen}^{o\to n}}\right] \tag{8.15}$$

As shooting moves are performed in such a way that total energy is conserved, the microcanonical distribution function simplifies to a test of whether or not the new trajectory is reactive *via* the characteristic functions,

$$P_{acc}^{o\to n} = \min\left[1, h_A\left(x_0^n\right)H_B\left(x_0^n\right)\frac{P_{gen}^{n\to o}}{P_{gen}^{o\to n}}\right] \tag{8.16}$$

The shooting point is selected at random and the trajectory generation is symmetric aside from the magnitude of the perturbation, so the generation probability is equivalent to the distribution we defined for the perturbation size distribution of the trajectory (Eq. (8.9)).

$$P_{acc}^{o\to n} = \min\left[1, h_A\left(x_0^n\right)H_B\left(x_0^n\right)\frac{P_{pert}^{n}\left(\left|\delta p\right|\right)}{P_{pert}^{o}\left(\left|\delta p\right|\right)}\right] \tag{8.17}$$

Expansion and simplification of $P_{pert}\left(\left|\delta p\right|\right)$ yields an acceptance probability dependent on the perturbation size chosen, $\left|\delta p\right|$, and the optimal perturbation size for that shooting point in the old and new trajectories,

$$P_{acc}^{o\rightarrow n} = \min\left[1, h_A\left(x_0^n\right) H_B\left(x_0^n\right) \exp\left(\frac{2|\delta p|\left(|\delta p|_{opt}^{n} - |\delta p|_{opt}^{o}\right) + \left(|\delta p|_{opt}^{o}\right)^2 - \left(|\delta p|_{opt}^{n}\right)^2}{2\sigma^2}\right)\right] \tag{8.18}$$

References

1. Chandler, D. In *Computer Simulation of Rare Events and Dynamics of Classical and Quantum Condensed-Phase Systems – Classical and Quantum Dynamics in Condensed Phase Simulations*; Berne, B. J., Ciccotti, G., Coker, D. F., Eds.; World Scientific: Singapore, 1998, p 51.

2. Dellago, C.; Bolhuis, P. G.; Chandler, D. *J. Chem. Phys.* **1998**, *108*, 9236.

3. Bolhuis, P. G.; Dellago, C.; Geissler, P. L.; Chandler, D. *J. Phys.: Condens. Matter* **2000**, *12*, A147.

4. Dellago, C.; Bolhuis, P. G.; Geissler, P. L. *Adv. Chem. Phys.* **2002**, *123*, 1.

5. Dellago, C.; Bolhuis, P. G. In *Advanced Computer Simulation Approaches for Soft Matter Sciences III,*; Springer: Berlin / Heidelberg, 2008; Vol. 221, p 167.

6. Hu, J.; Ma, A.; Dinner, A. R. *J. Chem. Phys.* **2006**, *125*, 114101/1.

7. Rowley, C. N.; Woo, T. K. *J. Chem. Phys.* **2007**, *126*, 024110/1.

8. Dellago, C.; Bolhuis, P. G.; Chandler, D. *J. Chem. Phys.* **1999**, *110*, 6617.

9. Allen, M. P.; Tildesley, D. J. *Computer Simulation of Liquids*; Clarendon: Oxford, 1987.

10. Bolhuis, P. G. *J. Phys.: Condens. Matter* **2003**, *15*, S113.

11. Andersen, H. C. *J. Chem. Phys.* **1980**, *72*, 2384.

12. Grunwald, M.; Dellago, C.; Geissler Phillip, L. *J. Chem. Phys.* **2008**, *129*, 194101.

13. Peters, B.; Trout, B. L. *J. Chem. Phys.* **2006**, *125*, 054108/1.

14. Peters, B.; Beckham, G. T.; Trout, B. L. *J. Chem. Phys.* **2007**, *127*, 034109.

15. Zahn, D. *J. Solid State Chem.* **2004**, *177*, 3590.

16. Bolhuis, P. G.; Dellago, C.; Chandler, D. *Proc. Natl. Acad. Sci. USA* **2000**, *97*, 5877.

17. Geissler, P. L.; Dellago, C.; Chandler, D. *J. Phys. Chem. B* **1999**, *103*, 3706.

18. Jorge, R.; Manuel, L. *J. Chem. Phys.* **2001**, *115*, 7285.

19. Vlugt, T. J. H.; Dellago, C.; Smit, B. *J. Chem. Phys.* **2000**, *113*, 8791.

20. ten Wolde, P. R.; Chandler, D. *Proc. Natl. Acad. Sci. USA* **2002**, *99*, 6539.

21. Bolhuis, P. G. *Proc. Natl. Acad. Sci. USA* **2003**, *100*, 12129.

22. Marti, J. *J. Phys.: Condens. Matter* **2004**, *16*, 5669.

23. Marti, J.; Csajka, F. S. *Phys. Rev. E: Stat. Nonlin. Soft Matter Phys.* **2004**, *69*, 061918/1.

24. Best, R. B.; Hummer, G. *Proc. Natl. Acad. Sci. USA* **2005**, *102*, 6732.

25. Bolhuis, P. G. *Biophys. J.* **2005**, *88*, 50.

26. Jang, H.; Woolf, T. B. *J. Comput. Chem.* **2006**, *27*, 1136.

27. Juraszek, J.; Bolhuis, P. G. *Proc. Natl. Acad. Sci. USA* **2006**, *103*, 15859.

28. Borrero, E. E.; Escobedo, F. A. *J. Chem. Phys.* **2007**, *127*, 164101/1.

29. Dellago, C.; Bolhuis, P. G. *Transition Path Sampling Simulations of Biological Systems*; Springer: Berlin / Heidelberg, 2007; Vol. 268.

30. Jimenez, A.; Crehuet, R. *Theor. Chem. Acc.* **2007**, *118*, 769.

31. Ma, L.; Cui, Q. *J. Am. Chem. Soc.* **2007**, *129*, 10261.

32. Chopra, M.; Reddy, A. S.; Abbott, N. L.; de Pablo, J. J. *J. Chem. Phys.* **2008**, *129*, 135102/1.

33. Juraszek, J.; Bolhuis, P. G. *Biophys. J.* **2008**, *95*, 4246.

34. Laria, D.; Rodriguez, J.; Dellago, C.; Chandler, D. *J. Phys. Chem. A* **2001**, *105*, 2646.

35. Leoni, S.; Zahn, D. *Z. Kristallogr.* **2004**, *219*, 339.

36. Zahn, D.; Leoni, S. *Z. Kristallogr.* **2004**, *219*, 345.

37. Zahn, D.; Leoni, S. *Phys. Rev. Lett.* **2004**, *92*, 250201.

38. Zahn, D.; Grin, Y.; Leoni, S. *Phys. Rev. B* **2005**, *72*, 064110/1.

39. Zahn, D.; Hochrein, O.; Leoni, S. *Phys. Rev. B* **2005**, *72*, 094106/1.

40. Grunwald, M.; Rabani, E.; Dellago, C. *Phys. Rev. Lett.* **2006**, *96*, 255701.

41. Zahn, D.; Leoni, S. *J. Phys. Chem. B* **2006**, *110*, 10873.

42. Boulfelfel, S. E.; Zahn, D.; Hochrein, O.; Grin, Y.; Leoni, S. *Phys. Rev. B* **2006**, *74*, 094106/1.

43. Zahn, D. *J. Chem. Phys.* **2008**, *128*, 184707.

44. Geissler, P. L.; Dellago, C.; Chandler, D. *Phys. Chem. Chem. Phys.* **1999**, *1*, 1317.

45. Geissler, P. L.; Dellago, C.; Chandler, D.; Hutter, J.; Parrinello, M. *Science* **2001**, *291*, 2121.

46. Zahn, D.; Seifert, G. *J. Phys. Chem. B* **2004**, *108*, 16495.

47. Crehuet, R.; Field, M. J. *J. Phys. Chem. B* **2007**, *111*, 5708.

48. Basner, J. E.; Schwartz, S. D. *J. Am. Chem. Soc.* **2005**, *127*, 13822.

49. Snee, P. T.; Shanoski, J.; Harris, C. B. *J. Am. Chem. Soc.* **2005**, *127*, 1286.

50. Bergeron, D. E.; Coskuner, O.; Hudgens, J. W.; Gonzalez, C. A. *J. Phys. Chem. C* **2008**, *112*, 12808.

51. Rowley, C. N.; Woo, T. K. *Organometallics* **2008**, *27*, 6405.

52. Rowley, C. N.; Woo, T. K. *J. Am. Chem. Soc.* **2008**, *130*, 7218.

53. Zahn, D. *J. Chem. Theory Comput.* **2006**, *2*, 107.

54. Straub, J. E.; Borkovec, M.; Berne, B. J. *J. Chem. Phys.* **1988**, *89*, 4833.

55. Weeks, J. D.; Chandler, D.; Andersen, H. C. *J. Chem. Phys.* **1971**, *54*, 5237.

56. Moroni, D.; Bolhuis, P. G.; van Erp, T. S. *J. Chem. Phys.* **2004**, *120*, 4055.

57. Swope, W. C.; Andersen, H. C.; Berens, P. H.; Wilson, K. R. *J. Chem. Phys.* **1981**, *76*, 637.

58. Bolhuis, P. G. *J. Chem. Phys.* **2008**, *129*, 114108.

59. Fincham, D.; Quirke, N.; Tildesley, D. J. *J. Chem. Phys.* **1986**, *84*, 4535.

60. Friedberg, R.; Cameron, J. E. *J. Chem. Phys.* **1970**, *52*, 6049.

61. Bolhuis, P. G.; Dellago, C.; Chandler, D. *Faraday Discuss.* **1998**, *110*, 421.

CHAPTER 9

Summary and Outlook

Throughout this thesis, we have attempted to go beyond the standard techniques for modelling organometallic chemistry using QC methods. In Chapters 3 and 5, we demonstrated the ability of static QC calculations to explore complex organometallic catalytic cycles by elucidating the mechanism of the Ru–hydride catalyzed H_2-hydrogenation of olefins and then designing a new catalyst based on our results. These studies also serve to highlight the limitations of these methods, as only optimized structures were examined and it was necessary to employ the harmonic oscillator approximation to calculate the reaction free energy profiles. This illustrates the potential benefits of using MD to characterize organometallic reaction mechanisms more thoroughly.

Straightforward MD simulations cannot be used to study most chemical reactions, as the system will only cross the reaction barrier after an impractically long simulation. This is a fundamental problem in molecular simulation known as the rare event problem. TPS is an exciting new tool for overcoming this problem; however, it was necessary to develop methods to generate the initial trajectory for these simulations, which is particularly challenging for AIMD simulations. In Chapter 2, we proposed several methods for generating these initial trajectories, including orbital-biased dynamics and high temperature simulations, although initiating an MD simulation from the potential-energy TS is a simple and effective solution. We used this technique successfully in both of our TPS simulations of organometallic reactions (Chapters 4 and 6). This issue is not completely resolved, as it may not be practical to identify a potential-energy TS in some complex organometallic reactions. In these instances, it may be necessary to use a more sophisticated technique, such the bias annealing method of Hu and Dinner[1] or metadynamics.[2]

TPS allowed us to study the unbiased dynamics of two important organometallic reactions: the Ru-hydride catalyzed H_2-hydrogenation of ethylene and β-hydrogen transfer in a model zirconocene olefin polymerization catalyst. These simulations revealed surprising features about the structures, bonding, intermediate lifetime, and fluctuations associated with these reactions. MD was essential for identifying these features, as they could not be determined directly from the reaction PES.

The TPS simulations on the Ru–hydride olefin insertion reported in Chapter 4 represent an interesting new method to study apparent non-RRKM effects in unimolecular reactions. The Ru(IV)–dihydride formed from the ethylene insertion step of this reaction had a much shorter lifetime than was predicted using classical RRKM theory due to a localization of vibrational energy in the $Ru(H)_2$ bending modes. By performing a TPS simulation on the step immediately preceding unimolecular decay, we generated more realistic vibrational energy distributions, where vibrational energy was localized in reactive vibrational modes, as opposed to the random distributions assumed in RRKM theory. Based on its success in this example, TPS has excellent potential for studying non-RRKM effects chemical reactions, as well as other dynamic rate effects, such as barrier recrossing.

Our AIMD simulations of the β-hydrogen transfer reaction, presented in Chapter 6, focused on the structures and dynamics of this reaction. Although equilibrium MD was effective for modelling the configurational freedom of the reactant complex and the facile in-place methyl rotation, TPS was needed to model the β-hydrogen transfer reaction. In this instance, the analysis of the transition path ensemble showed that trajectories could cross the barrier at a wide range of structures. This highlights a second deficiency of static calculations, in that only minimum-energy structures are considered, despite the large degree of configurational freedom found in some organometallic complexes. Bonding analysis of selected TPE trajectories also showed a surprising deviation from the static results. The Zr–H bonding at the transition state was found to be systematically greater in the dynamic simulations than in the static structures. The use of bonding analysis in conjunction with AIMD is an exciting avenue for research in the future.

Chapter 7 represents the most sophisticated modelling of this thesis. Using a QM/MM model, we incorporated the effects a borate counteranion on the olefin-complex of a zirconocene polymerization catalyst. The bare-cation and borate ion pair were simulated using MD in an explicit pentane solvent using periodic boundary conditions. Even in this complex, where the electronic structure is surprisingly impervious to the effect of the counteranion, there was a sizeable energetic preference for an ion pair orientation with the most favourable interaction between the dipole of zirconocene and the counteranion. This dipole-counteranion interaction induces an isomerization of the zirconocene alkyl ligand to an α-agostic configuration instead of the β-agostic configuration that is preferred in the cation-only complex. AIMD is well-suited for modelling the solution dynamics of organometallic ion pairs, as these structures have a significant freedom of movement and are difficult to represent using MM force fields. Inorganic complexes with a more polar ligand structure or occupied polarizable d-orbitals could show a more pronounced counteranion influence and are exciting subjects for AIMD simulations in the future.

While the equilibrium dynamics simulations of Chapter 7 and the reaction dynamics of the β-transfer reaction that were modelled using TPS in Chapter 6 are descriptively useful, we also wanted to demonstrate the ability of AIMD as a means to quantitatively determine activation free energies. In the second part of Chapter 7, we used Weighted Histogram Analysis Method (WHAM) in conjunction with AIMD to calculate the PMF of the β-hydrogen transfer reaction. Although computationally demanding, this method provides a rigorous alternative to the use of the harmonic approximation to calculate free energies. The vibrational entropy of activation calculated using the harmonic oscillator approximation was much smaller than the vibrational entropy of activation estimated from the PMF, suggesting that static calculations of absolute free energies of activation could be significantly in error in some organometallic reactions.

Despite the success of these simulations, there are significant issues to be resolved in further research. The TPS simulations of Ru-catalyzed hydrogenation and the β-hydrogen transfer each took several months to generate a sufficient number of distinct trajectories (150 and 350, respectively) to perform a quantitative analysis of this ensemble. The statistical inefficiency of transition path sampling is also a major problem, as conventional shooting moves generate strongly correlated trajectories. The varied perturbation shooting algorithm we propose in Chapter 8 provides a significant improvement to the sampling efficiency and further development of trajectory generation algorithms could make it more practical to generate a representative ensemble.

More broadly, the inherent computational cost of AIMD simulations remains a major obstacle to their more widespread use. Both the AIMD TPS simulations and PMF calculations we presented in this thesis required months of computation to yield quantitative results. In contrast, static modelling of a reaction mechanism can be completed within weeks. Although the time and computational cost of these AIMD simulations is justifiable if the static calculations fail to provide a complete model of the reaction mechanism, these simulations are currently too expensive to be used for routine modelling. Furthermore, our AIMD simulations were restricted to moderate-sized catalysts (17 and 34 atoms for the Ru hydrogenation catalyst and Zr polymerization catalysts, respectively); larger catalysts that cannot be approximated with QM/MM methods will be even more computationally demanding. Continued improvements in computer hardware will make it possible to run these simulations within shorter time frames; however, the full DFT energy and gradient evaluation at each time step is intrinsically computationally demanding. Tight-binding DFT[3] could help resolve this issue, as these recently-developed methods have a much lower computational cost than traditional DFT and have been moderately successful in modelling some transition metal containing complexes.[4]

A final aspect of organometallic reaction dynamics that would benefit from further research is nuclear-quantum effects, such as zero-point energy and the quantization of vibrational energy. Throughout this thesis, these effects were neglected due to our use of Born-Oppenheimer MD. This approximation is especially significant for reactions where bonds involving hydrogen are broken or formed, which is common in homogenous catalysis. Path-integral methods[5] can be used to correct for these nuclear-quantum effects within the framework of MD and could be particularly useful in modelling organometallic complexes where nuclear quantum effects are known to be significant, such as β-agostic and nonclassical dihydrogen complexes.[6,7]

Computer modelling is already an integral component of research in organometallic catalysis, a role that is likely to grow further in the coming years. Realistic models of increasingly sophisticated catalysts will require the computational organometallic research community to move beyond the standard approximations used in static QC studies. The TPS simulations and PMF calculations presented in this thesis provide powerful tools to model the reaction dynamics and free energy profiles of organometallic reactions in a rigorous but practical manner.

References

1. Hu, J.; Ma, A.; Dinner, A. R. *J. Chem. Phys.* **2006**, *125*, 114101.
2. Park, J. M.; Laio, A.; Iannuzzi, M.; Parrinello, M. *J. Am. Chem. Soc.* **2006**, *128*, 11318.
3. Elstner, M. *Theor. Chem. Acc.* **2006**, *116*, 316.
4. Zheng, G.; Witek, H. A.; Bobadova-Parvanova, P.; Irle, S.; Musaev, D. G.; Prabhakar, R.; Morokuma, K.; Lundberg, M.; Elstner, M.; Kohler, C.; Frauenheim, T. *J. Chem. Theory Comput.* **2007**, *3*, 1349.
5. Marx, D.; Tuckerman, M. E.; Martyna, G. J. *Comput. Phys. Commun.* **1999**, *118*, 166.
6. Crabtree, R. H. *The Organometallic Chemistry of the Transition Metals*; 4th ed.; John Wiley and Sons, Inc.: Hoboken, NJ, 2005.
7. *Metal Dihydrogen and σ-Bond Complexes*; Kubas, G. J., Ed.; Kluwer: New York, 2001.

APPENDIX A

Molecular Simulation Algorithms

A.1. Equations of Motion for Molecular Dynamics

The molecular dynamics (MD) simulations are one of the most powerful tools used in molecular modelling, they allows the microscopic motion of a chemical system to be modeled. To perform an MD simulation, the classical equations of motion must be solved for the set of N particles subject to the forces acting on these particles (f).

$$m\frac{d^2r}{dt^2}=f \tag{A.1}$$

Newton's second law (Eq. (A.1)) provides the basic relation that can be used to derive a solution to these equations of motion. In this equation, r is a vector of all the positions of the particles, m is the particle masses, and f is the forces on the particles. The force on a particle is equal to the negative of the gradient of the potential with respect to the position of the particle (Eq. (A.2)).

$$f=-\nabla_r U \tag{A.2}$$

For some simple two-body systems such as the harmonic oscillator or a particle moving in a field, the equations of motion can be solved analytically, yielding an expression which gives the positions and velocities of the particles at any point in time. MD simulations of more complex, many-body systems require the application of a finite-difference method, where the positions of the particles are propagated through time through a sequence of time steps with a length denoted δt.

One of the most popular MD propagation methods is the Verlet algorithm.[1] This algorithm is derived by expressing the position of a particle one time step later in time using a Taylor series expansion of the position of the particles, r, about time t. In this instance, the Taylor series expansion is terminated at the second derivatives of the positions and time,

$$r(t+\delta t)=r(t)+v(t)\delta t+\frac{1}{2}a(t)(\delta t)^2+\Theta\left((\delta t)^3\right) \tag{A.3}$$

Likewise, an expression can be written for the positions one time step earlier in time,

$$r(t-\delta t)=r(t)-v(t)\delta t+\frac{1}{2}a(t)(\delta t)^2+\Theta\left((\delta t)^3\right) \tag{A.4}$$

By neglecting higher order terms in Eq. (A.4) we can create expression for the velocities in terms of the positions at the current and previous time steps, as well as the accelerations at the current time step,

$$v(t)=\frac{r(t)-r(t-\delta t)+\frac{1}{2}a(t)(\delta t)^2}{\delta t} \tag{A.5}$$

Substitution of the Eq. (A.5) for the velocity term in Eq. (A.3) yields the Verlet equation for the positions of the particles,

$$r(t+\delta t)=2r(t)-r(t-\delta t)+a(t)(\delta t)^2 \tag{A.6}$$

Note that this expression for the positions at the next time step depends only on the positions at the current and immediately previous time step, as well as the accelerations at the current time step. It is not necessary to compute the particle velocities in this algorithm, although these can be calculated after the fact using the mean value theory,

$$v(t)=\frac{r(t+\delta t)-r(t-\delta t)}{2\delta t} \tag{A.7}$$

An alternative, velocity-dependent implementation of the Verlet equations has been proposed by Swope et al.[2] The velocity-Verlet algorithm is derived by defining a new function,

$$z(t)=\frac{r(t+\delta t)-r(t)}{\delta t} \tag{A.8}$$

Eqs. (A.3) and (A.4) can be rewritten in terms of z,

$$r(t+\delta t)=r(t-\delta t)+z(t-\delta t)\delta t \tag{A.9}$$

$$z(t)=z(t-\delta t)+f(t)\delta t \tag{A.10}$$

Similarly, the velocities can be expressed as,

$$v(t)=\frac{z(t)-z(t-\delta t)}{2} \tag{A.11}$$

Now expressions for the positions and velocities can be derived,

$$r(t+\delta t)=r(t)+v(t)\delta t+\frac{a(t)(\delta t)^2}{2} \tag{A.12}$$

$$v(t+\delta t)=v(t)+\frac{\left[a(t+\delta t)+a(t)\right]\delta t}{2} \tag{A.13}$$

Algorithmically, the calculation of the next MD time step occurs in three stages. In the first stage, Eq. (A.12) is used to calculate the positions at the next time step. Using these positions, the forces at this time step are calculated to determine the acceleration of the particles at this step. Now Eq. (A.13) is used to calculate the velocities at the next step, completing the integration of equations of motion for this time step.

This form of the Verlet equations has several advantages; the next point in phase space is now expressed only in terms of the positions and velocities at the current step, which simplifies the derivation of some algorithms and theorems. The algorithm also intrinsically generates velocities, which are needed to calculate some properties of a simulation, such as temperature or the velocity auto-correlation function. In some cases, the velocity-Verlet algorithm is also more numerically stable than the conventional Verlet algorithm.

A.2. Periodic Boundary Conditions

Many systems of interest to the simulation community have extremely long spatial length scales. These include periodic solids, liquids, and biological membranes, which are too large to represent in their full scales computationally. Instead, these systems are typically modeled using periodic boundary conditions, where a small but representative cell of the system is simulated and this cell is repeated infinitely in all spatial dimensions.

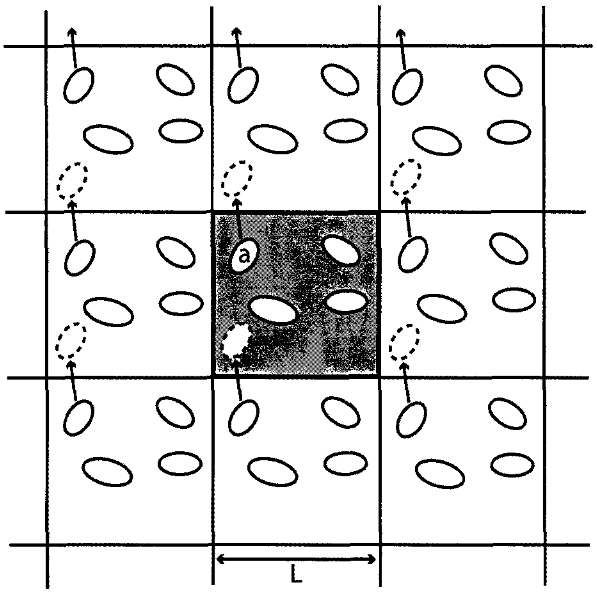

Figure A.1. A periodic system with length L in two dimensions. The central cell (grey) is repeated infinitely in both dimensions. Adapted from Ref. 3.

An MD simulation with periodic boundaries system can be performed using the same algorithms that are described in Section A.1 with a small modification due to the boundary conditions. The force between two atoms is calculated using the minimum distance between the pair for all the images of the particles in the neighbouring cells. As a particle in the central box and the images of this particle in neighbouring boxes move in an identical manner, a particle that crosses the boundary of the central box will re-enter the simulation on the opposite side of the box, resulting in periodic behaviour. Periodic boundary conditions eliminate so-called surface effects of non-periodic, *in vacuo* simulations, where contact between the edge of the system and the vacuum surrounding it introduces nonphysical effects.

A.3. Thermostats

As the equations of motion satisfy the law of conservation of energy, the sum of the potential (U) and kinetic (P) energies at each time step of the MD simulation will have a constant total energy (E), expressed in Eq. (A.14). These simulations will sample the microcanonical ensemble (NVE); a system of N particles, in a volume V, and a constant total energy of E.

$$U(r)+T(p)=E \tag{A.14}$$

The canonical ensemble (NVT), where the number of particles (N), the volume (V) and the temperature (T) are constant is often more relevant to chemical applications. To sample this ensemble using MD, it is necessary to employ a thermostat to maintain a constant temperature in the simulation. Although a great variety of thermostats have been developed, we will focus on the two used in this thesis.

A.3.1. The Andersen Thermostat

The Andersen thermostat maintains a constant temperature in a molecular dynamics simulation by coupling the simulation to a heat bath at the target temperature, T.[4] This is accomplished through stochastic collisions, where a velocity of a randomly selected particle in the MD simulation is replaced with a velocity drawn from a Maxwell-Boltzmann distribution corresponding to that temperature. This technique requires the researcher to choose the strength of the coupling between the heat bath and the system. This is defined by the coupling frequency (υ), which relates to the likelihood that a particle will undergo a collision with the heat bath.

A.3.2. Lowe-Andersen Thermostat

A minor variation to the Andersen thermostat that conserves linear and angular momentum has been proposed by Lowe.[5] This thermostat is advantageous for constant-temperature simulations of isolated molecules. These simulations are generally performed with zero translational and angular momentum; however, the stochastic collisions of an Andersen thermostat can induce translation or rotation of the molecule. The Lowe-Andersen thermostat avoids this by performing the stochastic collisions simultaneously on pairs of particles and only modifying the component of the velocity parallel to the line of centers. This has the effect of conserving the linear and angular momentum. The new velocities for a pair of particles (i and j) after a stochastic collision is given by,

$$\begin{aligned} v_i^* &= v_i - \left(\frac{\mu_{ij}}{m_i}\right)\left(\lambda - \left(v_i - v_j\right)\cdot\hat{\sigma}_{ij}\right)\hat{\sigma}_{ij} \\ v_j^* &= v_j + \left(\frac{\mu_{ij}}{m_j}\right)\left(\lambda - \left(v_i - v_j\right)\cdot\hat{\sigma}_{ij}\right)\hat{\sigma}_{ij} \end{aligned} \tag{A.15}$$

where $\hat{\sigma}_{ij}$ is the unit separation vector, m_i and m_j are the masses of particles i and j, respectively, and μ_{ij} is the reduced mass of the pair. λ is a stochastic variable defined as,

$$\lambda = \xi\sqrt{\frac{k_B T}{\mu_{ij}}} \tag{A.16}$$

where ζ is a random variable drawn from a Gaussian distribution of unit variance.

A.3.3. The Langevin Thermostat

The Langevin thermostat is another type of stochastic thermostat.[6] This thermostat functions by coupling each particle to a heat bath and a frictional force at every time step. As each particle is constantly under the effect of the heat bath and frictional force, particles that are moving faster or slower than the ensemble dictates will be rapidly adjusted. The equations of motion are modified to include the effect of the heat bath and the frictional force,

$$\frac{dv_i}{dt} = \frac{-\nabla_{r_i} U}{m_i} + \frac{R_i}{m_i} - \chi v_i \tag{A.17}$$

The first term on the r.h.s. the typical gradient-dependent term from Newton's second law. The second term on the r.h.s. is the random force (R_i) exerted by the heat bath. The third term on the r.h.s. is the frictional force, proportional to the velocity of the system, where χ is a positive frictional constant. The random force is generated such that is uncorrelated by particle and time,

$$\left\langle R_i(t) \cdot R_j(t') \right\rangle = 6\chi k_B T \delta_{ij} \delta(t - t') \tag{A.18}$$

References

1. Verlet, L. *Phys. Rev.* **1967**, *159*, 98.

2. Swope, W. C.; Andersen, H. C.; Berens, P. H.; Wilson, K. R. *J. Chem. Phys.* **1981**, *76*, 637.

3. Allen, M. P.; Tildesley, D. J. *Computer Simulation of Liquids*; Clarendon: Oxford, 1987.

4. Andersen, H. C. *J. Chem. Phys.* **1980**, *72*, 2384.

5. Koopman, E. A.; Lowe, C. P. *J. Chem. Phys.* **2006**, *124*, 204103/1.

6. Grest, G. S.; Kremer, K. *Phys. Rev. A* **1986**, *33*, 3628.

APPENDIX B

Calculation of the Potential of Mean Force

B.1. The Potential of Mean Force

The calculation of relative free energies is a longstanding and fundamental objective of computer simulations. A key concept used in these calculations is the potential of mean force (PMF), was introduced by Kirkwood to define the free energy of the system when one of its spatial coordinates holds a given value.[1] The PMF (W) is defined from the distribution function (ρ) of the system in the coordinate, denoted ξ,

$$W(\xi)=W(\xi^*)-k_BT\ln\left(\frac{\rho(\xi)}{\rho(\xi^*)}\right) \tag{B.1}$$

where $W(\xi^*)$ and ξ^* are arbitrary constants. In turn, these distribution functions can be defined from the configurational integrals over the spatial dimensions of the system,

$$\rho(\xi)=\frac{\int\exp\left(\frac{-U(r)}{k_BT}\right)\delta(\xi'-\xi)\,dr}{Z} \tag{B.2}$$

where U is the potential energy of the system at a given set of coordinates, r. Z is the configurational integral over all the spatial variables,

$$Z=\int\exp\left(\frac{-U(r)}{k_BT}\right)dr \tag{B.3}$$

B.2. Umbrella Sampling

In principle, the PMF could be calculated by directly determining the probability distribution along the coordinate from a sufficiently long MD simulation of the system then using Eq. (B.1) to determine the PMF. In practice this is generally not feasible, as the simulation must sample the full range of interest of the coordinate. A conventional MD simulation will predominantly sample the low energy sections of the coordinate, leaving the higher energy states insufficiently sampled.

Umbrella sampling was proposed by Valleau and Torrie as a general means to calculate free energy differences in systems where a conventional simulation will not sample all the states sufficiently to determine a the free energy differences between them with a high statistical accuracy.[2] Umbrella sampling introduces a weighting function that causes the simulation to sample the regions of phase space which have a low statistical weight within a Boltzmann distribution but are nevertheless important sections of the PMF. The resultant distributions are then corrected to eliminate the effect of this bias. For the purpose of calculating the PMF of a coordinate, umbrella sampling is typically performed by adding a bias potential (w) to the original potential of the system (U_o) (Eq. (B.4)).

$$U_{bias} = U_0 + w(\xi) \tag{B.4}$$

The bias potential is selected by the researcher to sample the configurational space of a section of the PMF coordinate more heavily. Although a broad range of bias potentials could be used, harmonic potentials are most common (Eq. (B.5)). In order to sample the PMF on the full range of interest, an umbrella sampling simulation typically consists of many simulations with different bias potentials ($w_i(\xi)$). Each of these biased simulations samples the region near the minimum of the harmonic bias potential ($\xi'\{i\}$).

$$w_i(\xi)=\frac{1}{2}k_i\left(\xi-\xi'\{i\}\right)^2 \tag{B.5}$$

The distribution function of a simulation with a bias potential $w_i(\xi)$ takes the form,

$$\rho_{bias}(\xi)=\frac{\int\delta(\xi-\xi')\exp\left(\frac{-U_{bias}}{k_BT}\right)dr}{\int\exp\left(\frac{-U_{bias}}{k_BT}\right)dr} \tag{B.6}$$

For a given bias potential, $w_i(\xi)$, the distribution function can be expressed as,

$$\rho_i(\xi)=\frac{\int\delta(\xi-\xi')\exp\left(\frac{-\left(U_0+w_i(\xi)\right)}{k_BT}\right)dr}{\int\exp\left(\frac{-\left(U_0+w_i(\xi)\right)}{k_BT}\right)dr} \tag{B.7}$$

As the bias potential is added to the unbiased potential and only depends on the coordinate ξ, it can be separated from the integral in the numerator entirely and factored from the unbiased potential term in the configurational integral in the denominator,

$$\rho_i(x_0)=\frac{\exp\left(\frac{-w_i(\xi)}{k_BT}\right)\int\delta(\xi-\xi')\exp\left(\frac{-U_0}{k_BT}\right)dr}{\int\exp\left(\frac{-w_i(\xi)}{k_BT}\right)\exp\left(\frac{-U_0}{k_BT}\right)dr} \tag{B.8}$$

This form allows the biased distribution to be related to the unbiased distribution, ρ_0,

$$\rho_i(\xi)=\frac{\exp\left(\frac{-w_i(\xi)}{k_BT}\right)\rho_0(\xi)}{\left\langle \exp\left(\frac{-w_i(\xi)}{k_BT}\right)\right\rangle_0}, \tag{B.9}$$

where $\langle\cdots\rangle_0$ is the ensemble average of an unbiased simulation. Substitution of Eq. (B.9) into (B.1) gives a new expression for the PMF using biased simulations,

$$W_i(x_0)=W(\xi^*)-k_BT\ln\left(\frac{\rho_i(\xi)}{\rho_0(\xi^*)}\right)-w_i(\xi)-k_BT\left\langle \exp\left(\frac{-w_i(\xi)}{k_BT}\right)\right\rangle_0 \tag{B.10}$$

The fourth term on the r.h.s. of Eq. (B.10) is not immediately available from the simulation, although for the purposes of calculating the PMF, it is not necessary to determine its value directly (*vide infra*). This term is defined as a constant corresponding to the free energy of introducing the biasing potential to the simulation,

$$F_i=-k_BT\left\langle \exp\left(\frac{-w_i(\xi)}{k_BT}\right)\right\rangle_0 \tag{B.11}$$

The presence of these F_i terms introduces a significant issue into the calculation of the PMF via an umbrella sampling simulation; as the PMF of each simulation will have a different, unknown constant F_i, the full PMF from all the biased simulations can not be combined immediately. This is resolved by selecting the biases such that adjacent distributions overlap. In this way, relative values of the F_i terms are selected so that the overlapping region of each section of the PMF can be aligned with the neighbouring biases to generate a continuous, complete PMF.

One drawback of umbrella sampling is that selecting the biases of the simulations to generate a complete PMF is an involved process. The biased simulations that are adjacent to each other must overlap significantly and be determined with high accuracy in the overlapping region in order for them to be aligned. This introduces a significant inefficiency into the simulation and requires the user to select bias potentials that satisfy these requirements and still sample the balance of the coordinate sufficiently.

B.3. The Weighted Histogram Analysis Method

The Weighted Histogram Analysis Method (WHAM) makes use of the concepts of umbrella sampling but is modified to be more efficient and robust.[3] The derivation of the WHAM equations we present here follows Ref. 4. The key advantage WHAM over traditional umbrella sampling is the automatic generation for the distribution function (ρ_o) from the unbiased distributions found from the biased simulations. The distribution function is expressed as a linear combination of the unbiased distribution functions,

$$\rho_0(\xi) = C\sum_{i}^{N_{hist}} P_i(\xi)\rho_i^{(u)}(\xi) \qquad \text{(B.12)}$$

N_{hist} is the number of the biased simulations, C is a normalization constant, and P_i is the weight of the i^th^ biased simulation. The distribution functions are represented as histograms and the term "weighted histogram analysis" refers to the determination of appropriate weights of these histograms to generate the final distribution, ρ_o. These weights are required to be normalized,

$$\sum_{i}^{N_{hist}} P_i = 1 \qquad \text{(B.13)}$$

The weights are determined so that they minimize the standard error of the final distribution function under the constraint imposed by Eq. (B.13). The standard error on ρ_o is a linear combination of the standard errors on the unbiased histograms, $\sigma^2\left[\rho_i^{(u)}(\xi)\right]$,

$$\sigma^2\left[\rho_0(\xi)\right]=C\sum_i^{N_{hist}}P_i^2\sigma^2\left[\rho_i^{(u)}(\xi)\right] \tag{B.14}$$

The method of Lagrange multipliers is used to determine the optimal values of P_i, where the function to minimize is,

$$\Lambda(P_i,\lambda)=C\sum_i^{N_{hist}}P_i^2\sigma^2\left[\rho_i^{(u)}(\xi)\right]+\lambda\left[\left(\sum_i^{N_{hist}}P_i\right)-1\right] \tag{B.15}$$

The setting the derivative with respect to the weights (P_i) to zero yields the first equation used in this minimization,

$$\frac{\partial\Lambda(P_i,\lambda)}{\partial P_i}=2C\cdot P_i\sigma^2\left[\rho_i^{(u)}(\xi)\right]+\lambda=0 \tag{B.16}$$

A second equation results from the normalization of weights constraint,

$$\frac{\partial\Lambda(P_i,\lambda)}{\partial\lambda}=\sum_i^{N_{hist}}P_i-1=0 \tag{B.17}$$

Eqs. (B.16) and (B.17) can be used to derive an expression for the probability weights,

$$P_i(\xi)=\frac{\lambda}{2C\sigma^2\left[\rho_i^{(u)}(\xi)\right]} \tag{B.18}$$

$$\sum_i^{N_{hist}}P_i(\xi)=\frac{\lambda}{2C}\sum_i^{N_{hist}}\sigma^2\left[\rho_i^{(u)}(\xi)\right]^{-1}=1 \tag{B.19}$$

Eqs. (B.18) and (B.19) can be combined to give an expression for the probability weights,

$$P_i(\xi)=\frac{\sigma^2\left[\rho_i^{(u)}(\xi)\right]^{-1}}{\sum_i^{N_{hist}}\sigma^2\left[\rho_i^{(u)}(\xi)\right]^{-1}} \tag{B.20}$$

Eq. (B.9) can be used to derive the standard error on the unbiased distributions from the standard error on the biased distributions they were generated from,

$$\sigma^2\left[\rho_i^{(u)}(\xi)\right]=\exp\left(2\beta\left(w_i(\xi)-F_i\right)\right)\sigma^2\left[\rho_i^{(b)}(\xi)\right] \tag{B.21}$$

The statistical error on the biased distribution can be estimated from

$$\sigma^2\left[\rho_i^{(b)}(\xi)\right]=\frac{1+\frac{\tau}{\delta t}}{n_i\Delta x_0}\overline{\rho_i^{(b)}(\xi)} \tag{B.22}$$

where $\overline{\rho_i^{(b)}(\xi)}$ is the biased distribution function of an infinitely long simulation, n_i is the number of samples in the simulation with that bias potential, τ is the correlation time of the sampling, and δt is the time step used in the simulation. $\overline{\rho_i^{(b)}(\xi)}$ is unknown, however we can approximate that the infinitely long simulation will yield the same result as the distribution function ρ_0 modified by the bias potential.

$$\overline{\rho_i^{(b)}(\xi)}=\exp\left(-\beta\left(w_i(\xi)-F_i\right)\right)\rho_0(\xi) \tag{B.23}$$

Substitution of Eqs. (B.21), (B.22), and (B.23) into (B.20), then cancelation of terms dependent on τ, δt, and $\Delta\xi$ provides a simple expression for the probability weights,

$$P_i(\xi)=\frac{n_i\exp\left(-\beta\left(w_i(\xi)-F_i\right)\right)}{\sum_j^{N_{hist}}n_j\exp\left(-\beta\left(w_j(\xi)-F_j\right)\right)} \tag{B.24}$$

Using Eq. (B.24), the weight of a given histogram at a point ξ can be determined from the number of samples in the simulations, the value of the bias potentials at the point ξ, and the constants F_i. While the other terms are immediately available, the values of F_i cannot be determined immediately from the simulations. Using Eq. (B.11), the optimal values of F_i can be determined by integrating the weighting function over the distribution function of the PMF coordinate,

$$F_i = -k_B T \ln\left(\int \exp\left(\frac{-w_i(\xi)}{k_B T} \right) \rho_0(\xi) d\xi \right) \tag{B.25}$$

Eq. (B.25) provides a means to estimate optimal values of F_i based on the distribution function. Although the values of F_i and ρ_0 are interdependent, an iterative process can be used to generate self-consistent values of these terms. An initial guess the $\{ F_i \}$ constants are generated and used to determine an initial distribution function. This distribution can be used to generate improved values of $\{F_i\}$, which are in turn used to generate a new ρ_o distribution. This process is continued until self-consistency is achieved.

The key advantage of WHAM over umbrella sampling is that many simulations can be combined trivially, with minimal involvement by the researcher. The PMF can be refined by incorporating additional biased simulations if sampling of one section of the PMF is insufficient. As in conventional umbrella sampling techniques, the histograms must overlap in order to determine the appropriate values of F_i; however, in practice WHAM is less sensitive to the overlap between distributions. This approach makes efficient use of the sampling, with each configuration contributing to the final PMF.

References

1. Kirkwood, J. G. *J. Chem. Phys.* **1935**, *3*, 300.

2. Torrie, G. M.; Valleau, J. P. *Chem. Phys. Lett.* **1974**, *28*, 578.

3. Kumar, S.; Rosenberg, J. M.; Bouzida, D.; Swendsen, R. H.; Kollman, P. A. *J. Comput. Chem.* **1992**, *13*, 1011.

4. Roux, B. *Comput. Phys. Commun.* **1995**, *91*, 275.

APPENDIX C

Unimolecular Reaction Rates

C.1. RRKM Theory

Predicting the rates of unimolecular reactions has been an objective of physical chemists since the earliest development of chemical kinetics.[1-3] Decomposition of a reaction intermediate is a preeminent example of a unimolecular reaction and statistical rate theories have been used extensively to predict the lifetimes of these species.

Unimolecular rate theories are based on the Lindemann mechanism, where a complex must have sufficient energy in its internal modes to surmount the reaction barrier. Through an intermolecular collision with another molecule (M), an activated complex (A^*) will form which has sufficient energy present to undergo the unimolecular reaction,

$$A + M \underset{k_{-1}}{\overset{k_1}{\rightleftharpoons}} A^* + M \tag{C.1}$$

Having formed this activated complex, the second step is the rearrangement of this species into the products (C.2).

$$A^* \xrightarrow{k_2} \text{Products} \tag{C.2}$$

The calculation of the rate, k_2, of this step has been the subject of a variety of rate theories. The theory of Rice, Ramsperger,[4] Kassel,[5] and Marcus[6] (RRKM) is a straightforward but remarkably successful model, which has led to its extensive application in unimolecular reaction kinetics. The basis of RRKM theory is a simple model of the PES of the reactant species (Figure C.1). For the basic, microcanonical model, the complex has a total energy, E, which is the sum of the potential and kinetic energies of the system. Decomposition of A* into the products occurs through intramolecular vibrational-energy redistribution (IVR) into one of the vibrational modes designated as the reaction coordinate. A transition state exists on this reaction coordinate with a barrier height of $E^{\ddagger}$. Complexes which cross this point on the reaction coordinate are assumed to proceed irreversibly towards decomposition into the products. Based on this model, a rate equation can be derived that calculates the rate of decomposition from the probability of localizing sufficient vibrational energy into the reactive mode for the complex to cross the TS.

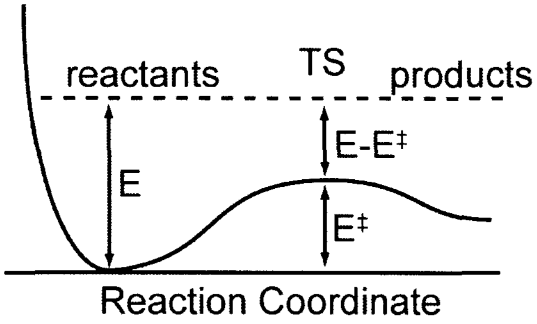

Figure C.1. Illustration of the RRKM model of a unimolecular reaction, showing the potential energy surface of the reaction coordinate in a system with a total energy of E and a barrier height of $E^{\ddagger}$.

The derivation of RRKM theory requires three definitions relating to phase space. The first is the phase space volume,

$$V_{PS} = \int_{H=0}^{H=E} \cdots \int dp_1 \cdots dp_m dq_1 \cdots dq_m \,, \tag{C.3}$$

which is the volume of phase space available to the system with a total energy in the range of energies from 0 to a maximum of E. This allows the number of states to be defined using a phase space integral,

$$N(E)=\frac{1}{h^m}\int_{H=0}^{H=E}\cdots\int dp_1\cdots dp_m dq_1\cdots dq_m \tag{C.4}$$

The sum of states (N) is the number of quantum states available to the system when the maximum energy is E. The number of states is simply the phase space volume divided by h^m, where m is the number of internal degrees of freedom in the complex.

The equation for the phase space volume also allows the definition of the density of states, ρ(E), which is the number of quantum states available in the system per unit energy. This density of states is simply the derivative of the number of states with respect to the energy,

$$\rho(E)=\frac{dN(E)}{dE} \tag{C.5}$$

Substitution of Eq. (C.4) into Eq. (C.5) yields an expression for the density of states as a phase space integral with a prefactor exponent of h,

$$\rho(E)=\frac{1}{h^m}\int_{H=E}\cdots\int dp_1\cdots dp_m dq_1\cdots dq_m \tag{C.6}$$

The RRKM rate equation is derived using phase space integrals for the coordinate and momentum space of the complex. The position and momenta of the system along the reaction coordinate are referred to using the variables $q^{\ddagger}$ and $p^{\ddagger}$ respectively. For a system of N molecules, the fraction of molecules at the transition state can now be expressed as the ratio of two phase space integrals,

$$\frac{d\mathbb{N}\left(p^{\ddagger},q^{\ddagger}\right)}{\mathbb{N}}=\frac{dp^{\ddagger}dq^{\ddagger}\int\cdots\underset{H=E-E^{\dagger}-\varepsilon_t}{\int}\cdots\int\cdots dp_1{}^{\ddagger}dq_1{}^{\ddagger}\cdots dp_{m-1}{}^{\ddagger}dq_{m-1}{}^{\ddagger}}{\int\cdots\underset{H=E}{\int}\cdots\int\cdots dp_1dq_1\cdots dp_mdq_m} \tag{C.7}$$

The term in the denominator represents the complete phase space integral over the m = 3N – 6 vibrational degrees of freedom of the complex subject to the restriction of a total energy of H. The term in the numerator integrates over all phase space in the transition state region, representing the volume of phase space in the range from $q^{\ddagger}$ to $q^{\ddagger} + dq^{\ddagger}$ and $p^{\ddagger}$ to $p^{\ddagger} + dp^{\ddagger}$. The integral covers this region of phase space under the restriction that the total energy of the system, H, is equal to $E - E^{\ddagger} - \epsilon_t$, where ϵ_t is the translational energy of the momentum, $p^{\ddagger}$, along the reaction coordinate. The total energy is reduced by $E^{\ddagger} + \epsilon_t$ in this integral because this amount of energy is not available to the remaining n – 1 coordinates of $p^{\ddagger}$ and $q^{\ddagger}$.

This expression of the number of molecules at the transition state can be used to derive an expression for the flux across the barrier, which is the reaction rate of unimolecular decay. This rate is simply the time derivative of $\mathbb{N}\left(p^{\ddagger},q^{\ddagger}\right)$,

$$rate=\frac{d\mathbb{N}\left(p^{\ddagger},q^{\ddagger}\right)}{dt}=\frac{1}{dt}\frac{\mathbb{N}dp^{\ddagger}dq^{\ddagger}\int\cdots\underset{H=E-E^{\dagger}-\varepsilon_t}{\int}\cdots\int\cdots dp_1{}^{\ddagger}dq_1{}^{\ddagger}\cdots dp_{m-1}{}^{\ddagger}dq_{m-1}{}^{\ddagger}}{\int\cdots\underset{H=E}{\int}\cdots\int\cdots dp_1dq_1\cdots dp_mdq_m} \tag{C.8}$$

The reaction coordinate is assumed to be separable from all other degrees of freedom, so the only the $dp^{\ddagger}$ and $dq^{\ddagger}$ are functions of time. The derivative of these two terms can be simplified using the definition of momentum from classical mechanics,

$$\begin{aligned}\frac{dp^{\ddagger}dq^{\ddagger}}{dt} &= \left(\frac{dp^{\ddagger}}{dt}\right)dq^{\ddagger} \\ &= \left(\frac{p^{\ddagger}}{u^{\ddagger}}\right)dq^{\ddagger}\end{aligned} \tag{C.9}$$

where $u^{\ddagger}$ is the reduced mass of the complex at the transition state. This can be further simplified by noting that the translational momentum in the $p^{\ddagger}$ coordinate can be expressed as its translation kinetic energy, ϵ_t. Implicit differentiation of Eq. (C.9) yields Eq. (C.10).

$$\begin{aligned}\varepsilon_t &= \frac{p^{\ddagger\,2}}{2\mu^{\ddagger}} \\ d\varepsilon_t &= \frac{p^{\ddagger}dp^{\ddagger}}{\mu^{\ddagger}}\end{aligned} \tag{C.10}$$

The result of these substitutions is a straightforward expression for the reactive flux.

$$rate = \frac{d\mathbb{N}\left(p^{\ddagger},q^{\ddagger}\right)}{dt} = \frac{\mathbb{N}d\varepsilon_t \underset{H=E-E^{\ddagger}-\varepsilon_t}{\int\cdots\int\cdots\int}\cdots dp_1^{\ddagger}dq_1^{\ddagger}\cdots dp_{m-1}^{\ddagger}dq_{m-1}^{\ddagger}}{\underset{H=E}{\int\cdots\int\cdots\int}\cdots dp_1dq_1\cdots dp_mdq_m} \tag{C.11}$$

This equation can be rewritten as,

$$rate = k\left(E,\varepsilon_t\right)\cdot\mathbb{N} \tag{C.12}$$

where k, the rate constant, is defined as,

$$k\left(E,\varepsilon_t\right) = \frac{d\varepsilon_t \underset{H=E-E^{\ddagger}-\varepsilon_t}{\int\cdots\int\cdots\int}\cdots dp_1^{\ddagger}dq_1^{\ddagger}\cdots dp_{m-1}^{\ddagger}dq_{m-1}^{\ddagger}}{\underset{H=E}{\int\cdots\int\cdots\int}\cdots dp_1dq_1\cdots dp_mdq_m} \tag{C.13}$$

Using Eq. (C.6) to replace the phase space integrals in (C.13) gives,

$$k\left(E,\varepsilon_t\right) = \frac{\rho\left(E-E^{\ddagger}-\varepsilon_t\right)}{h\rho\left(E\right)} \tag{C.14}$$

This rate constant is an expression for the reaction rate for a given value of translational energy, ϵ_t. The total rate is determined by integration over all possible values of ϵ_t, ranging from 0 to the entirety of the available energy, $E - E^{\ddagger}$,

$$\begin{aligned} k(E) &= \int_0^{E-E^{\ddagger}} k(E,\varepsilon_t)d\varepsilon_t \\ &= \int_0^{E-E^{\ddagger}} \frac{\rho\left(E-E^{\ddagger}-\varepsilon_t\right)}{h\rho(E)}d\varepsilon_t \end{aligned} \tag{C.15}$$

The integration of the density of states in the numerator results in the number of states in the range 0 to $E - E^{\ddagger}$ at the transition state. Thus, the RRKM expression for rate constant of a unimolecular reaction is,

$$k(E) = \frac{N^{\ddagger}\left(E-E^{\ddagger}\right)}{h\rho(E)} \tag{C.16}$$

Significantly, the expression for the microcanonical rate constant is now simply a ratio of the sum of states available at the transition state with the number of states in the reactant state. The number and density of states can be calculated by direct enumeration using the harmonic oscillator approximation, where the vibrational modes of the complex are represented by a set of m separable harmonic oscillators with vibrational frequencies, v_i. This can be achieved computationally using normal-mode analysis to compute the vibrational frequencies in the reactant and TS. See Appendix D for further details on the calculation of vibrational frequencies.

C.2. Classical RRKM Theory

The classical limit of RRKM theory can be derived by from Eq. (C.16) by using the harmonic oscillator expression for the density of states, where v_i is the set of vibrational frequencies of the transition state.

Within the harmonic oscillator approximation, the Hamiltonian of the complex is,

$$H = \sum_i^m \left(\frac{p_i^2}{2\mu_i} + \frac{k_i q_i^2}{2} \right) \tag{C.17}$$

Where p is the momentum along coordinate i, μ is the reduced mass of this coordinate, k is the force constant of the vibrational mode, and q is the displacement from the equilibrium value along this coordinate.

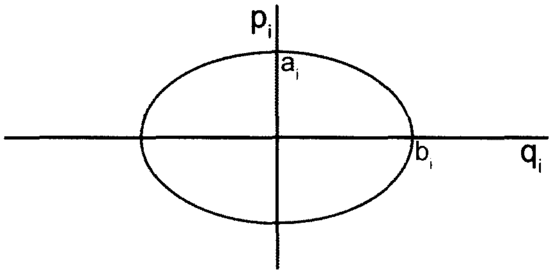

Figure C.2. Phase space volume of p_i and q_i variables of a harmonic oscillator with axis a_i and b_i.

A harmonic oscillator with constant energy E will follow a trajectory described by an ellipse in the coordinates q_i and p_i (Figure C.2), with axis a_i and b_i,

$$a_i = \sqrt{2\mu_i} \tag{C.18}$$

$$b_i = \sqrt{\frac{2}{k_i}} \tag{C.19}$$

$$E = \sum_i^m \left(\frac{p_i^2}{a_i^2} + \frac{q_i^2}{b_i^2} \right) \tag{C.20}$$

The phase space volume element corresponding to this oscillator is the volume of this ellipse. The volume of the full integral can be determined by transforming to a new set of coordinates ($p_i^{'} = p_i / a_i$ and $q_i^{'} = q_i / a_i$).

$$H = \sum_{i}^{m} \left(p_i^{'2} + q_i^{'2} \right) \qquad \text{(C.21)}$$

This casts the Hamiltonian in the form of an m dimensional hypersphere, which has a volume of,

$$V = \frac{\pi^m E^m}{m!} \qquad \text{(C.22)}$$

The transformation from coordinates $\left(p_i, q_i\right) \rightarrow \left(p_i^{'}, q_i^{'}\right)$ introduces an additional factor of $\prod_{i=1}^{m} a_i b_i$, so the final form of the phase space integral is,

$$V_{PS} = \frac{\pi^m E^m}{m!} \prod_{i=1}^{m} a_i b_i \qquad \text{(C.23)}$$

Substitution of Eq. (C.18) and Eq. (C.19) into Eq. (C.23) results in a simple expression for the phase space integral,

$$V_{PS} = \frac{E^s}{s!} \prod_{i=1}^{m} v_i \qquad \text{(C.24)}$$

where v_i is the i^{th} normal-mode vibrational frequency of the complex.

From this phase space volume, we can deduce expressions for the number of states and density of states of the forms,

$$N\left(E\right) = \frac{E^m}{m! \prod_{i=1}^{m} h v_i} \qquad \text{(C.25)}$$

$$\rho(E)=\frac{E^{m-1}}{(m-1)!\prod_{i=1}^{m}hv_i} \tag{C.26}$$

The sum of states at the transition state can be expressed using an analogous expression, where $v_i^{\ddagger}$ represents the vibrational frequencies of the complex at the transition state.

$$N^{\ddagger}\left(E-E^{\ddagger}\right)=\frac{\left(E-E^{\ddagger}\right)^{m-1}}{(m-1)!\prod_{i=1}^{m-1}hv_i} \tag{C.27}$$

When these expressions are substituted into the RRKM rate coefficient equation, factorial terms and of h cancel and a purely classical expression results,

$$k(E)=\left(\frac{E-E^{\ddagger}}{E}\right)^{m-1}\frac{\prod_{i=1}^{m}v_i}{\prod_{i=1}^{m-1}v_i^{\ddagger}} \tag{C.28}$$

Using this equation, the rate of unimolecular decomposition in the microcanonical ensemble can be calculated given the total energy, E, the barrier height, $E^{\ddagger}$, and the vibrational frequencies of the complex in the reactant state (v_i) and at the transition state ($v_i^{\ddagger}$).

C.3. Assumptions of RRKM Theory

There are several assumptions inherent to this implementation of the RRKM model. The first is the use of the harmonic oscillator approximation to represent the vibrational modes of the complex. Anharmonicity in these vibrational modes can cause the calculation of the number and density of states to be inaccurate;[7] however, because the rate coefficient is a ratio of the number of states at the transition state and the density of states of the reactants, these errors will partially cancel. Significantly, truly independent harmonic oscillators would be unable to accomplish the redistribution of kinetic energy required to undergo dissociation, so the presence of a small degree of anharmonicity is necessary for IVR to occur within this model.

The second critical assumption stems from the use of phase space integrals to derive the number and density of states of the transition state and reactant complex. This makes the implicit assumption that each volume element of phase space is populated statistically and all regions of phase space are correctly sampled. In practice, this means that the initial distribution of kinetic energy in the reactant complex is assumed to be random and IVR of energy occurs rapidly between all vibrational modes. Early experiments on the reaction of methylene with olefins provided strong support for rapid IVR;[8] however, this approximation can fail if kinetic energy is initially localized in specific vibrational modes and redistribution into other vibrational modes is slow. This behaviour is common in reaction intermediates, where excess kinetic energy is located in modes related in the initial reaction step. If the subsequent unimolecular reaction requires localization of kinetic energy in a reaction mode that is poorly coupled to these modes, RRKM theory may overestimate the rate of reaction. Conversely, if the unimolecular reaction coordinate is strongly coupled to modes that are vibrationally excited in the previous reaction step, RRKM theory can underestimate the reaction rate, as the reactive mode will have sufficient energy to cross the barrier almost immediately.

The last major assumption is that after crossing the transition state the system will irreversibly proceed to the product state without recrossing into the reactant form. This approximation causes RRKM theory to overestimate the reaction rate because trajectories that recross are counted as reactive within this theory. Situations where the total energy of the complex greatly exceeds the barrier height tend to have a greater degree of recrossing, as well some reactions where the topology of the potential energy surface favours reflection reactive trajectories back across the transition state after crossing the barrier. Generally, reactions with a large reverse barrier height have small probabilities of recrossing[9] and complexes with a large number of degrees of freedom tend not to recross, as the number of states at the transition state is small relative to the number of states in the products in large complexes.

Despite these assumptions, RRKM has been demonstrated to be a remarkably robust and reliable theory for modelling the kinetics of unimolecular reactions. Its success in calculating rate constants from very limited data about the reactant complex and the transition state has made it an ideal tool for computer modelling of unimolecular reactions and for comparison to experimental rate constants and lifetimes.

References

1. Robinson, P. J.; Holbrook, K. A. *Unimolecular Reactions*; Wiley-Interscience: London, 1972.

2. Baer, T.; Hase, W. L. *Unimolecular Reaction Dynamics*; Oxford University Press: New York, 1996.

3. Frost, W. *Unimolecular Reactions*; University Press: Cambridge, 2003.

4. Rice, O. K.; Ramsperger, H. C. *J. Am. Chem. Soc.* **1927**, *49*, 1617.

5. Kassel, L. S. *J. Phys. Chem.* **1928**, *32*, 225.

6. Marcus, R. A.; Rice, O. K. *J. Phys. Chem.* **1951**, *55*, 894.

7. Lourderaj, U.; Hase, W. L. *J. Phys. Chem. A* **2009**, *113*, 2236.

8. Butler, J. N.; Kistiakowsky, G. B. *J. Am. Chem. Soc.* **1960**, *82*, 759.

9. Cho, Y. J.; Vande Linde, S. R.; Zhu, L.; Hase, W. L. *J. Chem. Phys.* **1992**, *96*.

APPENDIX D

Free Energy Calculations with Static Calculations

D.1. Partition Functions

The calculation of free energies using static PES calculations is based definition of partition functions for the translational, rotational, the vibrational degrees of freedom of a molecule in the gas phase. We will briefly summarize these functions here. The full development of these equations is given in Ref. 1.

The translational partition function is,

$$q_{trans}(V,T)=\left(\frac{2\pi m k_B T}{h^2}\right)^{3/2} V \qquad \text{(D.1)}$$

This partition function depends on the mass of the complex (m) but is independent of the molecular structure.

The rotational partition function is,

$$q_{rot}(T)=\frac{\pi^{1/2}}{\sigma}\left(\frac{8\pi^2 I_A k_B T}{h^2}\right)^{1/2}\left(\frac{8\pi^2 I_B k_B T}{h^2}\right)^{1/2}\left(\frac{8\pi^2 I_C k_B T}{h^2}\right)^{1/2} \qquad \text{(D.1)}$$

The rotational partition function depends on the three moments of inertia of the molecule (I_A, I_B, and I_C) and the symmetry factor, σ.

The vibrational partition function, based on the quantum harmonic oscillator approximation is,

$$q_{vib}(T)=\prod_{i=1}^{3N-6}\frac{\exp\left(-h\nu_i/2k_B T\right)}{1-\exp\left(-h\nu_i/k_B T\right)} \qquad \text{(D.2)}$$

where v represents the normal-mode vibrational frequencies of the molecule. For a system of N indistinguishable particles, the partition function of the system is equal to,

$$Q = \frac{q^N}{N!} \tag{D.3}$$

For a given ensemble, the thermodynamic functions can now be derived from the partition functions. For instance, in the canonical ensemble (NVT), the Helmholtz free energy has simple logarithmic relationship to the partition function,

$$A(N,V,T) = -k_B T \ln Q(N,V,T) \tag{D.4}$$

D.2. Calculation of Vibrational Frequencies

The translational and rotational partition functions can be determined trivially based on the molecular structure; however, the vibrational frequencies of a molecule must be determined to calculate the vibrational partition function. This can be accomplished computationally through normal-mode analysis. Although this is an involved procedure, the basic process involves the calculation of the second derivations of the potential with respect to the displacements of the Cartesian coordinates (ξ) at a stationary point to generate the Hessian matrix for this molecule.[2]

$$f_{ij} = \left(\frac{\partial^2 V}{\partial \xi_i \partial \xi_j} \right)_0 \tag{D.5}$$

This Hessian matrix is mass-weighted, transformed into internal coordinates, and diagonalized to yield a set of eigenvalues (λ_i) that can be related to the vibrational frequencies of the molecule (v_i) using Eq. (D.6).

$$\nu_i = \sqrt{\frac{\lambda_i}{4\pi^2}} \tag{D.6}$$

D.3. Classical Free Energies

To make direct comparisons between free energies calculated using classical MD simulations and those calculated using static calculations, it is necessary to use expressions based on classical statistical mechanics rather than quantum statistical mechanics. This is accomplished by representing the vibrational modes of the complex as classical harmonic oscillators rather than quantum harmonic oscillators in the derivation of the vibrational partition function. The Hamiltonian of a system of 3N–6 independent classical harmonic oscillators is,

$$H\left(p_1, p_2, \ldots, p_{3N-6}, q_1, q_2, \cdots q_{3N-6}\right) = \sum_i^{3N-6} \frac{p_i}{2\mu_i} + \frac{k_i}{2} q_i^2 \tag{D.7}$$

where p_i and q_i are the momenta and displacements of the vibrational modes, respectively. Using this Hamiltonian, a classical partition function can be derived,

$$q_{class} = \frac{1}{h^{3N-6}} \int_{-\infty}^{\infty} \cdots \int_{-\infty}^{\infty} \exp\left(\frac{-p_i^2}{2\mu_i k_B T}\right) dp_1 \cdots dp_{3N-6} \int_{-\infty}^{\infty} \cdots \int_{-\infty}^{\infty} \exp\left(\frac{-k_i q_i^2}{2k_B T}\right) dq_1 \cdots dq_{3N-6} \tag{D.8}$$

after integration, this function becomes,

$$\begin{aligned} q_{class} &= \frac{1}{h^{3N-6}} \prod_i^{3N-6} \sqrt{2\pi\mu_i k_B T} \sqrt{\frac{2\pi k_B T}{k_i}} \\ &= \frac{1}{h^{3N-6}} \prod_i^{3N-6} 2\pi k_B T \sqrt{\frac{\mu_i}{k_i}} \end{aligned} \tag{D.9}$$

The vibrational frequency of a harmonic oscillator can be expressed in terms of its spring constant and reduced mass,

$$\nu_i = \frac{1}{2\pi}\sqrt{\frac{k_i}{\mu_i}} \tag{D.10}$$

Substitution of Eq. (D.10) into (D.9) gives,

$$q_{class} = \frac{1}{h^{3N-6}}\prod_{i}^{3N-6}\frac{2\pi k_B T}{\nu_i} \tag{D.11}$$

Using Eq. (D.11) with Eqs. (D.3) and (D.4) gives an expression for the change in Helmholtz free energy from state A to B that depends only of the vibrational frequencies of these molecules,

$$\Delta A = -RT\ln\left(\frac{\prod_{i}^{3N-6}\nu_{i;A}}{\prod_{i}^{3N-6}\nu_{i;B}}\right) \tag{D.12}$$

where $\nu_{i;A}$ and $\nu_{i;B}$ are the vibrational frequencies of the system in states A and B, respectively. Classical activation energies can also be calculated using this method, although in this instance, the vibrational mode in the reactants that corresponds to the reaction coordinate is excluded from the product over the vibrational modes (Eq. (D.13)).

$$\Delta A^{\ddagger} = -RT\ln\left(\frac{\prod_{i}^{3N-5}\nu_{i}}{\prod_{i}^{3N-5}\nu_{i}^{\ddagger}}\right) \tag{D.13}$$

References

1. McQuarrie, D. A. *Statistical Mechanics*; University Science Books: Sausalito, 2000.

2. Wilson, E. B.; Decius, J. C.; Cross, P. C. *Molecular Vibrations: The Theory of Infrared and Raman Vibrational Spectra* McGraw-Hill: New York, 1955.

APPENDIX E

Copyright Agreements

Copyright agreements from the following publishers are included in this appendix:

1. American Physical Society. Regarding work published in *J. Chem. Phys.* (Chapter 2).
2. American Chemical Society. Regarding work published in *Organometallics* (Chapters 3 and 6) and *J. Am. Chem. Soc.* (Chapter 4).
3. NRC Research Press. Regarding work published in *Can. J. Chem.* (Chapter 5).

1. American Chemical Society's Policy on Theses and Dissertations

Thank you for your request for permission to include **your** paper(s) or portions of text from **your** paper(s) in your thesis. Permission is now automatically granted; please pay special attention to the implications paragraph below. The Copyright Subcommittee of the Joint Board/Council Committees on Publications approved the following:

> Copyright permission for published and submitted material from theses and dissertations
> ACS extends blanket permission to students to include in their theses and dissertations their own articles, or portions thereof, that have been published in ACS journals or submitted to ACS journals for publication, provided that the ACS copyright credit line is noted on the appropriate page(s).
>
> Publishing implications of electronic publication of theses and dissertation material
> Students and their mentors should be aware that posting of theses and dissertation material on the Web prior to submission of material from that thesis or dissertation to an ACS journal may affect publication in that journal. Whether Web posting is considered prior publication may be evaluated on a case-by-case basis by the journal's editor. If an ACS journal editor considers Web posting to be "prior publication", the paper will not be accepted for publication in that journal. If you intend to submit your unpublished paper to ACS for publication, check with the appropriate editor prior to posting your manuscript electronically.

If your paper has **not** yet been published by ACS, we have no objection to your including the text or portions of the text in your thesis/dissertation in **print and microfilm formats**; please note, however, that electronic distribution or Web posting of the unpublished paper as part of your thesis in electronic formats might jeopardize publication of your paper by ACS. Please print the following credit line on the first page of your article: "Reproduced (or 'Reproduced in part') with permission from [JOURNAL NAME], in press (or 'submitted for publication'). Unpublished work copyright [CURRENT YEAR] American Chemical Society." Include appropriate information.

If your paper has already been published by ACS and you want to include the text or portions of the text in your thesis/dissertation in **print or microfilm formats**, please print the ACS copyright credit line on the first page of your article: "Reproduced (or 'Reproduced in part') with permission from [FULL REFERENCE CITATION.] Copyright [YEAR] American Chemical Society." Include appropriate information.

Submission to a Dissertation Distributor: If you plan to submit your thesis to UMI or to another dissertation distributor, you should not include the unpublished ACS paper in your thesis if the thesis will be disseminated electronically, until ACS has published your paper. After publication of the paper by ACS, you may release the entire thesis (**not the individual ACS article by itself**) for electronic dissemination through the distributor; ACS's copyright credit line should be printed on the first page of the ACS paper.

Use on an Intranet: The inclusion of your ACS unpublished or published manuscript is permitted in your thesis in print and microfilm formats. If ACS has published your paper you may include the manuscript in your thesis on an intranet that is not publicly available. Your ACS article cannot be posted electronically on a publicly available medium (i.e. one that is not password protected), such as but not limited to, electronic archives, Internet, library server, etc. The only material from your paper that can be posted on a public electronic medium is the article abstract, figures, and tables, and you may link to the article's DOI or post the article's author-directed URL link provided by ACS. This paragraph does not pertain to the dissertation distributor paragraph above.

2. American Institute of Physics License

AMERICAN INSTITUTE OF PHYSICS LICENSE
TERMS AND CONDITIONS

Oct 18, 2009

License Number	2292191430072
License date	Oct 18, 2009
Licensed content publisher	American Institute of Physics
Licensed content publication	Journal of Chemical Physics
Licensed content title	Generation of initial trajectories for transition path sampling of chemical reactions with ab initio molecular dynamics
Licensed content author	Christopher N. Rowley, Tom K. Woo
Licensed content date	Jan 14, 2007
Volume number	126
Issue number	2
Type of Use	Thesis/Dissertation
Requestor type	Author (original article)
Portion	Excerpt (> 800 words)
Title of your thesis / dissertation	Overcoming the Rare Event Problem for ab initio Molecular Dynamics Simulations of Organometallic Reactions using Transition Path Sampling

American Institute of Physics -- Terms and Conditions: Permissions Uses

American Institute of Physics ("AIP") hereby grants to you the non-exclusive right and license to use and/or distribute the Material according to the use specified in your order, on a one-time basis, for the specified term, with a maximum distribution equal to the number that you have ordered. Any links or other content accompanying the Material are not the subject of this license.

1. You agree to include the following copyright and permission notice with the reproduction of the Material: "Reprinted with permission from [FULL CITATION]. Copyright [PUBLICATION YEAR], American Institute of Physics." For an article, the copyright and permission notice must be printed on the first page of the article or book chapter. For photographs, covers, or tables, the copyright and permission

notice may appear with the Material, in a footnote, or in the reference list.

2. If you have licensed reuse of a figure, photograph, cover, or table, it is your responsibility to ensure that the material is original to AIP and does not contain the copyright of another entity, and that the copyright notice of the figure, photograph, cover, or table does not indicate that it was reprinted by AIP, with permission, from another source. Under no circumstances does AIP, purport or intend to grant permission to reuse material to which it does not hold copyright.

3. You may not alter or modify the Material in any manner. You may translate the Material into another language only if you have licensed translation rights. You may not use the Material for promotional purposes. AIP reserves all rights not specifically granted herein.

4. The foregoing license shall not take effect unless and until AIP or its agent, Copyright Clearance Center, receives the Payment in accordance with Copyright Clearance Center Billing and Payment Terms and Conditions, which are incorporated herein by reference.

5. AIP or the Copyright Clearance Center may, within two business days of granting this license, revoke the license for any reason whatsoever, with a full refund payable to you. Should you violate the terms of this license at any time, AIP, American Institute of Physics, or Copyright Clearance Center may revoke the license with no refund to you. Notice of such revocation will be made using the contact information provided by you. Failure to receive such notice will not nullify the revocation.

6. AIP makes no representations or warranties with respect to the Material. You agree to indemnify and hold harmless AIP, American Institute of Physics, and their officers, directors, employees or agents from and against any and all claims arising out of your use of the Material other than as specifically authorized herein.

7. The permission granted herein is personal to you and is not transferable or assignable without the prior written permission of AIP. This license may not be amended except in a writing signed by the party to be charged.

8. If purchase orders, acknowledgments or check endorsements are issued on any forms containing terms and conditions which are inconsistent with these provisions, such inconsistent terms and conditions shall be of no force and effect. This document, including the CCC Billing and Payment Terms and Conditions, shall be the entire agreement between the parties relating to the subject matter hereof.

This Agreement shall be governed by and construed in accordance with the laws of the State of New York. Both parties hereby submit to the jurisdiction of the courts of New York County for purposes of resolving any disputes that may arise hereunder.

2. NRC Research Press License

NRC RESEARCH PRESS LICENSE TERMS AND CONDITIONS

Oct 18, 2009

This is a License Agreement between Christopher N Rowley ("You") and NRC Research Press ("NRC Research Press") provided by Copyright Clearance Center ("CCC"). The license consists of your order details, the terms and conditions provided by NRC Research Press, and the payment terms and conditions.

License Number	2290010557491
License date	Oct 15, 2009
Licensed content publisher	NRC Research Press
Licensed content publication	Canadian Journal of Chemistry
Licensed content title	Computational design of ruthenium hydride olefin-hydrogenation catalysts containing hemilabile ligands[1,2]
Licensed content author	Christopher N. Rowley and Tom K. Woo
Licensed content date	Jul 1, 2009
Volume number	87
Issue number	7
Type of Use	Thesis/Dissertation
Requestor type	Author (original work)
Format	Print
Portion	Full article
Title of your thesis / dissertation	Overcoming the Rare Event Problem for ab initio Molecular Dynamics Simulations of Organometallic Reactions using Transition Path Sampling
Expected completion date	Dec 2009
Estimated size(pages)	200

General Terms & Conditions

Permission is granted upon the requester's compliance with the following terms and conditions:

1. A credit line will be prominently placed in your product(s) and include: for books the author, book title, editor, copyright holder, year of publication; for journals the author, title of article, title of journal, volume number, issue number, and the inclusive pages. The credit line must include the following wording: "© 2008 NRC Canada or its licensors. Reproduced with permission," except when an author of an original article published in 2009 or later is reproducing his/her own work.

2. The requester warrants that the material shall not be used in any manner that may be derogatory to the title, content, or authors of the material or to National Research Council Canada, including but not limited to an association with conduct that is fraudulent or otherwise illegal.

3. Permission is granted for the term (for Books/CDs-Shelf Life; for Internet/Intranet-In perpetuity; for all other forms of print-the life of the title) and purpose specified in your request. Once term has expired, permission to renew must be made in writing.

4. Permission granted is nonexclusive, and is valid throughout the world in English and the languages specified in your original request. A new permission must be requested for revisions of the publication under current consideration.

5. National Research Council Canada cannot supply the requester with the original artwork or a "clean copy."

6. If the National Research Council Canada material is to be translated, the following lines must be included: The authors, editors, and National Research Council Canada are not responsible for errors or omissions in translations.

v1.3

VITA

Name Christopher N. Rowley

Education Ph.D. (Chemistry)
University of Ottawa, 2005 – 2009 (Tom Woo)

B.Sc. Hons. Computational Chemistry with a minor in Mathematics
Carleton University, 2000 – 2004

Academic Honours and Awards

2010–2012	NSERC Postdoctoral Fellowship
2009	University of Ottawa Faculty of Science Teaching Assistant of the Year
2008	CSC Oral Presentation Award (Ottawa-Carleton Chemistry Institute 2008)
2007	Oral Presentation Competition (Inorganic Discussion Weekend 2007)
2007	Poster Competition, 2nd Prize (Inorganic Discussion Weekend 2007)
2006	Sun Microsystems of Canada Scholarship in the Computational Sciences and Engineering
2006	NSERC Postgraduate Scholarship – Doctoral Level
2005	Strategic Areas of Development Scholarship (University of Ottawa)
2005	Sun Microsystems of Canada Scholarship in the Computational Sciences and Engineering
2005	NSERC Postgraduate Scholarship – Master's Level
2004	Ontario Graduate Scholarship (Province of Ontario)
2004	Senate Medal for Academic Achievement (Carleton University)
2003–2004	The Canadian Society for Chemistry Medal (Carleton University)
2003–2004	Hyman Soloway Scholarship (Carleton University)
2002–2003	Dr. M. Ralph Berke Award in Chemistry (Carleton University)
2002–2003	A. Davidson Dunton Scholarship (Carleton University)

Papers

1. Rowley, C.N., Woo, T.K. New Shooting Algorithms for Transition Path Sampling: Centering Moves and Varied Perturbation Sizes for Improved Sampling. *J. Chem. Phys.* In press.
2. Tam, R.Y., Rowley, C.N., Petrov, I., Zhang, T., Afagh, N.A., Woo, T.K. Ben, R.N. Solution Conformation of C-Linked Antifreeze Glycoprotein Analogues and Modulation of Ice Recrystallization Inhibition (IRI) Activity. J. *Am. Chem. Soc.*, 131(43), 2009, 15745-15753
3. Rowley, C.N., Woo, T.K. Computational Design of Ruthenium Hydride Olefin-Hydrogenation Catalysts Containing Hemilabile Ligands. *Can. J. Chem.* 87 (7), 1030–1038, 2009, invited contribution for the Tom Ziegler special issue
4. Rowley, C.N., Mosey, N.J., Woo, T.K. A Computational Experiment of the endo vs. exo Preference in a Diels-Alder Reaction. *J. Chem. Ed.* 86 (2), 199-201, 2009
5. Rowley, C.N., Woo, T.K. Reaction Dynamics of β-Hydrogen Transfer in the Zirconocene Olefin Polymerization Catalyst: A DFT Path Sampling Study. *Organometallics.* 27(24), 6405-6407, 2008
6. Rowley, C.N., Ong, T.-G., Priem, J. Richeson, D., Woo, T. K. Analysis of the Critical Step in Catalytic Carbodiimide Transformation: Proton Transfer from Amines, Phosphines, and Alkynes to Guanidinates, Phosphaguanidinates, and Propiolamidinates with Li and Al Catalysts. *Inorg. Chem.* 47(24), 12024-12031, 2008
7. Rowley, C.N., van der Eide, E.F., Piers, W.E.; Woo, T.K. DFT Study of the Isomerization and Spectroscopic/Structural Properties of Ruthenacyclobutane Intermediates Relevant to Olefin Metathesis. *Organometallics.* 27 (23), 6043-6045, 2008
8. Rowley, C.N., Ong, T.-G. Priem, J., Richeson, D., Woo, T.K. Amidolithium and Amidoaluminum Catalyzed Synthesis of Substituted Guanidines: An Interplay of DFT Modeling and Experiment. *Inorg. Chem.*, 47 (20), 9660–9668, 2008
9. Rowley, C.N., Woo, T.K. A Path Sampling Study of Ru-Hydride Catalyzed H_2-Hydrogenation of Ethylene. *J. Am. Chem. Soc.*, 130 (23), 7218-7219, 2008
10. Dornan, P., Rowley, C.N., Priem, J., Barry, S.T., Woo, T.K. Richeson, D.S. Atom Efficient Cyclotrimerization of Dimethylcyanamide Catalyzed by Aluminium Amide: A Combined Experimental and Theoretical Investigation. *Chem. Commun.* 3645-3647, 2008

11. Rowley, C.N., Foucault, H.M., Woo, T.K.; Fogg, D.E. Mechanism of Olefin Hydrogenation Catalyzed by RuHCl(L)(PR_3)$_2$ Complexes (L = CO, PR_3): A DFT Study.*Organometallics*, 27 (8), 1661-1663, 2008
12. Rowley, C.N., Woo, T.K. Generation of initial trajectories for transition path sampling of chemical reactions with ab initio molecular dynamics. *J. Chem. Phys.*, 126, 024110-024118, 2007
13. Lafrance, M., Rowley, C.N.,Woo, T.K., Fagnou, K. Catalytic Intermolecular Direct Arylation of Perfluorobenzenes. *J. Am. Chem. Soc.* 128, 8754-8756, 2007
14. Brazeau, A.L., Wang, Z., Rowley, C.N., Barry, S.T. Synthesis and Thermolysis of Aluminum Amidinates: A Ligand-Exchange Route for New Mixed-Ligand Systems. *Inorg. Chem.*, 45 (5), 2276-2281, 2006
15. Rowley, C.N., DiLabio, G.A., and Barry, S.T. Theoretical and Synthetic Investigations of Carbodiimide Insertions into Al-CH_3 and Al-N(CH_3)$_2$Bonds. *Inorg. Chem.*, 44 (6), 1983-1991, 2005
16. Wright, J.S., Rowley, C.N., and Chepelev, L.L. A "universal" B3LYP-based method for gas-phase molecular dissociation enthalpy, ionization potential, electron and proton gas phase acidity. *Mol. Phys.* 103, (6-8), 815-823, 2005

Oral Presentations (presenter in **bold**)

1. **Rowley, C.N.** Woo, T.K. Simulating the dynamics of catalytic reactions: Using transition path sampling to overcome the rare event problem in QM/MM molecular dynamics. The 236th ACS National Meeting, Philadelphia, PA, USA. Aug. 17-21, 2008
2. **Rowley, C.N.** Woo, T.K. Simulating the "True" Dynamics of Catalytic Reactions. The 91st Canadian Chemistry Conference, Edmonton, AB, Canada. May 24-28, 2008
3. **Rowley, C.N.** Woo, T.K. Simulating Reaction Dynamics in Organometallic Chemistry. Ottawa-Carleton Chemistry Institute Day. Ottawa, ON., May 15, 2008 (awarded prize)
4. **Rowley, C.N.**, Woo. T.K. Simulating the Dynamics of Catalytic Reactions: Transition Path Sampling in Organometallic Chemistry Inorganic Discussion Weekend, Toronto, ON. Nov 2-4, 2007 (awarded prize)
5. **Rowley, C.N.**, Woo. T.K. Parallelization Methods for Transition Path Sampling for Rare Chemical Events. The 90th Canadian Chemistry Conference, Winnipeg, MB, Canada. May 26-30, 2007 (awarded first prize)

6. **Rowley, C.N.**, Foucault. H., Fogg, D., Woo. T.K. DFT Modeling of Alkene Hydrogenation by Ruthenium Hydride Catalysts. Inorganic Discussion Weekend, Ottawa, ON. Oct 27-29, 2006

Poster Presentations (presenter in **bold**)

1. **Rowley, C.N.**, Ong, T-G. Priem, J., Richeson, D., Woo T.K. Insight into the catalytic synthesis of substituted guanidines, phosphoguanidines, and propiolamines with amidolithium and amidoaluminum through DFT modeling. The 236th ACS National Meeting, Philadelphia, PA, USA. Aug. 17-21, 2008
2. **Rowley C.N.**, Foucault H.M., Fogg D.E., Woo T.K. Surprising Mechanistic Insights from DFT Modeling of Ruthenium Hydride Catalysts for Alkene Hydrogenation . The 90th Canadian Chemistry Conference, Winnipeg, MB, Canada. May 26-30, 2007. Also presented at the Inorganic Discussion Weekend, Toronto, ON, Canada, Nov 2-4, 2007 (awarded 2nd prize)
3. **Rowley, C.N.**, Woo. T.K. Computational Design of Amido Aluminum Catalysts for the Guanylation of Amines with Carbodiimide. Inorganic Discussion Weekend. Ottawa, ON. Oct 27-29, 2006
4. **Rowley, C.N.**, Woo. T.K. Generation of Initial Reactive Trajectories and Accelerated Sampling for Transition Path Sampling. 6th Canadian Computational Chemistry Conference. Vancouver, BC. July 26-30, 2008
5. **Rowley, C.N.**, Mosey, N.J., Woo. T.K, Techniques for efficiently studying reactive events with electronic structure based biasing and transition path sampling. 230th ACS National Meeting, Washington, DC. Aug 28-Sept 1, 2005
6. **Rowley, C.N.**, DiLabio, G.A, Barry, S.T., Mechanistic studies of carbodiimide insertions and ligand transfer reactions in aluminum amidinate. 230th ACS National Meeting, Washington, DC. Aug 28-Sept 1, 2005
7. **Rowley, C.N.**, Kenney, A.P., DiLabio, G.A, Barry, S.T., Synthesis and Theoretical Studies of Carbodiimide Insertions into Al-X Bonds to Form Novel Aluminum Amidinates for Atomic Layer Deposition. The 87th Canadian Chemistry Conference, London, ON, Canada. May 29 - June 1, 2004
8. **Rowley, C.N.**, Kenney, A.P., DiLabio, G.A., Barry, S.T., Synthesis of Novel Aluminum Amidinates. Ottawa-Carleton Chemistry Institute Poster Competition, Ottawa, ON, Canada. May 4, 2004
9. **Rowley, C.N.**, Wright, J.S., Mechanisms of Autoxidation: A DFT Study. The 86th Canadian Chemistry Conference, Ottawa, ON, Canada. August 14, 2003